# Studies of ionospheric parameters by means of electron plasma lines observed by EISCAT

P. Guio

*Université Joseph Fourier – Grenoble 1*
*Sciences & Géographie*

# THÈSE

présentée par

Patrick GUIO

pour obtenir le titre de

DOCTEUR DE L'UNIVERSITÉ JOSEPH FOURIER
et de
DOCTOR SCIENTARIUM DE L'UNIVERSITÉ DE TROMSØ

*Discipline : Astrophysique et milieux dilués*

---

# ÉTUDE DE PARAMÈTRES IONOSPHÉRIQUES À L'AIDE DES RAIES DE PLASMA ÉLECTRONIQUES OBSERVÉES À EISCAT

# STUDIES OF IONOSPHERIC PARAMETERS BY MEANS OF ELECTRON PLASMA LINES OBSERVED BY EISCAT

---

*Soutenue le 18 décembre 1998*

devant le jury composé de :

| | |
|---|---|
| M. Wlodek Kofman | *Président / Directeur de thèse* |
| M. Noralv Bjørnå | *Directeur de thèse* |
| M. Hans Pecseli | *Rapporteur* |
| M. Jean-Pierre Saint-Maurice | *Rapporteur* |

Thèse préparée à l'Université de Tromsø, Norvège

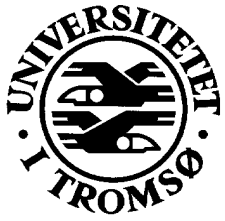

A DISSERTATION FOR THE DEGREE OF DOCTOR SCIENTARIUM
OF THE UNIVERSITY OF TROMSØ AND DOCTORAT DE
L'UNIVERSITÉ JOSEPH FOURIER - GRENOBLE 1

# Studies of ionospheric parameters by means of electron plasma lines observed by EISCAT

Patrick Guio

*October 1998*

Faculty of Science
Department of Physics
University of Tromsø, N-9037 Tromsø, Norway, Telephone +47 77 64 51 50, Telefax +47 77 64 55 80

Laboratoire des Images et des Signaux
ENSIEG
Université Jospeh Fourier, BP 53, 38041 Grenoble Cedex, France

First of all, a special thank to Noralv and Wlodek

Tusen Takk Margunn, Pierre, Jørn og Siv ....

som har hjelpt mæ og støttet mæ!!!!

Cesar, Christophe, Steinar, Tom, Anja og de andre ....

.... på Nordlysobservatoriet ....

.... og alle folkan på EISCAT ....

.... for gode diskusjoner om alt mulig !!!

Og mange andre i Tromsø ....

.... som har bidratt til et godt liv !!

Merci Jean, Maman, François, Pierre-Louis, Dominique, Béatrice ....

.... et tous ceux en France ....

qui m'ont supportés et aidés !!!!

The financial support from the Research Council of Norway ....

.... these years is also greatly appreciated

# Résumé

Ce travail présente une étude des raies de plasma observées à l'aide du radar à diffusion incohérente EISCAT. Le travail est centré sur deux points. Tout d'abord, la conception d'une expérience raies de plasma pour le radar EISCAT, avec une résolution spatiale améliorée. Puis, la comparaison de données raies de plasma acquises avec le radar EISCAT avec une théorie améliorée sur l'intensité et le décalage Doppler en fréquence des raies de plasma. Pour améliorer la résolution spatiale, nous avons conçu la première expérience raies de plasma mettant en œuvre la technique du code alternatif. Cette expérience a été tournée avec succès avec une résolution spatiale de $3\,\mathrm{km}$ au lieu de $40-50\,\mathrm{km}$ obtenu avec les techniques conventionnelles. Parce qu'il est très difficile de construire un modèle cohérent de la fonction de distribution des vitesses des électrons satisfaisant tous les intervalles d'énergies pertinents, nous avons construit une représentation adéquate de la distribution des vitesses des électrons en séparant la distribution en deux populations : la thermique et la suprathermique. La population thermique est représentée par la fonction de Spitzer qui tient compte de l'effet d'un champ électrique et/ou d'un gradient de température. La population suprathermique est déduite du flux angulaire d'énergie calculé grâce à un modèle numérique du transport des électrons. Un code numérique a été développé pour calculer la fonction diélectrique et la fonction réduite de distribution des vitesses pour toutes distributions des vitesses à deux dimensions dont nous avons besoin pour modéliser l'intensité et le décalage Doppler en fréquence des raies de plasma. Nous avons pu reproduire les caractéristiques de l'intensité et du décalage Doppler en fréquence des raies de plasma avec des données mesurées avec le radar VHF EISCAT. En particulier, nous avons identifié deux pics étroits dans la distribution des vitesses des suprathermiques comme la signature de la photo-ionisation de $\mathrm{N}_2$ et $\mathrm{O}$. Ces pics ont été observés sur les données. L'effet d'un gradient de température — qui produit une correction importante au décalage Doppler des raies de plasma — a été pris en compte plus précisement que précédemment en calculant numériquement les intégrales singulières, au lieu d'utiliser les premiers termes d'une expansion en séries comme auparavant. C'est important car cela a permis pour la première fois à un modèle de reproduire précisément l'intensité et le décalage Doppler des raies de plasma mesurés par une expérience EISCAT.

*Mots-clés* : EISCAT · distributions des vitesses électronique · dispersion de relation · ondes Langmuir

# Abstract

This work presents a study of the electron plasma lines observed by the incoherent scatter radar EISCAT. The work is focusing on two parts. On one hand, the design of a plasma line experiment for the EISCAT system with an improved spatial resolution. On the other hand, the comparison of the plasma line data collected with the EISCAT radar with an improved model for the intensity and the Doppler frequency shift of the plasma lines. In order to improve the spatial resolution of the plasma line experiment we have designed the first experiment that implements the recent technique of alternating code. The experiment has been run successfully with an altitude resolution of $3\,\mathrm{km}$ as opposed to $40-50\,\mathrm{km}$ obtained with the conventional techniques. Because it is very difficult to construct a self-consistent model of the velocity distribution function encompassing all of the relevant energy range, we have made an *ad hoc* model by separating the distribution into two parts: the thermal and the supra-thermal population. The thermal population is represented by the Spitzer function that takes into account the effect of an electric field and/or a temperature gradient. The supra-thermal population is derived from the angular energy flux of the supra-thermal electrons calculated by a numerical electron transport model. A numerical code has been developed to calculate the dielectric function and the reduced one-dimensional velocity distribution for any arbitrary two-dimensional velocity distribution which are needed to model the intensity and the Doppler frequency shift of the plasma lines. We have been able to reproduce peculiar features of the intensity as well as the Doppler shift of the plasma lines with data collected with the EISCAT VHF radar. Especially, two sharp peaks in the supra-thermal distribution were identified as the signature of photo-ionisation of $\mathrm{N}_2$ and $\mathrm{O}$ and were observed in the measured data. The effect of the temperature gradient — which produces a decisive correction to the Doppler shift of the plasma lines — was taken into account more accurately than previously by numerical evaluation of the singular integrals rather than by the use of the first terms of a series expansion as done in other studies. This is important because it has allowed a model for the first time to reproduce accurately the intensity and the Doppler shift of the plasma line as measured by actual experiment.

*Keywords*: EISCAT · electron velocity distribution function · dispersion relation · Langmuir waves

# Contents

# List of Figures

# List of Tables

*"Hver og en har sin måte å lære på", sa han til seg selv. "Hans måte er ikke min, og min måte er ikke hans. Men også han er på leting etter sin egen historie."*

Paulo COELHO, *Alkymisten*, 1988.

# Introduction

Among the planets of our solar system, the Earth presents the particularity to have both an atmosphere and an intrinsic magnetic field. Under the action of the photons created by the Sun, essentially EUV and UV, the constituents of the upper part of the neutral atmosphere, the thermosphere (approximately between $90\,\mathrm{km}$ and $2000\,\mathrm{km}$), are subject to ionisation processes. The ionised component of the thermosphere is called the ionosphere. In the lower part of the ionosphere and for normal conditions, the collision frequency between ions and neutral particles is important and the effect of the magnetic forces is weak so that the neutral atmosphere drives the behaviour of the ionosphere. In the upper part of the ionosphere, the gyro-frequency of the ionised particles is getting larger than the ion-neutral collision frequency and the charged particles are being trapped along the lines of the magnetic field. The region where the Earth's magnetic field exerts dominant control over the motions of charged particles is called the magnetosphere.

In the ionosphere, the gas contains enough ionised particles to cause measurable effects on the travel of radio waves. The incoherent scattering technique is a radar technique to sound the ionospheric plasma from about $60\,\mathrm{km}$ to over $1500\,\mathrm{km}$. Routinely, several such radar instruments around the world, measure the part of the spectrum called the ion line, a narrow double humped spectrum centred on the transmitted frequency. The ion line is the result of the scattering of the transmitted wave by ion acoustic waves travelling away and towards the transmitter, if backscatter, and for bi-static measurements, along the bisector between transmitted and received directions. Once the data are collected, mostly autocorrelation functions, a sophisticated analysis method based on inversion theory allows one to extract the plasma parameters such as the electron density, the electron and ion temperatures, the ion drift velocity and, in favourable conditions, the collision frequency and the ion composition.

The other main component of the incoherent scattering spectrum is called the electron plasma line. Electron plasma lines are the results of the scattering of the transmitted radio wave by natural Langmuir waves of the ionospheric plasma. Unlike the ion line, which is a narrow spectrum centred on the transmitted frequency,

the plasma lines consist of a pair of sharp spectral lines, Doppler shifted up and down with respect to the transmitted frequency corresponding to Langmuir waves travelling towards and away from the transmitter respectively, if backscatter, and for bi-static measurements, along the bisector between transmitted and received directions. The Doppler shift is roughly of the order of the plasma frequency, which is proportional to the square root of the electron density. Typically the plasma frequency varies between $2\,\mathrm{MHz}$ and $8\,\mathrm{MHz}$, depending on the altitude, the geographic location, the time and the solar activity.

The measurement of the plasma line using incoherent scattering radar technique is not as simple as the measurement of the ion line. In part due to the very low amount of scattered power in the lines — without any enhancement process, the intensity of the plasma line is expected to be less than one tenth of the intensity of the ion line — but also because of the time and space variations of the frequency of the plasma line itself due to variations of the electron density. But the measurement of these two narrow spectra provides supplementary and complementary informations to the one contained in the ion line. Particularly, at long term, the electron drift velocity would be an essential parameter to measure through the observation of plasma lines. Combined with the parameters provided by the ion line measurement, that would provide a *ground-based* technique to estimate the field-aligned electric currents independently of magnetic observations (Bauer *et al.*, 1976), which is by far the principal means of *in situ* field-aligned currents measurement, through satellite observations (Zmuda and Armstrong, 1974; Iijima and Potemra, 1976), or sounding rocket observations (Ledley and Farthing, 1974). But both the measurement technique and the theoretical understanding of the plasma lines are not yet properly developed for a correct estimation of the field-aligned currents.

The work presented in this thesis is focusing on the study of the plasma line and can be divided into two complementary parts: the design and implementation of a plasma line experiment as well as the reduction of the data, and the comparison and interpretation of the reduced data to a theoretical model of plasma line, especially an *ad hoc* representation of the electron distribution function.

The aim of the first part has been to design an experiment for the EISCAT (European Incoherent SCATter) radar systems, located in Northern Scandinavia, to collect both plasma line and ion line data, and to develop a suitable analysis tool to reduce the plasma lines data to parameters workable for the theoretical investigations, i.e. the frequency, the intensity and the width of the lines. The *long pulse* technique (Showen, 1979) and a similar technique, the chirp technique (Hagfors, 1982; Birkmayer and Hagfors, 1986) have been successfully used earlier to observe plasma lines at particular points of the ionosphere. The long pulse technique allows the measurement of the critical frequency at the peak or valley of the E- or F-region, while the chirp technique measures the plasma line at the altitude

where the electron density gradient matches the chirp rate of the transmitted pulse. These techniques do not provide many measurement points due to the mismatch between the scale height of the electron density and the receiver bandwidth/size of the probed volume by the pulse. Our objective when designing the experiment was to provide both high-frequency resolution measurements of the plasma lines and to improve the spatial resolution in order to increase the number of measurement points. The quality of the acquired data is essential for the further analysis of the spectra and the extraction of accurate parameters such as the difference in Doppler shift between the up- and down-shifted plasma lines and the intensity of the plasma lines. We have designed the first plasma line experiment at EISCAT that implements a recent incoherent scatter technique previously used for low altitude high resolution measurement of the ion line, the *alternating code* (Lehtinen and Häggström, 1987) which is a *phase coding* technique available at EISCAT. We performed successfully the first plasma line experiment using a $32\,\mathrm{bauds}$ strong condition alternating code on the EISCAT VHF radar system near Tromsø, Norway. To extract the frequency and intensity of both the up- and down-shifted plasma lines, a fitting routine built on a least-square minimisation method has been developed and implemented using the kernel of GUISDAP (Grand Unified Incoherent Scatter Data Analysis Program) of Lehtinen and Huuskonen (1996). This analysis program enables one to reduce data, either collected with the long pulse technique, or with the alternating code technique. It benefits from the commodity of GUISDAP, especially when it comes to the flexibility of handling new experiments.

In a second part, the data are compared with a theoretical model. The model consists in calculating both the plasma dielectric response function and the reduced one-dimensional distribution function. We have developed a numerical code to calculate these functions that lets us estimate theoretically the Doppler shift and the intensity of the plasma lines for any arbitrary two-dimensional velocity distribution function in spherical coordinates. Kofman *et al.* (1993) have shown, with UHF plasma lines data, that the thermal heat flow induced by a temperature gradient modifies the dispersion relation of the Langmuir waves and introduces a correction term in the estimate of the resonance frequency of the plasma lines. We have further investigated theoretically for the different EISCAT radars, the effect of a deviation of the distribution function from the Maxwellian on the frequency and intensity of the plasma lines. The effect of the fine structures in the energy range $20-30\,\mathrm{eV}$ of the supra-thermal population has been observed on data collected with the VHF radar and compared with our model. The model is based on the assumption that the the electron velocity distribution function can be represented to a good approximation by two parts: the thermal population and the supra-thermal population. The assumption is sensible for waves with phase energy far enough from the energy corresponding to the transition between ther-

mal and supra-thermal distribution ($0.15-0.3\,\mathrm{eV}$). For the VHF radar, the phase energy is in the range $12-25\,\mathrm{eV}$ and for the UHF radar it is in the range $3-6\,\mathrm{eV}$. The supra-thermal two-dimensional velocity distribution function is derived from the angular energy flux spectrum of the supra-thermal electrons calculated by a numerical model that solves a stationary electron transport equation along the magnetic field line, taking into account the collisions between a hot population of electrons (photoelectrons and/or precipitation) and the neutral atmosphere (Lummerzheim and Lilensten, 1994). This model has been widely tested against experiments and other models and has proved to have a very good behaviour to the data. The thermal part of the distribution function has been modelled by the classical two-dimensional velocity distribution of Spitzer and Härm (1953) which models the departure from the Maxwellian state as a consequence of either an electric field or a temperature gradient.

This thesis is built in the following way.

In Chapter 1, we introduce the theory of incoherent scatter and focus on the electron plasma line. We give a description of the numerical code we have developed to model the plasma line.

In Chapter 2, we describe the incoherent scatter measurement technique and focus on the experiments we designed.

In Chapter 3, we present the data reduction part.

In Chapters 4 and 5, we give a description of the theory which lies behind the model of the electron distribution that we used.

Following this introductory part, four articles are included, two of which are published and the other two are submitted for publication. References to these articles are found throughout the different introductory parts.

*"A chacun sa manière d'apprendre, se répétait-il* in petto. *Sa manière à lui n'est pas la mienne, et ma manière n'est pas la sienne. Mais nous sommes l'un et l'autre à la recherche de notre Légende Personnelle, et c'est pourquoi je le respecte."*

Paulo COELHO, *L'alchimiste*, 1988.

# Introduction (français)

Parmi les planètes de notre système solaire, la Terre présente la particularité de posséder à la fois une atmosphère et un champ magnétique. Sous l'action des photons crées par le Soleil, essentiellement EUV et UV, les constituants de la haute couche de l'atmosphère neutre, la thermosphère, située entre environ $90\,\mathrm{km}$ et $2000\,\mathrm{km}$, sont ionisés. La composante ionisée de la thermosphère est appelée l'ionosphère. Dans la partie inférieure de l'ionosphère, la fréquence de collisions entre les ions et les particules neutres est importante et l'effet des forces magnétiques est faible tel que l'atmosphère neutre force le comportement de l'ionosphère. Dans la partie supérieure de l'ionosphère, la fréquence de giration des particules ionisées devient plus grande que la fréquence de collisions entre ions et neutres et les particules chargées sont forcées de se déplacer le long des lignes du champ magnétique. La région où le champ magnétique terrestre exerce le contrôle du mouvement des particules chargées s'appelle la magnétosphère.

Dans l'ionosphère, le gaz contient suffisamment de particules ionisées pour modifier de façon mesurable le trajet des ondes radio. La technique de diffusion incohérente est une technique radar pour sonder le plasma ionosphérique à partir d'environ $60\,\mathrm{km}$ jusqu'à plus de $1500\,\mathrm{km}$. Ainsi, plusieurs radars à travers le monde, mesurent la partie du spectre à diffusion incohérente appelé la raie ionique, un spectre étroit et doublement épaulé centré sur la fréquence transmise. La raie ionique résulte de la diffusion de l'onde transmise par deux ondes accoustiques se déplaçant parallèlement et anti-parallèlement à la direction de transmission dans le cas d'un système simultané d'émission-réception et sinon le long de la bissectrice entre les directions de transmission et de réception. Une fois les données acquises, essentiellement des fonctions d'autocorrelation, une méthode sophistiquée d'analyse basée sur la théorie de l'inversion permet d'extraire les paramètres du plasma tels que la densité électronique, les températures électronique et ionique et dans certaines conditions la fréquence de collision et la composition ionique.

La deuxième composante essentielle du spectre à diffusion incohérente est appelée la raie de plasma ou raie électronique. La raie de plasma est le résultat de

la diffusion de l'onde transmise par une onde Langmuir du plasma ionosphérique. Contrairement à la raie ionique centrée sur la fréquence de transmission, les raies de plasma consistent en une paire de raies, dite basse et haute, très étroites, et décalées de part et d'autre de la fréquence transmise d'une valeur correspondant à deux ondes Langmuir se déplaçant parallèlement et anti-parallèlement à la direction de transmission dans le cas d'un système simultané d'émission-réception et sinon le long de la bissectrice entre les directions de transmission et de réception. Le décalage Doppler est de l'ordre de la fréquence plasma. Cette fréquence varie typiquement entre $2\,\mathrm{MHz}$ et $8\,\mathrm{MHz}$, en fonction de l'altitude, de la situation géographique, de l'heure et de l'activité solaire.

La mesure de la raie de plasma à l'aide de la technique de diffusion incohérente n'est pas une tâche aussi aisée que la mesure de la raie ionique. D'une part, du fait de la très faible quantité de puissance rétro-diffusée dans les raies plasma — sans mécanisme d'accroissement, l'intensité de la raie de plasma ne représente pas plus que le dixième de l'intensité de la raie ionique — d'autre part, à cause des variations temporelles et spatiales de la fréquence plasma elle-même due aux variations de la densité électronique. En contrepartie, la mesure de ces deux raies étroites apportent des informations complémentaires et supplémentaires aux informations contenues dans la raie ionique. En particulier, à long terme, la vitesse de dérive des électrons serait un paramètre essentiel à déterminer à l'aide de la diffusion incohérente. Combiné avec les paramètres déduits par la raie ionique, cela permettrait de mesurer les courants alignés à l'aide d'un instrument *sol*, indépendamment de mesures magnétiques (Bauer *et al.*, 1976), qui représente de loin le principal moyen de mesure *in situ* des courants alignés, soit par satellites (Zmuda and Armstrong, 1974; Iijima and Potemra, 1976) ou bien par sondes embarquées dans des fusées (Ledley and Farthing, 1974). Mais ni la technique d'observation, ni la compréhension théorique des raies de plasma ne sont correctement développées pour une estimation précise des courants alignés.

Le travail présenté dans cette thèse est centré sur l'étude des raies de plasma et se divise en deux parties complémentaires. La conception et la mise en œuvre d'une expérience raies de plasma ainsi que la réduction des données et la comparaison et l'interprétation des données avec un modèle, ce qui implique une représentation adéquate de la fonction de distribution des vitesse des électrons.

Le but de la première partie a été de concevoir une expérience pour le radar EISCAT (European Incoherent SCATter), situé au Nord de la Scandinavie, pour collecter des données raies de plasma et ionique, et développer un outil d'analyse adéquate pour réduire les données raies de plasma à des paramètres exploitables. Ces paramètres étant la fréquence, l'intensité et la largeur des raies. La technique de l'impulsion longue ou *"long pulse"* (Showen, 1979) et de la rampe de fréquence ou *"chirp"* (Hagfors, 1982; Birkmayer and Hagfors, 1986) ont déjà été utilisées avec succès pour observer la raie de plasma à des points particuliers de

l'ionosphère. La technique de l'impulsion longue permet de mesurer la fréquence critique aux pics et aux vallées des régions E et F de l'ionosphère et la technique de la rampe de fréquence permet la mesure à une altitude où le gradient de la densité électronique correspond au taux de rampe de fréquence transmise. Ces techniques ne fournissent pas énormément de points de mesures à cause du désaccord entre la hauteur d'échelle de la densité électronique d'une part, et la largeur de bande par rapport au volume sondé par l'impulsion d'autre part. Notre objectif a été de concevoir une expérience qui fournit à la fois une haute résolution fréquentielle de la raie de plasma et améliore la résolution spatiale afin d'accroître le nombre de points de mesure. La qualité des données acquises est essentielle pour l'analyse des spectres et l'extraction précise de paramètres tels que la différence Doppler entre la raie haute et basse ainsi que l'intensité des raies. Nous avons mis au point une expérience utilisant une technique récente de modulation déjà utilisée pour la mesure de la raie ionique, le *code alternatif* (Lehtinen and Häggström, 1987) qui est une technique de *codage de phase* disponible à EISCAT. Nous avons ainsi tourné la première expérience raie de plasma avec un code alternatif à condition forte de $32\,\mathrm{bauds}$ sur le radar VHF de EISCAT près de Tromsø en Norvège. Pour extraire la fréquence et l'intensité des raies de plasma, un programme d'ajustement de paramètres basé sur la minimisation par moindres carrés a été développé en utilisant le noyau de GUISDAP (Grand Unified Incoherent Scatter Data Analysis Program) de Lehtinen and Huuskonen (1996). Ce programme permet de réduire les données acquises avec la technique de l'impulsion longue ou bien la technique du code alternatif. Il bénéficie de la commodité de GUISDAP, en particulier dans sa flexibilité à traiter de nouvelles expériences.

Dans la seconde partie, les données réduites sont comparées à un modèle théorique. Le modèle est basé sur la connaissance de la réponse diélectrique du plasma ainsi que sur la fonction de distribution des vitesses réduite à une dimension. Nous avons développé un code numérique pour calculer ces fonctions. Ce qui nous permet d'estimer de manière théorique le décalage Doppler et l'intensité des raies de plasma pour n'importe quelle fonction de distribution de vitesses à deux dimensions décrites en coordonnées sphériques. Kofman *et al.* (1993) ont montré avec des données du radar UHF de EISCAT, que le chauffage thermique induit par le gradient de température des électrons modifiait la relation de dispersion des ondes Langmuir et introduisait une correction dans l'estimation de la fréquence de résonance des raies de plasma. Nous avons étudié pour les différents radars EISCAT, l'effet de la déviation de la distribution des vitesses par rapport à la Maxwellienne sur la fréquence et l'intensité des raies de plasma. L'effet des structures détaillées dans l'intervalle d'énergie $20-30\,\mathrm{eV}$ de la population suprathermique a été observé à l'aide du radar VHF et comparé avec notre modèle. Celui-ci est basé sur l'hypothèse que la fonction de distribution de vitesses des électrons peut être représentée avec une bonne approximation en deux populations : la ther-

mique et la suprathermique. Cette approximation est raisonnable pour des ondes ayant une énergie de phase suffisamment éloignée de l'énergie correspondant à la transition distribution thermique/suprathermique ($0.15-0.3\,\mathrm{eV}$). Pour le radar VHF, l'énergie de phase des ondes est de $12-25\,\mathrm{eV}$ et pour le radar UHF, elle est de $3-6\,\mathrm{eV}$. La fonction de distribution des vitesses des électrons est déduite du flux angulaire d'énergie des suprathermiques. Ce flux est calculé avec un code numérique qui résout l'équation de transport des électrons en régime stationnaire et le long du champ magnétique, en tenant compte des collisions entre la population chaude des électrons (photo-électrons et/ou précipitations électroniques) et l'atmosphère neutre (Lummerzheim and Lilensten, 1994). Ce modèle, largement testé et comparé avec des données et d'autres modèles du genre, a montré de bon résultats. La partie thermique de la distribution a été modélisée par la distribution classique de Spitzer and Härm (1953) qui décrit le départ d'une Maxwellienne du fait d'un champ électrique ou bien d'un gradient de température.

Cette thèse est construite de la manière suivante.

Dans le Chapitre 1, nous introduisons la théorie de la diffusion incohérente, en particulier sur la raie de plasma. Nous donnons une description du code numérique que nous avons développé pour modéliser la raie de plasma.

Dans le Chapitre 2, nous décrivons le principe de la mesure du spectre à diffusion incohérente à l'aide d'un radar, en particulier les expériences que nous avons écrites.

Dans le Chapitre 3, nous présentons la réduction des données.

Dans les Chapitres 4 et 5, nous donnons une description de la théorie qui sert au modèle de la fonction de distribution des vitesses que nous avons utilisé.

À la suite de cette partie, quatre articles sont inclus. Deux d'entre eux sont publiés et les deux autres sont soumis pour publication. Des références aux articles sont fournis tout au long de la première partie.

*"She looked at the steps; they were empty; she looked at her canvas; it was blurred. With a sudden intensity, as if she saw it clear for a second, she drew a line there, in the centre. It was done; it was finished. Yes, she thought, laying down her brush in extreme fatigue, I have had my vision."*

Virginia WOOLF, *To the Lighthouse*, 1927.

# Chapter 1

# Incoherent scatter theory

## 1.1 Introduction

As mentioned in the introduction, several parameters of the ionospheric plasma such as the electron density $n_e$, the electron and ion temperatures $T_e$ and $T_i$, the ion drift velocity $u_i$ and in some favourable cases the ion composition and the ion-neutral collision frequency $\nu_{in}$, can be derived from the scattering of radiation involving randomly distributed charges. Since the scattered power is inversely proportional to the square of the mass of the charge, the scattering from electrons dominates. Purely incoherent scattering occurs for radar wavelength $\lambda_0$ much smaller than the Debye length $\lambda_D$ of the medium. In this limit, the incident wave does not interact with the Debye-shielded charges and the scattering depends on the individual behaviour of charges. The scattering is then proportional to the electron velocity distribution function. When $\lambda_0$ is larger than $\lambda_D$, the shielding effects become important; as the electrons surround the ions in clouds such that the plasma remains neutral, the ion movement also controls the clouds of electrons and influences the property of the scattering. This is the condition of scattering we are interested in. A parameter commonly used in the literature (Bauer, 1975) to describe the type of scattering, which relates the scale of the observation to the characteristic scale of the plasma $1/\lambda_D$, is the dimensionless parameter $\alpha$ defined as

$$\alpha = \frac{1}{k\lambda_D}, \tag{1.1}$$

where $k$ is the magnitude of the scattering wave vector determined by the geometry of the experiment and the magnitude of the radar wave vector $k_0$ which is defined in Eq. (1.4).

Assuming the plasma to be *uniform* and *stationary*, the differential scattering cross section of the plasma is defined by (Hagfors, 1977)

$$\frac{d^2\sigma(\omega+\omega_0)}{d\Omega d\omega} = r_e^2|\boldsymbol{n}\times(\boldsymbol{n}\times\boldsymbol{p})|^2\langle|\Delta N_e(\boldsymbol{k},\omega)|^2\rangle, \tag{1.2}$$

where $r_e^2 = e^2/(4\pi\epsilon_0 m_e c^2)$ is the classical electron radius, $\boldsymbol{n}$ is the unit vector pointing from the scattering volume towards the receiver, $\boldsymbol{p}$ is the unit polarisation vector of the incident radiation, $\omega$ is the frequency shift between the transmitted radio wave $\omega_0$ and the received frequency $\omega_r$, $\boldsymbol{k}$ is the wave vector shift defined as the difference between the returned wave vector and the transmitted wave vector $\boldsymbol{k_0}$. $\omega$ and $\boldsymbol{k}$ are defined by

$$\omega = \omega_r - \omega_0, \tag{1.3}$$

$$\boldsymbol{k} = \frac{\omega_r}{c}\boldsymbol{n} - \boldsymbol{k_0}. \tag{1.4}$$

The quantity $\Delta N_e(\boldsymbol{r},t)$ represents the *fluctuations* of the microscopic electron density $N_e(\boldsymbol{r},t)$ relatively to its *average* $n_e = \langle N_e(\boldsymbol{r},t)\rangle$. The differential scattering cross section then corresponds to a particular spatial Fourier component of the fluctuation $\Delta N_e(\boldsymbol{r},t)$. This fluctuation is a purely real random process. Its time Fourier transform might not be defined, it is therefore necessary to calculate its autocorrelation function which has Fourier transform (Trulsen and Bjørnå, 1977)

$$\langle|\Delta N_e(\boldsymbol{k},\omega)|^2\rangle = \iint\langle\Delta N_e(\boldsymbol{r},t)\Delta N_e(\boldsymbol{r}+\boldsymbol{r'},t+\tau)\rangle e^{i(\omega\tau-\boldsymbol{k}\cdot\boldsymbol{r'})}d^3\boldsymbol{r'}\frac{d\tau}{2\pi}. \tag{1.5}$$

This expression is a version of the *Wiener-Khinchin theorem* in the theory of random noise. The problem is to estimate the power spectrum of the electron density fluctuations in the frequency and wave vector space $\langle|\Delta N_e(\boldsymbol{k},\omega)|^2\rangle$.

## 1.2 Incoherent scattering differential cross section

Several approaches have been used to calculate the thermal fluctuation of Eq. (1.5). The first approach, the dressed test particle principle (Rosenbluth and Rostoker, 1962; Rostoker, 1964), does not make any other assumptions about the state of the plasma than uniformity and stationarity. The second approach uses the fluctuation-dissipation theorem or Nyquist theorem and can be found in numerous articles in the literature (Dougherty and Farley, 1960; Farley *et al.*, 1961; Dougherty and Farley, 1963; Farley, 1966) and the third approach uses a perturbation method of a linearised Vlasov equation (Salpeter, 1960; Hagfors, 1961). In addition to the uniformity and stationarity assumptions, they require that each

species of the plasma should be in the Maxwellian state. The theory of thermal fluctuation for a non-uniform and non-stationary plasma has been developed (Weinstock, 1965, 1967) and is based on a separation of the scattering into coherent and incoherent parts. This theory might be of interest for disturbed conditions but is out of the scope in this study.

Finally, the differential scattering cross section $d^2\sigma/d\Omega d\omega$ per angular frequency $\omega$ and per solid angle $\Omega$ for a multi-component, uniform, stationary, non-magnetised and non-relativistic plasma with the collision effects included through a BGK model (Bhatnagar *et al.*, 1954) is then given by (Hagfors, 1961; Sheffield, 1975; Bjørnå and Trulsen, 1986)

$$\frac{d^2\sigma}{d\Omega d\omega} = n_e r_e^2 |\boldsymbol{n}\times(\boldsymbol{n}\times\boldsymbol{p})|^2 S(\boldsymbol{k},\omega), \tag{1.6}$$

where the spectral density function or dynamic structure factor $S$ (Ichimaru, 1992) is calculated using plasma theory.

$$S(\boldsymbol{k},\omega) = \left|1+\frac{C_e(\boldsymbol{k},\omega)}{D(\boldsymbol{k},\omega)}\right|^2 \frac{\operatorname{Im} P_e(\boldsymbol{k},\omega) - \nu_e\,|P_e(\boldsymbol{k},\omega)|^2}{\pi|X_e(\boldsymbol{k},\omega)|^2} + \sum_j \frac{n_j}{n_e} z_j^2 \left|\frac{C_e(\boldsymbol{k},\omega)}{D(\boldsymbol{k},\omega)}\right|^2 \frac{\operatorname{Im} P_j(\boldsymbol{k},\omega) - \nu_j\,|P_j(\boldsymbol{k},\omega)|^2}{\pi|X_j(\boldsymbol{k},\omega)|^2} \tag{1.7}$$

with

$$D(\boldsymbol{k},\omega) = 1 - \sum_\alpha C_\alpha(\boldsymbol{k},\omega), \tag{1.8}$$

$$C_\alpha(\boldsymbol{k},\omega) = Z_\alpha(\boldsymbol{k},\omega)/X_\alpha(\boldsymbol{k},\omega), \tag{1.9}$$

$$X_\alpha(\boldsymbol{k},\omega) = 1 + i\nu_\alpha P_\alpha(\boldsymbol{k},\omega), \tag{1.10}$$

$$Z_\alpha(\boldsymbol{k},\omega) = \sum_k Z_{\alpha,k}(\boldsymbol{k},\omega), \tag{1.11}$$

$$P_\alpha(\boldsymbol{k},\omega) = \frac{1}{n_\alpha}\sum_k n_{\alpha,k} P_{\alpha,k}(\boldsymbol{k},\omega), \tag{1.12}$$

$$Z_{\alpha,k}(\boldsymbol{k},\omega) = \frac{\omega_{\alpha,k}^2}{k^2}\int_{\mathrm{L}} \frac{\boldsymbol{k}\cdot\boldsymbol{\nabla}_{\boldsymbol{v}} f_{\alpha,k}(\boldsymbol{v})}{\boldsymbol{k}\cdot\boldsymbol{v} - \omega - i\nu_\alpha} d^3\boldsymbol{v}, \tag{1.13}$$

$$P_{\alpha,k}(\boldsymbol{k},\omega) = \int_{\mathrm{L}} \frac{f_{\alpha,k}(\boldsymbol{v})}{\boldsymbol{k}\cdot\boldsymbol{v} - \omega - i\nu_\alpha} d^3\boldsymbol{v}. \tag{1.14}$$

$f_{\alpha,k}$ denotes the velocity probability distribution function for the $k^{\mathrm{th}}$ component of the particle species $\alpha$ ($e$ for the electrons and $j$ for the ions). $D$ and $Z_\alpha$ are

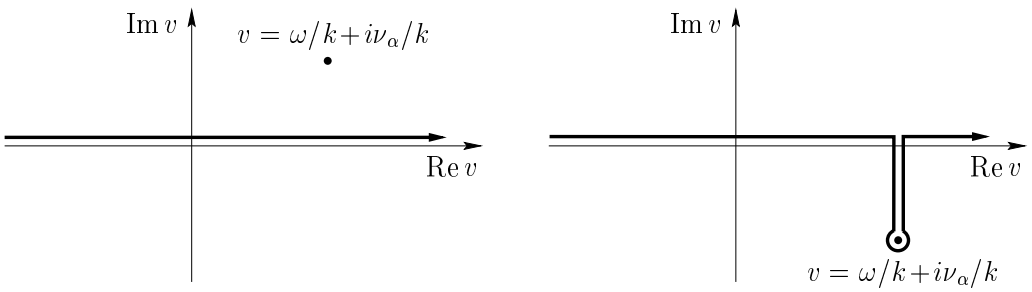


Figure 1.1: Landau contour of integration used to evaluate the integrals $Z$ and $P$ of Eq. (1.13) and (1.14). In the left panel, $\nu_\alpha > 0$ while in the right panel $\nu_\alpha < 0$

respectively the dispersion function and the susceptibility function for the particle species $\alpha$ and $\nu_\alpha$ is the collision frequency of species $\alpha$. $\omega_{\alpha,k}$ is the plasma frequency of the $k^{\text{th}}$ component of the species $\alpha$ defined as

$$\omega_{\alpha,k} = \sqrt{\frac{4\pi n_{\alpha,k} e^2}{m_\alpha}}, \qquad [\text{rad}\,\text{s}^{-1}] \tag{1.15}$$

where $n_{\alpha,k}$ is the density of the $k^{\text{th}}$ component of the species $\alpha$ in $\text{cm}^{-3}$. Note that whenever not specified, the Gaussian CGS unit system is used.

The contour $\text{L}$ of the integrals $P$ and $Z$ is the Landau contour of integration. These integrals are defined only on the half-plane where $\nu_\alpha > 0$ (left panel in Figure 1.1). The analytical continuation of these functions from the upper to the lower half-plane is given by the Landau prescription. When $\nu_\alpha < 0$, the contour is deformed to leave the pole at $\boldsymbol{v}$ such that $\boldsymbol{k} \cdot \boldsymbol{v} - \omega - i\nu_\alpha = 0$ over the contour of integration (right panel in Figure 1.1).

Figures 1.2 and 1.3 show the theoretical incoherent scattering spectra for a Maxwellian plasma for positive frequencies calculated for the EISCAT VHF and UHF radars respectively. Both abscissae and ordinate have logarithmic scale to accommodate the large range of intensity and frequency. The main spectral shape from 0 to a few $\text{kHz}$ is the ion line while the sharp line above $1\,\text{MHz}$ is the plasma line. Note the value of the parameter $\alpha = 1/(k\lambda_D)$ for the two different radars — for the VHF radar $\alpha = 10.9$ and for the UHF radar $\alpha = 2.6$ —. As expected the collective effect is more important with the VHF radar than with the UHF radar. The plasma line observed with the VHF radar is sharper because the associated Langmuir wave has a phase velocity situated far on the tail of the electron velocity distribution which causes little Landau damping.

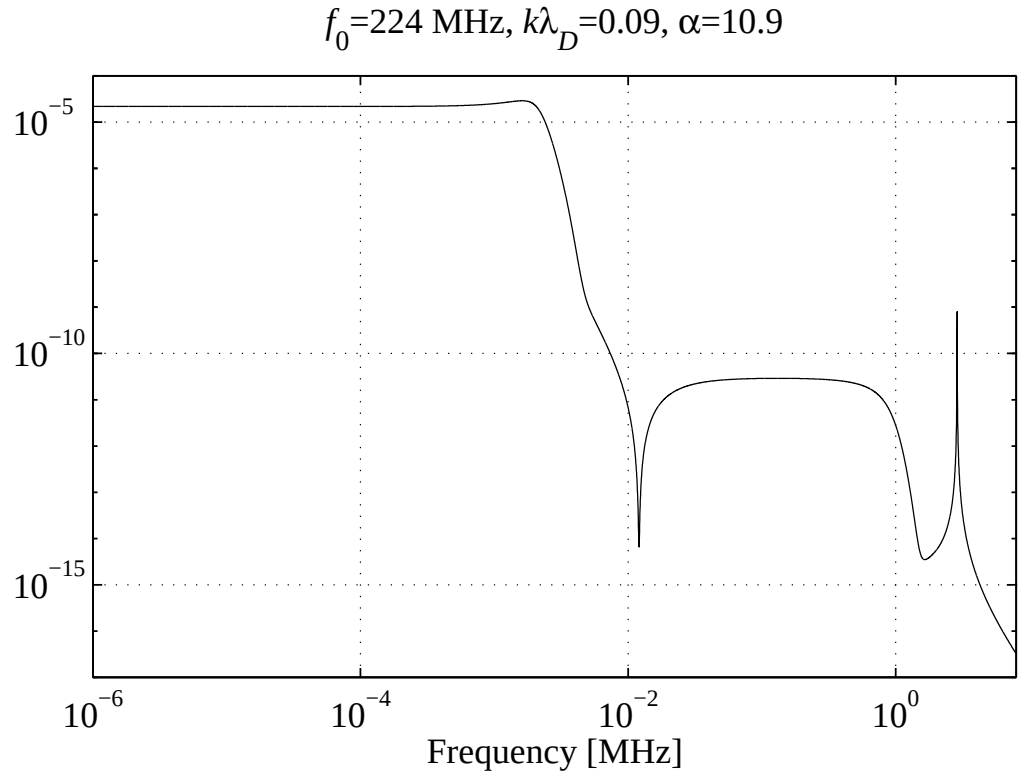


Figure 1.2: Theoretical incoherent scatter spectrum for the VHF EISCAT radar (224 MHz) for a Maxwellian plasma with $n_e = 10^5\,\mathrm{cm}^{-3}$, $T_e = 2000\,\mathrm{K}$, $T_i = 1500\,\mathrm{K}$, $\nu_i = 10^{-2}\,\mathrm{s}^{-1}$ and $\nu_e = 10^2\,\mathrm{s}^{-1}$ and using the differential cross section model of Eqs. (1.7) – (1.14)

## 1.3 The electron plasma line

When studying plasma lines, the expression of the scattering cross section can, to a good approximation, be simplified. The second term of Eq. (1.7) is small compared to the first term in the frequency range of the plasma line and can therefore be neglected. Assuming moreover that collisions can be neglected, the expression of the spectral density function can be approximated to

$$S(\boldsymbol{k},\omega) = \frac{f_e^1\left(\frac{\omega}{k}\right)}{k|1 - Z_e(\boldsymbol{k},\omega)|^2}, \tag{1.16}$$

where $f_e^1$ is the one-dimensional reduced probability distribution function parallel to the wave vector $\boldsymbol{k}$ and it is defined by

$$f_e^1\left(\frac{\omega}{k}\right) = k\int f_e(\boldsymbol{v})\delta(\boldsymbol{k}\cdot\boldsymbol{v} - \omega)d^3\boldsymbol{v}, \tag{1.17}$$

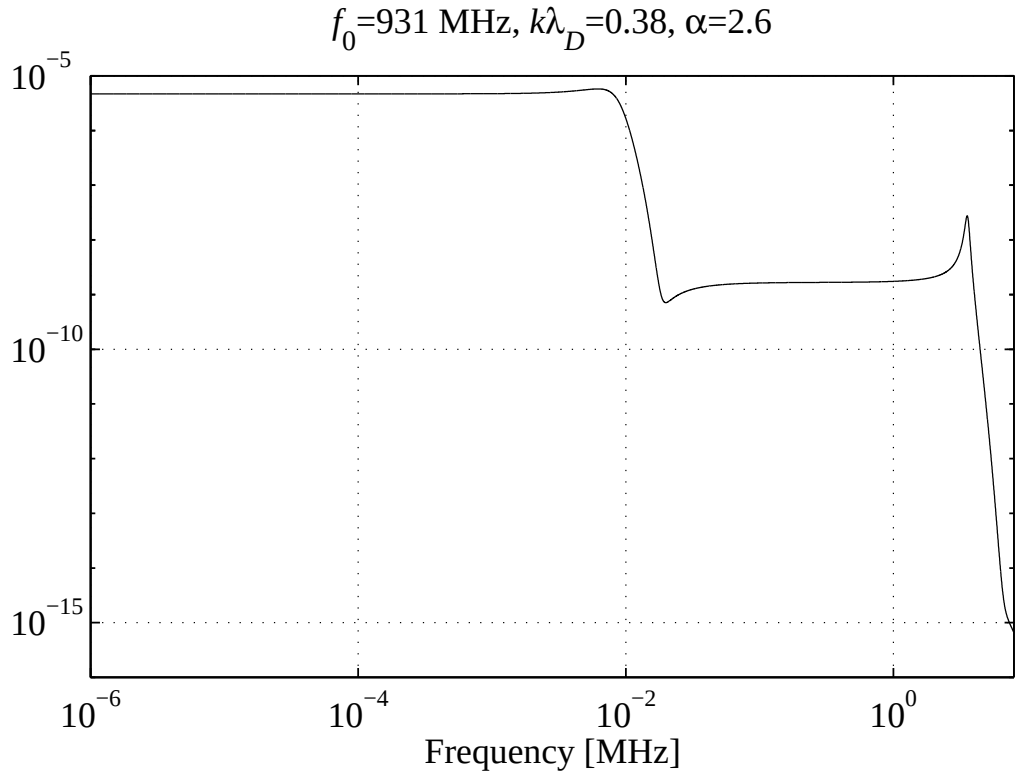


Figure 1.3: Theoretical incoherent scatter spectrum for the UHF EISCAT radar ($931\,\mathrm{MHz}$) for a Maxwellian plasma with the same ionospheric parameters as in Figure 1.2 and using the differential cross section model of Eqs. (1.7) – (1.14)

where $\delta$ represents the one-dimensional Dirac delta function.

In Eq. (1.16), the denominator represents the *dielectric response function* of the medium. Langmuir waves are high-frequency solutions of the *dispersion relation*. The dispersion relation is just the dielectric response function set equal to zero. The frequency of the wave with wave vector $\boldsymbol{k}$ is given by the real part of the complex frequency $\omega$ while the imaginary part gives the damping rate of the wave. For a given radar, two Langmuir waves will interact with the particles, one travelling away from and the other one travelling toward the radar in the backscatter geometry and otherwise along the bisector between the directions of transmission and reception. At such high phase velocity $v_\phi = \omega/k$, the electron distribution function is flattening out and there are nearly as many particles moving faster than the wave as there are particles moving slower, the wave is very little damped. The so-called Landau damping, which is proportional to the derivative of the reduced distribution at the phase velocity for an isotropic plasma, is small and the up- and down-shifted plasma lines at frequency $\omega_+ = \omega_{r+} - \omega_0$ and $\omega_- = \omega_{r-} - \omega_0$ are

respectively the signature of the Langmuir waves travelling along $\boldsymbol{k}_+$ and $\boldsymbol{k}_-$ with magnitude, in a backscatter geometry

$$k_\pm = \frac{1}{c}(\omega_0 + \omega_0 + \omega_\pm). \tag{1.18}$$

### 1.3.1 Intensity

The derivation of the intensity of the plasma line does not require the measurement of the spectrum. It is given by the value of the autocorrelation function at time delay $\tau = 0$ (*Parseval's theorem*), which can be estimated by power profile measurement with an incoherent scatter radar. It has been observed at different incoherent scatter radar facilities and is discussed in many papers, for instance Perkins and Salpeter (1965); Kofman *et al.* (1982); Fredriksen *et al.* (1989, 1992); Kirkwood *et al.* (1995).

In a collisionless plasma without a magnetic field and with the assumption that the electron velocity distribution function is *isotropic* but *not* necessarily Maxwellian, the incoherent scattering spectrum can be approximated in the neighbourhood of the up- and down-shifted plasma lines frequencies $\omega_\pm$ by the following expression (Perkins and Salpeter, 1965)

$$S_\pm(\boldsymbol{k},\omega) \simeq \frac{\omega_\pm^2 f_e^1(v_{\phi\pm})}{4k\left((\omega-\omega_\pm)^2 + \frac{\omega_\pm^2}{4}\left(\pi\frac{\omega_e^2 df_e^1}{k^2\ dv}(v_{\phi\pm})\right)^2\right)}, \tag{1.19}$$

where $k$ is the magnitude of the wave vector shift defined in Eq. (1.4) for $\omega_r = \omega_0$ and $v_{\phi\pm} = \omega_\pm/k$ is the phase velocity of the corresponding Langmuir wave. Since the isotropic Landau damping term $-\frac{\omega_\pm}{2}\pi\frac{\omega_e^2}{k^2}\frac{df^1}{dv}(v_{\phi\pm})$ of the wave is small, all the power lies in a small frequency interval (smaller than the frequency bandwidth of our observations) and the integrated power in one plasma line $I_p$ can be calculated analytically

$$I_p = \frac{1}{2\alpha^2}\frac{f_e^1(v_\phi)}{-\frac{v_e^2}{v_\phi}\frac{df_e^1}{dv}(v_\phi)}, \tag{1.20}$$

where $v_e = \sqrt{k_b T_e/m_e}$ is the electron thermal velocity.

The term in the numerator of Eq. (1.20) represents the excitation of the Langmuir wave by the fast electrons, while the denominator represents the Landau damping from the particles at the phase velocity of the wave. Thus, the presence of a high-energy tail in the velocity distribution function can lead to a substantial enhancement in the integrated power, as well as a broadening, of the plasma line.

Without any enhancement mechanism of the plasma line, the integrated power of the plasma line is smaller the larger is the parameter $\alpha$. This is seen in Figures 1.2 and 1.3.

Including the effect of collisions through a Fokker-Planck operator (Perkins *et al.*, 1965; Yngvesson and Perkins, 1968) leads to a similar expression

$$I_p = \frac{1}{2\alpha^2} \frac{f_e^1(v_\phi) + \chi_{ei}}{-\frac{v_e^2}{v_\phi}\frac{df_e^1}{dv}(v_\phi) + \chi_{ei}}, \tag{1.21}$$

where $\chi_{ei}$ is the electron-ion collision term that describes the excitation and damping of plasma waves due to electron-ion collisions with collision frequency $\nu_{ei}$

$$\chi_{ei} = \frac{2}{\pi}\frac{v_e^2}{v_\phi^4}\frac{\nu_{ei}}{k}. \tag{1.22}$$

It can be shown (Newman and Oran, 1981; Oran *et al.*, 1981; Kirkwood *et al.*, 1995) that the electron-neutral collision frequency $\nu_{en}$ can be included and $\nu_{ei}$ replaced by $\nu_e = \nu_{en} + \nu_{ei}$, the sum of the electron-neutral and electron-ion collision frequencies which are defined as

$$\nu_{en} = 5.4 \times 10^{-10} n_n T_e^{\frac{1}{2}}, \qquad [\mathrm{s}^{-1}] \tag{1.23}$$

$$\nu_{ei} = \left(34.0 + 4.18 \log \frac{T_e^3}{n_e}\right) n_e T_e^{-\frac{3}{2}}, \qquad [\mathrm{s}^{-1}] \tag{1.24}$$

where $n_n$ is the neutral density.

The term in the numerator of Eq. (1.21) represents the excitation of the Langmuir wave, while the denominator represents the Landau damping and the collision damping. Note that when the collisional damping $\chi_e$ is large compared to the Landau damping and the excitation term, the plasma line intensity also tends towards the thermal intensity $1/2\alpha^2$, but the spectrum is broadened due to the collisions. Enhancement of the plasma line is expected to take place because of the increase of the number of electrons in the velocity distribution at the phase velocity of the Langmuir wave due to the supra-thermal population. The supra-thermal population which excite the Langmuir wave consists either of photoelectrons or secondary electrons in the case of precipitation. At the same time, The Landau damping of the supra-thermal electrons dominates and keeps the plasma line in a steady-state with the supra-thermal population and broadens the plasma line (Bauer, 1975).

The integrated power of the plasma line $I_p$, without any enhancement, can be compared to the integrated power of the ion line $I_i$ given by (Bauer, 1975)

$$I_i = \frac{\alpha^4}{(1+\alpha^2)(1+\alpha^2+\alpha^2 T_e/T_i)}, \tag{1.25}$$

which reduces to $\frac{1}{1+T_e/T_i}$ for large values of $\alpha$. For the spectra shown in Figures 1.2 and 1.3, the ratio $I_p/I_i$ are equal to $10^{-2}$ and $2 \cdot 10^{-1}$ respectively. For a Maxwellian plasma the plasma lines are more powerful with the UHF radar than with the VHF radar.

Using the formalism that we develop in the next section (Guio *et al.*, 1998) about the numerical estimation of the $P$ and $Z$ functions with the $P^*$ and $Z^*$ functions of Eqs. (1.39) and (1.41), and together with the differential cross section of Eq. (1.7), we have derived an expression of the integrated power of the plasma line for any *arbitrary* anisotropic electron velocity distribution function. We used the same method of expansion around the plasma resonance frequency as Perkins and Salpeter (1965) and the integrated power in one plasma line is written

$$I_p = \frac{1}{2\alpha^2} \frac{v_\phi \operatorname{Im} P^*_{v_e}\left(\frac{v_\phi}{v_e}\right) - \frac{v_\phi}{v_e}\frac{\nu_e}{k}\left|P^*_{v_e}\left(\frac{v_\phi}{v_e}\right)\right|^2}{v_e \operatorname{Im} Z^*_{v_e}\left(\frac{v_\phi}{v_e}\right) + \frac{1}{\alpha^2}\frac{\nu_e}{k}\operatorname{Re} P^*_{v_e}\left(\frac{v_\phi}{v_e}\right)}. \tag{1.26}$$

Introducing the plasma line temperature $k_b T_p$ defined as

$$\frac{k_b T_p}{k_b T_e} = 2\alpha^2 I_p, \tag{1.27}$$

the integrated power $I_p$ of the plasma line is expressed as a temperature. In a Maxwellian plasma, the plasma line temperature reduces to the electron temperature. The ratio $k_b T_p / k_b T_e$ then describes the enhancement of the plasma line over the thermal level. The plasma line temperature for the expression of the intensity of Eq. (1.26) is written (Guio and Lilensten, 1998)

$$k_b T_p = k_b T_e \frac{v_\phi \operatorname{Im} P^*_{v_e}\left(\frac{v_\phi}{v_e}\right) - \frac{v_\phi}{v_e}\frac{\nu_e}{k}\left|P^*_{v_e}\left(\frac{v_\phi}{v_e}\right)\right|^2}{v_e \operatorname{Im} Z^*_{v_e}\left(\frac{v_\phi}{v_e}\right) + \left(\frac{v_e}{v_\phi}\right)^2 \frac{\nu_e}{k}\operatorname{Re} P^*_{v_e}\left(\frac{v_\phi}{v_e}\right)}. \tag{1.28}$$

Therefore if one is able to calculate the functions $P^*$ and $Z^*$ for any arbitrary anisotropic electron velocity distribution it is then possible to estimate the intensity of the plasma lines. The intensity of the plasma lines with an anisotropic supra-thermal electron velocity distribution has been investigated earlier (Lejeune and Kofman, 1977; Lejeune, 1979), but their formulation of the intensity did not take into account the pitch-angle dependence in the imaginary part of the dielectric function evaluated at the phase velocity of the wave; they neglected the second term on the right hand side of Eq. (1.43) and made the following approximation

$$\int_{\mathrm{L}} \boldsymbol{n} \cdot \boldsymbol{\nabla}_{\boldsymbol{v}} f(\boldsymbol{v}) \delta(\boldsymbol{k} \cdot \boldsymbol{v} - \omega) d^3\boldsymbol{v} \simeq \frac{d}{dv} \int_{\mathrm{L}} f(\boldsymbol{v}) \delta(\boldsymbol{k} \cdot \boldsymbol{v} - \omega) d^3\boldsymbol{v}. \tag{1.29}$$

We have used the formalism of the $P$ and $Z$ functions together with a model of the supra-thermal distribution and have calculated the intensity of the plasma lines given by Eq. (1.28). Our model has been compared with a good agreement to plasma lines data that we observed at a high time resolution with the EISCAT VHF radar (Guio and Lilensten, 1998).

### 1.3.2 Doppler frequency shift

The Doppler frequency shift $\omega_\pm$ of the up- and the down-shifted plasma lines are the real part of the roots of the dispersion relation

$$1 - Z_e(\boldsymbol{k}_\pm, \omega_\pm + i\gamma_\pm) = 0, \tag{1.30}$$

where $\gamma_\pm$ is the decay rate which we assume is much smaller than the real part $\omega_\pm$ of the complex frequency.

Then, we can expand in power series of $(\boldsymbol{k}\cdot\boldsymbol{v})/\omega$ the denominator which occurs in the integral of the plasma dielectric response $Z_e$ of Eq. (1.13) assuming that $|(\boldsymbol{k}\cdot\boldsymbol{v})/\omega| < 1$. Therefore the distribution function $f_e$ must tend toward zero for $\boldsymbol{v}$ such that $|(\boldsymbol{k}\cdot\boldsymbol{v})/\omega| \geq 1$ in order to do the expansion (Tsytovich, 1995)

$$-\frac{1}{\omega}\left(1 + \frac{(\boldsymbol{k}\cdot\boldsymbol{v})}{\omega} + \frac{(\boldsymbol{k}\cdot\boldsymbol{v})^2}{\omega^2} + \frac{(\boldsymbol{k}\cdot\boldsymbol{v})^3}{\omega^3} + \cdots + \frac{(\boldsymbol{k}\cdot\boldsymbol{v})^n}{\omega^n}\right). \tag{1.31}$$

After one integration by parts, the real part of $Z_e$ is rewritten as a series expansion

$$\mathrm{Re}\, Z_e(\boldsymbol{k},\omega) = \frac{\omega_e^2}{(\omega - ku_{e\|})^2}\left(1 + 3\frac{k^2\langle(v_\| - u_{e\|})^2\rangle}{(\omega - ku_{e\|})^2} + 4\frac{k^3\langle(v_\| - u_{e\|})^3\rangle}{(\omega - ku_{e\|})^3} + \right.$$
$$\left. \cdots + (n+1)\frac{k^n\langle(v_\| - u_{e\|})^n\rangle}{(\omega - ku_{e\|})^n}\right), \tag{1.32}$$

where the angle brackets denote the average of the distribution function

$$\langle A\rangle = \int A f_e(\boldsymbol{v}) d^3\boldsymbol{v}, \tag{1.33}$$

These bracketed terms correspond to moments of the distribution function. The potential mean drift velocity $u_{e\|} = \boldsymbol{k}\cdot\langle\boldsymbol{v}\rangle/k$ parallel to $\boldsymbol{k}$ has been included into the power expansion by replacing $(\boldsymbol{k}\cdot\boldsymbol{v})/\omega$ with $(\boldsymbol{k}\cdot\boldsymbol{v})/(\omega - \boldsymbol{k}\cdot\boldsymbol{u}_e)$ in Eq. (1.31) in order to eliminate the term relative to the mean drift velocity $(\boldsymbol{k}\cdot\boldsymbol{v})/\omega$.

Assuming $|\omega - ku_{e\|}| \gg kv_e$ and that the distribution does not deviate dramatically from a Maxwellian, the even-order moments are lumped into the W function of Ichimaru (1992), our Eq. (1.54), and the odd-order moments are truncated at the

third-order, which gives the *heat flow approximation* first introduced by Kofman *et al.* (1993)

$$\mathrm{Re}\, Z_e(\boldsymbol{k},\omega) = -\frac{\omega_e^2}{(kv_e^{\parallel})^2}\mathrm{W}\left(\frac{\omega - ku_{e\parallel}}{kv_e^{\parallel}}\right) + 4\frac{k^3 q_e^{\parallel}/(m_e n_e)}{(\omega - ku_{e\parallel})^5}, \tag{1.34}$$

where $v_e^{\parallel} = (k_b T_e^{\parallel}/m_e)^{1/2}$. $T_e^{\parallel}$ is the parallel temperature and $qe^{\parallel}$ is the heat flow for parallel energy. They are defined (Barakat and Schunk, 1982)

$$\frac{1}{2}k_b T_e^{\parallel} = \frac{1}{2}m_e\langle(v_{\parallel} - u_{e\parallel})^2\rangle, \tag{1.35}$$

$$q_e^{\parallel} = m_e n_e\langle(v_{\parallel} - u_{e\parallel})^2(v_{\parallel} - u_{e\parallel})\rangle. \tag{1.36}$$

The heat flow for parallel energy $q_e^{\parallel}$ is equal to $6/5$ the heat flow $q_e$ in the Spitzer theory (see Eq. (4.20) in Chapter 4). Comparing our term $q_e^{\parallel} = 6/5 q_e$ with the corresponding term $2q_e$ in the approximation of Kofman *et al.* (1993), we see that they have overestimated the heat flow contribution by a factor of $5/3$.

In Guio (1998), we have investigated the validity of the heat flow approximation of Eq. (1.34). We have built a simple analytic model, the 2-$T$ Maxwellian, of a velocity distribution that mimics the situation in a plasma with a temperature gradient. This model consists of two half-Maxwellians with different temperatures that are joined continuously at $v_{\parallel} = 0$. We have shown that it is possible to adjust the two temperatures of the distribution so that the temperature and the heat flow are equal to the ones given by the Spitzer theory (see section 4.4). We have used this model to investigate analytically the effect of a departure from the Maxwellian due to a heat flow on the Doppler frequency of the plasma lines. This simple model has been compared with the heat flow approximation. A good qualitative agreement was seen. However, for accurate calculations such as the calculation of the plasma line Doppler frequency, it was seen that the exact calculation of the dielectric function is important, together with a good representation of the distribution function. This is especially true for high-frequency radars and for low plasma frequency, i.e. when the ratio $|\omega|/kv_e$ is smaller than $5-6$.

We have not investigated the effect of the anisotropy of the 2-$T$ Maxwellian on the intensity of the plasma lines since this distribution is not meant to represent correctly the effect of a supra-thermal population, but rather the departure from the Maxwellian in the ambient electron population.

We have thus written a numerical code to calculate the $P$ and $Z$ functions of Eqs. (1.14) and (1.13). The distribution functions that we use to represent the electron population are known from numerical calculations. The thermal part is the Spitzer function described in Chapter 4. The supra-thermal part is derived from the angular energy flux of electrons calculated by a transport code described

in Chapter 5. Therefore the code should handle the calculation of the functions $P$ and $Z$ for such distribution functions that are defined numerically on a discrete grid.

## 1.4 Numerical code of the $P$ and $Z$ functions

Our assumption when writing the code was that the velocity distribution function should be represented in spherical coordinates with an axial symmetry. The distribution function is given at some discrete points both in velocity space $v$ and in the cosine of the pitch-angle space $\mu$, hereafter referred as the $(v, \mu)$-grid.

When collisions tend to zero, the pole occurring in the $P$ and $Z$ integrals is situated in the neighbourhood of the real axis and the integrals $P$ and $Z$ can be separated into their real and imaginary parts using the general *Plemelj* formula (Balescu, 1963) which reads for a function $g(x)$

$$\lim_{\eta\to 0^+} \int_{\mathrm{L}} \frac{g(x)}{x-\xi-i\eta} dx = \mathrm{PV}\int_{-\infty}^{\infty} \frac{g(x)}{x-\xi} dx + i\pi g(\xi), \tag{1.37}$$

where $\mathrm{PV}$ denotes a Cauchy principal value integral.

When the collisions are not negligible, the integral is also separated into its real and imaginary parts and the integral takes the following form

$$\int_{\mathrm{L}} \frac{g(x)}{x-\xi-i\eta} dx = \int_{-\infty}^{\infty} \frac{g(x)(x-\xi)}{(x-\xi)^2+\eta^2} dx + i\eta \int_{-\infty}^{\infty} \frac{g(x)}{(x-\xi)^2+\eta^2} dx. \tag{1.38}$$

We have expressed $P$ as a function of the normalised function $P^*_{v_e}$

$$P(\boldsymbol{k}, \omega) = \frac{1}{kv_e} P^*_{v_e}\left(\frac{\omega}{kv_e}\right). \tag{1.39}$$

where $v_e$ is a normalisation velocity. We justify this choice to follow the formulation of $P$ for a Maxwellian with the Z function of Fried and Conte (1961) defined in Eq. (1.53).

In the non-collisional case, $P^*_{v_e}$ is then written using Eq. (1.37)

$$\begin{aligned} P^*_{v_e}(\xi) = 2\pi \Bigg[ \sum_{\substack{j=-n \\ j\neq 0}}^{n} w_j \int_{x_{\min}}^{x_{\max}} \frac{x^2}{\mu_j} \frac{v_e^3 f(xv_e, \mu_j)}{x-\xi/\mu_j} dx + \\ i\pi \sum_{j=1}^{n} w_j \frac{|\xi|}{\xi} \frac{\xi^2}{\mu_j^3} v_e^3 f\left(\frac{\xi v_e}{\mu_j}, \mu_j\right) \Bigg], \end{aligned} \tag{1.40}$$

where the $(w_j, \mu_j)$ are respectively the weights and points of the pitch-angle quadrature. We have used the double-Gauss quadrature (Stamnes *et al.*, 1988) which gives the best results.

The integrals of the real part of $P^*_{v_e}$ are of two types depending on the sign of $\xi/\mu_j$. If $\xi/\mu_j$ is strictly positive then the integral has a singularity at $x = \xi/\mu_j$ and the integral is a Cauchy principal value integral. We have used the quadrature D01AQF of NAG (1993) which calculates an approximation to the Hilbert transform of its argument. As the velocity distribution function is defined on a discrete grid of normalised velocity, we need an interpolation strategy in order to calculate the integral. In our code, we have the possibility to interpolate the distribution function using the different methods: spline, linear or step function interpolation. In the case where $\xi/\mu_j$ is strictly negative then the integral has no singularity and we use the routine D01GAF of NAG (1993) which integrates a function specified numerically at four or more points, using a third-order finite difference formula.

We have proceeded in the same way for the $Z$ function. $Z$ has been expressed as a function of the normalised function $Z^*_{v_e}$

$$Z(\boldsymbol{k},\omega) = -\left(\frac{\omega_e}{kv_e}\right)^2 Z^*_{v_e}\left(\frac{\omega}{kv_e}\right), \tag{1.41}$$

where $v_e$ is a normalisation velocity. We justify this choice to follow the formulation of $Z$ for a Maxwellian with the $\mathrm{W}$ function of Ichimaru (1992) defined in Eq. (1.54).

In the non-collisional case, $Z^*_{v_e}$ is written using Eq. (1.37)

$$\begin{aligned} Z^*_{v_e}(\xi) = -2\pi\Bigg[ \sum_{\substack{j=-n \\ j\neq 0}}^{n} w_j \int_{x_{\min}}^{x_{\max}} \frac{x^2}{\mu_j} v_e^3 \frac{\boldsymbol{n}\cdot\boldsymbol{\nabla} f(xv_e,\mu_i)}{x-\xi/\mu_j} dx + \\ i\pi \sum_{j=1}^{n} w_j \frac{|\xi|}{\xi}\frac{\xi^2}{\mu_j^3} v_e^3 \boldsymbol{n}\cdot\boldsymbol{\nabla} f\left(\frac{\xi v_e}{\mu_j},\mu_j\right)\Bigg], \end{aligned} \tag{1.42}$$

where

$$\boldsymbol{n}\cdot\boldsymbol{\nabla} f(xv_e,\mu) = \mu\frac{\partial f}{\partial x}(xv_e,\mu) + \frac{1-\mu^2}{x}\frac{\partial f}{\partial \mu}(xv_e,\mu). \tag{1.43}$$

In the collisional case, similar expressions are found for the functions $P^*_{v_e}$ and $Z^*_{v_e}$ using Eq. (1.38)

$$P^*_{v_e}(\xi+i\eta) = 2\pi \sum_{\substack{j=-n \\ j\neq 0}}^{n} w_j \int_{x_{\min}}^{x_{\max}} \frac{x^2}{\mu_j} v_e^3 \frac{f(xv_e,\mu_i)(x-\xi/\mu_i+i\eta)}{(x-\xi/\mu_j)^2+\eta^2} dx \tag{1.44}$$

and

$$Z^*_{v_e}(\xi+i\eta) = -2\pi \sum_{\substack{j=-n \\ j\neq 0}}^{n} w_j \int_{x_{\min}}^{x_{\max}} \frac{x^2}{\mu_j} v_e^3 \frac{\boldsymbol{n}\cdot\boldsymbol{\nabla} f(xv_e,\mu_j)(x-\xi/\mu_j+i\eta)}{(x-\xi/\mu_j)^2+\eta^2} dx \tag{1.45}$$

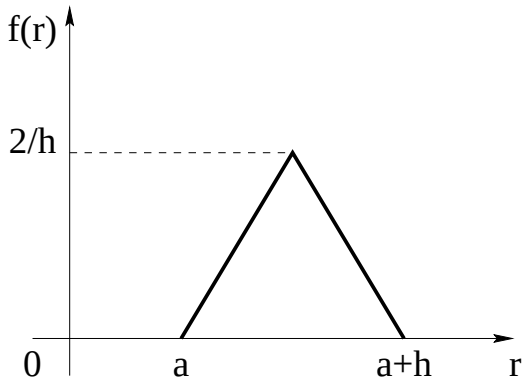


Figure 1.4: The synthetic triangle function with parameters $a = 2$ and $h = 3$

We have used again the routine D01GAF from NAG (1993) for numerically specified functions in order to calculate the integrals over the normalised velocity variable $x$.

We have first tested our numerical code against smooth functions like the Maxwellian and the Spitzer function using a cubic spline interpolation of these function for the integration over the velocity grid. The results are described in Guio *et al.* (1998). A 32-points double-Gauss quadrature gives a relative error better than $10^{-4}$ for small values of $\xi$, while at large values of $\xi$, the accuracy is not influenced and remains better than $10^{-7}$.

### 1.4.1 Test on a synthetic triangle function

As we shall see, the supra-thermal distribution is not as smooth as the Maxwellian or the Spitzer function. The supra-thermal distribution calculated on a discrete energy grid derived from the angular energy flux of electrons calculated by an electron transport code can be seen as a superposition of shifted triangles of different amplitude. We have run a simulation on a synthetic isotropic triangle function and have compared the functions $P^*$ and $Z^*$ calculated by our code with their analytical expressions.

We define the *isotropic* triangle function centred at $r = a + h/2$, with width $h$ and normalised such that its integral is equal to one by

$$f(r,\mu) = \begin{cases} \frac{4}{h^2}(r-a), & a \le r \le a+\frac{h}{2} \\ -\frac{4}{h^2}(r-a-h), & a+\frac{h}{2} \le r \le a+h \\ 0, & \text{otherwise} \end{cases} \tag{1.46}$$

Figure 1.4 shows the isotropic triangle function for the parameters $a = 2$ and $h = 3$.

We have calculated analytically the real and the imaginary parts of the $P^*$ and the $Z^*$ functions, for a real argument $\rho$, of the isotropic triangle function. Since the triangle function $f$ is isotropic, the real part of $P^*$ is an even function while the imaginary part is an odd function and the real part of $Z^*$ is an odd function while the imaginary part is an even function. They are written

$$\mathrm{Re}\,P^*(\rho) = \begin{cases} \pm\frac{\pi}{3h^2}\,[16a^3\log(2a) - 8h^2a + 32a^3\log 2 - \\ (16a^3 - h^3 - 6ah^2)\log\frac{4a+h}{h} - \\ 16a^3\log((4a+h)h) - \\ 4(a+h)(a^2+2ah-3a^2+h^2)\log\frac{2a+h}{h} + \\ 8a^3\log((2a+h)h)] & , \quad \rho = \pm a \\ \\ \pm\frac{\pi}{3h^2}\,\Big[(12(a+\frac{h}{2})^2a - 4a^3)\log\frac{4a+h}{h} + \\ 8(a+\frac{h}{2})^3\log((2a+\frac{h}{2})\frac{h}{2}) - 8h^2(a+\frac{h}{2}) + \\ 32(a+\frac{h}{2})^3\log 2 - 4(2a+h)^3\log(4(a+\frac{h}{2})) - \\ 4(a+h)(a^2+2ah - 3(a+\frac{h}{2})^2 + h^2) \\ \log\frac{4a+3h}{h} + 8(a+\frac{h}{2})^3\log((2a+\frac{3h}{2})\frac{h}{2})\Big] & , \quad \rho = \pm(a+\frac{h}{2}) \\ \\ \pm\frac{\pi}{3h^2}\,\Big[(12(a+h)^2a - 4a^3)\log\frac{2a+h}{h} + \\ 8(a+h)^3\log((2a+h)h) - 8h^2(a+h) + \\ 32(a+h)^3\log 2 - (h+2a)(11h^2+20ah+8a^2) \\ \log\frac{4a+3h}{h} - 16(a+h)^3\log((4a+3h)h) + \\ 16(a+h)^3\log(2(a+h))] & , \quad \rho = \pm(a+h) \\ \\ \frac{\pi}{3h^2}\,\Big[(12\rho^2a - 4a^3)\log\frac{|\rho+a|}{|\rho-a|} + 8\rho^3\log|\rho^2-a^2| - \\ 8h^2\rho + 32\rho^3\log 2 + \\ (8a^3+h^3-24\rho^2a+6ah^2-12h(\rho^2-a^2)) \\ \log\frac{|2\rho+2a+h|}{|2\rho-2a-h|} - 16\rho^3\log|4\rho^2-(2a+h)^2| - \\ 4(a+h)(a^2+2ah-3\rho^2+h^2)\log\left|\frac{\rho+a+h}{\rho-a-h}\right| + \\ 8\rho^3\log|\rho^2-(a+h)^2|] & , \quad \text{otherwise} \end{cases} \tag{1.47}$$

$$\mathrm{Im}\,P^*(\rho) = \begin{cases} \pi^2(2a+h), & |\rho| \le a \\ \\ \frac{\pi^2}{3h^2}(-4a^3+6ah^2+3h^3-8|\rho|^3+12a\rho^2), & a \le |\rho| \le a+\frac{h}{2} \\ \\ \frac{4\pi^2}{3h^3}(a+h+2|\rho|)(a+h-|\rho|)^2, & a+\frac{h}{2} \le |\rho| \le a+h \\ \\ 0, & \text{otherwise} \end{cases} \tag{1.48}$$

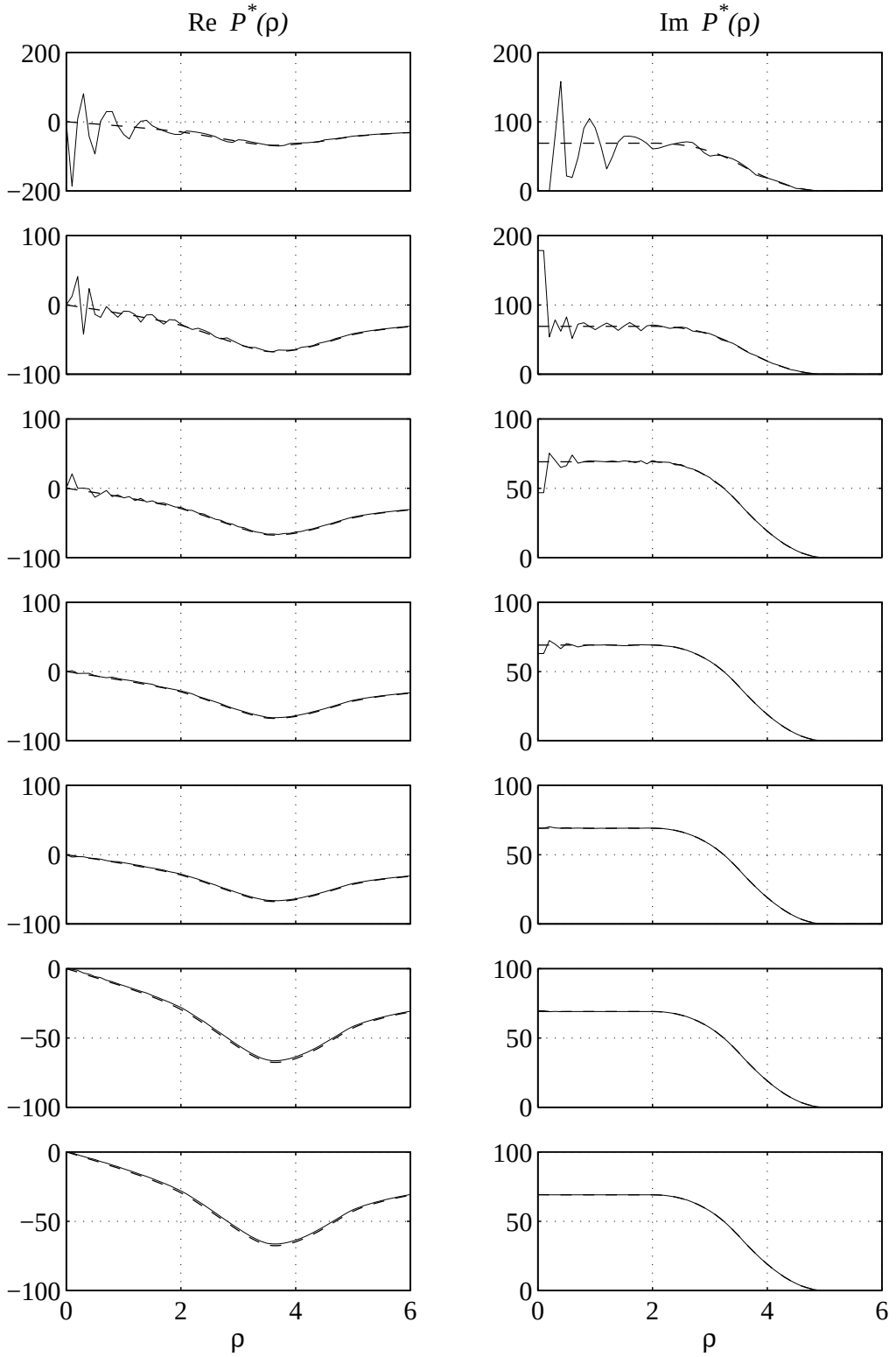


Figure 1.5: Test of the $P^*$ function, for $\rho \geq 0$, with the triangle function of parameters $a = 2$ and $h = 3$. From top to bottom the number of points in the quadrature are 16, 32, 64, 128, 256, 512 and 1024. The *dashed* lines are for the analytic expressions of Eqs. (1.47) and (1.48). The *solid* lines are for the numerical calculations with our code

$$\mathrm{Re}\,Z^*(\rho) = \begin{cases} -\frac{4\pi}{h^2}\left[-h^2+8a^2\log 2+4a^2\log(2a)- \right. \\ 2(2a+h)a\log\frac{4a+h}{h}-4a^2\log((4a+h)h)+ \\ \left. 2(a+h)a\log\frac{2a+h}{h}+2a^2\log((2a+h)h)\right] & |\rho|=a \\ -\frac{4\pi}{h^2}\left[-h^2+8(a+\frac{h}{2})^2\log 2+ \right. \\ 2a(a+\frac{h}{2})\log\frac{4a+h}{h}+2(a+\frac{h}{2})^2\log((2a+\frac{h}{2})\frac{h}{2})- \\ 8(a+\frac{h}{2})^2\log(4a+2h)+2(a+h)(a+\frac{h}{2})\log\frac{4a+3h}{h}+ \\ \left. 2(a+\frac{h}{2})^2\log((2a+\frac{3h}{2})\frac{h}{2})\right] & |\rho|=a+\frac{h}{2} \\ -\frac{4\pi}{h^2}\left[-h^2+8(a+h)^2\log 2+ \right. \\ 2a(a+h)\log\frac{2a+h}{h}+2(a+h)^2\log((2a+h)h)- \\ 2(2a+h)(a+h)\log\frac{4a+3h}{h}-4(a+h)^2 \\ \left. \log((4a+3h)h)+4(a+h)^2\log(2(a+h))\right] & |\rho|=a+h \\ -\frac{4\pi}{h^2}\left[-h^2+8\rho^2\log 2+ \right. \\ 2a\rho\log\frac{|\rho+a|}{|\rho-a|}+2\rho^2\log|\rho^2-a^2|- \\ 2(2a+h)\rho\log\frac{|2\rho+2a+h|}{|2\rho-2a-h|}-4\rho^2\log|4\rho^2-(2a+h)^2|+ \\ \left. 2(a+h)\rho\log\frac{|\rho+a+h|}{|\rho-a-h|}+2\rho^2\log|\rho^2-(a+h)^2|\right] & \text{otherwise} \end{cases} \tag{1.49}$$

$$\mathrm{Im}\,Z^*(\rho) = \begin{cases} \frac{8\pi^2}{h^2}\rho(|\rho|-a), & a\le|\rho|\le a+\frac{h}{2} \\ -\frac{8\pi^2}{h^2}\rho(|\rho|-a-h), & a+\frac{h}{2}\le|\rho|\le a+h \\ 0, & \text{otherwise} \end{cases} \tag{1.50}$$

We have compared the behaviour of our numerical code as a function of the number of points in the double-Gauss quadrature. When it comes to the velocity integration, we had to use a linear interpolation for such a non-smooth function as the triangle. The spline interpolation was introducing a systematic bias in the estimation of the $P^*$ and $Z^*$ functions for the triangle function defined by just three points.

Figures 1.5 and 1.6 show the results of the calculations for different values of the double-Gauss quadratures. Since the triangle function is not a smooth function as the Maxwellian, a 512 or even better a 1024-points double-Gauss quadrature was needed in order to get rid of the oscillations.

The signature of the triangle function is clearly identified in the shape of the $P^*$ and $Z^*$ functions. The imaginary part of the $Z^*$ function presents a maximum damping for $\rho = a + h/2$ which corresponds to the value of $r$ at the maximum of the triangle function. Similarly the real part of the $Z^*$ function presents an abrupt variation for $\rho = a + h/2$ which corresponds again to the value of $r$ at

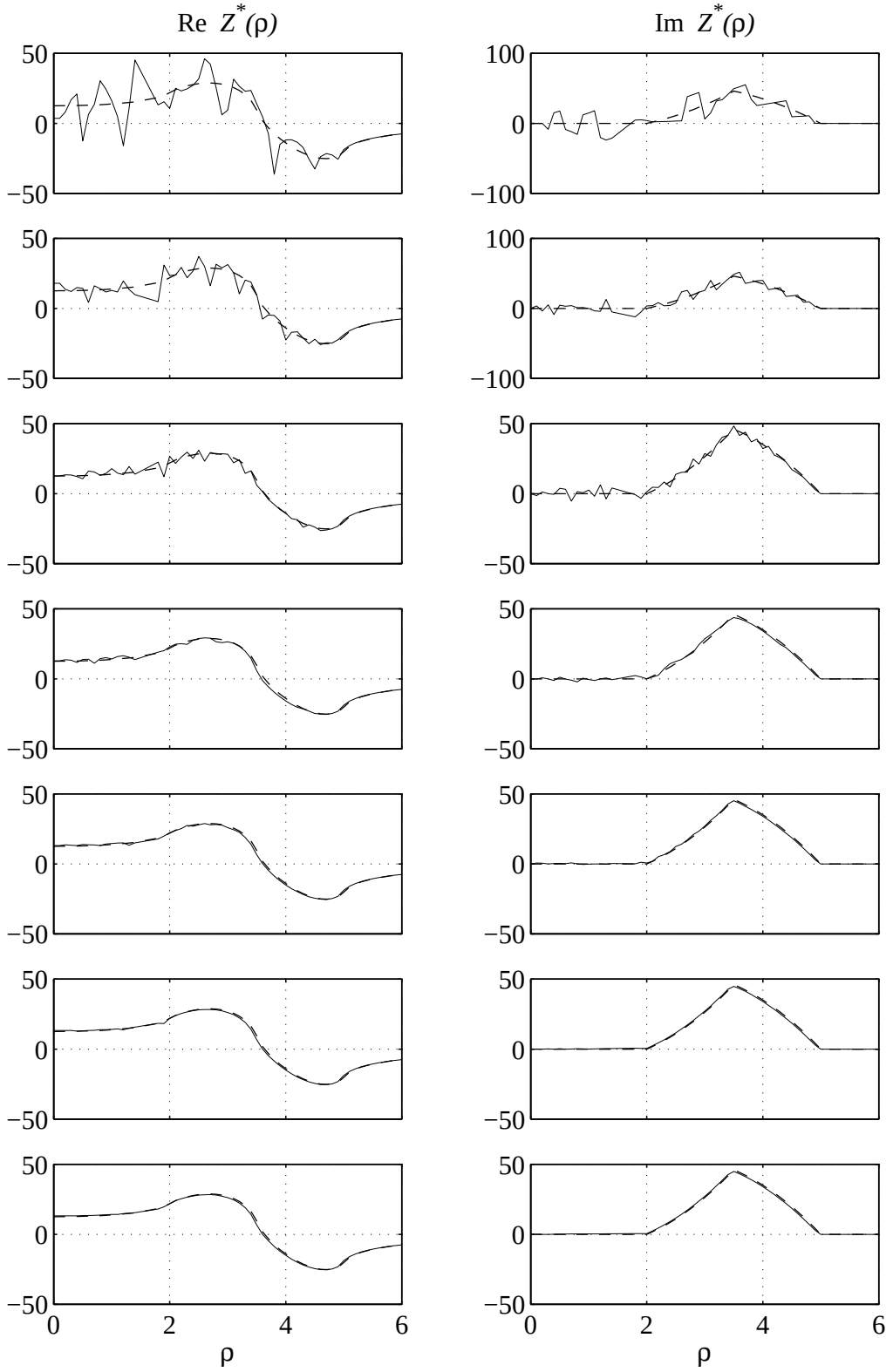


Figure 1.6: Test of the $Z^*$ function, for $\rho \geq 0$, with the triangle function of parameters $a = 2$ and $h = 3$. From top to bottom the number of points in the double-Gauss quadrature are 16, 32, 64, 128, 256, 512 and 1024. The *dashed* lines are for the analytic expressions of Eqs. (1.49) and (1.50). The *solid* lines are for the numerical calculations of our code

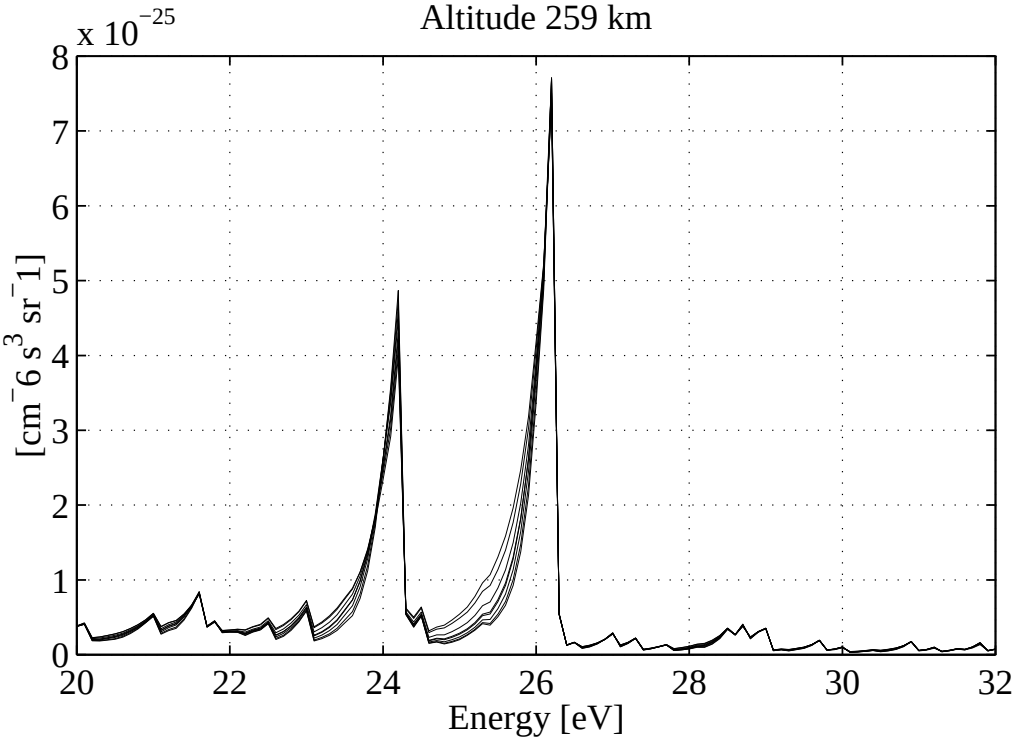


Figure 1.7: The angular supra-thermal distribution, plotted in the energy range $20-32\,\mathrm{eV}$, used to perform the tests shown in Figures 1.8 and 1.9. The distribution was calculated with an eight-stream run over Tromsø in July 1996 at $12:00\,\mathrm{UT}$ with a $\mathrm{F10.7}$ index of $80$ and an $\mathrm{A_p}$ index of $15$. The eight curves correspond to the eight angles of the double-Gauss quadrature

the maximum of the triangle function again. It can also be verified analytically that the imaginary part of $P^*$ will tend toward a rectangular window of width $2a$ when $h$ tends toward zero as expected if the distribution function $f$ were a Dirac function.

### 1.4.2 Test on a real supra-thermal distribution function

We have run a test on a real supra-thermal distribution function. The angular distribution function has been calculated by the transport code described in Chapter 5 with an eight-stream run. A detailed view of the angular distribution function in the energy range we have calculated the $P^*$ and $Z^*$ functions is shown in Figure 1.7. Note the anisotropy of the distribution function for energies lower than the energy corresponding to the two peaks ($24.25\,\mathrm{eV}$ and $26.25\,\mathrm{eV}$) while the distribution is rather isotropic otherwise.

Note also the similarity of the supra-thermal distribution, in this energy range, to a superposition of shifted triangle functions centred at $24.25\,\mathrm{eV}$ and $26.25\,\mathrm{eV}$. The two main peaks at $24.25\,\mathrm{eV}$ and $26.25\,\mathrm{eV}$ are the signature of the increase in the number of electrons produced by photoionisation of $\mathrm{N}_2$ and $\mathrm{O}$ respectively. The photons causing the ionisation are from the intense flux of monochromatic $\mathrm{HeII}$ radiation of wavelength $30.378\,\mathrm{nm}$ ($40.812\,\mathrm{eV}$) created in the chromospheric network and coronal holes These two peaks have been observed on data collected with the EISCAT VHF radar and the effect on the plasma line intensity and Doppler frequency is discussed in Guio and Lilensten (1998).

Figures 1.8 and 1.9 show the results of the calculations of the $P^*$ and $Z^*$ functions for different values of the double-Gauss quadratures and for both downward and upward energies. Note again the oscillations at energy lower than $26.25\,\mathrm{eV}$ when the number of points in the double-Gauss quadrature is small. The results are converging when the number of points in the double-Gauss quadrature is increasing and a number of points in the quadrature of 1024, or even better 2048, is needed to get satisfying results.

It is worth noting also the effect of the anisotropy of the supra-thermal angular distribution on the $P^*$ and $Z^*$ functions. The real part of $P^*$ and the imaginary part of $Z^*$ are not odd function any longer. The imaginary part of $P^*$ and the real part of $Z^*$ are not even function any longer.

## 1.5 The electron velocity distribution model

The usual description of electron behaviour in the Earth's ionosphere is based on the assumption that the electron gas consists of two components, the *ambient* electrons and the *supra-thermal* electrons (Takayanagi and Itikawa, 1970), although the ambient electrons and the arising supra-thermal electrons are physically indistinguishable.

We will assume that we can represent the electron plasma by those two components with velocity probability distribution function $f_a$ and density $n_a$ for the ambient electrons, and $f_s$ and $n_s$ for the supra-thermal electrons. The total electron density is then $n_e = n_a + n_s$ and we define the dimensionless number $\alpha = n_s/n_e$ which represents the percentage of supra-thermal electrons. The ion population will always be considered Maxwellian.

The ambient component is represented either by a Maxwellian distribution function with thermal velocity $v_e = \sqrt{k_b T_e/m_e}$, or by the Spitzer function that we describe in Chapter 4.

The supra-thermal distribution is derived from the angular electron flux calculated by the transport code described in Chapter 5.

We now have a representation for both the ambient and the supra-thermal

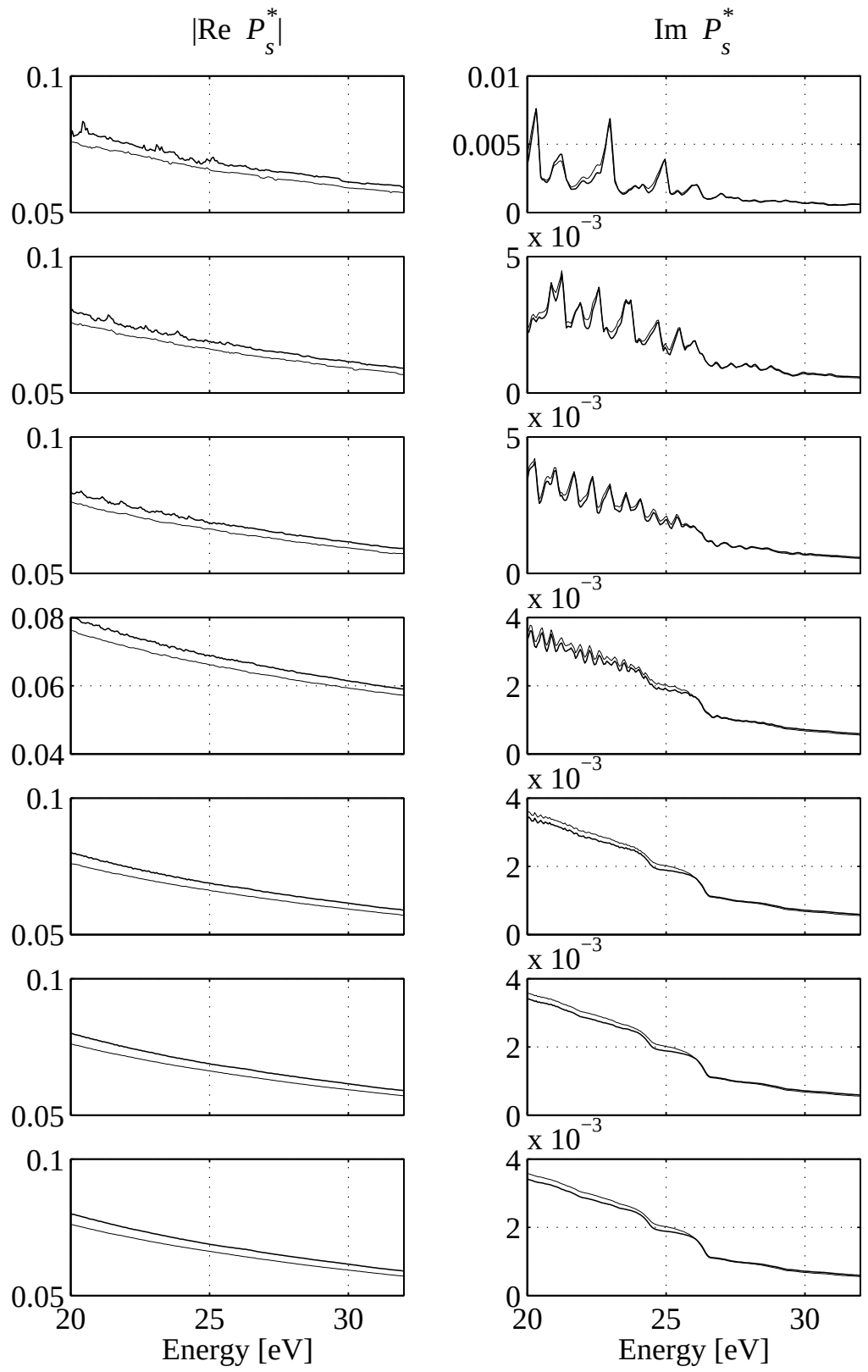


Figure 1.8: Test of the $P^*$ function with the supra-thermal velocity distribution calculated on a 8-streams run at $259\,\mathrm{km}$ (see Figure 1.7). From top to bottom the number of points in the quadrature are 32, 64, 128, 256, 512, 1024 and 2048. The *thick* line is for downward energy while the *thin* line is for upward energy

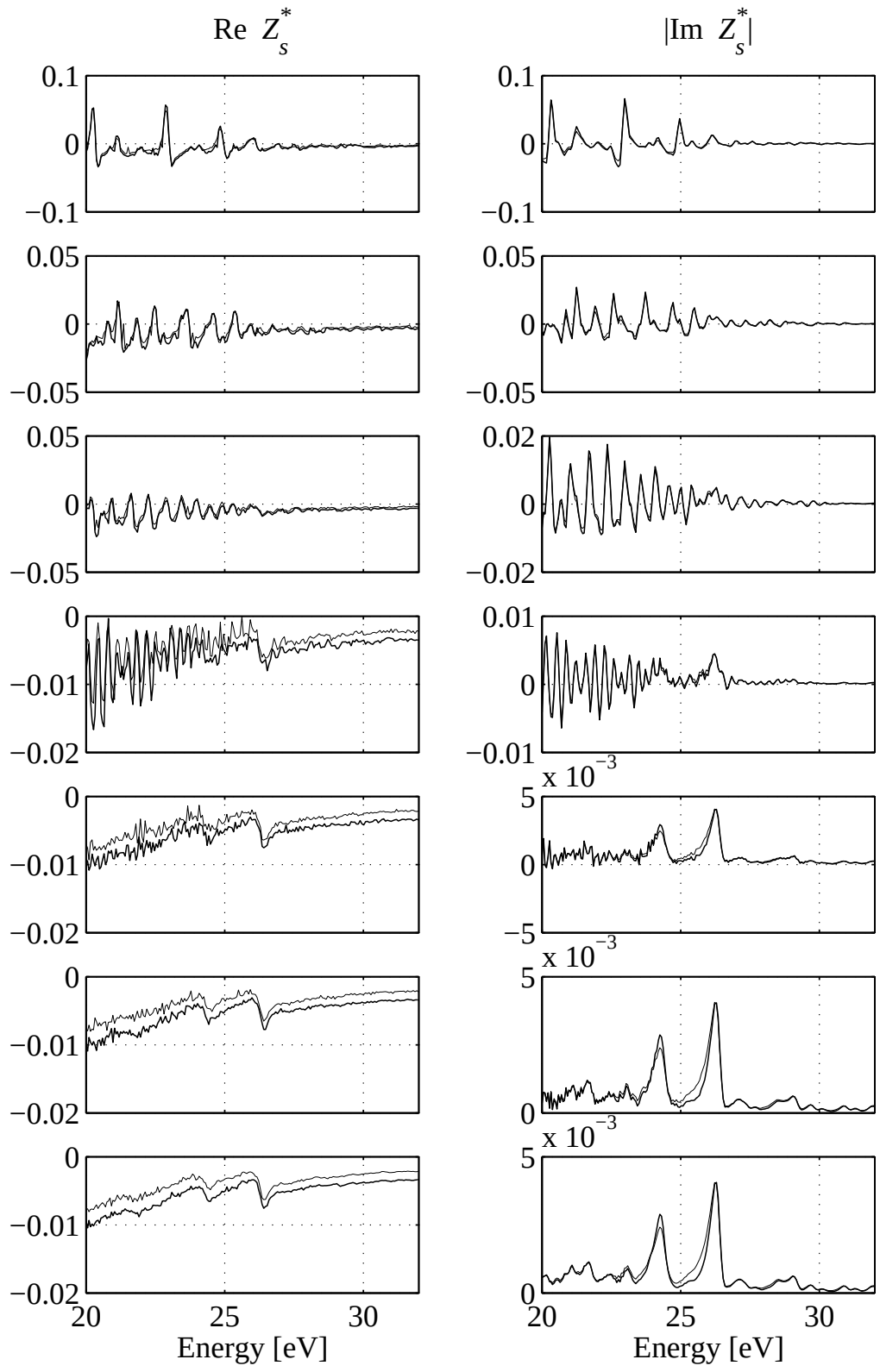


Figure 1.9: Test of the $Z^*$ function with the supra-thermal velocity distribution calculated on a 8-streams run at $259\ \mathrm{km}$ (see Figure 1.7). From top to bottom the number of points in the quadrature are 32, 64, 128, 256, 512, 1024 and 2048. The *thick* line is for downward energy while the *thin* line is for upward energy

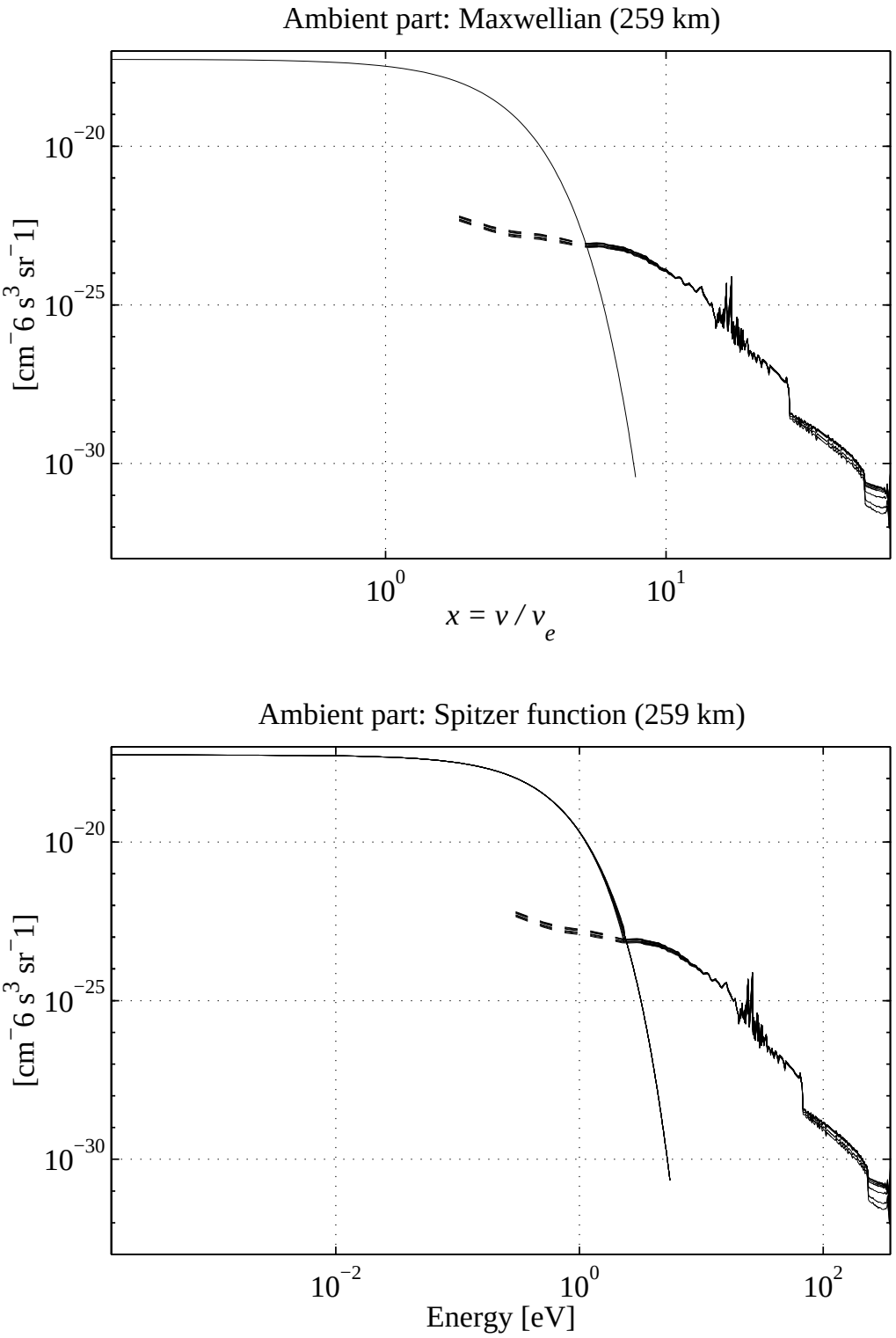


Figure 1.10: The upper plate shows both a Maxwellian and the supra-thermal distribution as a function of the dimensionless parameter $x = v/v_e$. The supra-thermal is truncated at the intersection with the Maxwellian. The lower plate presents the situation where the ambient distribution is the Spitzer function described in Chapter 4. The distributions are plotted as a function of the energy $v = 1/2m_e v^2$. The two plates are for the same altitude and same ionospheric parameters

electrons, the next operation consists in the treatment of the transition region between the supra-thermal and the ambient electrons. Sophisticated methods such as the numerical resolution of the nonlinear Boltzmann equation (Ashihara and Takayanagi, 1974; Jasperse, 1976), as well as full analytical treatment such as the one proposed by Krinberg (1973), have been studied to solve this problem. However, it was shown later that a good approximation for the complete distribution function can be obtained by joining the two distribution functions at the energy for which the two distributions have equal intensities (Krinberg and Akatova, 1978; Stamnes and Rees, 1983) and truncate the supra-thermal distribution at this energy. We have chosen for simplicity this method.

The truncation procedure is essential for the evaluation of the velocity moments as seen at the end of Chapter 5. The value of the moments of the supra-thermal distributions are substantially modified by the truncation procedure.

Figure 1.10 shows the ambient distribution function and the supra-thermal distribution truncated at the intersecting energy. Note again the two sharp peaks at $24.25\,\mathrm{eV}$ and $26.25\,\mathrm{eV}$ due to the photoionisation of $\mathrm{N}_2$ and $\mathrm{O}$ by the powerful emission of $\mathrm{HeII}$ radiation of wavelength $30.378\,\mathrm{nm}$.

For a Maxwellian distribution $f_a(\boldsymbol{v}) = 1/(2\pi)^{3/2}/v_e^3 \exp(-|\boldsymbol{v} - \boldsymbol{u}_e|^2/2v_e^2)$ with thermal velocity $v_e$ and mean drift velocity $\boldsymbol{u}_e$, the functions $P_a$ and $Z_a$ can be expressed with the well-known functions Z, defined in Fried and Conte (1961), and W, defined in Ichimaru (1992), both for complex argument $z$.

$$P_a(\boldsymbol{k},\omega) = \frac{1}{kv_e}\mathrm{Z}\left(\frac{\omega - \boldsymbol{k}\cdot\boldsymbol{u}_e}{kv_e}\right), \tag{1.51}$$

$$Z_a(\boldsymbol{k},\omega) = -\left(\frac{\omega_e}{kv_e}\right)^2 \mathrm{W}\left(\frac{\omega - \boldsymbol{k}\cdot\boldsymbol{u}_e}{kv_e}\right) \tag{1.52}$$

with

$$\mathrm{Z}(z) = \frac{1}{2\pi}\int_{-\infty}^{\infty}\frac{\exp(-x^2/2)}{x - z}dx, \tag{1.53}$$

$$\mathrm{W}(z) = \frac{1}{2\pi}\int_{-\infty}^{\infty}\frac{x\exp(-x^2/2)}{x - z}dx. \tag{1.54}$$

Z and W are related by $\mathrm{Z}(z) = 1 + z\mathrm{W}(z)$.

In the case of the Spitzer function (Chapter 4), the functions $P_a$ and $Z_a$ have to be estimated with our numerical code and so it is for the functions $P_s$ and $Z_s$ for the supra-thermal distribution (Chapter 5). The functions $P_e$ and $Z_e$ for the total electron distribution function are then written (Guio *et al.*, 1998)

$$P_e(\boldsymbol{k},\omega) = (1-\alpha)P_a(\boldsymbol{k},\omega) + \alpha P_s(\boldsymbol{k},\omega), \tag{1.55}$$

$$Z_e(\boldsymbol{k},\omega) = (1-\alpha)Z_a(\boldsymbol{k},\omega) + \alpha Z_s(\boldsymbol{k},\omega), \tag{1.56}$$

and are used to calculate the intensity and the Doppler frequency shift of the plasma lines.

## 1.6 Summary

Our contribution in this part is a numerical code to calculate the plasma dispersion function — the $Z$ function — and the reduced one-dimensional distribution — the imaginary part of the $P$ function — for any arbitrary two-dimensional distribution function described on a discrete $(v, \mu)$-grid.

The numerical calculation of the $P$ and $Z$ functions together with a model of the electron velocity distribution allows the theoretical calculation of the intensity and the Doppler frequency shift of the plasma lines. It is therefore possible by comparing the measured intensity and the Doppler shift of the plasma line in an incoherent scatter experiment to check the validity of the model for the electron distribution function.

In Guio (1998), the effect of an electron temperature gradient and the presence of an electron supra-thermal population on the Doppler frequency of the plasma lines have been studied for different radar wavelength (EISCAT VHF, ESR and UHF radars). In Guio and Lilensten (1998), plasma lines data collected with the EISCAT VHF radar have been analysed, and the intensity and the Doppler shift of the plasma lines have been compared successfully with our model for the electron distribution function.

"EXPERIENCE *is the name everyone gives to their mistakes."*
Oscar Wilde.

# Chapter 2

# Incoherent scattering measurement: EISCAT

## 2.1 Introduction

The idea that the backscattering of powerful radio waves from ionospheric thermal electrons should be detectable by large antennae was due to Gordon (1958). First, Bowles (1958) demonstrated the existence of ionospheric incoherent scatter using a $1\,\mathrm{MW}$ transmitter tuned to a wavelength of $7.5\,\mathrm{m}$ and a large antenna of cross-section about $20000\,\mathrm{m}^2$. Three years later in 1961, Bowles observed echoes with a bandwidth a factor 10 less than the predicted width: the ion line. The discrepancy was due to the Coulomb coupling between the electrons and the ions when observing with a radar of wavelength much larger than the Debye length!

Incoherent-scatter radars (ISR) are expensive to build and operate, due to the required high-power transmitters, large antennae and highly sensitive receivers. At the present time, there are seven major ISR in operation around the world. They cover a wide latitude range from the magnetic equator to the polar cap. The EISCAT radars sit in the auroral zone.

ISR may be either *monostatic* or *multistatic*. Monostatic radars use the same antenna to transmit and to receive signals. The transmitted signal is pulsed in order to resolve the scattering volume, allowing the measurement of the ionosphere over a wide range simultaneously. The height resolution of these measurements is determined by the pulse length. Multistatic radars use separate antennae to transmit and to receive signals. The transmitted signal does not need to be pulsed, and the echoing region is selected by pointing the receiving antenna in a direction which intersects the transmitted beam. It allows measurements with height reso-

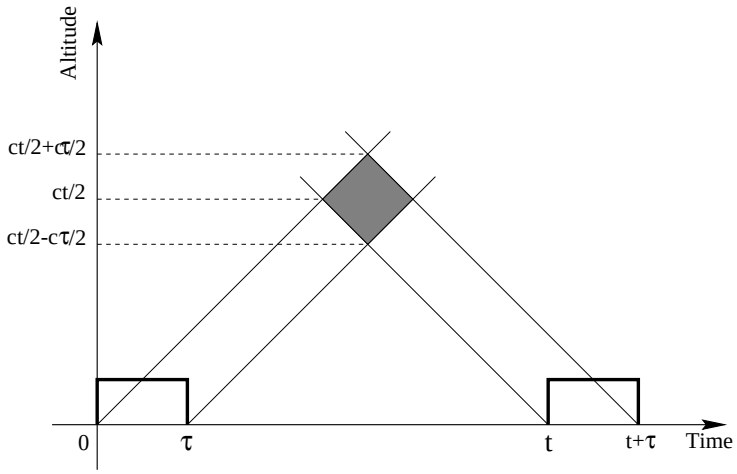


Figure 2.1: Sketch of the transmission-reception scheme for a transmitted pulse of length $\tau$ and a receiving interval $\tau$ delayed by a time $t$ after the pulse is transmitted

lution determined by the intersection of the two antenna beams. *Tri-static* systems give the possibility to derive both the intensity and the direction of vectorial parameters such as the ion drift velocity and also possibly anisotropic parameters such as the ion temperature.

## 2.2 Measurement principle

An incoherent scatter radar experiment consists basically in sending an electromagnetic wave of wavelength $\lambda_0$ on a time interval $\tau$. The pulsed wave is travelling in the ionosphere and a small fraction of the transmitted signal is scattered. The receiver is opened after a time $t$ and the signal is sampled over a time interval $\tau$. The time $t$ separating the transmission and the reception determines the altitude of the volume which scattered the incident wave. When sampling at time $t$ after the start of the transmission, the pulse has travelled at height $ct/2$ and is illuminating a volume in the range $ct/2$ to $c(t+\tau)/2)$ — assuming a zeroth-order sampler — as seen in Figure 2.1. In fact the finite impulse response of the receiver will also have to be taken into account in the calculation of the range. It is then possible to build the autocorrelation function (ACF) of the signal by calculating cross products of the received samples and adding them properly (Farley, 1969). The ACF is the Fourier transform of the power density spectrum, or periodogram, of the signal. In order to subtract the *background noise* (sky and receiver noises), signal is collected independently in the absence of any transmitted signal. The noise subtracted ACF is then calibrated using the measurement of a noise source of calibrated temperature injected in the receiver system. This procedure has to

be repeated many times in a time interval of a few seconds in order to get a good statistical accuracy of the ACF.

Depending on the scale height of the ionospheric parameters and the correlation time of the medium — mainly depending on the electron and ion temperatures as well as the radar wave vector —, the length of the pulse has to be optimised. Long pulses allow to measure long correlation time but since the probed volume is large, they require the scale height of the ionospheric parameters to be large. Short pulses are well suited for regions with small scale height but they do not allow the measurement of long correlation time. In the lower ionosphere where the scale height is small and the correlation time of the medium is long, the multiple pulse technique (Farley, 1972; Kofman and Lathuillere, 1985) allows one to estimate ACF's with a long correlation time without the disadvantage of smearing them because of the large volume probed. The technique consists of the transmission of short pulses separated by suitable time intervals in order to calculate the ACF at the wanted time delays. This technique has the disadvantage that it does not fill completely the available transmission time. The phase coding technique (Sulzer, 1989) is a recent technique that alleviates this problem without using frequency commutated multiple pulse technique.

## 2.3 The EISCAT radar systems

| | Tromsø | | Kiruna | Sodankylä | Longyearbyen |
|---|---|---|---|---|---|
| Geograph. coord. | $69'35°$ N | | $67'52°$ N | $67'22°$ N | $78'09°$ N |
| | $19'14°$ E | | $20'26°$ N | $26'38°$ N | $16'03°$ N |
| Geomagn. inclination | $77'30°$ E | | $76'48°$ E | $76'43°$ E | $82'06°$ E |
| Invariant latitude | $66'12°$ N | | $64'27°$ E | $63'34°$ E | $75'18°$ E |
| Band | VHF | UHF | UHF | UHF | UHF |
| Frequency $(\mathrm{MHz})$ | 224 | 931 | 931 | 931 | 500 |
| Wavelength $(\mathrm{m})$ | 1.3 | 0.3 | 0.3 | 0.3 | 0.6 |
| Wave vector $(\mathrm{m}^{-1})$ | 4.7 | 19.5 | 13.8 [1] | 13.8 [1] | 10.5 |
| Rx Channels | 8 | 8 | 8 | 8 | 6 |
| Peak power $(\mathrm{MW})$ | 2×1.5 | 1.5 | — | — | 1.0 |
| Max. duty cycle $(\%)$ | 12.5 | 12.5 | — | — | 25 |
| Pulse duration $(\mu\mathrm{s})$ | 10 – 2000 | 10 – 2000 | — | — | <10 – 2000 |
| Min. inter-pulse $(\mathrm{ms})$ | 1.0 | 1.0 | — | — | 0.1 |
| Sys. temperature $(\mathrm{K})$ | 250 – 350 | 90 – 110 | 30 – 35 | 30 – 35 | 80 – 85 |

Table 2.1: The EISCAT radar systems characteristics

[1] Geometry dependent, $k = 2k_0 \sin\theta/2$, where $\theta$ is the angle of the bisector between transmitted and received directions. The value given is when the two antennae beams intersect at $\alpha = 30\,°$

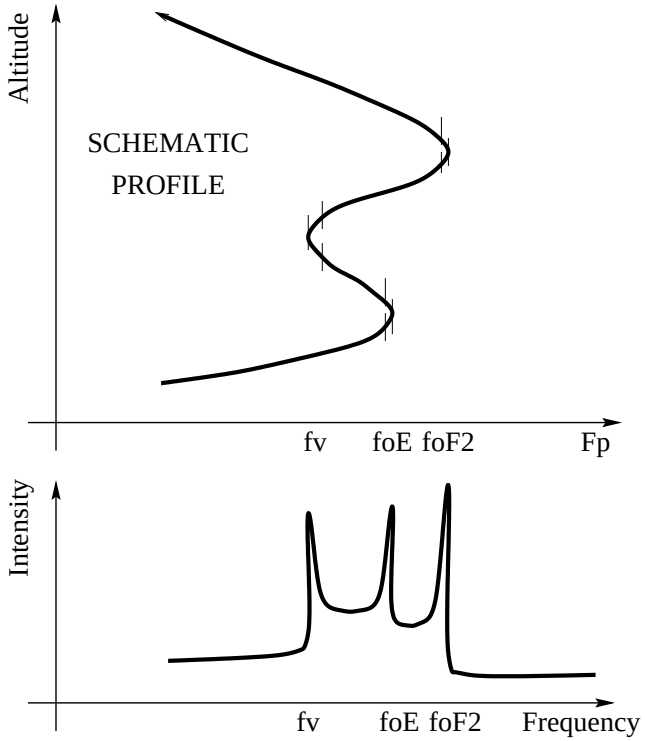


Figure 2.2: Principle of the long pulse measurement of the plasma lines. The critical frequencies fv, foE and foF2 can be estimated by locating the abrupt signal drop in the power spectrum

The EISCAT mainland system consists of a UHF tri-static radar and a VHF monostatic radar. Both UHF and VHF transmitters are located near Tromsø, Norway while the two remote UHF receiving antennae are located in Sodankylä, Finland and in Kiruna, Sweden. The EISCAT radar system is widely described in the literature, and detailed descriptions can be found in e.g. Brekke (1977) and Folkestad *et al.* (1983). Recently, EISCAT has extended its observation capabilities with the inauguration in August 1996 of a new radar, the EISCAT Svalbard Radar (ESR) at Longyearbyen on the archipelago of Svalbard (Wannberg *et al.*, 1997) which has now been operating regularly since April 1997.

Table 2.1 presents the important technical characteristics of the mainland EISCAT systems and the new ESR system.

## 2.4 Long pulse technique

At the peak or valley of a layer, more electrons are resonant within a specific frequency resolution cell. When fine-frequency measurements are made of the echo from a long radar pulse, the abrupt signal intensity variations as a function of the frequency (see Figure 2.2) permit accurate determination of the critical frequencies (Showen, 1979). The long pulse technique consists of transmitting a pulse of $300-500\ \mu$s, and allows one to measure the plasma line at the critical frequency of a region like at the peak of the F-region. This technique has been used at different ISR at the peak of the E-region (Kofman and Wickwar, 1980) as well as at the peak of the F-region (Showen, 1979; Kofman and Wickwar, 1980; Kofman *et al.*, 1981; Heinselman and Vickrey, 1992b; Kofman *et al.*, 1993; Showen, 1995).

### 2.4.1 The experiment ECHO-D-V

We have designed a long pulse plasma line experiment for the EISCAT VHF radar (ECHO-D-V) based on the experiment described in Kofman *et al.* (1993). The principle is to send one long pulse at the frequency $f_0$ and to receive signal simultaneously on three different channels tuned at three different frequencies, $f_0$ for the ion line, $f_0+f_+$ for the up-shifted plasma line and $f_0+f_-$ (where $f_-<0$) for the down-shifted plasma line. The ACF's from these channels are calculated in the same way, therefore the measurement of the three spectral lines is performed in the same volume. In ECHO-D-V the transmitted pulse is $450\ \mu$s and the received signal is sampled at $10\ \mu$s over a time interval that enables to build 5 ACF's with 33 lags. It means that the correlation function is evaluated at 33 lag delays from 0 to $320\ \mu$s by step of $10\ \mu$s.

Figure 2.3 shows the timing diagram of the transmitted pulses and the receiving intervals of signal, calibration and background of our long pulse experiment. Two channels (channels 4 and 5) are dedicated to the plasma lines, channel 3 is used to measure the ion line in the same volume as the plasma lines. Channel 6 is used for the transmission of a very long pulse. This very long pulse is used to estimate, by ion line measurement, the standard ionospheric parameters at higher altitude. The complete cycle is run in $17.5\,$ms which provides good statistical accuracy in a short integration time. We have collected valuable data at a time resolution of $2\,$s with ECHO-D-V. The collected data have been used to analyse both the intensity and the Doppler frequency shift of the up- and down-shifted plasma lines and the results have been compared with our model for the intensity and the Doppler frequency shift (Guio and Lilensten, 1998).

When running the experiment, a plasma line tracking program interacts with the radar. This program monitors the spectra of the measured plasma lines and

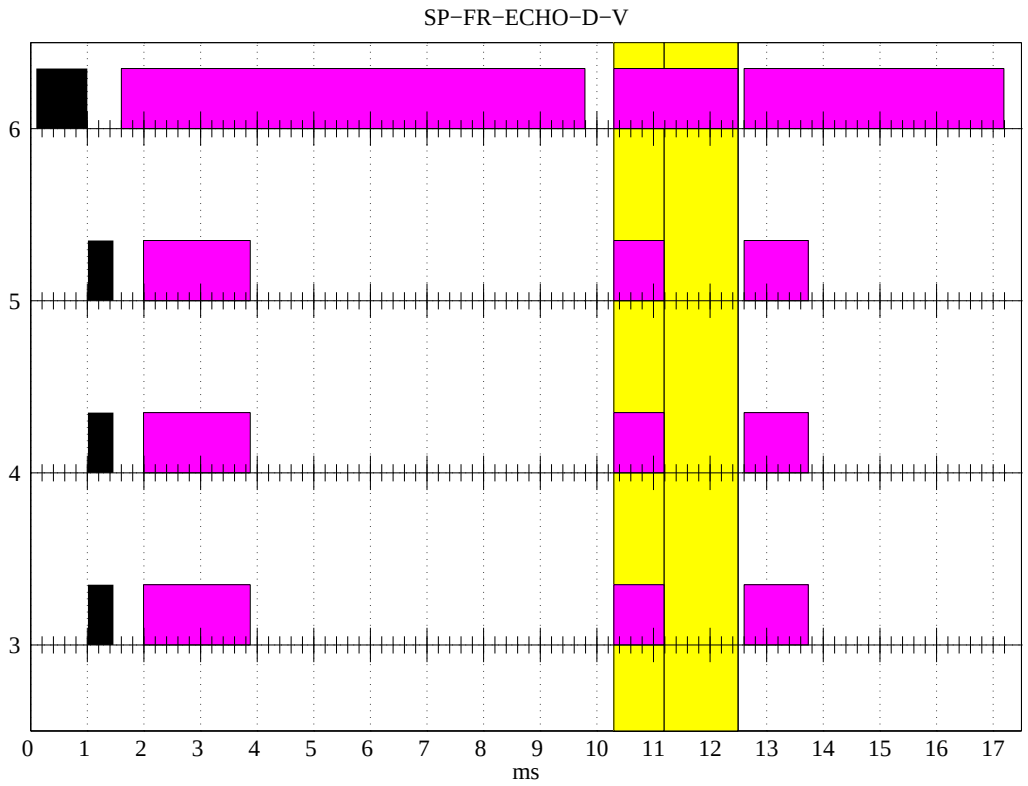


Figure 2.3: Time diagram of the pulsing of the EISCAT long pulse experiment ECHO-D-V. *black* is for the transmitted pulses, *dark gray* is for the receiving periods and *light gray* is when the calibrated noise source is injected. The background measurement is performed at the end of the cycle. The whole cycle is run in $17.5\,\mathrm{ms}$ and provides good statistical accuracy in a short time

changes the frequency of the plasma line receiver channels every time it is necessary in order to get the plasma lines in the centre of the $100\,\mathrm{kHz}$ observation window.

Figure 2.4 shows the reduced spatial ambiguity function of each lag of the first ACF *gate*, and the range of each gates. The $x$-axis represents the time $t$ it takes to a radio signal to travel a range $r$ and back again. This is the range $r$ where the scattering takes place ($r = ct/2$ where $c$ is the light speed). The reduced spatial ambiguity function of a lag is the range function which measures the power gain inside the scattering volume to estimate this lag product. It is also referred as the effective pulse form when considered as a function of time (Lehtinen, 1986). The reduced spatial ambiguity is defined as the product of the convolution between the receiver impulse response $p$ and the envelope of the transmitted pulse $\mathrm{env}$ evaluated at the range $r$ corresponding to the first sample and at the range $r + c\tau/2$

corresponding to the second sample delayed by $\tau$

$$W_\tau(r) = (p*\mathrm{env})(r)(\overline{p*\mathrm{env}})(r + c\tau/2) \tag{2.1}$$

The left panel in Figure 2.4 is for the long pulse of channel 3 which is used to measure the plasma lines. The right panel is for the very long pulse of Channel 6 that measures the ion line. Each trapezium represents the range ambiguity functions for the labelled lag. The tick marks are the range of the centre of every gates.

The ambiguity function is about the same for every lag of one ACF. It is about $45\,\mathrm{km}$ ($300\,\mu\mathrm{s}$) for the long pulse of channels 3, 4 and 5 and $100\,\mathrm{km}$ ($666\,\mu\mathrm{s}$) for the very long pulse of channel 6. The range separation between two gates is $37.5\,\mathrm{km}$ ($250\,\mu\mathrm{s}$) for the long pulse and $90\,\mathrm{km}$ ($600\,\mu\mathrm{s}$) for the very long pulse. 5 gates are calculated from $178\,\mathrm{km}$ to $328\,\mathrm{km}$ ($1190\,\mu\mathrm{s}$ to $2190\,\mu\mathrm{s}$) for the long pulse and 11 gates from $317\,\mathrm{km}$ to $1217\,\mathrm{km}$ ($2110\,\mu\mathrm{s}$ to $8115\,\mu\mathrm{s}$) for the very long pulse.

The algorithm used to calculate the ACF's is from the GEN-LIB system (Turunen, 1985, 1986). The GEN-LIB system consists in a collection of ACF algorithms for the EISCAT correlator based on the lag profile matrix (Turunen, 1983; Turunen and Silen, 1984). The summation strategy of the ACF algorithm for a long pulse in the GEN-LIB system is such that every lag of the ACF has a range ambiguity function with the same absolute volume boundaries and the nominal middle point of the volume is located at the same range. At the same time, the shape of the ambiguity function inside this volume differs from lag to lag as seen in Figure 2.4, but the effective pulse length remains about the same for every lag.

The description of the experiment displayed in Figure 2.4 is calculated by GUISDAP (see Chapter 3). In GUISDAP, a set of MATLAB variables contains the necessary information for the complete description of the experiment which is needed to analyse measured data.

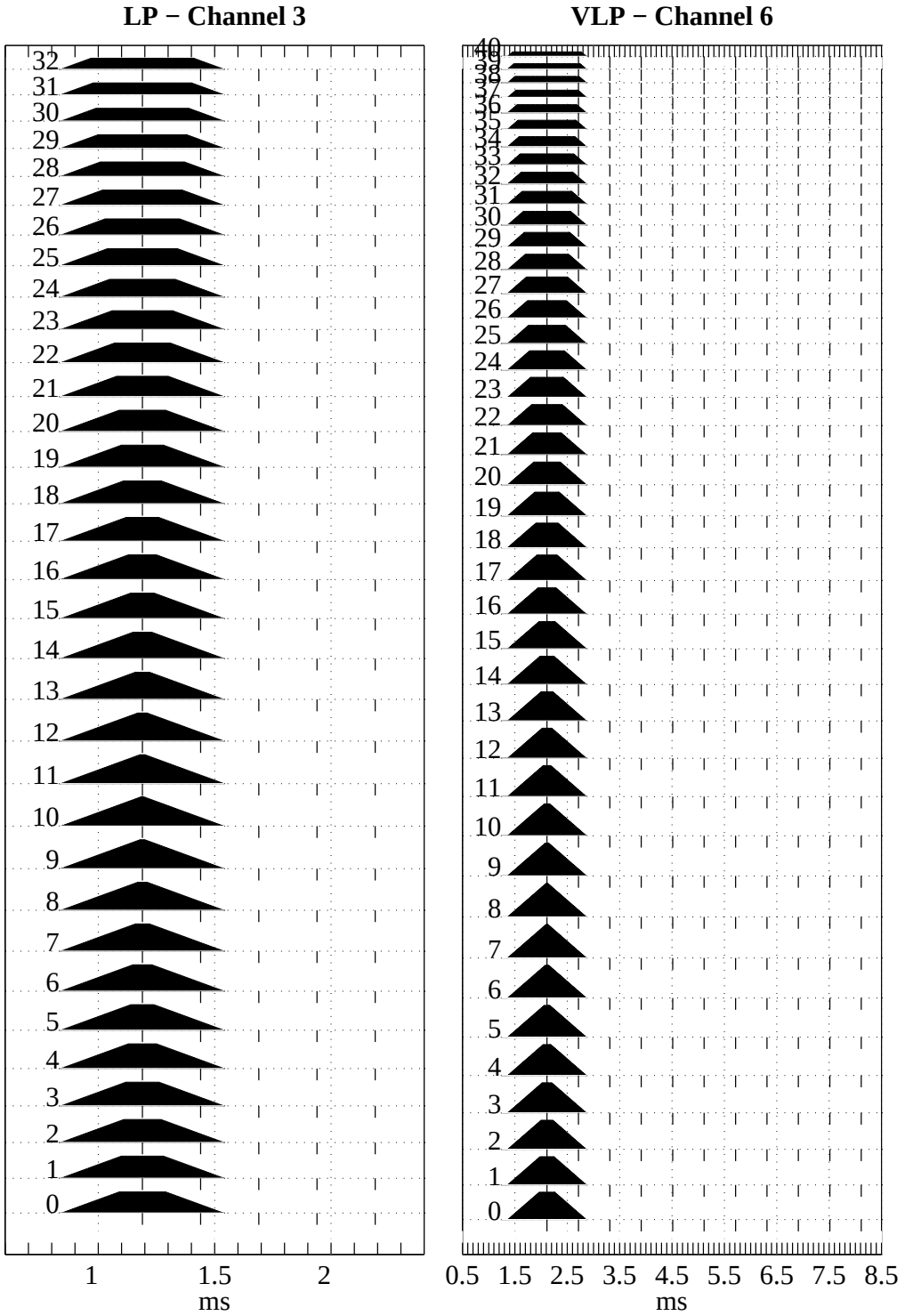


Figure 2.4: Reduced range ambiguity function of the 33 lags of the long pulse of channel 3 and the 41 lags of the very long pulse of channel 6 of the experiment ECHO-D-V. The reduced range ambiguity functions for the lags of the ACF's of channels 4 and 5 are identical to the ones of channel 3

## 2.5 Alternating code technique

Transmitting pulses at different frequencies within a sequence presents the disadvantage that information provided by the cross-product of samples is lost, as is the case in frequency switched multiple pulse modulations. If the entire duty cycle can be used to transmit a coded pulse at a single frequency, every cross-product between samples in the received signal up to the pulse length provides useful information. Good spatial and temporal resolution can be obtained provided the self-clutter cancels out on average. This can be achieved by the so-called phase-coding techniques (Sulzer, 1986, 1989). The alternating code is one of these techniques (Lehtinen and Häggström, 1987; Sulzer, 1993; Nygren *et al.*, 1996). Random code (Djuth *et al.*, 1994, 1997) is another one, but this technique cannot be implemented without extra hardware on the present EISCAT system.

The alternating code technique consists in transmitting a *sequence* of long pulse *phase modulated* in a predefined manner which improves dramatically the spatial resolution of the autocorrelation functions.

Finding a suitable sequence that fulfils the condition of cancellation was not an easy task. At first, Lehtinen and Häggström (1987) restricted the number of possible combinations using the theory of Walsh sequences and expressed their solution as a Walsh sequence. The Walsh sequences are *binary* orthogonal sequences that have been used as a multiplication-free alternative to the fast Fourier transform methods. For a strong condition alternating code, as the one we have used for our experience, $2n$ sequences $SC$ indexed from 0 to $2n-1$ of phase modulated long pulse are transmitted. The phases of each long pulse are defined by a sign sequence $(s_i)$ (equal to +1 or -1) of length $n$ called the number of bauds (or bits) and indexed from 0 to $n-1$. The total length of the pulse is $n$ times the duration of one baud. The sign sequence $(s_i)$ for the sequence $SC$ is defined by

$$s_i(SC) = \mathrm{Walsh}(a_i, SC) = (-1)^{\sum_{n=0}^{\infty} (a_i)_n \wedge (SC)_n} \tag{2.2}$$

where $(a_i)_n$ and $(SC)_n$ are the *binary* representations of the integer numbers $a_i$ and $SC$ and $\wedge$ is the logical and operator. The number sequence $(a_i)$ to calculate the code sequences $s_i(SC)$ were found by a computer search (Lehtinen and Häggström, 1987).

Figure 2.5 shows the 64 sequences $SC$ of phase modulated long pulse based on the signs sequences $(s_i)$ of length 32 needed to run the $32\,\mathrm{bits}$ strong condition alternating code available at EISCAT (Guio *et al.*, 1996).

Few EISCAT experiments have been designed with an alternating code, mainly EISCAT CP's (Common Program) and it does not exist any program to design an alternating code experiment. In order to design our experiment with the $32\,\mathrm{bits}$

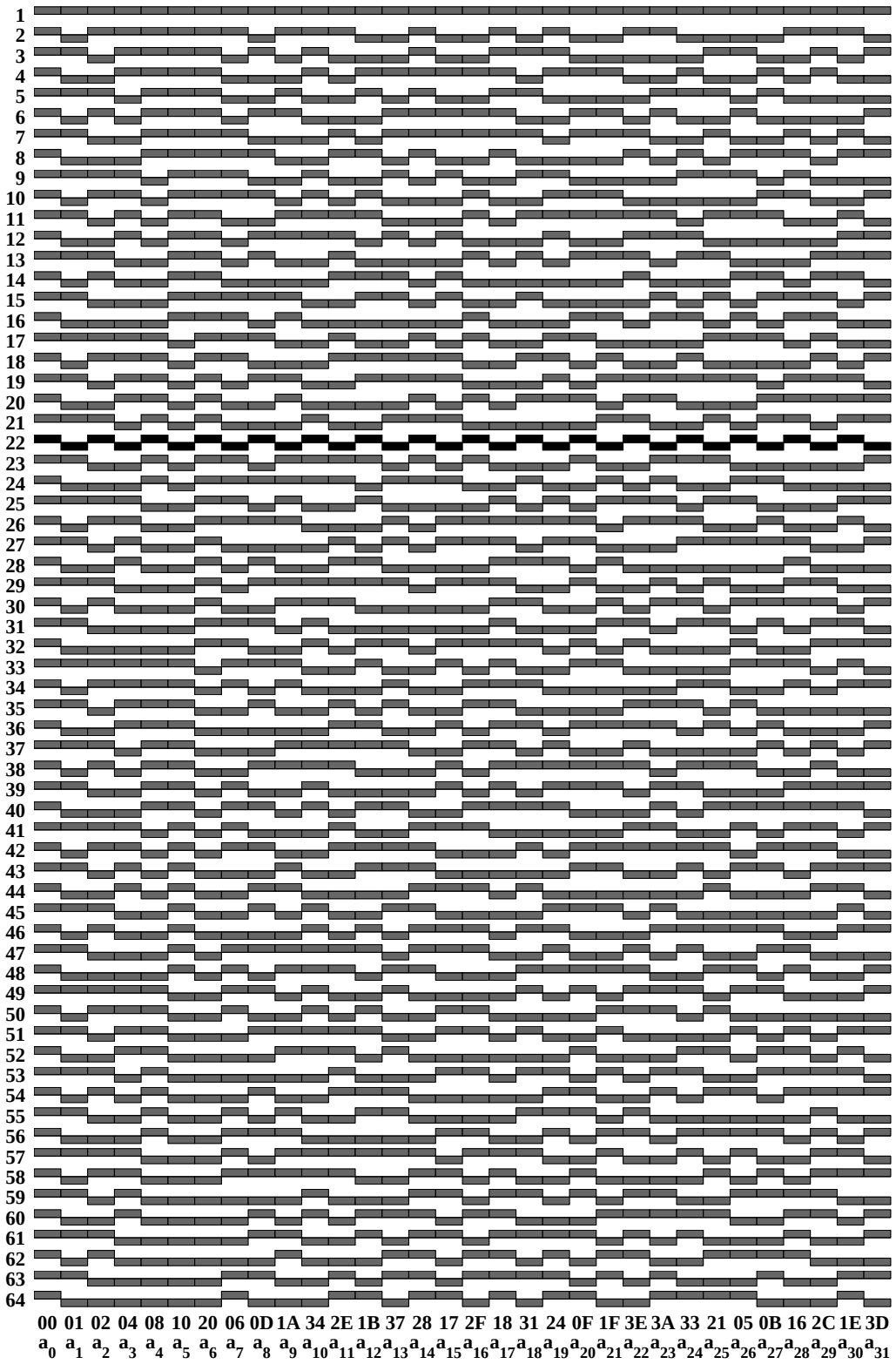


Figure 2.5: The 64 pulse sequences required for the $32\,\mathrm{bits}$ strong condition alternating code available at EISCAT. The $a_i$ is the sequence of numbers needed to calculate the signs of the pulse with Eq. (2.2). The sequence $SC = 22$ in *dark gray* is a regularly alternated modulation of period two times the length of the baud

strong condition alternating code for the EISCAT VHF radar, we wrote a MATLAB programme that generates automatically the necessary files to describe the experience. This programme is completely parametrised and handles a variable number of ACF gates, a variable number of lags to be computed and a variable range profile of ACF's to be measured.

Following is a summary of the different properties of the alternating code technique:

- ☞ The range resolution of each lag of the ACF is defined by the time length of one baud, i.e. the duration of one sign $s_i$. An exception is the zero lag which has a range resolution corresponding to the total pulse length.
- ☞ Normally, the ACF is computed at time delays multiple of the baud length.
- ☞ The ACF can be computed at a maximum delay equal to the total pulse length, i.e. the number of bauds times the duration of one baud.
- ☞ A necessary condition for the alternating code to work correctly is that the ionospheric plasma remains stationary over the time it takes to the $2n$ pulse sequences to be transmitted so that the self-clutters cancel correctly.

### 2.5.1 The experiment ALT-32-2-V

Our aim when designing a plasma line experiment using the alternating code technique was to drastically improve the height resolution compared to the long pulse technique in order to be able to measure a profile of plasma lines. The situation is sketched in Figure 2.6. For favourable measurement conditions, the measurement of the plasma line can be done at more than ten gates.

The problem when writing an alternating code experiment is to find a compromise between the sample rate (the duration of one baud) which defines the range resolution and the spectral bandwidth, the lag extent (limited to the baud length times the number of bauds) which defines the spectral resolution and the range to be covered by the experiment (the number of ACF to be calculated). In addition is the constraint due to the limitations of the time it takes to compute the ACF's and the limited size of the correlator memory. These conflicting parameters have to be handled carefully when designing an alternating code experiment.

We have designed the first $32\,\mathrm{bits}$ strong condition alternating code plasma line experiment. The duration of one baud was chosen to be $20\ \mu\mathrm{s}$ which provides a gate resolution and a gate separation of $3\,\mathrm{km}$ and a $50\,\mathrm{kHz}$ bandwidth observation window. In addition to the alternating code, a long pulse of $500\ \mu\mathrm{s}$ was added in a newer version than the one presented in Guio *et al.* (1996) to estimate the ionospheric parameters given by the ion line at a higher range.

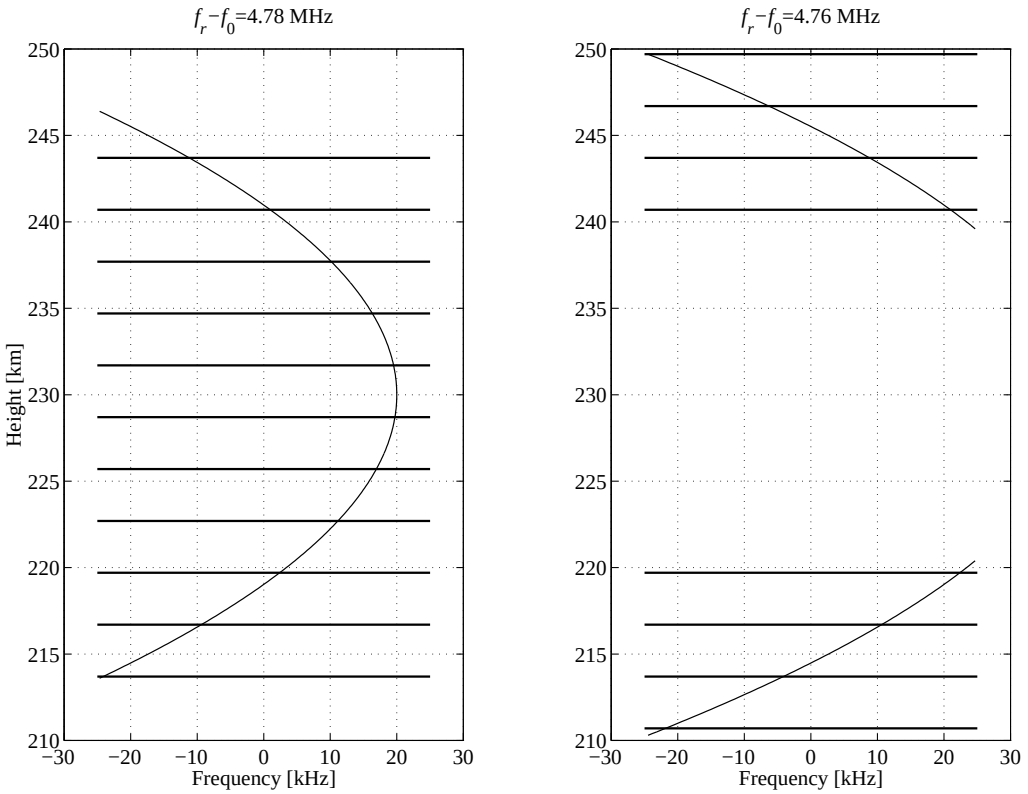


Figure 2.6: Parabolic height distribution of the plasma line frequency with a scale height of $65\,\mathrm{km}$ showing two different tuning of a $50\,\mathrm{kHz}$ receiving window and the corresponding cells of $3\,\mathrm{km}$ contributing to the scattering

We present here the characteristics of the new experiment ALT-32-2-V. The principle of this experiment is the same as the long pulse experiment. The alternating code is transmitted once and received on three different channels simultaneously tuned at three different frequencies. One channel is for ion line measurement (channel 5), the two other channels (channel 3 and 4) are for measurement of the up- and down-shifted plasma lines. Channel 6 is for the ion line long pulse.

Figure 2.7 shows the timing diagram of the transmitted pulse as well as the receiving intervals of signal, background and calibration for one sequence. Two channels (channels 4 and 5) are dedicated to the plasma lines, channel 3 measures the ion line in the same volume as channels 4 and 5. Channel 6 is used for the transmission of a long pulse in order to measure ionospheric parameters from the ion line at high range. The 64 cycles are run in $764\,\mathrm{ms}$ which means that the ionospheric plasma has to remain stationary in that time for the ACF's to be correctly estimated.

Figure 2.8 shows the reduced ambiguity of the 28 lags computed using the

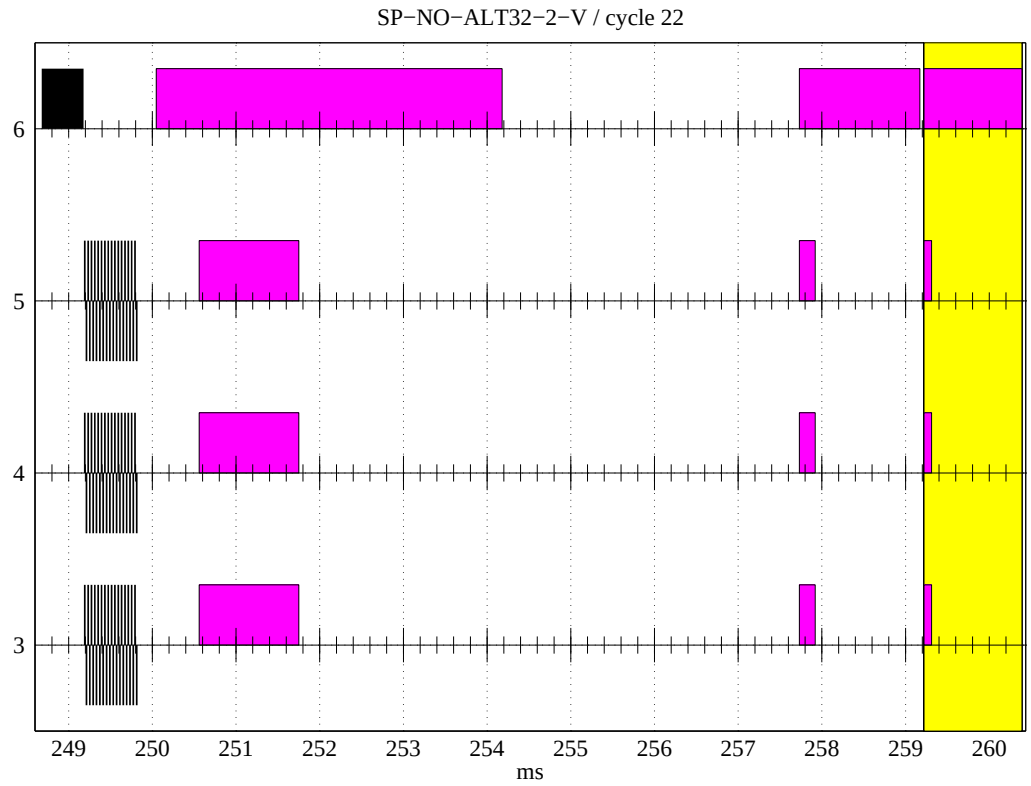


Figure 2.7: Time diagram of the pulsing of the $22^{\mathrm{nd}}$ cycle of the $32\,\mathrm{bits}$ strong condition alternating code of ALT-32-2-V . *black* is for the transmitted pulses, *dark gray* is for the receiving periods and *light gray* is when the calibrated noise source is injected. The background and calibration measurements are performed at the end of each cycle. The whole 64 cycles are run in $764\,\mathrm{ms}$ and have been optimised for a $10\,\mathrm{s}$ pre-integration time

alternating code (left panel, channel 3) and the 29 lags computed for the long pulse (right panel, channel 6). The ACF of the alternating code is computed by the algorithm of the G2-LIB system (Wannberg, 1993). The G2-LIB is an extension to GEN-LIB to compute ACF for the alternating code. The range ambiguity function of each lag of the ACF is $3\,\mathrm{km}$ ($20\,\mu\mathrm{s}$) for the alternating code and $50\,\mathrm{km}$ ($330\,\mu\mathrm{s}$) for the long pulse. The range separation between two gates is $3\,\mathrm{km}$ ($20\,\mu\mathrm{s}$) for the alternating code and $37.5\,\mathrm{km}$ ($250\,\mu\mathrm{s}$) for the long pulse. 32 gates are calculated from $202.8\,\mathrm{km}$ to $295.8\,\mathrm{km}$ ($1352\,\mu\mathrm{s}$ to $1972\,\mu\mathrm{s}$) for the alternating code and 12 gates from $251.3\,\mathrm{km}$ to $663.8\,\mathrm{km}$ ($1675\,\mu\mathrm{s}$ to $4425\,\mu\mathrm{s}$) for the long pulse.

The data presented in Guio *et al.* (1996) were collected using the first version of this experiment ALT-32-1-V which did not include the long pulse and contained 40 gates instead of the 32 gates of the present experiment. Data collected with

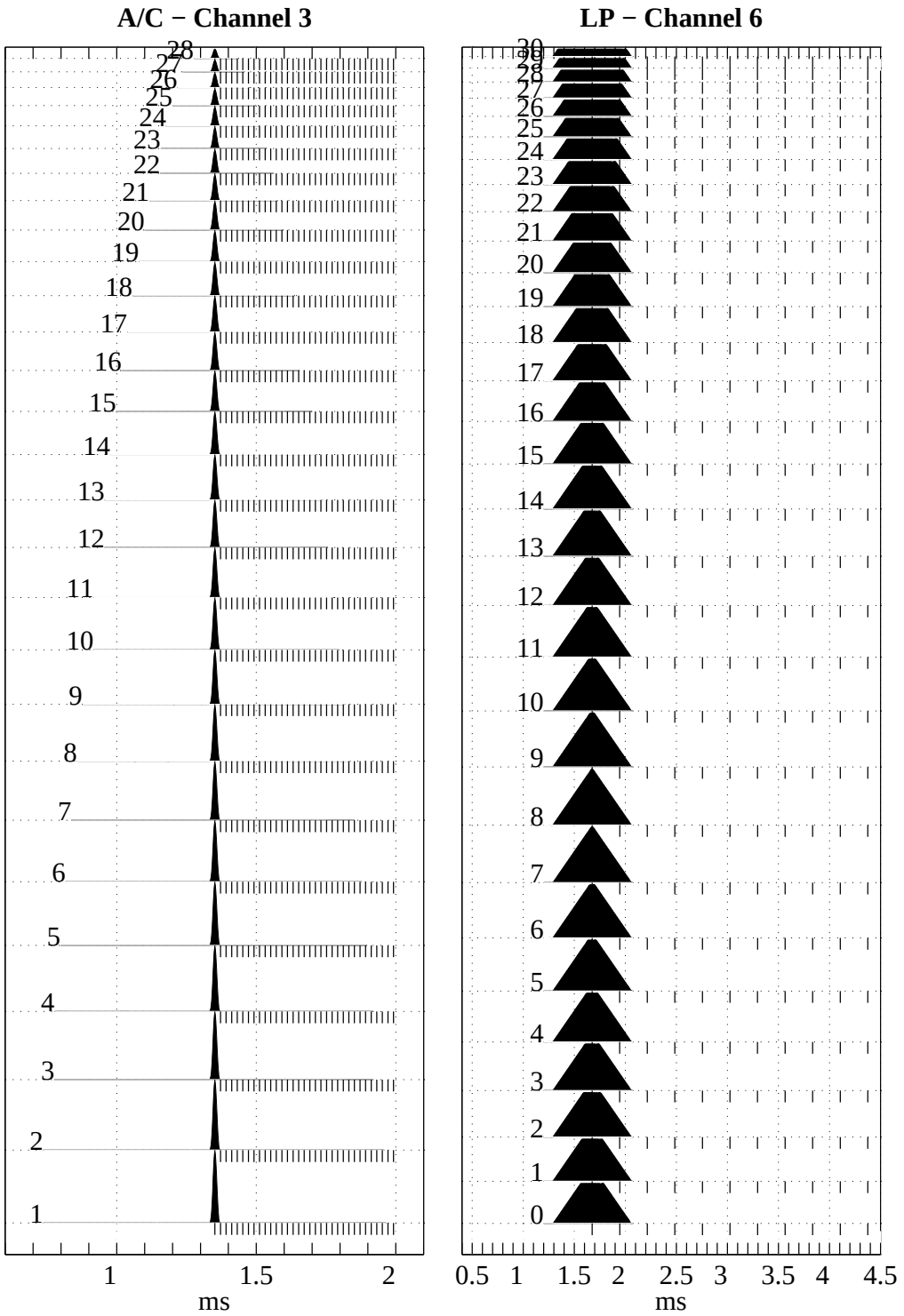


Figure 2.8: Reduced range ambiguity function of the 28 lags of the alternating code of channel 3 and the 31 lags of the long pulse of channel 6 of ALT-32-2-V. Note that, as the long pulse experiment ECHO-D-V, the lags of the ACF's of channels 4 and 5 have the same reduced range ambiguity functions as the ones of channel 3

ALT-32-2-V have been analysed and are shown in Chapter 3.

## 2.6 Summary

We have designed two different plasma line experiments for the EISCAT VHF radar. The first experiment makes use of the classic long pulse technique and the second one the alternating code technique.

For the first time at EISCAT, the alternating code technique has been successfully used in the frame of a plasma line experiment. Our experiment implements a $32\,\mathrm{bits}$ alternating code strong condition on the VHF EISCAT radar. It was seen that the alternating technique greatly improves the height resolution and therefore allows one to measure the plasma line at several ranges instead of the one range as done with the classic techniques (Guio *et al.*, 1996).

The long pulse experiment has been run successfully and has provided valuable high time resolution plasma line data. Such a data set, collected at high time resolution, has been used to compare the measured intensity and Doppler frequency shift of the plasma lines with our model (Guio and Lilensten, 1998). This data set has allowed us to identify the effect on the plasma line intensity and to some extent on the Doppler frequency of the fine structures in the supra-thermal distribution function in the energy range $20-30\,\mathrm{eV}$.

*"Talking about music is like dancing about architecture."*

Laurie ANDERSON.

# Chapter 3

# Data analysis

## 3.1 Introduction

Once the autocorrelation functions (or the power density spectra) have been computed using an incoherent scatter experiment, the large amount of collected data needs to be reduced to *estimated* ionospheric parameters and their associated *uncertainties*. This is done on a computer by an analysis program that attempts to fit the data to a theoretical model. Ideally, the data should *not* be modified by any calculations, so the model has to include

- ☞ An "ideal" theoretical model. For our purpose, it consists in a model for the intensity and the Doppler frequency shift of the up- and down-shifted plasma lines (Chapter 1).
- ☞ The effect of measuring with an "imperfect" instrument. In an incoherent scatter experiment, this is:
  - The finite pulse length of the transmitted power
  - The finite impulse response of the receiver system

  and the effect on the measurement is the spatial ambiguity function (Chapter 2).

GUISDAP is a package designed to analyse incoherent scattering ion line data. It is written partly in C and interfaced to MATLAB. The current stable version (v1.6) allows one to analyse each ACF independently as gates or to analyse grouped lags from different modulations with spatial ambiguity function within

the same volume. A new version (v2.0) to come will be able to analyse simultaneously one range profile of ACF data in one fit (Holt *et al.*, 1992; Lehtinen and Huuskonen, 1996).

## 3.2 GUISDAP

The theoretical foundations used in GUISDAP concerning the radar theory and the ambiguity functions are found in Lehtinen (1986), while the theory of statistics of multi-parameter fits is found in Vallinkoski (1989).

This program is able to translate the files describing the experiment into a set of variables describing the experiment and to calculate the effect of the radar which has to be taken into account when analysing data. It has anyway some limitations. It can not handle automatically ion species other than $O^+$ and a mixture of the molecular ions ${O_2}^+$ and $NO^+$. This is a serious problem when it comes to analyse VHF data at high altitude (presence of $H^+$). The analysis of the ion composition in general is not handled.

## 3.3 Plasma line analysis

We have developed a plasma line analysis programme which widely uses the GUISDAP package. The specifications of the experiment are calculated by GUISDAP and we have changed the fitting procedure for the ion line to our own fitting procedure which handles plasma line data. This procedure is based on the Levenberg-Marquardt method. This method performs a minimisation of the sum of the squares of the residuals — the differences between the measured and the values given by the model for a given set of parameters — (Bard, 1974). The method is optimised to switch continuously from a method which quickly approaches the minimum (the steepest descent method), when far from the minimum, to a more precise but slower method (the Newton method), when approaching the minimum. The variances of the ACF are estimated by GUISDAP using the ambiguity function (Lehtinen, 1986) in order to estimate the uncertainties of the fitted parameters.

Our analysis tool handles both plasma line data collected with the long pulse technique and the alternating code technique. It would not be an important work to integrate other models of the ACF of the plasma line.

#### Long pulse

The model for this spectral signature is described in (Kofman *et al.*, 1981; Heinselman and Vickrey, 1992a) and has also been used in Kofman *et al.* (1993).

In a long pulse experiment, the ACF signature of the plasma line is depending on the variation of the plasma frequency $\omega_p(r)$ as a function of range around the peak of the observed region and the range ambiguity function.

The variation of the plasma frequency around the peak of the F-region can be described by a parabola $\omega_p(z) = \omega_{p\max}(1 - z^2/8)$, where $z = (r - r_{\max})/H$. $\omega_{p\max}$ is the maximum frequency at the peak located at the range $r_{\max}$ and with scale height $H$.

The power density $S(\omega, r)$ of the plasma line at the range $r$ is assumed constant over the frequency bandwidth $\delta f$ centred at $\omega_p$ and with an integrated power equal to $a_p$ which is constant with range. The autocorrelation function at the range $r$ of the power density $S(\omega, r)$ is called $\rho_S(\tau, r)$.

The effect of the radar is taken into account with the range ambiguity functions $W_\tau(r)$, presented in Figure 2.4. $W_\tau(r)$ is calculated by GUISDAP. The measured ACF $\rho$ at the delay $\tau$ is then the range-integrated (over the range $R$ of the gate), of the product of $\rho_S(\tau, r)$ with the range ambiguity function $W_\tau(r)$

$$\rho(\tau; \omega_{p\max}, r_{\max}, H, \delta f, a_p) = \int_R W_\tau(r)\rho_S(\tau, r)dr. \tag{3.1}$$

Figure 3.1 shows an example of a fit done for a dump collected by our experiment ECHO-D-V described in Chapter 2 at $2\,\mathrm{s}$ resolution. The fit is done on the ACF shown in the two upper panels. The two lower panels are just Fourier transforms of the ACF to give a clearer image of the spectral signature of the plasma line when using the long pulse technique. Note that we are able to measure the critical frequency with uncertainties of a few hundred Hertz.

Figure 3.2 presents the results of a data set collected with a time resolution of $2\,\mathrm{s}$ (Guio and Lilensten, 1998). One can clearly see the role of the monitoring program which for every new dump collected attempts to follow the critical frequency of the spectrum in the $100\,\mathrm{kHz}$ observation window. The parameters shown are from top to bottom the Doppler frequency shift of the up- and down-shifted plasma lines $(\omega_+/2\pi) + 0.2\,\mathrm{MHz}$ and $-\omega_-/2\pi$, the Doppler frequency between the plasma lines $(\omega_+ + \omega_-)/2\pi$, the temperature, or intensity, of the plasma lines $T_{p+}$ and $T_{p-}$ and the frequency width of the plasma lines $\delta f_{p+}$ and $\delta f_{p-}$.

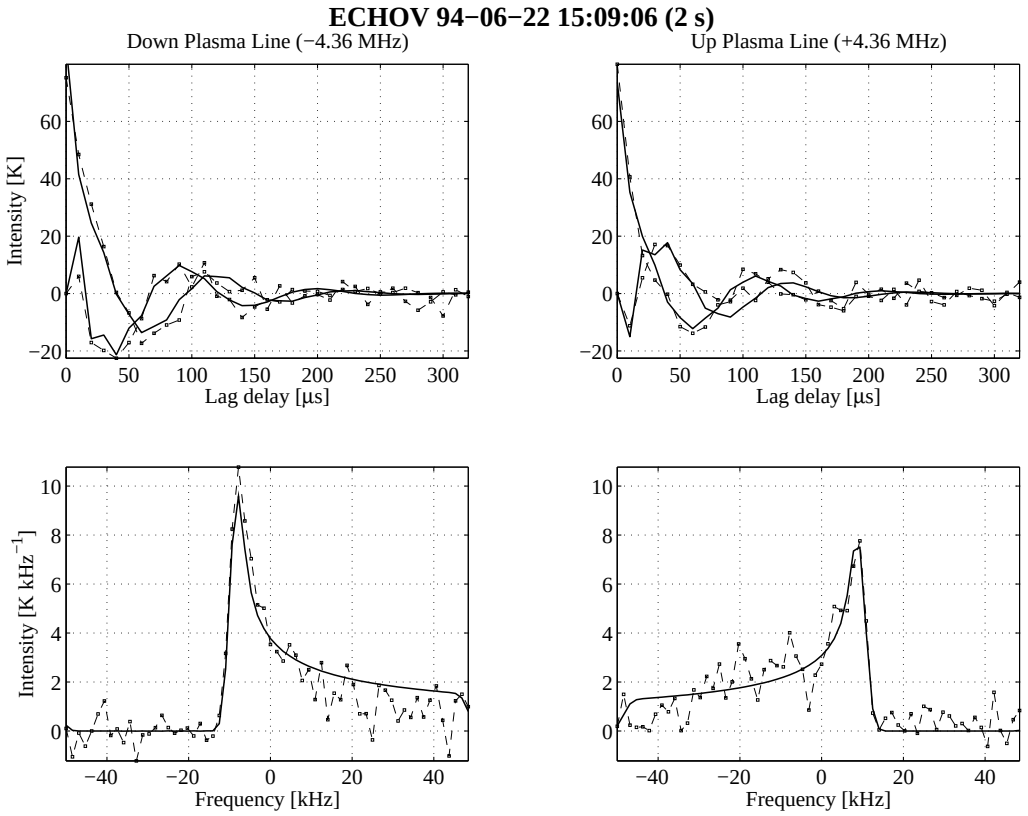


Figure 3.1: Long pulse fit of data collected with ECHO-D-V. The two upper panels show the measured complex autocorrelation functions expressed in units of antenna temperature (*dashed line* and the theoretical model (*solid line*) of Eq. (3.1). The curves with the intensity equal to zero at zero lag delay are the imaginary parts. The two lower panels present the corresponding power density spectrum where the critical frequency is more easily identified

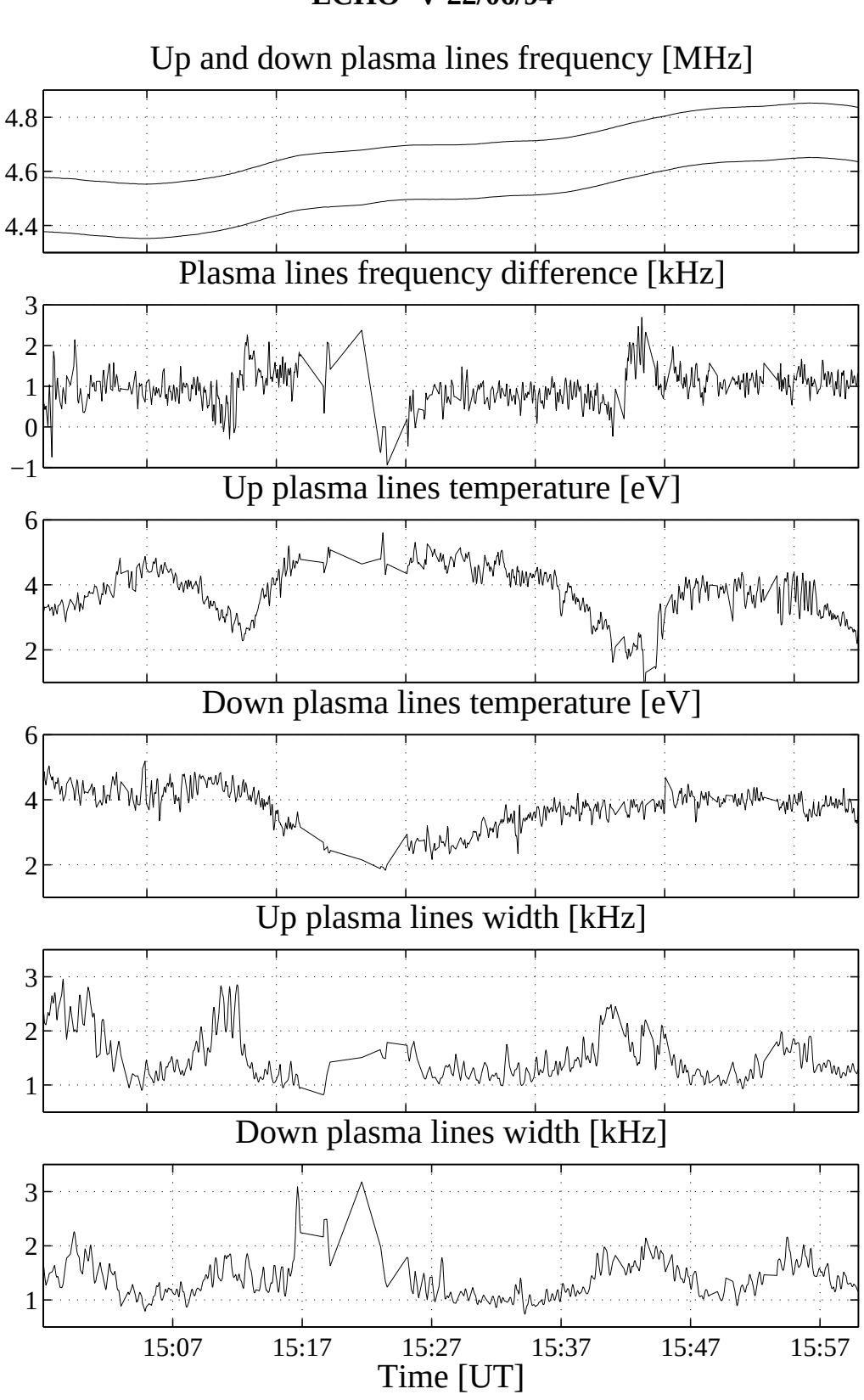


Figure 3.2: The parameters as a function of time that result of the analysis of a 1 hour data set collected at 2 s resolution with our long pulse experiment ECHO-D-V

### Alternating code

The spectral signature of the spectra collected with the alternating code technique is quite different from the one of the spectra collected with the long pulse technique.

In an alternating code experiment, the spectral signature of the plasma line can be approximated by a truncated parabola. Since the sensitivity is maximum at the centre of the range and falls linearly to zero one baud length away on each side, due to the correlation of the signal with the code and assuming a perfect receiver, the power will just be the square of this triangular function. This is the shape of the ambiguity function of every lags of the alternating code (it is seen in the left panel in Figure 2.8 of Chapter 2 for all the computed lags). The plasma frequency is changing approximately linearly with height inside the range of one gate ($3\,\mathrm{km}$), and therefore this square triangle function becomes the spectral shape. Of course, it has to be convolved with the inherent line width, but this would appear to have little effect in this case. This means that the spectrum falls to zero at a certain frequency.

The ACF measured with the alternating code can therefore be modelled by the following expression which is the Fourier transform of a parabola with a maximum at frequency $\omega_p$, the Doppler shift of the line, a frequency width at half the power $\delta f$ and a power $a_p$ assuming the intensity of the plasma line is constant with height. The ACF $\rho$ at lag delay $\tau$ is (Guio *et al.*, 1996)

$$\rho(\tau;\omega_p,\delta f,a_p) = 3a_p\frac{\sin(4\pi\delta f\tau) - 4\pi\delta f\tau\cos(4\pi\delta f\tau)}{(4\pi\delta f\tau)^3}\exp(i\omega_p\tau). \quad (3.2)$$

Figure 3.3 shows an example of a fit done on a dump collected by the last version of our experiment ALT32-2-V at $10\,\mathrm{s}$. For this analysed dump, our fitting procedure analysed successfully 13 gates. Note that as for the long pulse technique, the uncertainties on the Doppler frequency of the plasma lines are of a few hundred Hertz. The peak of the F-region can clearly be identified in the shape of the Doppler frequency as a function of altitude.

Figure 3.4 shows the results of the parameters fitted for a data set collected at a time resolution of $10\,\mathrm{s}$ with the last version of our experiment ALT32-2-V. The parameters shown are from top to bottom the Doppler frequency shift of the up- and down-shifted plasma lines $\omega_+/2\pi$ and $-\omega_-/2\pi$, the Doppler frequency between the plasma lines $(\omega_+ + \omega_-)/2\pi$, the temperature, or intensity, of the plasma lines $T_{p+}$ and $T_{p-}$ and the frequency width of the plasma lines $\delta f_{p+}$ and $\delta f_{p-}$.

Note the difference in term of fitted data between the alternating code data of Figure 3.4 and the long pulse data of Figure 3.2. The long pulse experiment provides one data point for each dump while the alternating code technique provides

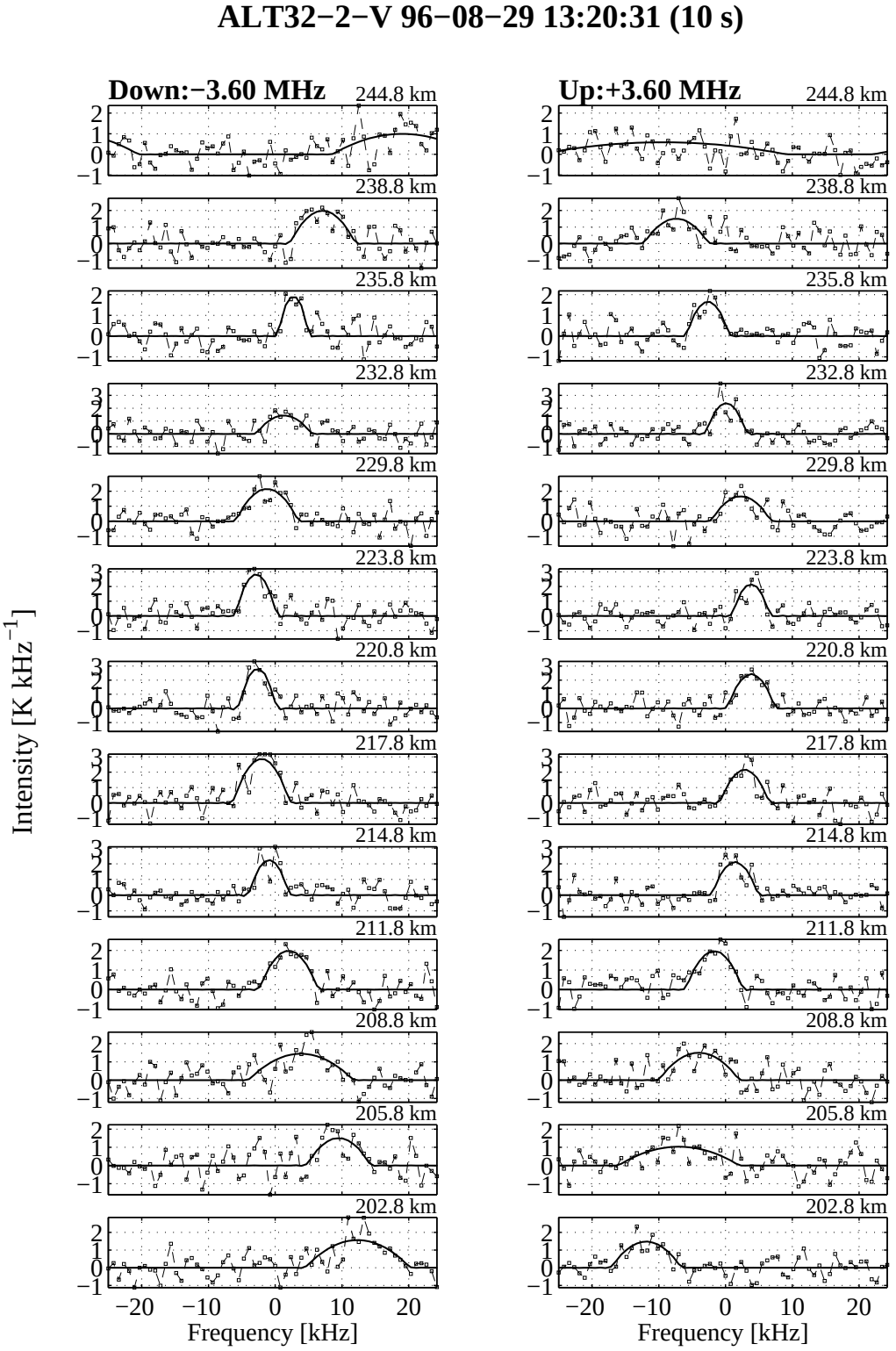


Figure 3.3: Alternating code fit of plasma line data collected with ALT32-2-V. The right panels are for the up-shifted plasma lines and the left panels are for the down-shifted plasma lines. The *dashed* lines are the estimated intensity spectra from the ACF's and the *solid line* is the fitted theoretical model

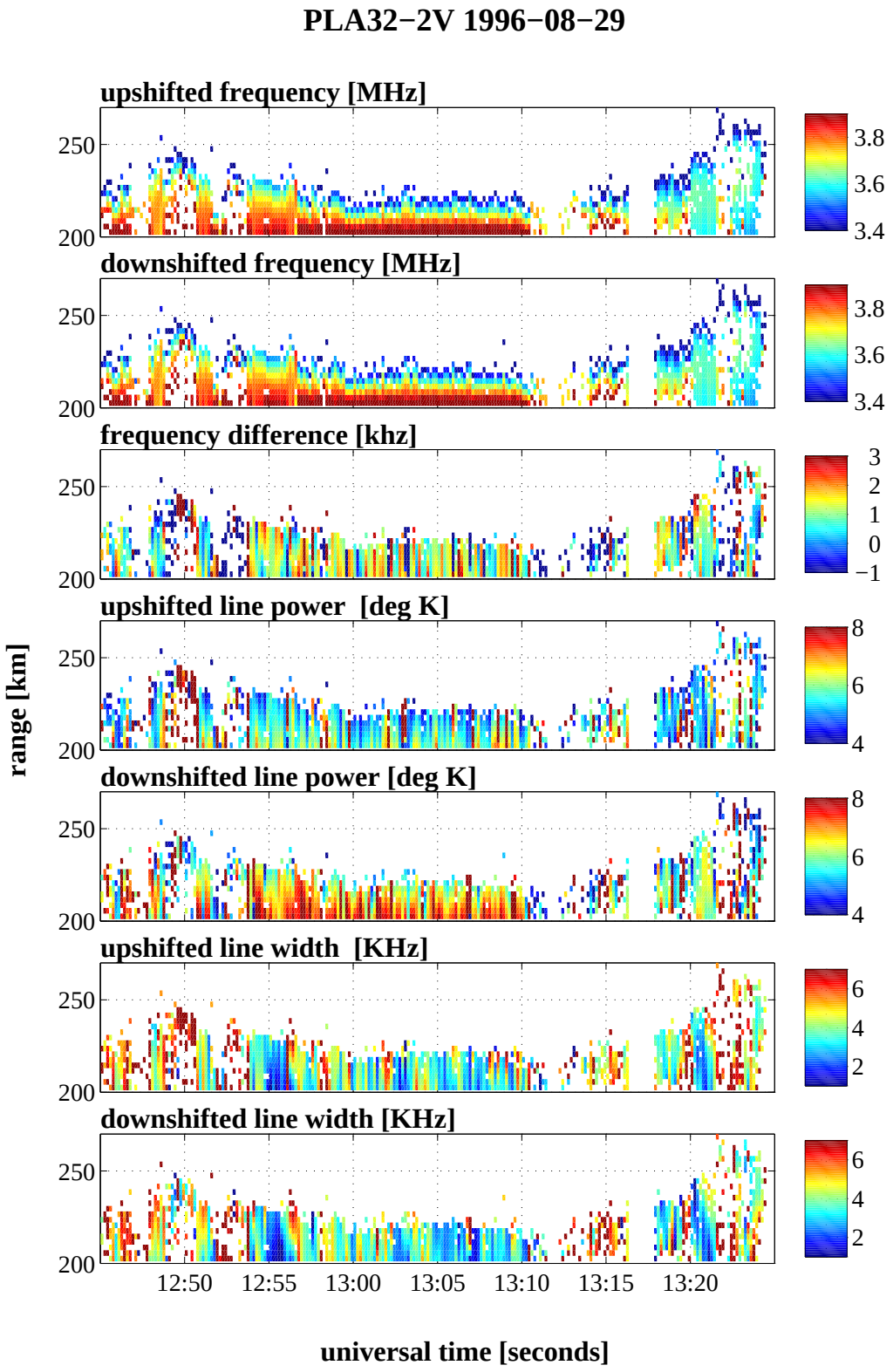


Figure 3.4: The parameters as a function of time and height that result of the analysis of alternating codes data at 10 s resolution collected with ALT32-2-V

several points for each dump.

## 3.4 Comparison data — model

**Plasma line temperature**

The temperature plotted in Figures 3.1 and 3.3 are expressed in term of the antenna temperature while in Figures 3.2 and 3.4 the temperatures are plasma line temperature. They have been converted in order to be compared with the modelled intensity also expressed in temperature. The radar equation is used to convert the temperature.

The radar equation for the plasma line observed at the Doppler frequency $\omega_p$ with an antenna temperature $T_A^p$ is written

$$k_b T_A^p B_w = \frac{P_T}{r^2}\sigma_p \frac{c\tau}{2} A(\omega_0 + \omega_p), \tag{3.3}$$

where $\sigma_p = r_e^2 \frac{n_e}{2\alpha^2}\frac{T_p}{T_e}$ is the plasma line cross section derived from Eq. (1.27) in Chapter 1. $B_w$ is the bandwidth of the receiver, $P_T$ the transmitted power, $r$ the distance to the volume probed, $c$ the light speed, $\tau$ the length of the transmitted pulse and $A(\omega_0 + \omega_p)$ is the frequency-dependent effective antenna area at the received frequency $\omega_0 + \omega_p$. Note that $\sigma_p$ expressed as a function of the plasma line temperature $T_p$ does not depend on the electron density $n_e$.

In the same way, the radar equation for the ion line is written

$$k_b T_a^i B_w = \frac{P_T}{r^2}\sigma_i \frac{c\tau}{2} A(\omega_0), \tag{3.4}$$

where $\sigma_i = r_e^2 \frac{n_e}{(1+\alpha^2)}\frac{\alpha^4}{(1+\alpha^2+\alpha^2 T_e/T_i)}$ is the ion line cross section derived from Eq. (1.25) in Chapter 1. $A(\omega_0)$ is the frequency-dependent effective antenna area at the received frequency (which is the same as the transmitted frequency for the ion line).

We define the radar system constant as $C_s = r_e^2 A(\omega_0) c/2$. We correct this constant so that the electron density given by the plasma line frequency corresponds to the electron density given by the ion line. We call this calibrated constant $C_s'$. This is commonly done when one has a way to calibrate absolutely the electron density, as for instance the plasma line frequency given by a plasma line experiment or foF2 derived from ionosonde data.

In GUISDAP the quantity $\mathcal{K}(r) = \frac{P_T}{r^2}\frac{C_s'}{k_b B_w}\tau$ is calculated for each gate. The plasma line temperature is then given by (in SI units)

$$k_b T_p = \frac{T_a^p}{\mathcal{K} G(\omega_r)}\frac{2e^2}{\epsilon_0 k^2}, \tag{3.5}$$

where $G(\omega_r) = A(\omega_0 + \omega_r)/A(\omega_0)$ is the relative antenna gain as a function of the frequency which is known by measurement of radio source.

The plasma line temperature of Eq. (3.5) can then be compared with the modelled plasma line temperature using the model of Chapter 1.

### Electron Doppler velocity and plasma frequency

The Doppler frequency $\omega_+$ and $\omega_-$ of the up- and down-shifted plasma lines have been estimated by the plasma line analysis. They are the real part of the solutions of the dispersion relation described by Eq. (1.30). Eliminating $\omega_e$ and $v_e$ between these two equations and replacing $Z$ by the model of the Section 1.5, the Doppler velocity $u_e$ of the *ambient* electron population is the solution of the following equation (Guio and Lilensten, 1998)

$$k_+^2 \left[ (1-\alpha)\,\mathrm{Re}\, Z_{v_e}^{*\,a}\left(\frac{v_{\phi_-} - u_e}{v_e}\right) + \alpha\,\mathrm{Re}\, Z_{v_e}^{*\,s}\left(\frac{v_{\phi_-}}{v_e}\right)\right] = \tag{3.6}$$

$$k_-^2 \left[ (1-\alpha)\,\mathrm{Re}\, Z_{v_e}^{*\,a}\left(\frac{v_{\phi_+} - u_e}{v_e}\right) + \alpha\,\mathrm{Re}\, Z_{v_e}^{*\,s}\left(\frac{v_{\phi_+}}{v_e}\right)\right], \tag{3.7}$$

where the drift velocity $u_e$ appears only in the terms relative to the ambient component $Z_{v_e}^{*\,a}$. The dimensionless number $\alpha$ denotes the percentage of supra-thermal electrons.

Once the Doppler velocity $u_e$ is found, the plasma frequency $\omega_e$ is given by

$$\omega_e = \frac{k_\pm v_e}{\sqrt{-(1-\alpha)\,\mathrm{Re}\, Z_{v_e}^{*\,a}\left(\frac{v_{\phi\pm} - u_e}{v_e}\right) - \alpha\,\mathrm{Re}\, Z_{v_e}^{*\,s}\left(\frac{v_{\phi\pm}}{v_e}\right)}}, \tag{3.8}$$

either for the down-going wave ($v_{\phi_+}$,$k_+$) or the up-going wave ($v_{\phi_-}$, $k_-$).

This is the method described in Guio and Lilensten (1998) which has been used on EISCAT VHF data collected with the ECHO-D-V experiment of Chapter 2.

*"Jeg har nu vandret ganske godt omkring i mine dager og jeg har blit dum og avblomstret. Men jeg har ikke den perverse gammelmandstro at jeg har blit visere end jeg var. Og jeg håper at jeg heller aldrig blir vis. Det er tegnet på avfældighet. Når jeg takker Gud for livet så sker det ikke i kraft av en større modenhet som har kommet med alderen, men fordi jeg altid har hat glede av å leve. Alder skjænker ingen modenhet, alder den skjænker intet andet end alderdom."*

Knut Hamsun, *En vandrer spiller med sordin*, 1909.

# Chapter 4

# Spitzer theory

## 4.1 Introduction

In a non-homogeneous plasma, such as the ionospheric plasma, the distribution function of particles deviates from the Maxwellian. At *low* energy and for a *fully* ionised plasma consisting of electrons and one ion species, in a highly collisional regime, i.e. in a regime where the velocity distribution does not *deviate* dramatically from a Maxwellian (Gombosi and Rasmussen, 1991), and in the absence of a magnetic field, the electron distribution function can be approximated by the so-called Spitzer distribution function described in Cohen *et al.* (1950); Spitzer and Härm (1953); Spitzer (1962). Cohen *et al.* (1950) calculated the time-independent electron distribution function which results from the presence of a *weak* electric field whereas Spitzer and Härm (1953) combined the effects of both a weak electric field and a *moderate* temperature gradient. Their solution is based on a perturbation analysis of a Fokker-Planck equation linearised around a Maxwellian. Contrary to most existing works, the kinetic equation is not treated by any expansion method, but is solved numerically to yield the electron distribution function. This feature is very important since we are interested in calculating the $P^*$ and $Z^*$ integrals of the distribution function described in Chapter 1.

## 4.2 The Spitzer function

The velocity distribution function is expanded about a local Maxwellian as a power series in the *Knudsen number* $\epsilon = \lambda/L$ which represents the ratio of the microscopic length scale $\lambda$ to the macroscopic length scale $L$ associated to a source of inhomogeneity in the plasma. In the Spitzer theory, only the first-order term in $\epsilon$

is kept which is known as the principle of *local action* (Woods, 1993). This restriction to distributions deviating weakly from the Maxwellian implies that the electron mean free path $\lambda_e$ (the microscopic length scale $\lambda$) should be much smaller than the different macroscopic scale lengths $L$ considered $1/\nabla \log T_e$, $1/\nabla \log p_e$ and $k_b T_e/eE$ (Ljepojevic and McNeice, 1989). Since $\epsilon$ is an increasing function of the electron velocity (the collision frequency of an electron is decreasing with increasing velocity $\nu \sim v^{-3}$), the Spitzer theory will always break down at high electron velocity. Nevertheless for weak electric fields and moderate temperature gradients this breakdown does not significantly compromise the ability of the Spitzer solution to describe the transport properties of the plasma as in the typical F-region plasma (Guio *et al.*, 1998). However, this is no longer the case when $\epsilon$ reaches values larger than $2 \cdot 10^{-2}$ (Gray and Kilkenny, 1980; Ljepojevic and McNeice, 1989). An accurate model of the high energy particles part is then needed to describe how electrons with sufficient energy move freely between regions with different temperatures and lead to strong distortion of the distribution function in the supra-thermal part (Gurevitch and Istomin, 1979; Luciani *et al.*, 1983; Ljepojevic and McNeice, 1989; Ljepojevic and Burgess, 1990; Ljepojevic, 1990; Mishin and Hagfors, 1994). This effect is often called the thermal runaway.

We shall briefly outline the derivation and assumptions behind the Spitzer solution. The approach used is based on the successive approximation method of Chapman-Enskog (Chapman and Cowling, 1970). This procedure is valid under the assumptions that the distribution function exhibits slow temporal variations compared to the collision time scale of the electrons and weak spatial gradients compared to the electron mean free path, and is subject to weak electromagnetic fields. The distribution function is expanded in powers of $\epsilon$ and is written

$$f(\boldsymbol{v}) = f_0(\boldsymbol{v}) + \epsilon f_1(\boldsymbol{v}) + \epsilon^2 f_2(\boldsymbol{v}) + \cdots, \tag{4.1}$$

where successive terms represent increasingly smaller corrections. The zeroth-order term $f_0$ is taken to be an isotropic Maxwellian of temperature $T_e$ and thermal velocity $v_e = (k_b T_e/m_e)^{1/2}$. The scheme adopted by Spitzer to calculate the first-order term $f_1$ assumes a cylindrically symmetry along the direction of the non-homogeneity and is written as a perturbation $X$ from the zeroth-order Maxwellian

$$f_1(v, \mu) = f_0(v) X(v) \mu. \tag{4.2}$$

The perturbation $X$ is a function of the electron velocity determined by substituting for the $f$ in the Boltzmann equation. In the Boltzmann equation only the *long range* electron-electron and electron-ion interactions have been taken into account by two linearised Fokker-Planck collision operators. Two second-order linear differential equations, one for the perturbation function $X_E$ due to an electric field, and the other one for the perturbation function $X_T$ due to the temperature

gradient are obtained. These equations are Eq. (40) of Spitzer and Härm (1953) and Eqs. (6)−(13) of Cohen *et al.* (1950) with the initial conditions $X_E(0) = 0$, $X_T(0) = 0$ and the two boundary conditions Eqs. (14)−(15) of Spitzer and Härm (1953) to ensure the conservation of momentum.

The Spitzer distribution function which takes into account both the effect of an electric field and a temperature gradient is then written

$$f(v,\mu) = f_0(v)\left[1 + Z\mu\left(\epsilon_E X_E\left(\frac{v}{v_e\sqrt{2}}\right) + \epsilon_T X_T\left(\frac{v}{v_e\sqrt{2}}\right)\right)\right], \quad (4.3)$$

where $f_0$ is the Maxwellian $f_0(v) = n_e/(2\pi)^{3/2}/v_e^3\exp(-(v/v_e)^2/2)$ and $\epsilon_E$ and $\epsilon_T$ are the Knudsen numbers associated to the electric field $E$ and the temperature gradient respectively

$$\epsilon_E = \lambda_e\left(\frac{eE}{k_b T_e} - \frac{\nabla p_e}{p_e}\right), \quad (4.4)$$

$$\epsilon_T = 2\lambda_e\frac{\nabla T_e}{T_e}. \quad (4.5)$$

$p_e = n_e T_e$ is the electron pressure and $Z$ is the charge number of the ion species.

We have recalculated the perturbations functions $X_E$ and $X_T$ (Guio, 1998) using the shooting method. The shooting method is a numerical method which consists in successive attempts to integrate the equation from the first boundary point $v = 0$ with the condition $X_{(E/T)}(0) = 0$ up to the other boundary $x_{\max} = v_{\max}/v_e$ using a fifth-order Runge-Kutta step ordinary differential equation (ODE) solver, until the boundary condition (the Eq. (14) for $X_E$ and the Eq. (15) for $X_T$ of Spitzer and Härm (1953)) is fulfilled at a satisfactory precision (Press *et al.*, 1992). The upper boundary with value $v_{\max}$ should not be too large compared to the thermal velocity $v_e$ since we are looking for a solution for low energy where the representation is valid.

We have calculated the perturbation functions $X_E$ and $X_T$ for different values of the upper boundary of integration $x_{\max}$. Figure 4.1 shows the functions $X_E$ and $X_T$ for these different values of the upper boundary condition. Note the diverging behaviour of the perturbation function for large values of the upper boundary condition which confirms that these perturbation functions are inappropriate to model the high energy electrons.

In the original theory, the factor $\lambda_e$ is the mean free path of a thermal electron due to electron-electron collisions and electron-ion collisions. In order to correct for the partially ionised ionospheric plasma, we correct the electron mean free path to include also an electron-neutral collision term (Banks, 1966). The electron mean free path is then replaced by

$$\frac{1}{\lambda_e} = \frac{1}{\lambda_{ee}} + \frac{1}{\lambda_{ei}} + \frac{1}{\lambda_{en}}, \quad (4.6)$$

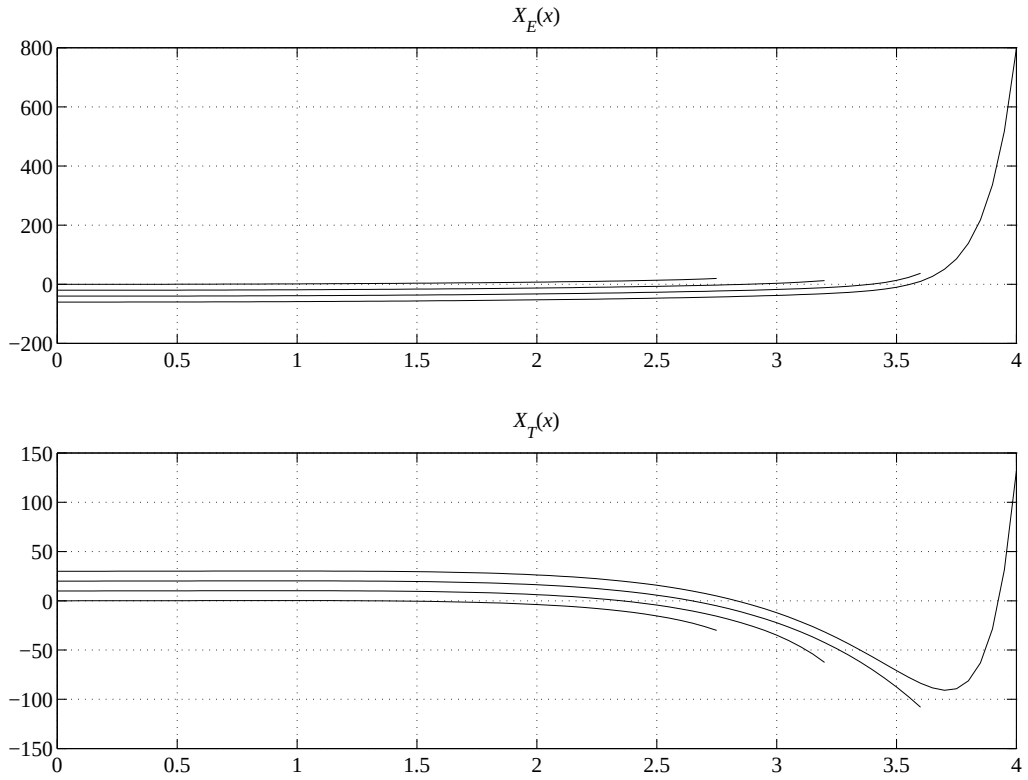


Figure 4.1: The $X_E$ and $X_T$ functions for different values of the upper boundary of integration $x_{\max} = v/v_e\sqrt{2}e = 2.8, 3.2, 3.6$ and $4.0$, and for an ion charge number $Z=1$. The $X_E$'s are shifted by $-20$ with each other, the $X_T$'s are shifted by $+10$ with each other, the reference curves (i.e. not shifted) are for $x_{\max} = 2.8$

where $\lambda_{en}$ is the mean free path of a thermal electron due to electron-neutral collisions. The effect of the electron-neutral collisions is to reduce the electron mean free path, and in the limit of low neutral particle densities we recover the electron mean free path value of a fully ionised plasma (Banks, 1966). It is important to note that the differential equations for the perturbation functions $X_E$ and $X_T$ have not been modified, thus the departure of the velocity distribution function from the Maxwellian is still caused by Coulomb interactions through the two Fokker-Planck collision operators for distant interactions.

## 4.3 The transport coefficients

The classical theory of transport is characterised by a set of closure relations expressing the dissipative fluxes, e.g. the current density $\boldsymbol{J}_e$ and the heat flux $\boldsymbol{q}_e$

as linear combinations of the thermodynamic forces, e.g. the electric field $\boldsymbol{E}$, the gradient of pressure $\boldsymbol{\nabla} p_e$ and the temperature gradient $\boldsymbol{\nabla} T_e$, with *constant* transport coefficients. These relations are called the transport equations (Balescu, 1988). Taking the first- and third-order moments of the electron velocity distribution, one obtains the electron current density $\boldsymbol{J}_e = -en_e\boldsymbol{u}_e$, where the mean velocity $\boldsymbol{u}_e$ is defined as in Eq. (5.27) and the electron heat flow $\boldsymbol{q}_e$ is also defined as in Eq. (5.33)

$$\boldsymbol{J}_e = \sigma_e \left( E + \frac{k_b}{en_e} \boldsymbol{\nabla} p_e \right) + \tau_e \boldsymbol{\nabla} T_e, \tag{4.7}$$

$$\boldsymbol{q}_e = -\mu_e \left( E + \frac{k_b}{en_e} \boldsymbol{\nabla} p_e \right) - \kappa_e \boldsymbol{\nabla} T_e, \tag{4.8}$$

where $\sigma_e$ is the electrical conductivity, $\tau_e$ is the current flow conductivity due to a temperature gradient at constant electron density, $\mu_e$ is the heat flow conductivity due to an electric field at constant electron temperature and $\kappa_e$ is the thermal conductivity.

These transport coefficients are defined in terms of the first- and third-order velocity moments of the perturbation functions $X_E$ and $X_T$. $\gamma_E$, $\delta_E$, $\gamma_T$ and $\delta_T$ are the normalised transport coefficients relative to a Lorentzian gas (Spitzer and Härm, 1953; Shkarofsky, 1961). A Lorentzian gas is a gas where electron-electron interactions are neglected, the protons are assumed to be at rest and the interactions electron-protons are described by a linearised Fokker-Planck collision operator. Eqs. (4.9)−(4.12) show the relations between these normalised coefficients, the velocity moments of the perturbation functions $I_3(X_E)$, $I_5(X_E)$, $I_3(X_T)$, $I_5(X_T)$ and the transport coefficients $\sigma_e$, $\tau_e$, $\mu_e$ and $\kappa_e$.

$$\gamma_E = \frac{1}{3} I_3(X_E) = \frac{\sqrt{\pi} m_e v_e}{4\sqrt{2} Z e^2 n_e \lambda_e} \sigma_e, \tag{4.9}$$

$$\delta_E = \frac{1}{12} I_5(X_E) = \frac{\sqrt{\pi} m_e v_e}{6\sqrt{2} Z e n_e k_b \lambda_e} \mu_e, \tag{4.10}$$

$$\gamma_T = -\frac{4}{9} I_3(X_T) = \frac{3\sqrt{\pi} v_e}{16\sqrt{2} Z e n_e \lambda_e} \tau_e, \tag{4.11}$$

$$\delta_T = -\frac{1}{15} I_5(X_T) = \frac{\sqrt{\pi} v_e}{40\sqrt{2} Z n_e k_b \lambda_e} \kappa_e, \tag{4.12}$$

where

$$I_n(X_{E/T}) = \int_0^{x_{\max}} y^{n-2} X_{E/T}(y) \exp(-y^2) y^2 dy \tag{4.13}$$

is the $(n-2)^{\text{th}}$-order moment of the distribution function $X_{E/T}(y)\exp(-y^2)$.

We have recalculated these transport coefficients using the perturbation functions of Figure 4.1. Table 4.1 gives the transport coefficients for different values of $x_{\max}$ and a comparison with the results given by Spitzer and Härm (1953). With the exception of the values for $x_{\max} = 2.8$ which deviate by about $10\%$, the other values of the transport coefficients are in good agreement (about $1\%$) with the values calculated by Spitzer ($x_{\max} = 3.2$). The deviation for $x_{\max} = 2.8$ might be the result of the low boundary of integration leading to an inaccurate description of the perturbation functions.

| $x_{\max}$ | 2.8 | 3.2 | Spitzer | 3.6 | 4.0 |
|---|---|---|---|---|---|
| $\gamma_E$ | 0.5740 | 0.5811 | 0.5816 | 0.5826 | 0.5832 |
| $\gamma_T$ | 0.2507 | 0.2677 | 0.2727 | 0.2715 | 0.2718 |
| $\delta_E$ | 0.4436 | 0.4622 | 0.4652 | 0.4672 | 0.4698 |
| $\delta_T$ | 0.1877 | 0.2149 | 0.2252 | 0.2228 | 0.2237 |

Table 4.1: The normalised transport coefficients as defined in Eqs. (4.9)–(4.12) calculated for different values of $x_{\max}$ and compared with the ones given by Spitzer ($x_{\max} = 3.2$)

In the ionosphere, a so-called polarisation electric field $\boldsymbol{E}_s$ builds up such that the thermal ions and electrons are constrained to drift as a single gas, which maintains bulk charge neutrality. $\boldsymbol{E}_s$ is determined by the current $\boldsymbol{J}_e$ and it exists whenever there is a gradient in the electron density or in the temperature (Ljepojevic and McNeice, 1989; Min *et al.*, 1993). It is given by

$$\boldsymbol{E}_s = \frac{\boldsymbol{J}_e}{\sigma_e} + \frac{\boldsymbol{\nabla} p_e}{e n_e} - \frac{\tau_e}{\sigma_e} \boldsymbol{\nabla} T_e. \tag{4.14}$$

If the field-aligned current is attributed to the flow of the supra-thermal electrons *only*, then the $\boldsymbol{J}_e/\sigma_e$ is equal to zero and we get the following relation between the electric field $\boldsymbol{E}_s$ and the gradient terms

$$\boldsymbol{E}_s = \frac{\boldsymbol{\nabla} p_e}{e n_e} - \frac{\tau_e}{\sigma_e} \boldsymbol{\nabla} T_e. \tag{4.15}$$

Using Eq. (4.4)–(4.12), it leads to the following relationship between the two Knudsen numbers $\epsilon_E$ and $\epsilon_T$

$$4\epsilon_E \gamma_E + 3\epsilon_T \gamma_T = 0. \tag{4.16}$$

In this case, the conductivity $\kappa_e$ is reduced by a factor $1 - 3\delta_E\gamma_T/(5\delta_T\gamma_E)$

$$\boldsymbol{q}_e = -\kappa_e (1 - \frac{3\delta_E \gamma_T}{5\delta_T \gamma_E}) \boldsymbol{\nabla} T_e, \tag{4.17}$$

and the mean drift velocity $u_E$ due to the electric field is exactly the opposite of the thermal drift velocity $u_T$ due to the gradient of temperature

$$u_E = -u_T = \frac{8}{\sqrt{2\pi}} v_e \gamma_E \epsilon_E. \tag{4.18}$$

In the case of a fully ionised gas and taking the Coulomb logarithm $\ln \Lambda$ to be equal to 15, the heat flow of Eq. (4.17) reduces to (Banks, 1966)

$$\boldsymbol{q}_e = -7.7 \times 10^5 T_e^{\frac{5}{2}} \boldsymbol{\nabla} T_e. \qquad [\mathrm{eV\,cm^{-2}\,s^{-1}}] \tag{4.19}$$

In addition to the classic transport coefficients, we have calculated the heat flow for parallel and perpendicular energy (Guio, 1998)

$$\boldsymbol{q}_e^{\parallel} = \frac{6}{5}\boldsymbol{q}_e, \qquad \boldsymbol{q}_e^{\perp} = \frac{2}{5}\boldsymbol{q}_e, \tag{4.20}$$

that we needed to estimate for the heat flow approximation of Eq. (1.34) in Chapter 1.

## 4.4 Comparison with the 2-$T$ Maxwellian

In Guio (1998), we have introduced a simple model for the particle velocity distribution in presence of a temperature gradient, the 2-$T$ Maxwellian.

For the electrons, the 2-$T$ Maxwellian, denoted $f_{T_{e\pm}}$, is defined as two half-Maxwellians with temperature $T_{e+}$ and $T_{e-}$ over the two half-spaces where respectively $v_{\parallel} < 0$ and $v_{\parallel} \geq 0$ and a Maxwellian with temperature $T_{e\perp}$ over the perpendicular velocity space $v_{\perp}$. The two half-Maxwellians along $v_{\parallel}$ are joined continuously at $v_{\parallel} = 0$ and are normalised such that the integral over the velocity space is equal to the electron density $n_e$. Thus the 2-$T$ Maxwellian can be seen as a modified bi-Maxwellian with a temperature inhomogeneity along the parallel velocity $v_{\parallel}$. The 2-$T$ Maxwellian is written

$$f_{T_{e\pm}}(v_{\parallel}, v_{\perp}) = \begin{cases} \dfrac{n_e}{(2\pi)^{\frac{3}{2}}} \dfrac{1}{v_{e\parallel} v_{e\perp}^2} \exp -\Big(\dfrac{v_{\parallel}^2}{2v_{e-}^2} + \dfrac{v_{\perp}^2}{2v_{e\perp}^2}\Big), & v_{\parallel} \geq 0 \\ \dfrac{n_e}{(2\pi)^{\frac{3}{2}}} \dfrac{1}{v_{e\parallel} v_{e\perp}^2} \exp -\Big(\dfrac{v_{\parallel}^2}{2v_{e+}^2} + \dfrac{v_{\perp}^2}{2v_{e\perp}^2}\Big), & v_{\parallel} < 0 \end{cases} \tag{4.21}$$

where $v_{e\perp}^2 = T_{e\perp}/m_e$ is the square of the thermal velocity of the electrons along the perpendicular direction, $v_{e\pm}^2 = T_{e\pm}/m_e$ are the squares of the mean velocities in the parallel direction and $v_{e\parallel} = (v_{e+} + v_{e-})/2$ is the normalisation constant such that the two half-Maxwellians are continuous at $v_{\parallel} = 0$.

This velocity distribution function is both inhomogeneous and anisotropic and sketches the electron velocity distribution at the particular point of space $r = 0$ between two regions with different temperature. This model mimics the presence of a temperature gradient where the hot plasma of temperature $T_{e+}$ is diffusing toward the region of cold plasma of temperature $T_{e-}$ and vice-versa (Guio, 1998).

As explained in Guio (1998), it is possible to find $T_{e+}$ and $T_{e-}$ so that the leading term of the heat flow equals the heat flow of the Spitzer theory. In particular, we want to find $T_{e+}$ and $T_{e-}$ so that the heat flow of the 2-$T$ Maxwellian equals the heat flow of Eq. (4.17), i.e. with the condition $J_e = 0$, or $u_e = 0$. In order to get $u_e = 0$ for the 2-$T$ Maxwellian, we modify $f_{T_{e\pm}}(v_\parallel, v_\perp)$ in $f_{T_{e\pm}}(v_\parallel - u_E, v_\perp)$ where $u_E$ is a mean drift velocity introduced in the 2-$T$ Maxwellian so that $u_e = 0$, i.e. (Guio, 1998)

$$u_E = -\langle \boldsymbol{v} \rangle_\parallel = \frac{2}{\sqrt{2\pi}} \frac{v_{e+}^2 - v_{e-}^2}{v_{e+} + v_{e-}}. \tag{4.22}$$

$u_E$ can be seen as the mean drift velocity due to an hypothetical electric field that guarantees the condition $u_e = 0$.

Figure 4.2 presents a comparison of the velocity moments given by the Spitzer theory and the simple model of the 2-$T$ Maxwellian for an altitude profile with typical ionospheric parameters.

The upper right panel shows the mean drift velocity $u_E$ to subtract in the 2-$T$ Maxwellian, so that the mean drift velocity $u_e = 0$. This mean drift velocity is of the same order as the mean drift velocity $u_E$ due to the polarisation electric field in the Spitzer theory. At the same time, the values of the two temperatures $T_{e+}$ and $T_{e-}$ are such that the temperature and the heat flow of the 2-$T$ Maxwellian are the same as the temperature of the Spitzer function and the heat flow of Eq. (4.17). In addition the two lowest panels presents the parameters that describes the non-homogeneity. In the left panel, the Knudsen numbers $\epsilon_T$ and $\epsilon_E$ of the Spitzer theory are presented. In the right panel, we have calculated the dimensionless inhomogeneity parameter $(T_{e+} - T_{e-})/T_e$ of the 2-$T$ Maxwellian. Note that the behaviour of this parameter is quite similar and of the same order as $\epsilon_T$.

This justify that the 2-$T$ Maxwellian is able to reproduce to a good approximation the behaviour of the Spitzer function.

It can also be noted how the approximated formula for the heat flow in a fully ionised plasma given by Eq. (4.19) (*dashed* line in the right and middle panel in Figure 4.2) overestimates the value for the heat flow (*solid* line).

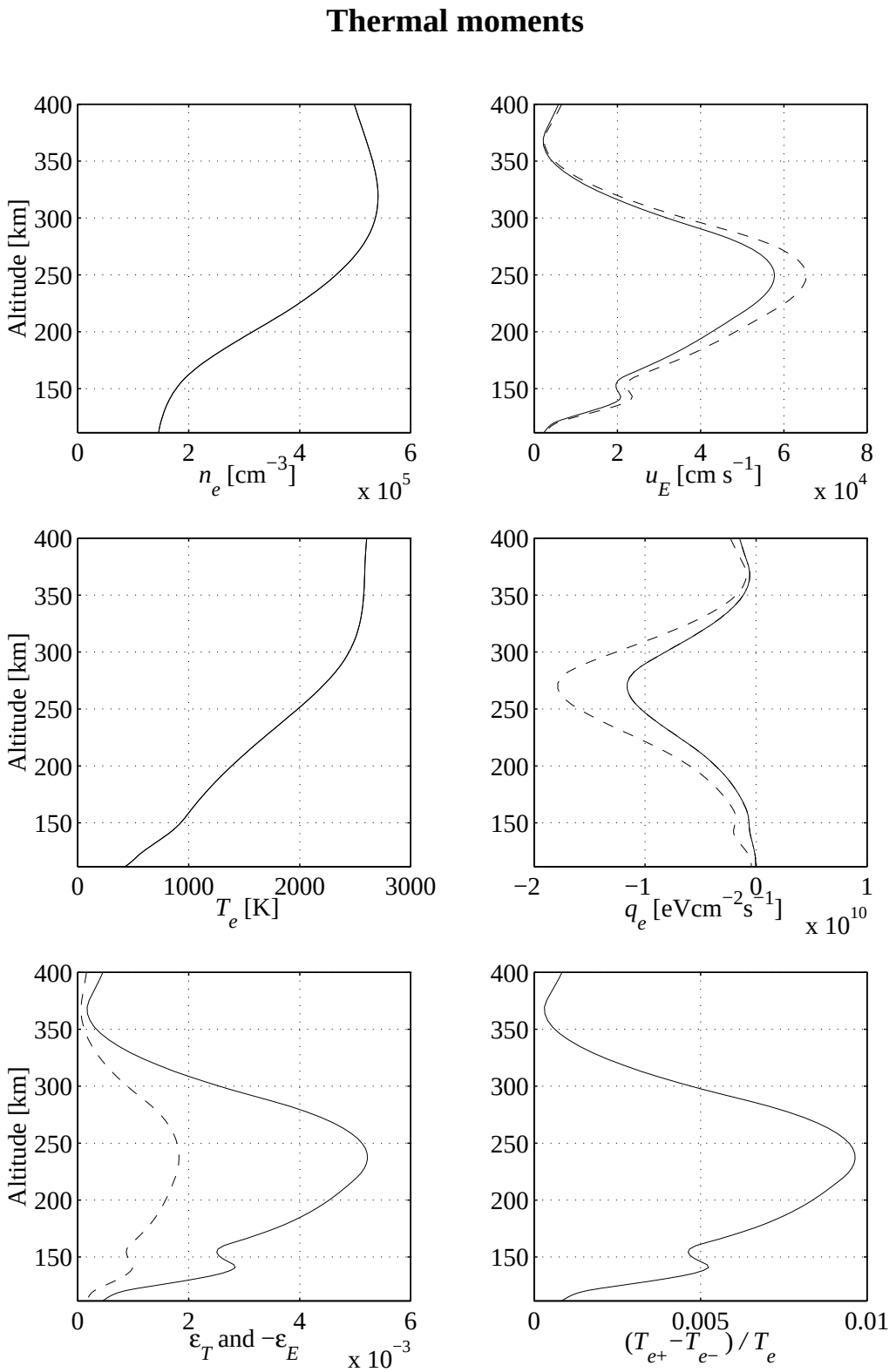


Figure 4.2: The moments for the Spitzer theory and the 2-$T$ Maxwellian from $110\,\mathrm{km}$ to $400\,\mathrm{km}$. In the upper right panel, the *dashed* line is $u_E$ of Eq. (4.18). The *solid* line is the velocity $u_E$ necessary in the 2-$T$ Maxwellian so that the mean velocity $u_e = 0$. In the middle right panel, the *dashed* line is $q_e$ of Eq. (4.19), the *solid* line is for Eq. (4.17) and is the same as the one of the 2-$T$ Maxwellian. In the lower right panel, the *dashed* line is for $\epsilon_E$ while *solid* line is for $\epsilon_T$

*"Um soli lyser på himlen blanke,*
*no ser ho deg! Det er all min tanke;*
*um dagen dovnar og skuming fell:*
*skal tru han tenkjer på meg i kveld?"*
Arne Garborg, Elsk, *Haugtussa*.

# Chapter 5

# Electron transport theory

## 5.1 Introduction

In the ionosphere, primary photoelectrons or precipitating electrons move along the magnetic field, produce heat and provoke processes such as excitation and ionisation. In a photoionisation process, the emitted electron is called the *primary electron*, and often has enough energy to produce several ionisations. The newly emitted electrons have lower energy than the primary and are called *secondary electrons*. In a collisional ionisation process, the incident electron is mostly scattered forward and is called the *primary electron*, while the extracted electron may be scattered in any direction and is called the *secondary electron*.

The approaches to model this relationship are based on electron transport theory which yields the electron flux as a function of altitude, energy and pitch-angle. Transport calculations can be carried out using Monte-Carlo simulations (Berger *et al.*, 1974) or by solving a transport equation numerically. A review of these different methods is found in Cicerone (1974).

Several numerical methods have been developed to solve numerically the transport equation (Banks and Nagy, 1970; Banks *et al.*, 1974; Strickland *et al.*, 1976). The transport code calculates the energy flux of the electrons by solving the vertical or field-aligned kinetic transport equation. This conservation equation simply expresses the fact that the variation of the steady-state electron flux with the scattering depth for a given altitude, energy and pitch-angle, is the difference between whatever leaves that energy, altitude or angle slab and whatever enters it. The variations in energy or angle due to collisions are described through differential cross sections. An additional energy loss arises from the heating of the ambient thermal electron gas due to hot-electrons to thermal-electrons interactions. This

loss process is assumed to be a continuous energy loss of the hot electrons to the thermal electrons, without any deflection during the process.

Recognising the formal equivalence of the electron transport equation to the radiative transfer equation (Chandrasekhar, 1960; Stamnes, 1977, 1980) adapted the discrete ordinate method developed for solving the radiative transfer equation to solve the electron transport equation. The transport code that we have been using implements this numerical method and is described in numerous papers in the literature (Stamnes and Rees, 1983; Stamnes, 1985; Lummerzheim, 1987).

## 5.2 Continuity equation — Transport equation

### 5.2.1 Continuity equation

The temporal and spatial evolution of a dilute system of particles interacting through *binary* collisions may be described by the Boltzmann equation, if we assume that the velocities of two particles prior to collision are uncorrelated. The electron continuity equation for the electron velocity distribution function $f(\boldsymbol{r}, \boldsymbol{v}, t)$ (in units $\mathrm{cm}^{-6}\,\mathrm{s}^3$) takes the following form (Stamnes and Rees, 1983)

$$\frac{\partial f}{\partial t} + \boldsymbol{\nabla}_{\boldsymbol{r}} \cdot (\boldsymbol{v} f) + \boldsymbol{\nabla}_{\boldsymbol{v}} \cdot \left( \frac{\boldsymbol{F}}{m_e} f \right) = \left( \frac{\delta f}{\delta t} \right)_{\mathrm{coll}} + \left( \frac{\delta f}{\delta t} \right)_{\mathrm{prod}} + \left( \frac{\delta f}{\delta t} \right)_{\mathrm{loss}}, \quad (5.1)$$

where $\boldsymbol{v}$ is the velocity, $\boldsymbol{r}$ the position, $t$ the time, $\boldsymbol{F}$ the external forces as well as a frictional force between the supra-thermal and the ambient electrons, and $m_e$ the electron mass. For *conservative* systems (i.e. such that $\boldsymbol{\nabla}_{\boldsymbol{v}} \cdot \boldsymbol{F} = 0$), Eq. (5.1) reduces to the Boltzmann equation.

The external forces $\boldsymbol{F}$ are electro-magnetic forces. In the *absence* of macroscopic electric fields and in homogeneous magnetic fields, this term reduces to the forces due to microscopic electro-magnetic fields that result from an inhomogeneous charged environment. It is then common to assume that the energy loss of supra-thermal electrons to ambient electrons is a frictional or continuous dissipative force acting on the streaming fast electrons.

The terms on the right hand side (in units $\mathrm{cm}^{-6}\,\mathrm{s}^2$) describe the change of the distribution function due to binary collisions through different kinds of processes such as Coulomb collisions, production by excitation (sometimes referred to as source) and loss by recombination (sometimes referred to as sink).

### 5.2.2 Velocity distribution function — Angular flux

In order to derive the transport equation one has to transform the velocity variable $\boldsymbol{v}$ to kinetic energy $E = \frac{1}{2} m_e v^2$ and unity direction vector $\boldsymbol{\Omega} = \boldsymbol{v}/v$

$$f(\boldsymbol{r}, \boldsymbol{v}, t) d^3\boldsymbol{v} = \frac{v}{m_e} f(\boldsymbol{r}, E, \boldsymbol{\Omega}, t) dE d^2\boldsymbol{\Omega}, \quad [\,\mathrm{cm}^{-3}] \tag{5.2}$$

Then the intensity (or flux) $I$ per unit area, unit time, unit energy and unit direction is defined by multiplying the velocity distribution $f$ by $v$

$$I(\boldsymbol{r}, E, \boldsymbol{\Omega}, t) dE d^2\boldsymbol{\Omega} = v f(\boldsymbol{r}, v, \boldsymbol{\Omega}, t) v^2 dv d^2\boldsymbol{\Omega}, \quad [\,\mathrm{cm}^{-2}\,\mathrm{s}^{-1}] \tag{5.3}$$

or if we express both the electron flux $I$ and the electron velocity distribution function $f$ with the same set of coordinates $\boldsymbol{r}$, $E$ and $\boldsymbol{\Omega}$

$$I(\boldsymbol{r}, E, \boldsymbol{\Omega}, t) = \frac{v^2}{m_e} f(\boldsymbol{r}, E, \boldsymbol{\Omega}, t), \quad [\,\mathrm{cm}^{-2}\,\mathrm{s}^{-1}\,\mathrm{eV}^{-1}\,\mathrm{sr}^{-1}]. \tag{5.4}$$

Figures 5.1 and 5.2 show the electron flux $I$ and the electron velocity distribution function $f$ calculated by the numerical code described hereafter at the altitude of $249\ \mathrm{km}$ over Tromsø in the summer at noon.

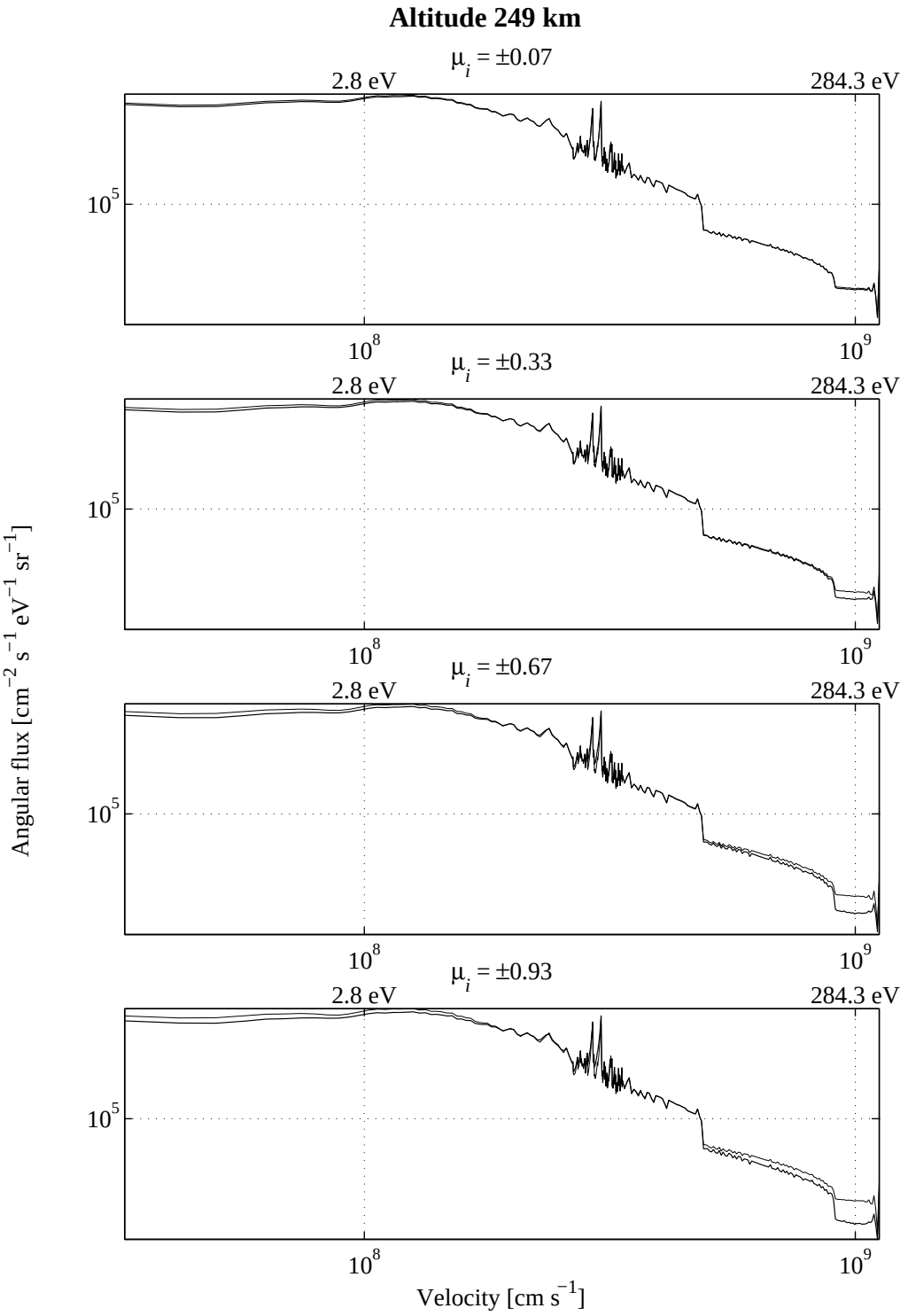


Figure 5.1: Example of the angular flux calculation for an 8-streams run over Tromsø in June 1996 at $12:00\,\mathrm{UT}$ with a $\mathrm{F10.7}$ index of $80$ and an $\mathrm{A_p}$ index of $15$. The *thin* line is for the downward direction and the *thick* line is for the upward direction

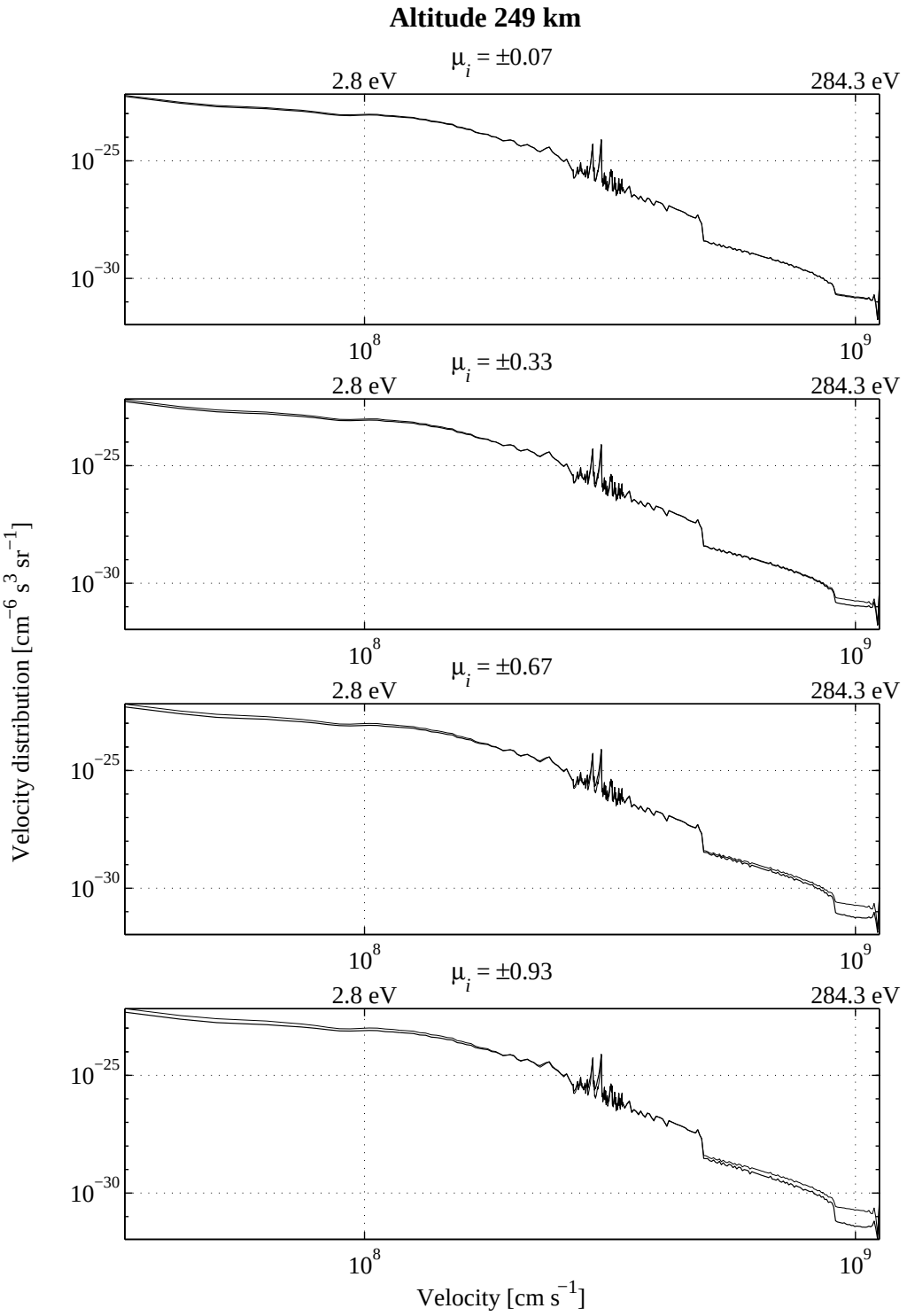


Figure 5.2: Example of the angular distribution function calculation for the same 8-streams run. The *thin* line is for the downward direction and the *thick* line is for the upward direction

### 5.2.3 Transport equation

In order to obtain a linear electron transport equation a number of approximations can be made to the non-linear continuity equation of Eq. (5.1). The time used by the supra-thermal electrons to penetrate the ionosphere is short compared to changes in the host medium. Thus steady state can be assumed allowing to neglect the explicit time dependence of the velocity distribution function, i.e. $\partial f/\partial t = 0$.

The gyro-frequency at ionospheric heights is much larger than the collision frequency, we can thus assume the motion of the particles to be their guiding centre. As a consequence the average motion is symmetric with respect to the azimuth and one-dimensional along the direction of the magnetic field (Lummerzheim, 1987). With this approximation, $I$ and $f$ are functions of the path $s$ along the magnetic field, the cosine $\mu$ of the pitch-angle $\theta$ to the magnetic field and the energy $E$. In that case, the second term $\boldsymbol{\nabla_r} \cdot (\boldsymbol{v} f)$ can be rewritten $(\partial f/\partial s)(ds/dt) + (\partial f/\partial \mu)(d\mu/dt)$ where $ds/dt = \mu v$ and $d\mu/dt = (\partial \mu/\partial s)(ds/dt)$. The term $\partial \mu/\partial s$ is calculated using the conservation of the first adiabatic invariant $(1 - \mu^2)/B = \text{constant}$ (i.e. the magnetic moment).

The third term $\boldsymbol{\nabla_v} \cdot (\boldsymbol{F} f/m_e)$ is transformed using the continuous slowing down approximation that assumes that the ambient electrons exert a "frictional" force on the fast electrons (Galand, 1996).

$$m_e \frac{d\boldsymbol{v}}{dt} = -n_e L(E) \frac{\boldsymbol{v}}{v} \tag{5.5}$$

where $n_e$ is the ambient electron density and $L(E)$ is the stopping cross section in the approximation of a continuous energy loss process.

Replacing the function distribution $f$ by the intensity $I$ in the electron continuity equation yields the transport equation

$$\mu \frac{\partial I}{\partial s} - \frac{1-\mu^2}{2B} \frac{\partial B}{\partial s} \frac{\partial I}{\partial \mu} - n_e \frac{\partial L(E) I}{\partial E} = \frac{1}{v} \left( \frac{\delta I}{\delta t} \right)_{\text{coll}} + \frac{1}{v} \left( \frac{\delta I}{\delta t} \right)_{\text{prod}} + \frac{1}{v} \left( \frac{\delta I}{\delta t} \right)_{\text{loss}} \tag{5.6}$$

The terms on the right hand side of the transport equation Eq. (5.6) represent the change of momentum in the electron intensity.

The charged particle collision processes term includes electron-electron collisions, electron-ion collisions as well as momentum transfer in electron-neutral collision.

The electron production processes term includes photo-electron production, production of slow, scattered and ejected electrons in ionising collisions of fast electrons, rotational excitation and vibrational excitation.

The electron loss processes term includes the fine-structure transitions in atomic oxygen, rotational de-excitation, vibrational de-excitation, electronic de-excitation and recombination.

The Coulomb collision term is dropped on the right hand side and is included through the third term on the left hand side which means that Coulomb collisions with the ambient electrons lead to energy loss but no deflections.

### 5.2.4 Cross sections

To describe the collision processes, the concept of cross section has to be introduced. When an electron passes through the thermosphere with velocity $\boldsymbol{v}$, the probability of a particular type of collision process $\alpha$ (i.e. ionisation, excitation of a particular state, etc.) to take place within the unit path length is given by

$$n_l \sigma_l(\alpha; \boldsymbol{v}) \tag{5.7}$$

where $n_l$ is the number density of the target particles of the type $l$ and $\sigma_l(\alpha; \boldsymbol{v})$ is the differential cross section of the process. The frequency at which an electron with velocity $\boldsymbol{v}$ induces the process $\alpha$ is thus given by

$$v n_l \sigma_l(\alpha; \boldsymbol{v}) \tag{5.8}$$

When a collision occurs, it generally consists in the loss of the particle from the point $(\boldsymbol{r}, \boldsymbol{v})$ and the production of the particle at another point $(\boldsymbol{r}, \boldsymbol{v}')$ of the phase space. The loss $J$ of particles from the phase space volume $d^3\boldsymbol{r}d^3\boldsymbol{v}$ is then $n_l \sigma_l(\alpha; \boldsymbol{v}) f(\boldsymbol{r}, \boldsymbol{v})$. Assuming, in addition, that the collision is independent of the direction of the incident particle —$\sigma_l(\alpha; v)$ is the effective cross section— the loss as a function of the intensity $I$ is

$$J(\boldsymbol{r}, E, \mu) = -n_l(\boldsymbol{r}) \sigma_l(\alpha; E) I(\boldsymbol{r}, E, \mu) \tag{5.9}$$

For the production, one uses the phase function $p(\boldsymbol{v} \to \boldsymbol{v}')$ which describes the probability of creating secondary particles with velocity $\boldsymbol{v}'$ from an incident particle of velocity $\boldsymbol{v}$. The number of secondary particles created is described by $c(\boldsymbol{r}, \boldsymbol{v})$, where $\int c(\boldsymbol{r}, \boldsymbol{v}) d^3\boldsymbol{v} = 1$ for an excitation or an elastic collision and 2 for ionisation. The production $Q$, as a function of the intensity $I$, is written

$$Q(\boldsymbol{r}, E, \mu) = \iint n_l(\boldsymbol{r}) \sigma_l(\alpha; E', \mu') p(E', \mu' \to E, \mu) c(\boldsymbol{r}, E, \mu) \times I(\boldsymbol{r}, E', \mu') dE' d\mu' \tag{5.10}$$

and the collision kernel $n_l(\boldsymbol{r}) \sigma_l(\alpha; E', \mu') p(E', \mu' \to E, \mu) c(\boldsymbol{r}, E, \mu)$ is simplified depending on the type of process involved.

Thus, the right hand side of the transport equation (5.6) can be calculated and takes the form

$$\mu \frac{\partial I}{\partial s} - \frac{1-\mu^2}{2B} \frac{\partial B}{\partial s} \frac{\partial I}{\partial \mu} - n_e \frac{\partial L(E) I}{\partial E} = - \sum_j n_j \sigma_j^{\mathrm{tot}} I + \sum_{j,\alpha} Q_{j,\alpha} + Q_{\mathrm{photo}} \tag{5.11}$$

where $\sigma_j^{\rm tot}$ is the total cross section for particle $j$, $Q_{j,\alpha}$ are the sources of collision process and $Q_{\rm photo}$ is the source of photoionisation.

To solve this equation, the cross sections, phase functions, loss functions, intensity flux of the solar radiation and neutral atmosphere need to be specified.

The path $s$ of a particle is a straight line through the ionosphere and the angle between the horizontal plane and this path is $\alpha$ (the altitude $z$ is given by $z = s\sin\alpha$). We introduce the scattering depth $\tau$ defined by

$$d\tau = -\sum_j \left( n_j(z)\sigma_j^{\rm tot}(E) + n_e(z)\frac{L(E)}{\Delta E} \right) dz \tag{5.12}$$

and the transport equation can be written

$$\begin{aligned} \frac{\mu}{\sin\alpha}\frac{\partial I(\tau,E,\mu)}{\partial\tau} &= I(\tau,E,\mu) \\ &- \frac{\omega(\tau,E)}{2}\int p(\mu'\to\mu)I(\tau,E,\mu')d\mu' + Q(\tau,E,\mu;I). \end{aligned} \tag{5.13}$$

The elastic scattering albedo $\omega$ is defined by

$$\omega(z,E) = \frac{\sum_j n_j(z)\sigma_j^{\rm el}(E)}{n_j(z)\sigma_j^{\rm tot}(E) + n_e(z)L(E)/\Delta E}. \tag{5.14}$$

The source term $Q_n = Q(\tau, E_n, \mu; I)$ at energy $E_n$ is given by

$$\begin{aligned} Q_n &= Q_{\rm photo}(\tau,E_n)\frac{dz}{d\tau} + \\ &\sum_{i=n+1}^{N} R_{\rm in} I(\tau,E_i)\Delta E_i + n_e(\tau)\frac{L(E_n)}{\Delta E_n} I(\tau,E_{n+1})\frac{dz}{d\tau}. \end{aligned} \tag{5.15}$$

where $R_{\rm in}$ is called the energy redistribution function.

### 5.2.5 Discrete ordinate method

The definitions of the scattering depth $\tau$ and the single scattering albedo $\omega$ make these quantities formally equivalent to their radiative counterparts. In the discrete ordinate approximation, the transport equation which is an integro-differential equation, is replaced by a system of $2n$ coupled differential equations. In these equations $I$ is sampled at $2n$ Gaussian quadrature points in $\mu$ and the phase function $p$ is expanded into Legendre polynomials. The source integral of the transport

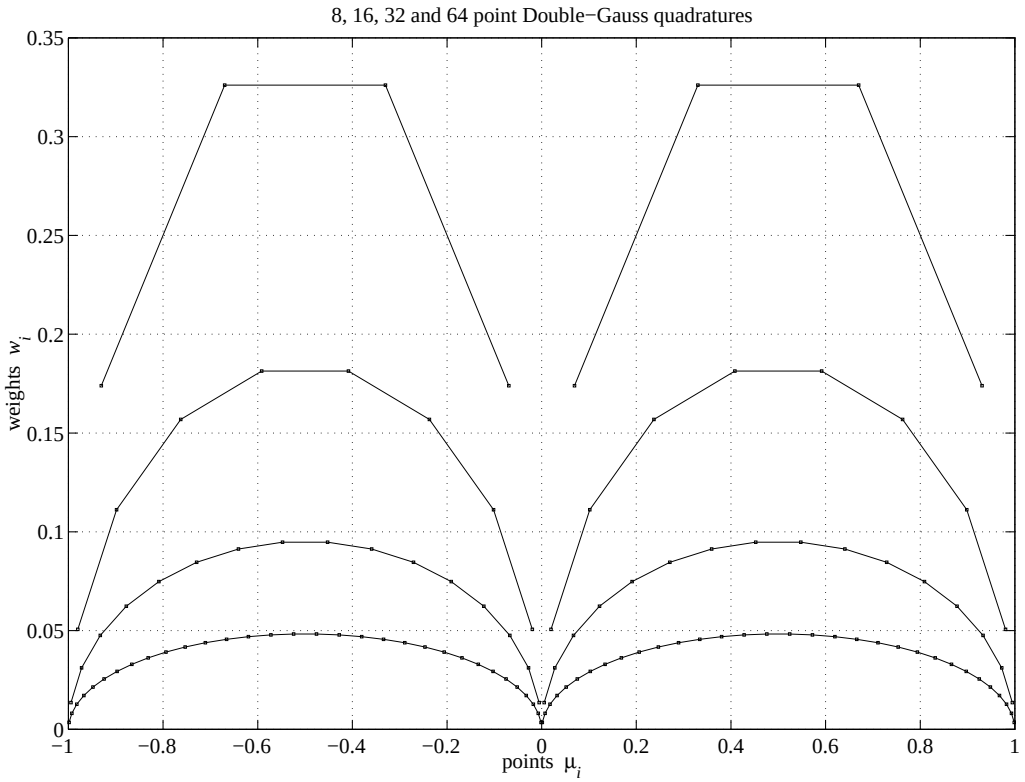


Figure 5.3: The weights $w_i$ as a function of the points $\mu_i$ of the 8, 16, 32 and 64-points double-Gauss quadratures

equation is replaced by a summation using the double-Gauss quadrature formula. The discrete ordinate approximation is written

$$\frac{\mu_i}{\sin\alpha}\frac{\partial I_i(\tau,E,\mu_i)}{\partial\tau} = I_i(\tau,E,\mu_i) - \frac{\omega(\tau,E)}{2}\sum_{\substack{j=-n\\ j\neq 0}}^{n} w_j p(\mu_j,\mu_i) I_j + Q(\tau,E,\mu_i;I_i), \quad i=\pm 1,\ldots,\pm n \tag{5.16}$$

where $\mu_i$ and $w_i$ are respectively the quadrature points and weights. The points and weights satisfy in the case of the Gauss quadrature $\mu_{-i} = -\mu_i$ and $w_{-j} = w_j$.

We use a double-Gauss quadrature rule where the Gaussian formula is applied separately to the half-ranges $-1 < \mu < 0$ and $0 < \mu < 1$. The main advantage of this double-Gauss scheme is that the quadrature points (in even orders) are distributed symmetrically around $|\mu| = .5$ and clustered both toward $|\mu| = 1$ and $\mu = 0$, whereas in the Gaussian scheme for the complete range, $-1 < \mu < 1$ they are clustered toward $\mu \pm 1$ (Stamnes *et al.*, 1988). The clustering toward $\mu = 0$ will

give superior results near the boundaries where the intensity varies rapidly around $\mu = 0$. A half-range scheme is also preferred since the intensity is discontinuous at the boundaries. Another advantage is that upward and downward quantities are obtained immediately without further approximations. Figure 5.3 shows the double-Gauss quadrature weights $w_i$ as a function of the points $\mu_i$ for a 32-points quadrature.

Assuming the vertical axis positive upward, then the pitch-angle in the range $[\pi/2, \pi]$ is downward and the pitch-angle in the range $[0, \pi/2]$ is upward, the downward and upward hemispherical net intensities or net fluxes are defined by

$$\Phi^{-}_{\text{net}}(z, E) = 2\pi \int_0^{-1} \mu I(z, E, \mu) d\mu, \tag{5.17}$$

$$\Phi^{+}_{\text{net}}(z, E) = 2\pi \int_0^{1} \mu I(z, E, \mu) d\mu. \tag{5.18}$$

In the discrete ordinate method, the two fluxes are estimated by means of the described double-Gauss quadrature

$$\Phi^{-}(z, E) \simeq -2\pi \sum_{i=-n}^{-1} w_i \mu_i I_i(z, E, \mu_i), \tag{5.19}$$

$$\Phi^{+}(z, E) \simeq 2\pi \sum_{i=1}^{n} w_i \mu_i I_i(z, E, \mu_i). \tag{5.20}$$

## 5.3 Electron velocity distribution moments

### Angular moments

The hemispherical net flux can be seen as the first-order angular moment of the intensity $I$ (Strickland *et al.,* 1976). Let us define the $n^{\text{th}}$-order angular moment $\Phi_n$ of the intensity $I$ by

$$\Phi_n(z, E) = 2\pi \int_{-1}^{1} \mu^n I(z, E, \mu) d\mu, \tag{5.21}$$

which can be approximated with the double-Gauss quadrature by

$$\Phi_n(z, E) \simeq 2\pi \sum_{\substack{j=-n \\ j\neq 0}}^{n} w_i \mu_j^n I(z, E, \mu_j). \tag{5.22}$$

In the next subsections, the altitude variable of the functions is not written explicitly but is implied. We have calculated the moments of the supra-thermal distribution using the definition of the moments given by Balescu (1988) and expressed the moments in terms of the angular moments defined in Eq. (5.22).

## Supra-thermal electron density

The electron density $n_s$ is the zeroth-order moment of the electron velocity distribution function.

$$n_s = \int f_s(\boldsymbol{v}) d^3\boldsymbol{v}, \qquad [\mathrm{cm}^{-3}] \tag{5.23}$$

Let us replace the electron velocity distribution $f_s$ with the intensity $I$ and identify the zeroth-order angular moment $\Phi_0$. $n_s$ is then expressed

$$n_s = \sqrt{\frac{m_e}{2}} \int \frac{\Phi_0(E)}{\sqrt{E}} dE, \tag{5.24}$$

or by integrating over $v$

$$n_s = m_e \int \Phi_0(v) dv, \tag{5.25}$$

or if we define the dimensionless variable $x = v/v_e$, where $v_e$ is the thermal velocity of the electrons

$$n_s = m_e v_e \int \Phi_0(x) dx. \tag{5.26}$$

## Supra-thermal electron average velocity

The electron average velocity $\boldsymbol{u}_s$ is related to the first-order moment of the electron velocity distribution function through

$$n_s \boldsymbol{u}_s = \int \boldsymbol{v} f_s(\boldsymbol{v}) d^3\boldsymbol{v}, \qquad [\mathrm{cm}^{-2}\,\mathrm{s}^{-1}] \tag{5.27}$$

The mean velocity $\boldsymbol{u}_s$ is related to the flux $\boldsymbol{\Gamma}_s$ (in units $\mathrm{cm}^{-2}\,\mathrm{s}^{-1}$) through the relation $\boldsymbol{\Gamma}_s = n_s \boldsymbol{u}_s$.

Let us replace the electron velocity distribution $f_s$ with the intensity $I$. Due to the azimuthal symmetry $\boldsymbol{u}_s$ is a vector along the magnetic field with magnitude $u_s$. The magnitude $u_s$ can be expressed as a function of the first-order angular moment $\Phi_1$

$$u_s = \int \Phi_1(E) dE = m_e \int v \Phi_1(v) dv = m_e v_e^2 \int x \Phi_1(x) dx. \tag{5.28}$$

## Supra-thermal electron temperature

The electron temperature $T_s$ (in units $\mathrm{K}$) is related to the second-order centred moment of the electron velocity distribution function through

$$\frac{3}{2}n_s k_b T_s = \frac{1}{2}m_e \int |\boldsymbol{v} - \boldsymbol{u}_s|^2 f_s(\boldsymbol{v}) d^3\boldsymbol{v}, \qquad [\mathrm{eV\,cm^{-3}}] \tag{5.29}$$

Let us replace the electron velocity distribution $f_s$ with the intensity $I$. The temperature $T_s$ is expressed as a function of the zeroth-order angular moment $\Phi_0$

$$\frac{3}{2}n_s k_b T_s = \frac{\sqrt{2m_e}}{2} \int \sqrt{E}\Phi_0(E) dE - \frac{1}{2}n_s m_e u_s^2 \tag{5.30}$$

$$= \frac{m_e^2}{2} \int v^2 \Phi_0(v) dv - \frac{1}{2}n_s m_e u_s^2 \tag{5.31}$$

$$= \frac{m_e^2}{2} v_e^3 \int x^2 \Phi_0(x) dx - \frac{1}{2}n_s m_e u_s^2. \tag{5.32}$$

## Supra-thermal electron heat flux

The electron heat flux $\boldsymbol{q}_s$ is related to the third-order centred moment of the electron velocity distribution function through

$$\boldsymbol{q}_s = \frac{1}{2}m_e \int |\boldsymbol{v} - \boldsymbol{u}_s|^2 (\boldsymbol{v} - \boldsymbol{u}_s) f_s(\boldsymbol{v}) d^3\boldsymbol{v}, \qquad [\mathrm{eV\,cm^{-2}\,s^{-1}}] \tag{5.33}$$

Let us replace the electron velocity distribution $f_s$ with the intensity $I$. Due to the azimuthal symmetry $\boldsymbol{q}_s$ is a vector along the magnetic field with magnitude $q_s$. $q_s$ can be expressed as a function of the first- and second-order angular moments $\Phi_1$ and $\Phi_2$

$$q_s = \int E\Phi_1(E) dE - \sqrt{2m_e}u_s \int \sqrt{E}\Phi_2(E) dE + \frac{1}{2}n_s m_e u_s^3 \tag{5.34}$$

$$= \frac{1}{2}m_e^2 \int v^3 \Phi_1(v) dv - m_e^2 u_s \int v^2 \Phi_2(v) dv + \frac{1}{2}n_s m_e u_s^3 \tag{5.35}$$

$$= \frac{1}{2}m_e^2 v_e^4 \int x^3 \Phi_1(x) dx - m_e^2 u_s v_e^4 \int x^2 \Phi_2(x) dx + \frac{1}{2}n_s m_e u_s^3. \tag{5.36}$$

Figure 5.4 presents the moments from the electron supra-thermal distribution function before truncation and after the truncation with the strategy described in Section 1.5 and using the expressions for the moments that we have calculated below.

The difference between the moments calculated before truncation and after truncation is rather important, especially we note that heat flow changes of sign

after $350\,\mathrm{km}$. Therefore, special care has to be taken when truncating the suprathermal distribution function. The truncation has to be done at the correct energy in order to approximate correctly the $P^*$ and $Z^*$ functions.

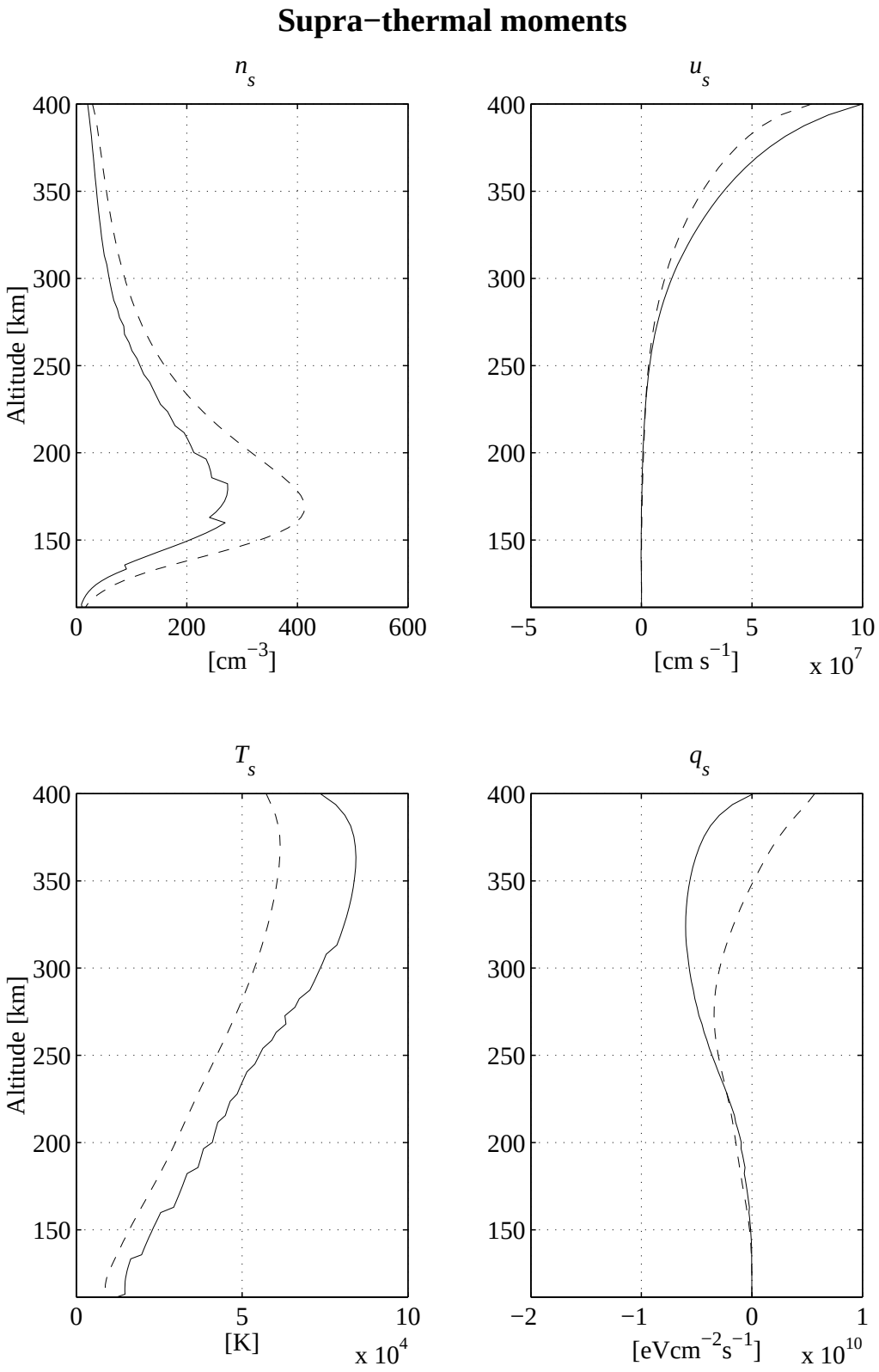


Figure 5.4: Calculation of the supra-thermal moments for the distribution function of the electrons calculated by the numerical transport code and the truncated one with the strategy described in Section 1.5 from $110\,\mathrm{km}$ to $400\,\mathrm{km}$ and for the 8-streams run of Figure 5.2

# Conclusion

While the study of the intensity of the electron plasma line has given valuable results on the enhancement mechanisms of the line for sometime, work on the exact localisation of the plasma line in the incoherent scatter spectrum has progressed rather slowly, in part because of coarse time or frequency resolution problems as well as coarse spatial resolution.

This work has been motivated by the first measurement at EISCAT of the plasma line in a continued manner. We have concentrated on two part:

- ☞ The design of a new plasma line experiment for the EISCAT radar making use of the alternating code technique to improve the spatial resolution.
- ☞ The development of an improved model for the intensity and the Doppler frequency shift of the plasma lines in the direction parallel to the magnetic field.

The benefit of the alternating code technique is to improve drastically the spatial resolution of the measurement. Our experiment has been run successfully with an altitude resolution of $3\,\mathrm{km}$ as opposed to $40-50\,\mathrm{km}$ obtained with the conventional technique of the long pulse. It has allowed, for the first time at EISCAT, the simultaneous measurement of the plasma line at several altitudes, providing the plasma line parameters, i.e. the intensity and Doppler frequency shift, for an altitude profile with a temporal resolution of $10\,\mathrm{s}$.

In order to refine the model of the intensity and Doppler frequency shift of the plasma line, we have developed a numerical code that calculates the dielectric function of the medium and the reduced one-dimensional velocity distribution along the magnetic field for any two-dimensional velocity distribution function. Because it is very difficult to construct a self-consistent model of the velocity distribution function encompassing all of the relevant energy range, we have made an *ad hoc* model by separating the distribution into two parts: the thermal and the supra-thermal population. The thermal population is represented by the Spitzer function that takes into account the effect of an electric field and/or a temperature gradient. The supra-thermal population is derived from the angular energy flux of the supra-thermal electrons calculated by a numerical electron transport model.

This project has contributed to a better understanding of plasma line interpretation in two ways:

- ☞ It is seen that the Doppler frequency of the plasma line is strongly dependent on the frequency of operation of the radar. When using low frequency radars, i.e. VHF radars, the position of the line is clearly influenced by the supra-thermal population while for high frequency radars, i.e. UHF radars, the deviation of the Doppler frequency from the theoretical frequency associated to a Maxwellian gas is due to a departure of the distribution function in the thermal part, particularly the anisotropy that develops in the presence of a gradient of the electron temperature modifies substantially the dispersion relation.

- ☞ The effect of photo-ionisation of $\mathrm{N}_2$ and $\mathrm{O}$ by the solar emission of $\mathrm{HeII}$ has been identified when we analysed a plasma line data set that we have collected on the EISCAT VHF radar. The effect observed is a damping of the intensity and a modification of the Doppler frequency of the plasma lines around the phase energies of $24.25\,\mathrm{eV}$ and $26.25\,\mathrm{eV}$.

However, it is important to point out the limits of our present model:

- ☞ Our calculations of the intensity and the Doppler frequency shift are limited to radar observations along the magnetic field.

- ☞ The Spitzer theory of a fully ionised plasma in the presence of a temperature gradient has been adapted to a partially ionised plasma in a non-consistent way. The effect of the collisions between the electrons and the neutral particles has been taken into account in the electron mean free path while the collision operator has not been modified.

- ☞ The model of collisions used in the differential cross section to estimate the incoherent scatter spectra is not the same as the one that describes the electron velocity distribution function.

Therefore, further works could be done. It would be interesting, for example, to generalise the calculations of the $P^*$ and $Z^*$ functions in directions different than parallel to the magnetic field. The evoked lack of consistency between the models could be investigated. The problem of the connection of the thermal and the supra-thermal component of the velocity distribution function is also of interest. Finally, more plasma line data with radars of different frequencies should be analysed to verify further the fine structures of the supra-thermal distribution as well as verify the effect on the Doppler frequency and therefore improve the kinetic model of the thermal and supra-thermal electrons.

# Conclusion (français)

Alors que l'étude de l'intensité de la raie de plasma a apporté des résultats intéressants sur les mécanismes de l'augmentation de la raie depuis un certain temps, le travail sur sa fréquence dans le spectre à diffusion incohérente a progressé plutôt lentement, à cause de la pauvre résolution en fréquence et d'autres problèmes expérimentaux.

Ce travail a été motivé par la première mesure à EISCAT de la raie de plasma de manière continue. Nous nous sommes concentrés sur deux points :

- ☞ La conception d'une nouvelle expérience de raie de plasma pour le radar EISCAT utilisant la technique du code alternatif dans le but d'améliorer la résolution spatiale.

- ☞ Le développement d'une théorie améliorée de l'intensité et du Doppler en fréquence de la raie de plasma pour une visée le long du champ magnétique.

Le bénéfice de la technique du code alternatif est d'améliorer de manière substantielle la résolution spatiale des mesures. Notre expérience a été tournée avec succès avec une résolution en altitude de $3\,\mathrm{km}$, à comparer à la résolution de $40-50\,\mathrm{km}$ obtenue avec la technique classique de l'impulsion longue. Cela a permis, pour la première fois à EISCAT, de mesurer simultanément la raie de plasma à plusieurs altitudes, procurant ainsi les paramètres de la raie de plasma, c'est à dire l'intensité et le Doppler en fréquence, pour un profile en altitude avec une résolution temporelle de $10\,\mathrm{s}$.

Pour raffiner le modèle de l'intensité et du Doppler en fréquence de la raie de plasma, nous avons développé un code numérique qui calcule la fonction diélectrique du plasma ainsi que la distribution réduite le long du champ magnétique pour n'importe quelle distribution des vitesses à deux dimensions. Parce qu'il très difficile de construire un modèle unique de la distribution des vitesses satisfaisant toute les gammes d'énergie, nous avons construit un modèle *ad hoc* en scindant la distribution des vitesses en deux parties: la population thermique et la suprathermique. La population thermique est représentée par la fonction de Spitzer qui tient compte de l'effet d'un champ électrique et/ou d'un gradient de tempéra-

ture. La population supra-thermique est déduite du flux angulaire d'énergie calculé grâce à un modèle numérique du transport des électrons.

Ce projet a contribué à une meilleure compréhension de l'interprétation de la raie de plasma de deux façons :

- ☞ Il est montré que le Doppler en fréquence de la raie de plasma est fortement dépendante de la fréquence de fonctionnement du radar. Avec un radar basse fréquence de type VHF, la position de la raie de plasma est clairement influencée par la population supra-thermique des électrons alors que pour un radar haute fréquence de type UHF, la déviation du Doppler associé à une classique Maxwellienne est due à la partie thermique de la distribution des vitesses des électrons, en particulier l'anisotropie due à la présence d'un gradient de température électronique modifie la relation de dispersion de l'onde Langmuir.

- ☞ L'effet de la photo-ionisation de $\mathrm{N}_2$ et $\mathrm{O}$ par l'émission solaire provenant de $\mathrm{HeII}$ a été identifié quand nous avons analysé des données raie de plasma que nous avons mesuré avec le radar VHF d'EISCAT. L'effet observé est un amortissement de l'intensité ainsi qu'une modification du Doppler en fréquence au voisinage de $24.25\,\mathrm{eV}$ et $26.25\,\mathrm{eV}$ correspondant à l'énergie de phase de l'onde Langmuir.

Cependant, il est important de noter les limites de notre modèle actuel :

- ☞ Nos calculs de l'intensité et du Doppler en fréquence sont limités à la direction parallèle au champ magnétique.

- ☞ La théorie de Spitzer d'un plasma complètement ionisé en présence d'un gradient de température a été adaptée pour un plasma partiellement ionisé de manière non consistante. En effet, les collisions des electrons avec les particules neutres a été pris en compte dans le libre parcours moyen des électrons alors que l'opérateur de collision n'a pas été modifié.

- ☞ Le modèle des collisions utilisé dans la section efficace différentielle pour estimer le spectre à diffusion incohérente n'est pas le même que celui utilisé pour décrire la distribution des vitesses des électrons.

Par conséquent, de plus amples travaux sont envisageables. Il serait intéressant, par exemple, de généraliser le calcul des fonctions $P^*$ et $Z^*$ dans les directions autres que parallèle au champ magnétique. Le manque de consistance évoqué entre les modèles de collisions utilisés pourrait aussi être approfondi. Le problème du raccord entre les composantes thermique et supra-thermique de la distribution des vitesses des électrons est aussi d'un intérêt certain. Enfin, l'acquisition

de plus amples données pour différentes fréquences de fonctionnement devrait être analysée pour vérifier les structures détaillées de la fonction de distribution des vitesses des supra-thermiques et ainsi améliorer le modèle cinétique des supra-thermiques, de même que vérifier l'effet prédit de la correction sur le Doppler en fréquence de la raie de plasma.

# ARTICLE I

Ann. Geophysicae 14, 1473–1479 (1996) 

Annales Geophysicae

# Alternating-code experiment for plasma-line studies

**P. Guio**[1], **N. Bjørnå**[1], **W. Kofman**[2]

[1] The Auroral Observatory, University of Tromsø, Tromsø, N-9037 Norway
[2] CEPHAG Domaine Universitaire, BP 46, St-Martin-D'hères, F-38402 France

Received: 15 January 1996/Revised: 30 April 1996/Accepted: 2 May 1996

**Abstract.** We present results of the first plasma-line measurement of the incoherent spectrum using the alternating-code technique with the EISCAT VHF radar. This technique, which has earlier mostly been used to measure high-resolution E-region ion-line spectra, turned out to be a very good alternative to other techniques for plasma-line measurements. The experiment provides simultaneous measurement of the ion line and downshifted and upshifted plasma-line spectra with an altitude resolution of 3 km and a temporal resolution of 10 s. The measurements are taken around the peak of the F region, but not necessarily at the peak itself, as is the case with the long-pulse technique. The condition for success is that the scale height should be large enough such that the backscattered signal from the range extent of one gate falls inside the receiver filter. The data are analyzed and the results are combined with the results of the ion-line data analysis to estimate electron mean drift velocity and thereafter electric currents along the line of sight of the radar using both the standard dispersion relation assuming a Maxwellian electron velocity distribution and the more recent model including a heat-flow correction term.

## 1 Introduction

The incoherent scattering spectrum consists of two main components. The ion line, which contains most of the scattered power, is extensively being measured at the different facilities around the world, and standard parameters such as electron density, electron and ion temperature, ion mean drift velocity, and others are diagnosed. On the other hand, plasma lines are weak and broadband. The intrinsic spectral width of the plasma line is determined by the damping of the Langmuir wave causing the scattering (Landau damping or collisional damping). The damping depends on the density, temperature and collision frequency of the ambient electrons and on the presence of a suprathermal population (photoelectrons or secondary electrons produced in particle precipitation events) around the phase velocity of the wave (Perkins and Salpeter, 1965). It also depends on the angle between the scattering direction and the geomagnetic field. For small angles, as in this experiment, the effect is negligible. In the F region at daytime, where damping is mostly dominated by electron-ion collisions, and for field-aligned conditions, the width is a few kHz. Temporal fluctuations during the integration time artificially broaden the width. Under relatively stable conditions of the ionosphere, this broadening is a few kHz per 10 s, which is a typical integration time. The spatial variation depends on the electron-density scale height which is of the order of $1\,\mathrm{kHz\,km^{-1}}$ at regions with large scale height and around the peaks in the E and F regions up to $10\,\mathrm{kHz\,km^{-1}}$. The scattered power is usually less than 10% of the ion-line power, even in the presence of suprathermal particles. This leads to some conditions on the measurement of the autocorrelation function. The correlation time is inversely proportional to the bandwidth of the plasma line and is not larger than 500 μs. The lag increment $\tau$ determines the bandwidth of the measured spectra and should be around 10–20 μs for a spectral window of 50–100 kHz.

To perform the measurement of the autocorrelation function several techniques are available and can be classified into three categories. The long-pulse technique (Showen, 1979; Kofman and Wickwar, 1980) provides data at the cut frequency of the E or F region. It has the advantage of a good signal-to-noise ratio, which increases with increasing density scale height. On the other hand, this technique provides only one measurement point. The chirp technique (Hagfors, 1982; Birkmayer and Hagfors, 1986) is very similar to the long-pulse technique. The signal is chirped in order to tune it to the local density gradient, creating artificially the measurement conditions of a peak density in a region. In these techniques, no attempt is made to obtain good range resolution.

*Correspondence to:* P. Guio

The multipulse technique (Farley, 1972), by using ad hoc spatial patterns of short pulses, provides good range resolution and good lag resolution. Unfortunately, the multiple-frequency technique commonly used to improve the accuracy of the measurement of the ion line is not adequate for plasma-line measurements due to the $k$ dependence of the position of the plasma line which would broaden the spectra. In low signal-to-noise ratio measurements, like plasma-line measurements, one definitely needs to concentrate all of the energy on the same frequency. Also the accuracy of position estimation will be reduced unless special analysis techniques are used to account for it (using a 4-frequency multipulse would yield a broadening of $\sim$150 Hz with the EISCAT VHF radar and $\sim$1 kHz with the UHF radar).

The solution is to use phase patterns of short pulses instead of spatial patterns. One of these techniques is the alternating code (Lehtinen and Häggström, 1987). It provides good range and lag resolution and has been proven to give near optimum accuracy in the case of poor signal-to-noise ratio. The principle is to transmit a set of phase-coded pulses and decode them in such a way that only part of the pulse (one baud) is contributing to the scattering. An important assumption for the code to work properly is that the plasma correlation function must remain stationary in the time needed for the whole set of scans to be transmitted. A similar technique, the coded long pulse (Sulzer, 1989), has been used recently at the Arecibo Observatory facility (Djuth *et al.*, 1994). The results are promising, but the implementation of the technique for such very long codes (512 bits) requires dedicated hardware processing.

## 2 Experimental setup

We used the VHF EISCAT radar near Tromsø, Norway at daytime in June 1994. The radar cannot be steered south to be in a field-aligned position, thus the antenna was pointed vertically, which gives an angle of about 12° to the magnetic field line at 250 km. The experiment used a 32-bit strong condition alternating code of baud length 20 μs (actually the first alternating code run on the VHF system). Three receiving channels, one for upshifted, one for downshifted plasma lines, and one for the ion line, were used simultaneously with the same spatial characteristics, thus providing the two components of the incoherent scatter spectrum. Forty gates were formed from an altitude (or range) of 180 km up to 300 km with an altitude resolution of 3 km. The gate separation was also 3 km. The autocorrelation function was measured from a delay of 20–620 μs in steps of 20 μs. This means a spectrum of 50-kHz bandwidth and about 780-Hz resolution. To get the zero-lag of the autocorrelation function, a 1-baud-length pulse was also used with the same geometric characteristics. Each interpulse period was $\sim$13 ms and for a 32-bit alternating code one has to send 64 different coded long pulses, consequently the whole cycle was $\sim$0.8 s. This is the time we have to assume that the ionosphere remains stationary. The data were dumped every 10 μs. This setup is a good compromise for a high-enough height resolution, a large enough bandwidth of the receiver, and the physical limitation of the size of the memory of the acquisition system. For example, if we assume a Chapman layer in the neighborhood of the peak of the F region, with a characteristic scale height of 65 km, and if the receiver system is tuned at the peak or shifted inside the peak, we can expect to get at least six gates with signal falling within the bandwidth of the filter (Fig. 1).

## 3 Data analysis

### 3.1 Ion-line data

The ion-line data were analyzed in 10-s intervals, providing the four standard ionospheric parameters, i.e., electron density, electron and ion temperature, as well as ion mean drift velocity along the line of sight. Figure 2 shows the results of the analysis. One can see that the ionosphere had a very quiet and steady behavior, as well as a rather steep electron temperature gradient.

### 3.2 Power-profile data

The plasma-line power profiles were analyzed solving Eq. 1 below (Yngvesson and Perkins, 1968), a similar

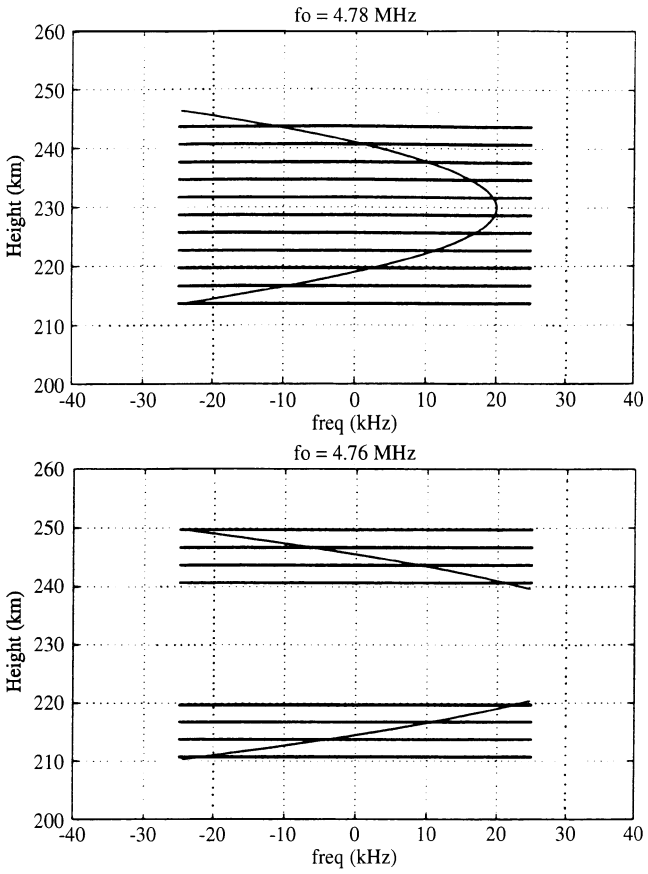


**Fig. 1.** Parabolic height distribution of the plasma-line frequency with scale height of 65 km showing two different tunings of the 50-kHz receiving filter and the corresponding height cells contributing to the scattering

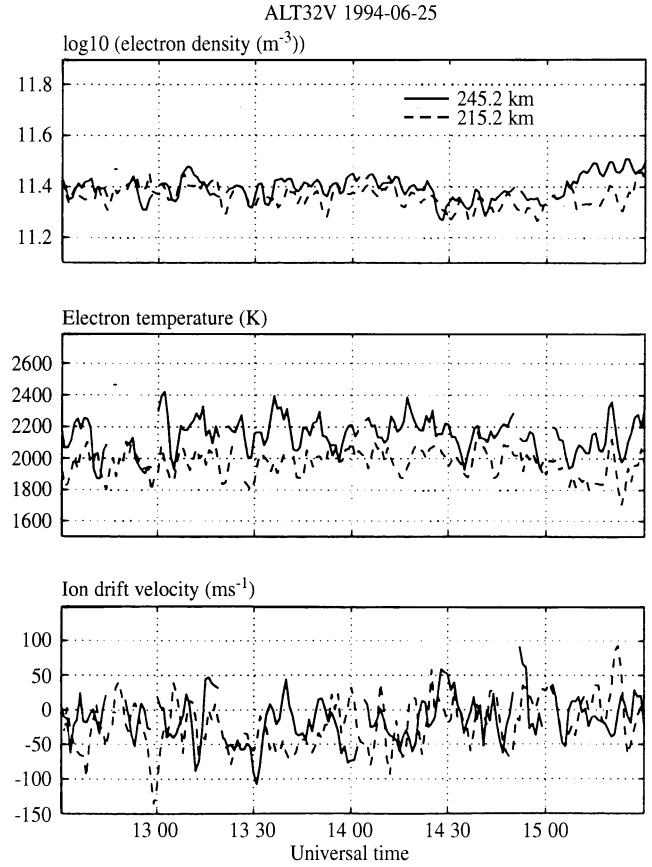


**Fig. 2.** Ionospheric parameters as function of range and time from the analysis of the ion line. The data have been smoothed with a 9 km × 30 s window

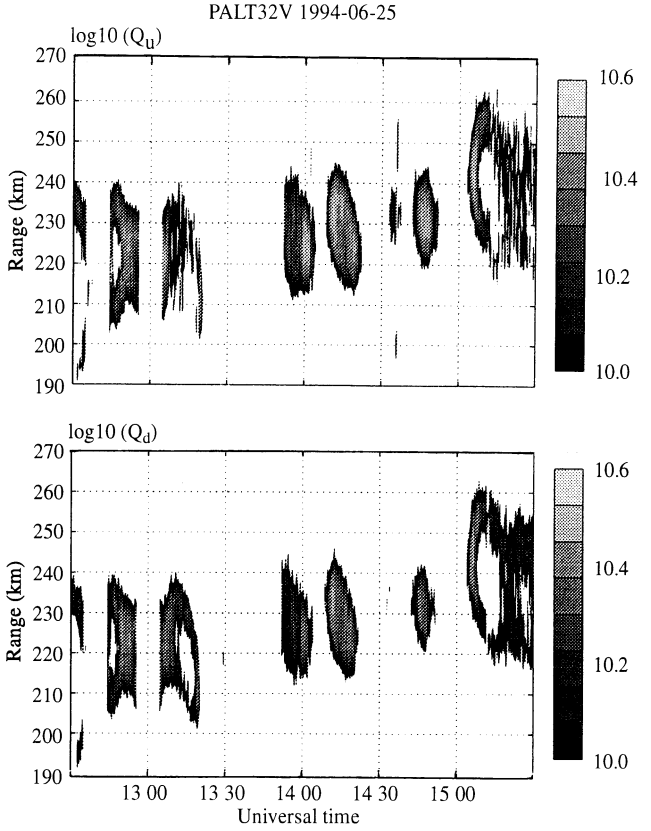


**Fig. 3.** The two parameters $Q_u$ and $Q_d$ of Eq. 1 as function of range and time from the analysis of the upshifted and downshifted plasma-line power profiles

radar equation as the one used for the ion line, yielding parameters $Q_u$ and $Q_d$ for the upshifted and downshifted lines (Fig. 3).

$$Q = \frac{P_R}{P_T}\frac{R^2}{\delta R}\left(C_s\frac{A(f)}{A(0)}\right)^{-1}. \quad (1)$$

Here, $P_T$ and $P_R$ denote transmitted and received power, $R$ is the distance to the probed volume, $\delta R$ is the volume extent (which is the minimum of the length of the transmitted pulse and the range with signal falling inside the receiver filter) and $C_s$ is the system constant. $A(f)$ is the frequency-dependent effective antenna area at frequency $f$ offset from the transmitted frequency. $A(f)/A(0)$ is the gain relative to the measurement of the ion line. It has been estimated for the VHF EISCAT system by measurement of the radio star Cassiopeia A.

The analysis shows a very similar enhancement of the upshifted and downshifted line, indicating the presence of isotropic photoelectrons. Situations where the receiving filter was tuned to a frequency not matching the frequency of the peak can be seen at different times on both lines, for example around 1245 and 1315 UT. Note also that the asymmetry after 1515 UT is artificial, and is produced by an increase in the receiver-filter bandwidth, thus increasing the noise level with aliased noise contributions.

### *3.3 Autocorrelation-function data*

The autocorrelation functions were analyzed using a least-square fit method. We have tried two different spectral models, a squared-triangle shape and a Gaussian, both yielding three parameters: the received frequency $f_r$, the bandwidth of the line $\delta_f$, and the power of the line $a_p$. The model of the autocorrelation function $\rho$ for a set of parameters and at time delay $\tau$ is given by Eq. 2 for the squared- triangle model and Eq. 3 for the Gaussian model. The squared triangle is based on physical arguments: the amplitude sensitivity is maximum at the center of a range gate and falls linearly to zero one baud length away on each side (neglecting the effect of the receiver filter). As the plasma frequency is changing approximately linearly in a range gate, the returned power spectrum will take the shape of a squared triangle falling to zero at a certain frequency. It should be convolved with the natural-line-width spectrum as well as multiplied by the receiver-filter response spectrum. The Gaussian shape is not rigorously true because it does not fall exactly to zero at a certain frequency, but it falls quickly enough toward zero to be justified. This spectral shape can be used to approximate a squared-triangle spectrum smoothed by the convolution effect of the natural line width. Figure 4 shows the results of both fit models for a 10-s dump. The curves are so similar that they are hardly separable from each other. In

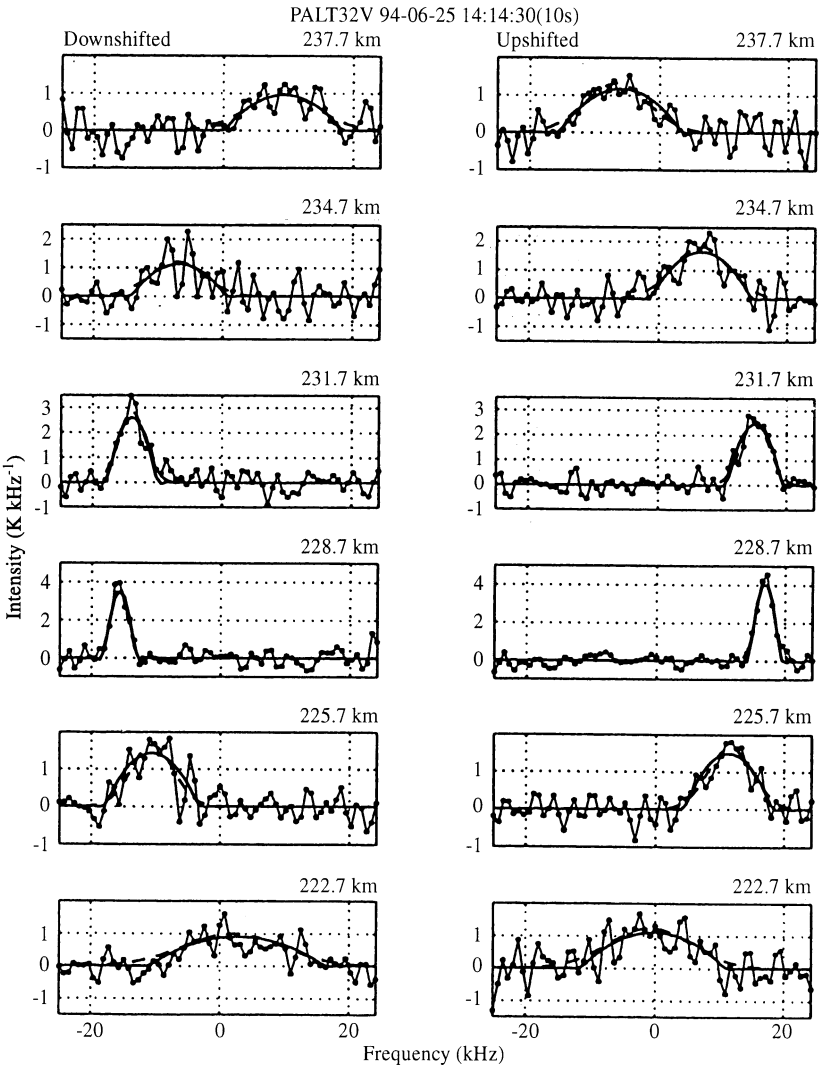


**Fig. 4.** Downshifted and upshifted spectra (*circle points and thin solid line*) from a 10-s dump fitted to the squared-triangle model (*thick solid line*) and the Gaussian model (*dashed line*). The scale is the same for each height

Fig. 5 the parameters of the fit models are plotted. All of the parameters exhibit a rather good agreement.

$$\rho_S(\tau; f_r, \delta_f, a_p) = 3a_p \frac{\sin(4\pi\delta_f\tau) - 4\pi\delta_f\tau\cos(4\pi\delta_f\tau)}{(4\pi\delta_f\tau)^3} \times \exp(i2\pi f_r\tau) \quad (2)$$

$$\rho_G(\tau; f_r, \delta_f, a_p) = a_p \exp\left(-\frac{(2\pi\delta_f\tau)^2}{2}\right)\exp(i2\pi f_r\tau). \quad (3)$$

Figures 4 and 5 show the analysis of one data dump where six gates were fitted. Note that in Fig. 5 the received frequency $f_r$ for the downshifted line is plotted positive. One can also see that the parameters exhibit very smooth behavior and very small error bars, $\sim 0.01\%$ for the received frequency.

Figures 6–8 show the result of the analysis of the autocorrelation functions of the plasma lines for the whole set of data in a similar way as for ion-line data, i.e., in time-range coordinates. One can see in Fig. 7 the general trend that the bandwidth of the line $\delta_f$ tends to increase as the position is moving away from a region of large scale height. This can also be seen in Fig. 6.

## 4 Further analysis

The solution of the real part of the dispersion relation for Langmuir waves gives the position of the frequency peak of the plasma-line spectrum. For a Maxwellian, homogeneous and unmagnetized electron plasma, this can be written as Eqs. 4 and 5 for the upshifted line (i.e., the downgoing Langmuir waves) and Eqs. 6 and 7 for the downshifted line (upgoing Langmuir wave).

$$k_+^2\lambda_D^2 + \mathrm{W_r}\left(\frac{\omega_{r^+} - k_+V_e}{k_+v_e}\right) = 0 \quad (4)$$

$$k_+ = \frac{2\pi f_{radar}}{c} + \left(\frac{2\pi f_{radar}}{c} + \frac{\omega_{r^+}}{c}\right) \quad (5)$$

$$k_-^2\lambda_D^2 + \mathrm{W_r}\left(\frac{\omega_{r^-} - k_-V_e}{k_-v_e}\right) = 0 \quad (6)$$

$$k_- = \frac{2\pi f_{radar}}{c} + \left(\frac{2\pi f_{radar}}{c} + \frac{\omega_{r^-}}{c}\right). \quad (7)$$

Here, $\omega_{r^+}$, $k_+$ and $\omega_{r^-}$, $k_-$ denote the frequency at the peak and the corresponding wave number of the upshifted and downshifted spectra, respectively. $V_e$ and $v_e$ are the

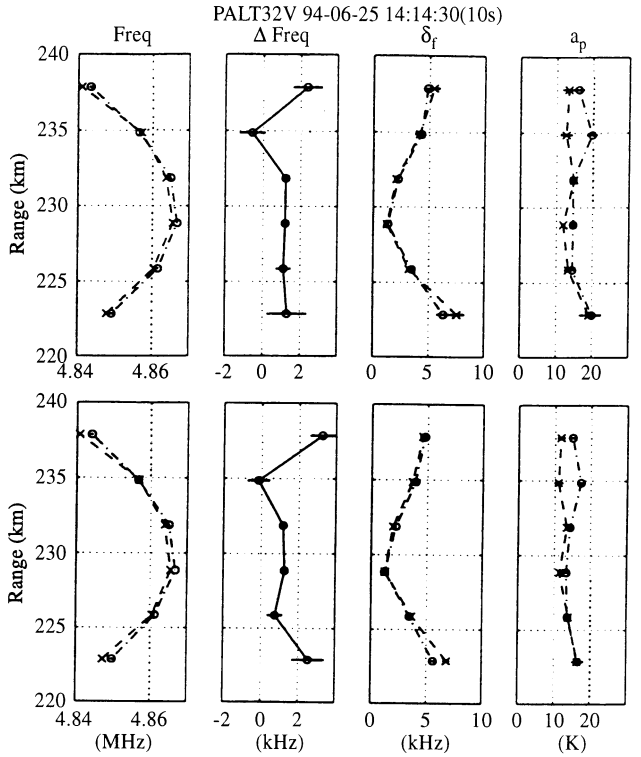


**Fig. 5.** The fitted parameters $f_r$, $\Delta f_r$, $\delta_f$ and $a_p$ as well as the error bars from the data of Fig. 4 as a function of range. The *dashdot line* is for the parameters from the upshifted line, and the *dashed one* is for the downshifted lines. The four upper panels show the parameters for the squared-triangle model, the four lower panels for the Gaussian model

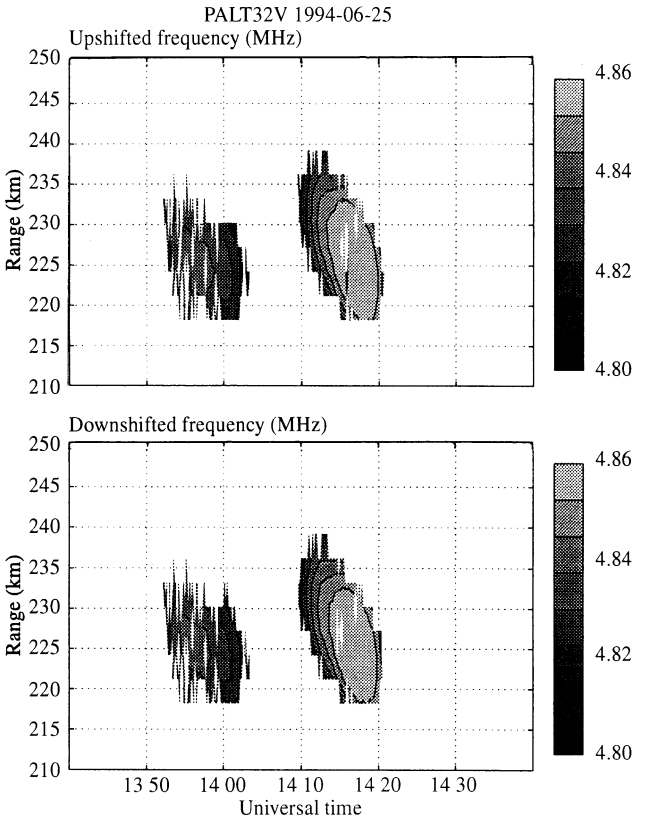


**Fig. 6.** The fitted upshifted and downshifted received frequencies displayed as a function of range and time for the Gaussian model

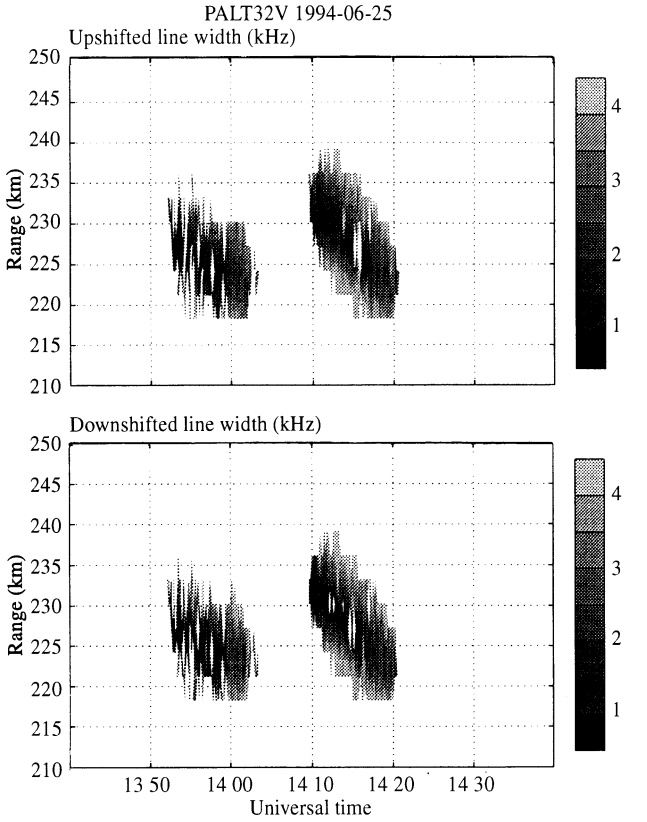


**Fig. 7.** The fitted upshifted and downshifted line bandwidth displayed as a function of range and time for the Gaussian model

electron drift velocity and the electron thermal velocity, $\lambda_D$ is the Debye length, and $W_r$ is the real part of the dispersion function W as defined by [Ichimaru (1973)].

By eliminating the Debye length $\lambda_D$, one can derive Eq. 8,

$$k_-^2 W_r\left(\frac{\omega_{r^+} - k_+ V_e}{k_+ v_e}\right) = k_+^2 W_r\left(\frac{\omega_{r^-} - k_- V_e}{k_- v_e}\right). \quad (8)$$

This equation can be solved for $V_e$ when $\omega_{r^+}$, $k_+$ and $\omega_{r^-}$, $k_-$ are taken from the results of the plasma-line analysis and $v_e$ is calculated from the electron temperature given by the ion-line analysis.

When one wants to take into account the electron heat flow contribution introduced by Kofman *et al.* (1993), Eqs. 4 and 6 are modified to Eqs. 9 and 10, where $\mathscr{E}_\pm$ is the electron heat-flow correction.

$$k_+^2 \lambda_D^2 (1 - \mathscr{E}_+) + W_r\left(\frac{\omega_{r^+} - k_+ V_e}{k_+ v_e}\right) = 0 \quad (9)$$

with

$$\mathscr{E}_+ = \frac{8}{(\omega_{r^+} - k_+ V_e)^5} \frac{k_+^3 e^2 q_e \cos\alpha}{m_e^2 \varepsilon_0}$$

$$k_-^2 \lambda_D^2 (1 - \mathscr{E}_-) + W_r\left(\frac{\omega_{r^-} - k_- V_e}{k_- v_e}\right) = 0 \quad (10)$$

with

$$\mathscr{E}_- = \frac{8}{(\omega_{r^-} - k_- V_e)^5} \frac{k_-^3 e^2 q_e \cos\alpha}{m_e^2 \varepsilon_0}.$$

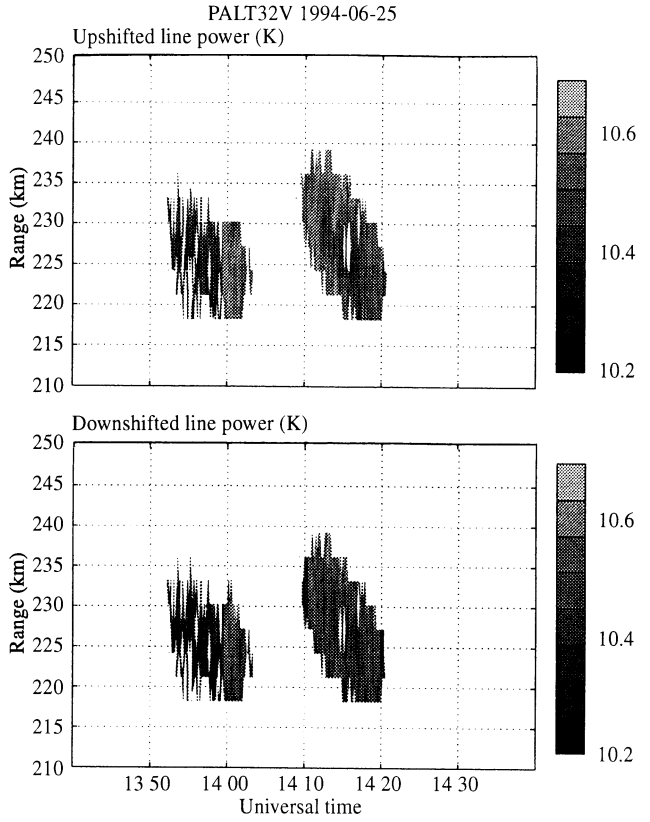


**Fig. 8.** The fitted upshifted and downshifted line power displayed as a function of range and time for the Gaussian model

This heat-flow correction is proportional to the third-order moment of the one-dimensional electron-velocity distribution function along the line of sight of the radar. It can be introduced in the dispersion relation by noting that when $W_r$ is expanded for waves with phase velocity much larger than the electron thermal velocity, as for Langmuir wave, it takes the form of a series of the successive moments of the electron-velocity distribution function. In the correction term $\mathscr{E}_{\pm}$, $q_e$ is the heat flow along the magnetic field, $\alpha$ is the angle between the line of sight of the radar and the magnetic field, $m_e$ and $e$ are the mass and charge of the electron; $q_e$ is in the limit of a fully ionized gas a function of the local electron-temperature gradient. At ionospheric heights and along the magnetic field, it is given by (Banks, 1966)

$$q_e = -1.23\,10^{-11} T_e^{5/2} \nabla T_e \quad \mathrm{J\,m^{-2}\,s^{-1}}. \tag{11}$$

In the same way as for Eqs. 4 and 6, $\lambda_D$ can be eliminated from Eqs. 9 and 10, leading to Eq. 12

$$k_-^2(1-\mathscr{E}_-)W_r\left(\frac{\omega_{r^+} - k_+ V_e}{k_+ v_e}\right) = k_+^2(1-\mathscr{E}_+)W_r\left(\frac{\omega_{r^-} - k_- V_e}{k_- v_e}\right). \tag{12}$$

This equation can also be solved for $V_e$ when $\omega_{r^+}$, $k_+$ and $\omega_{r^-}$, $k_-$ are taken from the results of the plasma-line analysis and $v_e$ is calculated from the electron temperature given by the ion-line analysis. Also, the electron-temperature gradient has to be estimated to calculate $\mathscr{E}_{\pm}$.

To get the gradient we have calculated an average electron-temperature profile during the time of the experiment, fitted it to a polynomial and then calculated the derivative from this model profile. This is justified by the fact that the electron temperature appears to have a very smooth behavior during the whole experiment. Figure 9 shows the model used for the gradient. Another justification to use an average profile is that the use of an estimated gradient for each dump would lead to unnecessarily noisy gradient estimates, whereas our estimate for the gradient shows a rather smooth behavior. At the considered heights between 200 and 260 km, the gradient was of the order of 5 K km$^{-1}$.

We now have an estimate of $V_e$. By use of one of Eqs. 4 and 6 (or similarly Eqs. 9 and 10 for the heat-flow model), we can calculate the electron density $n_e$ to a much better accuracy than the one we can get from the ion line. We now have all the necessary quantities to calculate the currents with Eq. 13,

$$J = n_e e(V_e - V_i) \quad \mathrm{Am^{-2}}, \tag{13}$$

where $V_i$ is taken from the results of the ion-line analysis.

Figure 10 shows the histograms of the estimated currents for both models, with and without the heat-flow term. These histograms exhibit a very good normal distribution of the values of the currents. For the expectation of

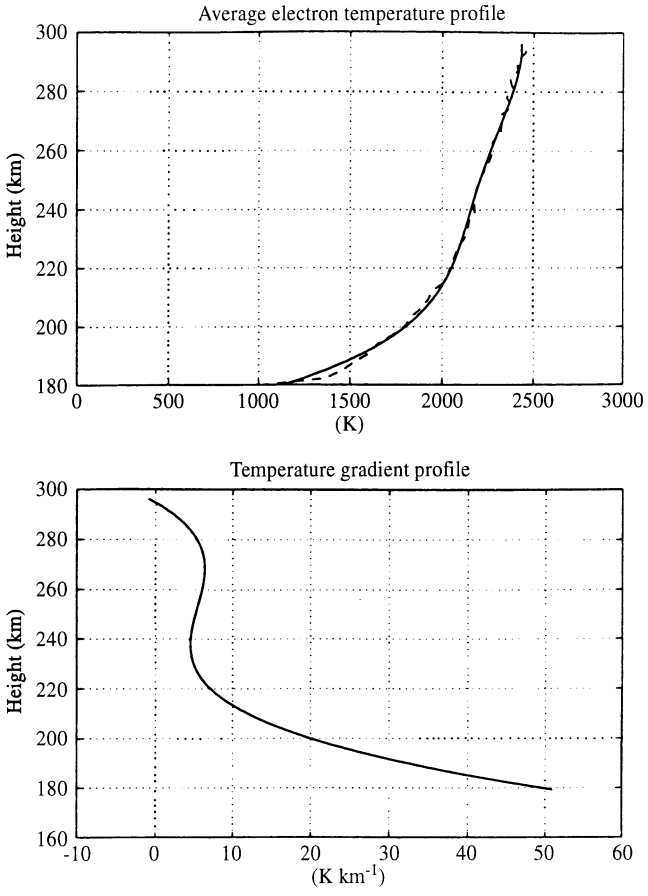


**Fig. 9.** Average electron-temperature profile for the considered period in *dashed line* and the polynomial approximation, and the deduced profile for temperature gradient

a normal distribution, a 95% confidence interval for the current J is given in Table 1. It shows a good independence of the result from the fitting model.

One can see that the heat-flow correction is very effective in the estimation of the mean drift current in the case of large gradient temperature, and thus is in better agreement with no net parallel current during the quiet daytime conditions. Note also that the uncertainty on the estimated current remains of the same order; this is certainly to be accounted to the way we have estimated the electron-temperature gradient.

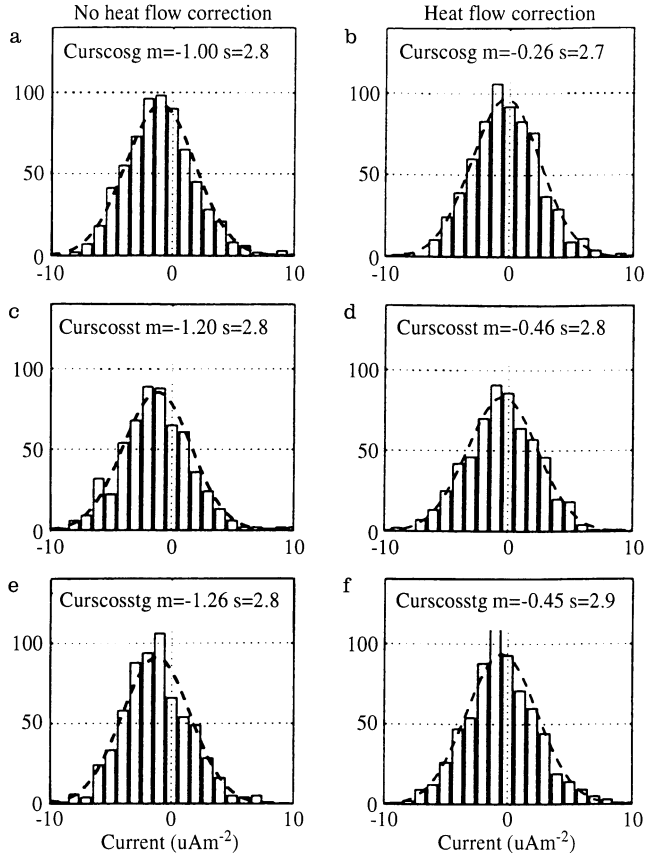


**Fig. 10a–f.** Histogram of the calculated currents without (*left panels*) and with heat-flow correction (*right panels*). The total population of each histogram is $\sim 700$. The *dashed lines* represent the best fit to a normal distribution. **a** and **b** are for the Gaussian model, **c** and **d** are for the squared-triangle model, and **e** and **f** are for a data analysis taking the parameters of the fit giving the smallest residuals of the squared-triangle and Gausian fits. Note that positive currents are upward currents

**Table 1.** 95% confidence interval for the currents J without heat-flow correction and $J_{hf}$ with heat-flow correction from the histograms of Fig. 10

| | J ($\mu A\,m^{-2}$) | $J_{hf}$ ($\mu A\,m^{-2}$) |
|---|---|---|
| Gaussian model (a) (b) | $-1.0 \pm 0.2$ | $-0.3 \pm 0.2$ |
| Squared-triangle model (c) (d) | $-1.2 \pm 0.2$ | $-0.5 \pm 0.2$ |
| Best of both models (e) (f) | $-1.3 \pm 0.2$ | $-0.4 \pm 0.2$ |

## 5 Conclusion

We have shown that the alternating code for studying plasma lines with an incoherent scatter radar is a valuable technique. It yields a greatly improved spatial resolution and a much larger amount of measured points (between five and six times more than for a long-pulse experiment).

We have been using our data to test the heat-flow dispersion-relation model under quiet and steady ionospheric conditions. We confirm that the use of the heat-flow model gives important corrections and improves the measurements of current.

The plans are to extend and improve the use of the alternating code in future experiments. On one hand, the experiment could be refined and improved to give better accuracy and larger quantities of data. On the other, analysis techniques such as constrained full profile analysis of both plasma-line and ion-line data should be investigated and tried.

*Acknwledgements.* The authors thank one of the referees for his valuable remark about the spectral models for the fitting procedure. The authors want to thank the EISCAT personnel for their efforts in making the radar available. EISCAT is funded by the CNRS of France, the SA of Finland, the MPG of Germany, the NFR of Norway, the NFR of Sweden, and the PPARC of United Kingdom.

Topical Editor D. Alcaydé thanks M. Lehtinen and another referee for their help in evaluating this paper.

## References

**Banks, P. M.,** Charged particle temperatures and electron thermal conductivity in the upper atmosphere, *Ann. Geophysicae*, **22,** 577–587, 1966.

**Birkmayer, W., and T. Hagfors,** Observational technique and parameter estimation in plasma line spectrum observations of the ionosphere by chirped incoherent scatter radar, *J. Atmos. Terr. Phys.*, **48,** 1009–1019, 1986.

**Djuth, F. T., M. P. Sulzer, and J. H. Elder,** Application of the coded long-pulse technique to plasma line studies of the ionosphere, *Geophys. Res. Lett.*, **21,** 2725–2728, 1994.

**Farley, D. T.,** Multiple-pulse incoherent-scatter correlation function measurements, *Radio Sci.*, **7,** 661–666, 1972.

**Hagfors, T.,** Incoherent scatter radar observations of the plasma line with a chirped pulse system, *Radio Sci.*, **17,** 727–734, 1982.

**Ichimaru S.,** *Basic principles of plasma physics*, W. A. Benjamin, Reading, Mass., 1973.

**Kofman, W., and V. Wickwar,** Plasma line measurements at Chatanika with high-speed correlator and filter bank, *J. Geophys. Res.*, **85,** 2998–3012, 1980.

**Kofman, W., J.-P. St-Maurice, and A.P. van Eyken,** Heat flow effect on the plasma line frequency, *J. Geophys. Res.*, **98,** 6079–6085, 1993.

**Lehtinen, M. S., and I. Häggström,** A new modulation principle for incoherent scatter measurements, *Radio Sci.*, **22,** 625–634, 1987.

**Perkins, F., E. E. Salpeter,** Enhancement of plasma density fluctuations by nomthermal electrons, *Phys. Rev. A*, **139,** 55–62, 1965.

**Showen, R. L.,** The spectral measurement of plasma line, *Radio Sci.*, **14,** 503–508, 1979.

**Sulzer, M. P.,** Recent incoherent scatter techniques, *Adv. Space Res.*, **9,** 153–161, 1989.

**Yngvesson, K. O., and F. W. Perkins,** Radar Thomson scatter studies of photoelectrons in the ionosphere and Landau damping, *J. Geophys. Res.*, **73,** 97–110, 1968.

This article was processessed by the author using the LaTeX style file *pljour2* from Springer-Verlag.

# ARTICLE II

Ann. Geophysicae 16, 1226–1240 (1998) © EGS – Springer-Verlag 1998

Annales Geophysicae

# Electron velocity distribution function in a plasma with temperature gradient and in the presence of suprathermal electrons: application to incoherent-scatter plasma lines

**P. Guio**[1], **J. Lilensten**[2], **W. Kofman**[2], **N. Bjørnå**[1]

[1] The Auroral Observatory, University of Tromsø, N-9037 Tromsø, Norway, Fax: +47 77 64 62 80; e-mail: patrick@phys.uit.no
[2] CEPHAG Domaine Universitaire, BP 46, F-38402 St-Martin-D'hères, France

Received: 6 January 1998 / Revised: 13 March 1998 / Accepted: 19 March 1998

**Abstract.** The plasma dispersion function and the reduced velocity distribution function are calculated numerically for any arbitrary velocity distribution function with cylindrical symmetry along the magnetic field. The electron velocity distribution is separated into two distributions representing the distribution of the ambient electrons and the suprathermal electrons. The velocity distribution function of the ambient electrons is modelled by a near-Maxwellian distribution function in presence of a temperature gradient and a potential electric field. The velocity distribution function of the suprathermal electrons is derived from a numerical model of the angular energy flux spectrum obtained by solving the transport equation of electrons. The numerical method used to calculate the plasma dispersion function and the reduced velocity distribution is described. The numerical code is used with simulated data to evaluate the Doppler frequency asymmetry between the up- and downshifted plasma lines of the incoherent-scatter plasma lines at different wave vectors. It is shown that the observed Doppler asymmetry is more dependent on deviation from the Maxwellian through the thermal part for high-frequency radars, while for low-frequency radars the Doppler asymmetry depends more on the presence of a suprathermal population. It is also seen that the full evaluation of the plasma dispersion function gives larger Doppler asymmetry than the heat flow approximation for Langmuir waves with phase velocity about three to six times the mean thermal velocity. For such waves the moment expansion of the dispersion function is not fully valid and the full calculation of the dispersion function is needed.

**Key words.** Non-Maxwellian electron velocity distribution · Incoherent scatter plasma lines · EISCAT · Dielectric response function

*Correspondence to:* P. Guio

## 1 Introduction

We want to estimate the field-aligned electron mean drift velocity $V_e$ from incoherent scatter Doppler measurement of the plasma lines (Vidal-Madjar *et al.*, 1975; Bauer *et al.*, 1976; Showen, 1979). In order to do this we need to solve accurately the plasma dispersion relation for electrostatic waves at high frequencies and thus to have an accurate model of the electron velocity distribution function.

A common way of representing the whole electron velocity distribution function is to separate it into two populations: the ambient or bulk population $f_a(\boldsymbol{v})$ and the suprathermal or tail population $f_s(\boldsymbol{v})$, and special care needs to be taken for the treatment of the transition region between the suprathermal and ambient electrons. At ionospheric heights about the $F2$ region, the bulk population of the electrons is collision-dominated and thus the velocity-space distribution is expected to be very close to a Maxwellian. In this case, the parameters describing the state of the thermal population are: the electron density $n_e$, the electron temperature $T_e$ and the potential source of inhomogeneity such as the spatial gradients of electron temperature $\nabla T_e$ and pressure $\nabla p_e$, as well as possibly an electric field $\boldsymbol{E}$. These parameters are provided by the analysis of the measurement of the ion line incoherent scattering. On the other hand, the suprathermal component $f_s(\boldsymbol{v})$ is taken from a complete kinetic electron transport code which takes into account the ionization and heating resulting from both solar insolation and particle precipitations.

In the first part, we describe and review the original theory developed to calculate the velocity distribution function of the ambient electrons in the presence of a temperature gradient and/or an electric field (Spitzer and Härm, 1953). Thereafter we present and discuss the calculations we use to represent the suprathermal part of the distribution function. We then describe a numerical method to calculate the full two-dimensional

dispersion relation. We test our numerical code and discuss the results on simulated Doppler asymmetry data for radars with different wave vector and compare the results given by the heat flow approximation of Kofman *et al.* (1993).

## 2 The ambient velocity distribution

For low energy and for a fully ionized plasma consisting of electrons and one ion species, the distribution function of the electrons in a highly collisional regime, i.e. in a regime where the velocity-space distribution of the electrons is close to a Maxwellian (Gombosi and Rasmussen, 1991), can be approximated by the Spitzer-Härm distribution function of Cohen *et al.* (1950) and Spitzer and Härm (1953).

This time-independent distribution function is the result of the presence of a weak electric field and a temperature gradient. The distribution function is expanded as a power series in the Knudsen number $\epsilon$ which represents the ratio of the microscopic length scale to the macroscopic length scale. In this theory only the first order in $\epsilon$ is kept, which is known as the principle of local action (Woods, 1993). This restriction to small values of $\epsilon$ implies that the electron mean free path $\lambda_e$ is much smaller than the different scale lengths considered $\nabla \log T_e$, $\nabla \log p_e$ and $eE/K_bT_e$ (Ljepojevic and MacNeice, 1989). The two Knudsen numbers associated are respectively $\epsilon_E$ and $\epsilon_T$ defined as

$$\epsilon_E = \lambda_e \left( \frac{eE}{K_b T_e} - \frac{\nabla p_e}{p_e} \right) \tag{1}$$

and

$$\epsilon_T = 2\lambda_e \frac{\nabla T_e}{T_e}, \tag{2}$$

where $E$ is the electric field, $T_e$ the electron temperature, $p_e$ the electron pressure and $\nabla$ represents the derivative along the line of sight. For small Knudsen numbers, i.e. $\epsilon_E \ll 1$ and $\epsilon_T \ll 1$, perturbation methods apply and the ambient electron velocity distribution function $f_a$ is expanded about a local Maxwellian $f_0(v) = n_e/(2\pi)^{3/2}/v_e^3 \exp(-(v/v_e)^2/2)$ with thermal velocity $v_e = (K_bT_e/m_e)^{1/2}$ and takes the following form

$$f_a(xv_e, \mu) = f_0(xv_e) \left[ 1 + Z\mu \left( \epsilon_E X_E\left(x/\sqrt{2}\right) + \epsilon_T X_T\left(x/\sqrt{2}\right) \right) \right], \tag{3}$$

where $\mu$ is the cosine of the pitch angle measured from an axis parallel to the direction of the temperature gradient and electric field, $Z$ is the charge number of the ion species and $x$ is the ratio $v/v_e$. The functions $X_E$ and $X_T$ are the solutions of two second-order differential equations [Eq. (40) of Spitzer and Härm (1953) and Eqs. (6)–(13) of Cohen *et al.* (1950)] derived from the Boltzmann's equation where only the long-range electron-electron and the electron-ion interactions have been taken into account through two Fokker-Planck collision operators. This approximation is valid for low energy only, so that the upper boundary of integration of these functions should not be too large compared to the mean thermal velocity $v_e$. We have recalculated the solutions to these equations for different values of the upper boundary. Figure 1 shows the two functions $X_E$ and $X_T$ for those different values of the upper boundary of integration $x_{\max}$.

By taking the first- and third-order velocity moments of the perturbation functions $X_E$ and $X_T$ one defines four transport coefficients $\gamma_E$, $\delta_E$, $\gamma_T$ and $\delta_T$. These are the normalized transport coefficients relative to a Lorentzian gas (Spitzer and Härm, 1953; Shkarofsky, 1961). Equations 4–7 show the relations between these coefficients, the velocity moments of the distribution function and the transport coefficients $\sigma_e$, $\tau_e$, $\mu_e$ and $\kappa_e$.

$$\gamma_E = \frac{1}{3} I_3(X_E) = \frac{\sqrt{\pi} m_e v_e}{4\sqrt{2} Z e^2 n_e \lambda_e} \sigma_e, \tag{4}$$

$$\delta_E = \frac{1}{12} I_5(X_E) = \frac{\sqrt{\pi} m_e v_e}{6\sqrt{2} Z e n_e K_b \lambda_e} \tau_e, \tag{5}$$

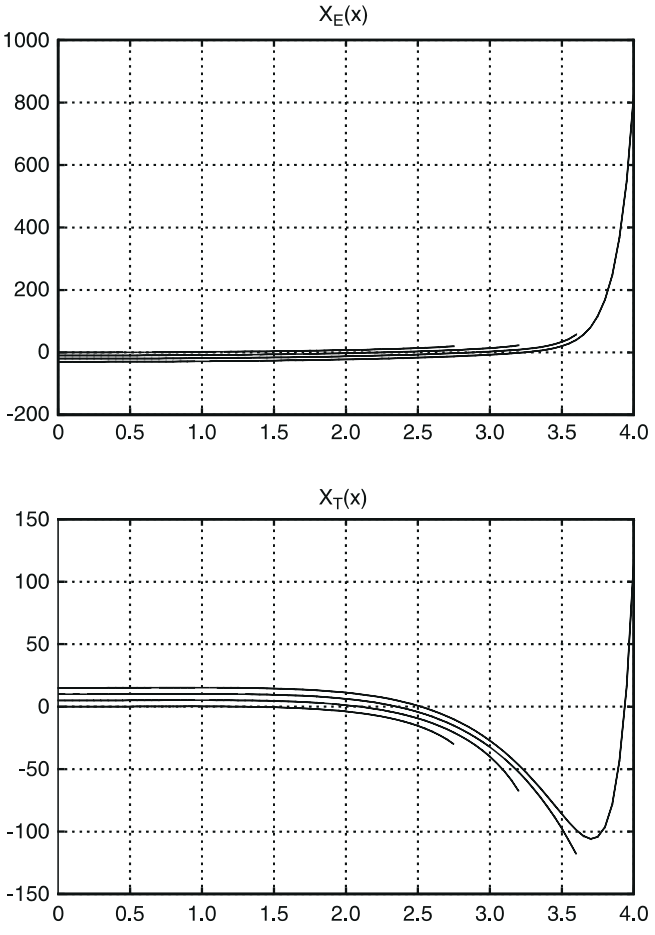


**Fig. 1.** The perturbation functions $X_E$ and $X_T$ integrated to different upper boundary $x_{\max} = v/\sqrt{2}v_e = 2.8, 3.2, 3.6$ and 4.0, and for an ion charge number $Z = 1$. Note that $X_E(0) = X_T(0) = 0$ and that the $X_E$'s are shifted by $-10$ with each other, the $X_T$'s are shifted by $+5$ with each other, the reference curves (i.e. not shifted) are for $x_{\max} = 2.8$

$$\gamma_T = -\frac{4}{9} I_3(X_T) = \frac{3\sqrt{\pi} v_e}{16\sqrt{2} Z e n_e \lambda_e} \mu_e, \tag{6}$$

$$\delta_T = -\frac{1}{15} I_5(X_T) = \frac{\sqrt{\pi} v_e}{40\sqrt{2} Z n_e K_b \lambda_e} \kappa_e, \tag{7}$$

with

$$I_n(f) = \int_0^{x_{\max}} y^n f(y) \exp(-y^2) dy, \tag{8}$$

where $\sigma_e$ is the electrical conductivity, $\tau_e$ is the current flow conductivity due to a temperature gradient at constant electron density, $\mu_e$ is the heat flow conductivity due to an electric field at constant electron temperature and $\kappa_e$ is the thermal conductivity.

Table 1 presents the values of the normalized transport coefficients we have recalculated and the original values of Spitzer and Härm (1953). With the exception of the values for $x_{\max} = 2.8$, the values of the transport coefficients are in good agreement (under 1%) with the values calculated by Spitzer and Härm ($x_{\max} = 3.2$).

In the work of Spitzer and Härm, the electron mean free path $\lambda_e$ is taken to be the mean free path due to electron-electron collisions and electron-ion collisions. We shall correct the electron mean free path to take into account the electron-neutral collision term (Banks, 1966). We define the electron mean free path as

$$\frac{1}{\lambda_e} = \frac{1}{\lambda_{ee}} + \frac{1}{\lambda_{ei}} + \frac{1}{\lambda_{en}}, \tag{9}$$

or as a function of the electron-charged particle free path $\lambda_{ec}$:

$$\lambda_e = \frac{\lambda_{ec}}{1 + \lambda_{ec}/\lambda_{en}}. \tag{10}$$

The electron-neutral collisions tend to reduce the electron mean free path, and in the limit of low neutral particle densities we recover the electron mean free path value of a fully ionized plasma (Banks, 1966). It is important to note that the differential equations for the perturbation functions $X_E$ and $X_T$ have not been modified, thus the departure of the velocity distribution function from the Maxwellian state is still caused by Coulomb interactions through the two Fokker-Planck collision operators for distant interactions.

In the ionosphere, a so-called polarization electric field $\boldsymbol{E}$ builds up such that the ions and electrons are constrained to drift as a single gas, which maintains bulk charge neutrality. $\boldsymbol{E}$ is determined by the current $\boldsymbol{J}$ and it exists whenever there is a gradient in the electron density or in the temperature (Min *et al.*, 1993). It is given by

$$\boldsymbol{E} = \frac{\boldsymbol{J}}{\sigma_e} + \frac{\nabla p_e}{e n_e} - \frac{\tau_e}{\sigma_e} \nabla T_e. \tag{11}$$

If the field-aligned current is attributed to the flow of the suprathermal electrons only then the $\boldsymbol{J}/\sigma_e$ term is small compared with the gradient terms and we get the following relation between the electric field $\boldsymbol{E}$ and the gradient of temperature $\nabla T_e$

$$\boldsymbol{E} = \frac{\nabla p_e}{e n_e} - \frac{3\gamma_T K_b}{2\gamma_E e} \nabla T_e. \tag{12}$$

Using Eqs. (1) to (7), this leads to the following relationship between the two Knudsen numbers $\epsilon_E$ and $\epsilon_T$

$$4\epsilon_E \gamma_E + 3\epsilon_T \gamma_T = 0. \tag{13}$$

In the rest of this paper we always consider the presence of such a polarization electric field. The two Knudsen numbers for the Spitzer-Härm distribution then always satisfy Eq. (13).

**Table 1.** The normalized transport coefficients as defined in Eqs. (4) to (7) calculated for different values of $x_{\max}$ and compared with the ones given by Spitzer and Härm ($x_{\max} = 3.2$)

| $x_{\max}$ | 2.8 | 3.2 | Spitzer-Härm | 3.6 | 4.0 |
|---|---|---|---|---|---|
| $\gamma_E$ | 0.5740 | 0.5811 | 0.5816 | 0.5826 | 0.5832 |
| $\gamma_T$ | 0.2507 | 0.2677 | 0.2727 | 0.2715 | 0.2718 |
| $\delta_E$ | 0.4436 | 0.4622 | 0.4652 | 0.4672 | 0.4698 |
| $\delta_T$ | 0.1877 | 0.2149 | 0.2252 | 0.2228 | 0.2237 |

## 3 The suprathermal velocity distribution

The suprathermal velocity distribution $f_s$ we use is derived from the angular energy flux $\phi$ calculated by the electron transport model code along the Earth magnetic field described in Lilensten *et al.* (1989) and Lummerzheim and Lilensten (1994).

In the ionosphere, primary photoelectrons or precipitating electrons move along the magnetic field, produce heat and provoke processes such as excitation and ionization. In an ionization process, the incident electron mostly scattered forward is called the primary electron, while the extracted electron may be scattered in any direction and is called the secondary electron. This code calculates the energy flux of the electrons by solving the vertical kinetic transport equation. This equation simply expresses the fact that the variation of the steady-state electron flux with the scattering depth for a given altitude, energy and pitch angle, is the difference between whatever leaves that energy, altitude or angle slab and whatever enters it. The variations in energy or angle due to collisions are described through differential cross-sections. An additional energy loss arises from the heating of the ambient thermal electron gas due to hot electrons to thermal electrons interactions. This loss process is assumed to be a continuous energy loss of the hot electrons to the thermal electrons, without any deflection during the process.

We are using the angular energy flux calculated by this code as our input to calculate the velocity distribution. The electron velocity distribution is simply related to the angular energy flux by

$$\phi(\boldsymbol{r}, E, \Omega, t) = \frac{v^2}{m_e} f_s(\boldsymbol{r}, E, \Omega, t) \quad \mathrm{eV}^{-1}\ \mathrm{cm}^{-2}\ \mathrm{s}^{-1} \tag{14}$$

where $E = \frac{1}{2} m_e v^2$ and $\Omega$ is the solid angle. With the assumption that the angular energy flux is symmetric

around the magnetic field, $f_s$ is a two-dimensional function of the energy $E$ or the velocity $v$ and of the pitch angle $\theta$ or the cosine of the pitch angle $\mu = \cos\theta$ to the magnetic field at a given altitude.

The angular energy flux $\phi$ is calculated over an energy grid of 215 points ranging from $E_{\min} = 0.3\,\text{eV}$ to $E_{\max} = 350\,\text{eV}$ and over a $\mu$-grid corresponding to the points of the double-Gauss quadrature integration rule (Stamnes *et al.*, 1988). The number of points in the $\mu$-grid is often referred to as the number of streams. The double-Gauss quadrature refers to two Gauss quadratures applied separately on the upper and lower hemispheres. The main advantage of this double-Gauss scheme is that the quadrature points (in even orders) are distributed symmetrically around $|\mu| = 0.5$ and clustered both towards $|\mu| = 1$ and $\mu = 0$, whereas in the single Gauss scheme they are clustered towards $|\mu| = 1$. This clustering towards $\mu = 0$ will give superior results near the boundaries where the functions to integrate vary rapidly or can even be discontinuous, i.e. around $\mu = 0$.

The angular flux calculations we are using were obtained by running the code for 25 June 1994 at 14:00 UT over Tromsø assuming an $A_p$ index of 3 and a F10.7 index of 75. The ionospheric parameters used as input to the code have been computed by the IRI 90 model (Bilitza, 1990).

Figures 2 and 3 show two examples of calculation of the distribution function for an eight-point angular quadrature. Figure 2 shows only the flux for one angle, the flux at this height is nearly isotropic and one could not separate the flux. From a height of about 200km and above, the velocity distribution starts to develop an anisotropy mostly in the direction of the magnetic field, i.e. for $|\mu| \simeq 1$. This feature is clearly seen in Fig. 3: the two angular distributions in the lowest plate are for nearly parallel and anti-parallel directions to the magnetic field and they clearly present differences in intensity, while in the highest plate (angular distributions for the directions nearly perpendicular to the magnetic field), the two curves cannot be separated.

An interesting function which illustrates the regions in phase space where the heat flux is predominantly carried is the ratio of the integrated heat flux up to velocity $v = xv_e$ and normalized to the total net heat flux $q_s$ (Gray and Kilkenny, 1980). We define in this way the function $\alpha(v/v_e)$

$$\alpha(x) = \frac{m_e}{2q_s}\int_0^v\int_{-1}^1 |\boldsymbol{u}-\boldsymbol{u_s}|^2(u\mu-u_s)f_s(u,\mu)2\pi u^2 d\mu\, du, \quad (15)$$

where $\boldsymbol{u_s}$ is the mean drift velocity of the suprathermal velocity distribution. Note that with the symmetry around the magnetic field both the mean drift velocity $\boldsymbol{u_s}$ and $\boldsymbol{q_s}$ are vectors parallel to the magnetic field of component $u_s$ and $q_s$, respectively.

Figure 4 shows the values of the parameter $\alpha$ at different altitudes for a standard set of suprathermal distribution function calculated by the transport code for an eight-stream run. At high altitudes (see Fig. 4 at 246 km for example), the local skewness is more than the net skewness for velocity $v \sim 30v_e$, which means that locally the distribution can have skewness of opposite sign compared to the total skewness of the distribution.

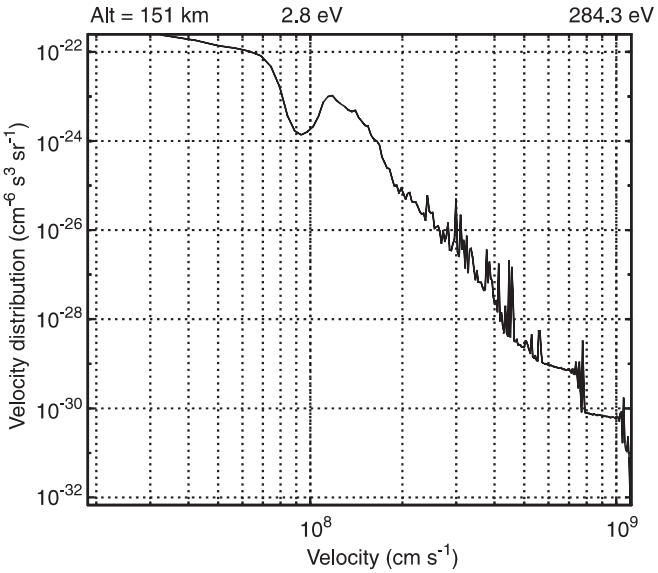


**Fig. 2.** The suprathermal angular velocity distribution function calculated by the transport code for an eight-stream calculation at 151 km and for a pitch angle of 86° (i.e. $\mu = 0.0694$). The distribution is nearly isotropic, and the data at the other pitch angles would not be distinguishable on the same plate

We now have a representation for the ambient and the suprathermal distributions, the next operation consists in the treatment of the transition region between the suprathermal and the ambient electrons. Sophisticated methods such as the numerical resolution of the non-linear Boltzmann equation (Ashihara and Takayanagi, 1974; Jasperse, 1976), as well as full analytical treatment such as the one proposed by Krinberg (1973) have been studied to solve this problem. However, it has been shown later that a good approximation for the complete distribution function can be obtained by joining the two distribution functions at the energy for which the two distributions have equal intensities (Krinberg and Akatova, 1978; Stamnes and Rees, 1983). For simplicity we choose this method and in the rest of this paper the terminology truncated distribution refers to a distribution cut at the velocity where the ambient population equals the suprathermal population.

## 4 Numerical two-dimensional plasma dispersion

In linear theory the differential scattering cross-section $d^2\sigma/d\Omega\, d\omega$ per angular frequency and per solid angle for a multi-component, uniform, stationary, along the magnetic field and non-relativistic plasma with the collisions effects included through a BGK model is given by (Sheffield, 1975; Bjørnå and Trulsen, 1986; Ichimaru, 1992)

$$\frac{d^2\sigma}{d\Omega d\omega} = \frac{1}{\sqrt{\pi}} n_e r_0^2 |\boldsymbol{n}\times(\boldsymbol{n}\times\boldsymbol{p})|^2 S(\boldsymbol{k},\omega), \quad (16)$$

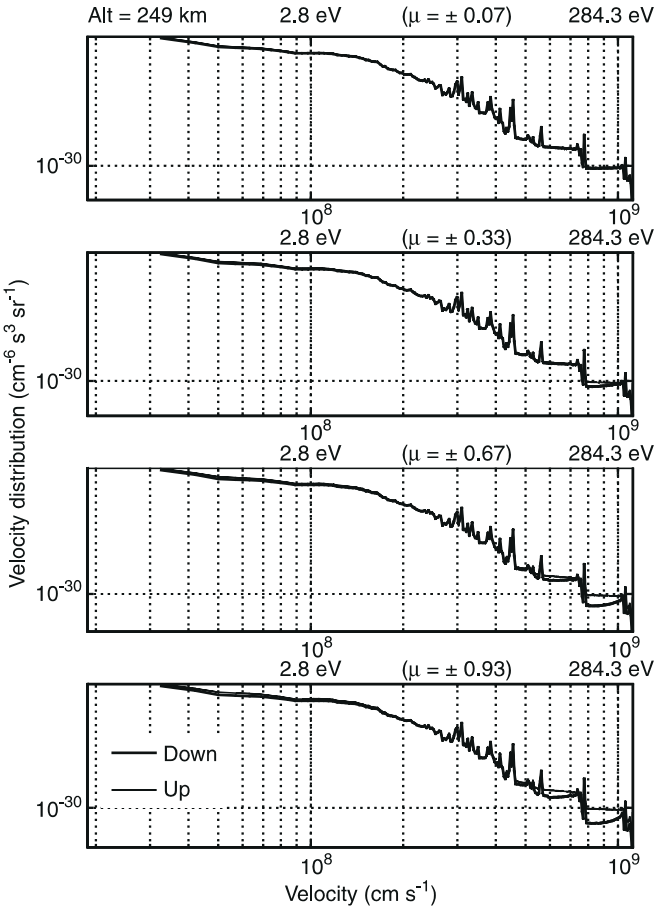


**Fig. 3.** The suprathermal angular velocity distribution function for the same eight-stream calculation at 249 km. Each plate contains two curves corresponding to two angles symmetric around the direction perpendicular to the magnetic field, i.e the upward angular flux (*thin solid line*) and the downward one (*thick solid line*). The upper horizontal scale on each plate is energy expressed in eV

where the spectral density function $S$ is defined as

$$S(\boldsymbol{k},\omega) = \left|1+\frac{C_e(\boldsymbol{k},\omega)}{D(\boldsymbol{k},\omega)}\right|^2 \frac{\mathrm{Im}\,P_e(\boldsymbol{k},\omega)-v_e|P_e(\boldsymbol{k},\omega)|^2}{\sqrt{\pi}|X_e(\boldsymbol{k},\omega)|^2} + \sum_j \frac{n_j}{n_e} z_j^2 \left|\frac{C_e(\boldsymbol{k},\omega)}{D(\boldsymbol{k},\omega)}\right|^2 \frac{\mathrm{Im}\,P_j(\boldsymbol{k},\omega)-v_j|P_j(\boldsymbol{k},\omega)|^2}{\sqrt{\pi}|X_j(\boldsymbol{k},\omega)|^2}, \quad (17)$$

with

$$D(\boldsymbol{k},\omega) = 1-\sum_\alpha C_\alpha(\boldsymbol{k},\omega), \quad (18)$$

$$C_\alpha(\boldsymbol{k},\omega) = Z_\alpha(\boldsymbol{k},\omega)/X_\alpha(\boldsymbol{k},\omega), \quad (19)$$

$$X_\alpha(\boldsymbol{k},\omega) = 1+iv_\alpha P_\alpha(\boldsymbol{k},\omega), \quad (20)$$

$$Z_\alpha(\boldsymbol{k},\omega) = \sum_k Z_{\alpha,k}(\boldsymbol{k},\omega), \quad (21)$$

$$Z_{\alpha,k}(\boldsymbol{k},\omega) = \frac{\omega_{\alpha,k}^2}{k^2}\int_L \frac{\boldsymbol{k}\cdot\nabla_{\boldsymbol{v}}\mathrm{f}_{\alpha,k}(\boldsymbol{v})}{\boldsymbol{k}\cdot\boldsymbol{v}-\omega-iv_\alpha}d^3\boldsymbol{v}$$

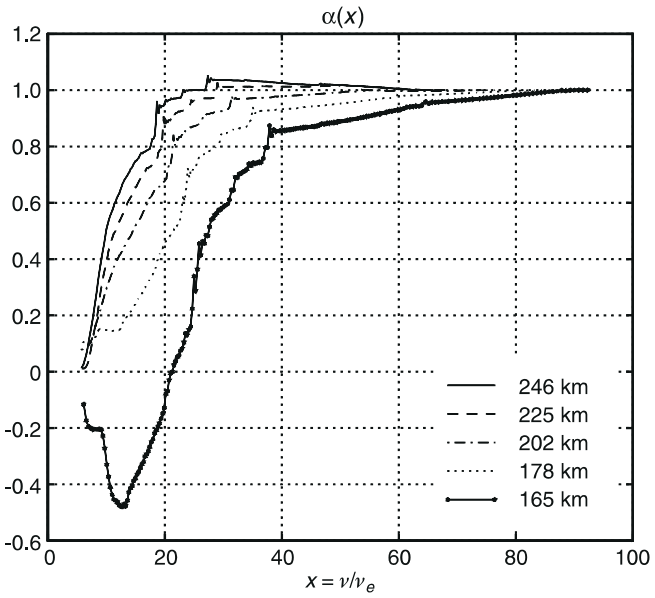


**Fig. 4.** The coefficient of location of the heat flux α of Eq. (15) for five different altitudes for the eight-stream calculation of the transport code of the 25 June 1994

$$P_\alpha(\boldsymbol{k},\omega) = \frac{1}{n_\alpha}\sum_k n_{\alpha,k}\int_L \frac{\mathrm{f}_{\alpha,k}(\boldsymbol{v})}{\boldsymbol{k}\cdot\boldsymbol{v}-\omega-iv_\alpha}d^3\boldsymbol{v}. \quad (23)$$

$\mathrm{f}_{\alpha,k}=f_{\alpha,k}/n_{\alpha,k}$ denotes the velocity probability distribution function for the $k^{\mathrm{th}}$ component of the particle species $\alpha$ ($e$ for the electrons and $j$ for the ions). $v_\alpha$ is the collision frequency of the particle species $\alpha$, $r_0^2=e^2/(4\pi\epsilon_0 m_e c^2)$ is the electron radius, $\boldsymbol{n}$ is the unit vector pointing from the scattering volume towards the receiver and $\boldsymbol{p}$ is the unit polarization vector of the incident radiation; $\omega$ is the frequency shift between the transmitted radio wave $\omega_0$ and the received frequency $\omega_r$, $\boldsymbol{k}$ is the wave vector shift defined as the difference between the returned wave vector and the transmitted radio-wave vector $\boldsymbol{k}_0$.

$$\omega = \omega_r-\omega_0, \quad (24)$$

$$\boldsymbol{k} = \frac{\omega_r}{c}\boldsymbol{n}-\boldsymbol{k}_0. \quad (25)$$

$D$ and $Z_\alpha$ are respectively the dielectric function and the opposite of the susceptibility function for the particle species $\alpha$.

In order to calculate the dispersion relation, we need to calculate integrals of the $P$ and $Z$ types defined by

$$Z(\boldsymbol{k},\omega) = \frac{\omega_e^2}{k^2}\int_{\mathrm{L}} \frac{\boldsymbol{k}\cdot\nabla_{\boldsymbol{v}}f(\boldsymbol{v})}{\boldsymbol{k}\cdot\boldsymbol{v}-\omega-iv}d^3\boldsymbol{v} \quad (26)$$

and

$$P(\boldsymbol{k},\omega) = \int_{\mathrm{L}} \frac{f(\boldsymbol{v})}{\boldsymbol{k}\cdot\boldsymbol{v}-\omega-iv}d^3\boldsymbol{v}, \quad (27)$$

for velocity probability distribution $f$ defined in a cylindrical coordinate system along the magnetic field (which is the same direction as the temperature gradient), and when the scattered wave vector $\boldsymbol{k}$ is aligned to the local magnetic field line.

When $v=0$, one can note by applying the Plemelj formula that the imaginary part of $P$ is proportional to

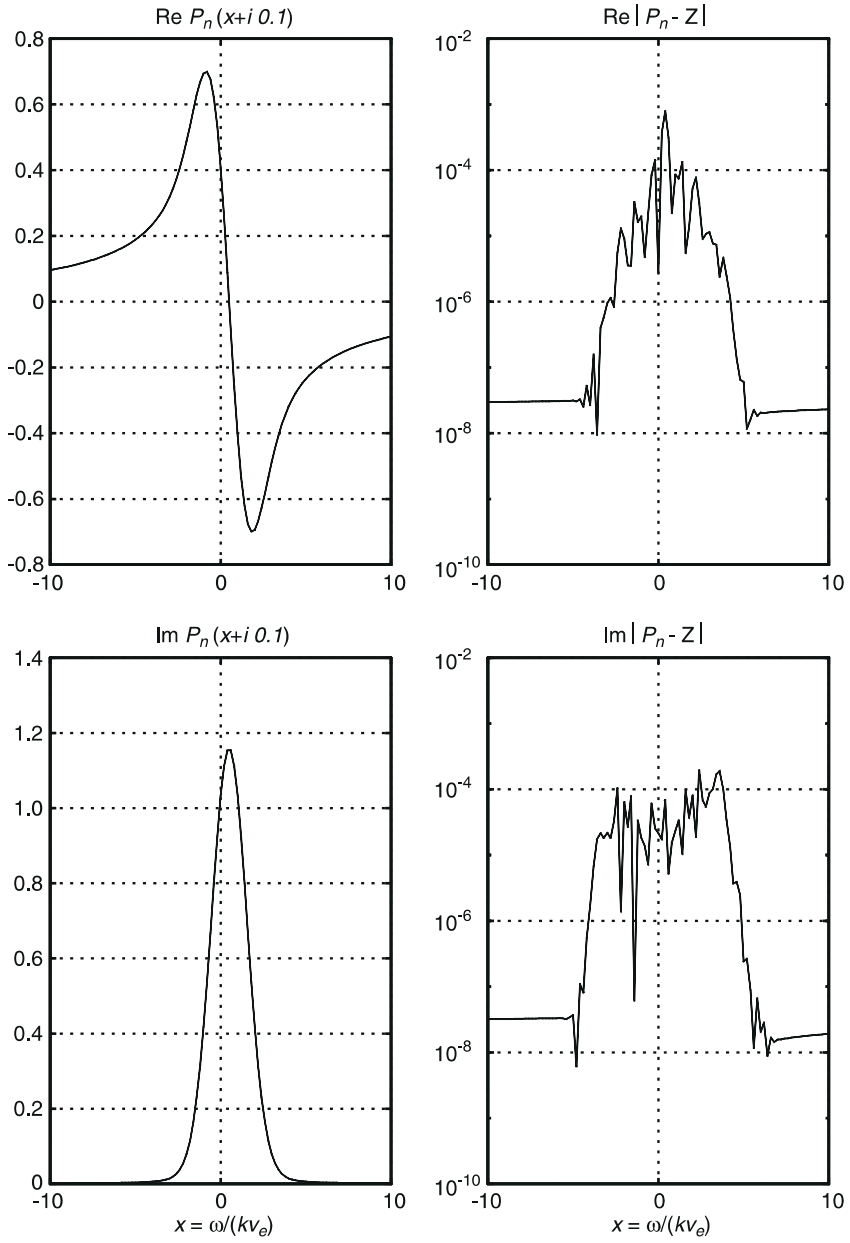


**Fig. 5.** On the left, the real and imaginary parts of the $P_n$ function given by Eq. (35) for complex argument such that the imaginary part $\eta = 0.1$. On the right, their relative error with the real and imaginary parts of $\mathbf{Z}(z/\sqrt{2})/\sqrt{2}$, where $\mathbf{Z}$ is the plasma dispersion function (Fried and Conte, 1961). The normalized Doppler shift of the Maxwellian distribution is $x_d = 0.5$

the reduced velocity distribution function $F_\parallel$ along the direction of $\boldsymbol{k}$.

$$F_\parallel\left(\frac{\omega}{k}\right) = \frac{k}{\pi}\mathrm{Im}\,P(\boldsymbol{k},\omega) = \int f(\boldsymbol{v})\delta(\boldsymbol{k}\cdot\boldsymbol{v}-\omega)\frac{d^3\boldsymbol{v}}{\pi}. \quad (28)$$

When the collision frequencies are very small, we found that $P$ can be expressed in the form

$$P(\boldsymbol{k},\omega) \simeq \frac{1}{kv_e}P_n\left(\frac{\omega}{kv_e}\right), \quad (29)$$

with

$$P_n(y) = 2\pi\left[\sum_{\substack{i=-n/2\\ i\neq 0}}^{n/2} w_i \int_{x_1}^{x_2}\frac{x^2}{\mu_i}\frac{v_e^3 f(xv_e,\mu_i)}{x-y/\mu_i}dx + i\pi\sum_{i=1}^{n/2} w_i\frac{|y|}{y}\frac{y^2}{\mu_i^3}v_e^3 f\left(\frac{yv_e}{\mu_i},\mu_i\right)\right], \quad (30)$$

where $w_i$ and $\mu_i$ are respectively the weights and points of a $n$-points double-Gauss quadrature. In the same way, $Z$ can be formulated

$$Z(\boldsymbol{k},\omega) \simeq -\left(\frac{k_s}{k}\right)^2 Z_n\left(\frac{\omega}{kv_e}\right), \quad (31)$$

with

$$Z_n(y) = -2\pi\left[\sum_{\substack{i=-n/2\\ i\neq 0}}^{n/2} w_i \int_{x_1}^{x_2}\frac{x^2}{\mu_i}v_e^3\frac{\boldsymbol{n}\cdot\boldsymbol{\nabla}_{\boldsymbol{v}} f(xv_e,\mu_i)}{x-y/\mu_i}dx\right.$$

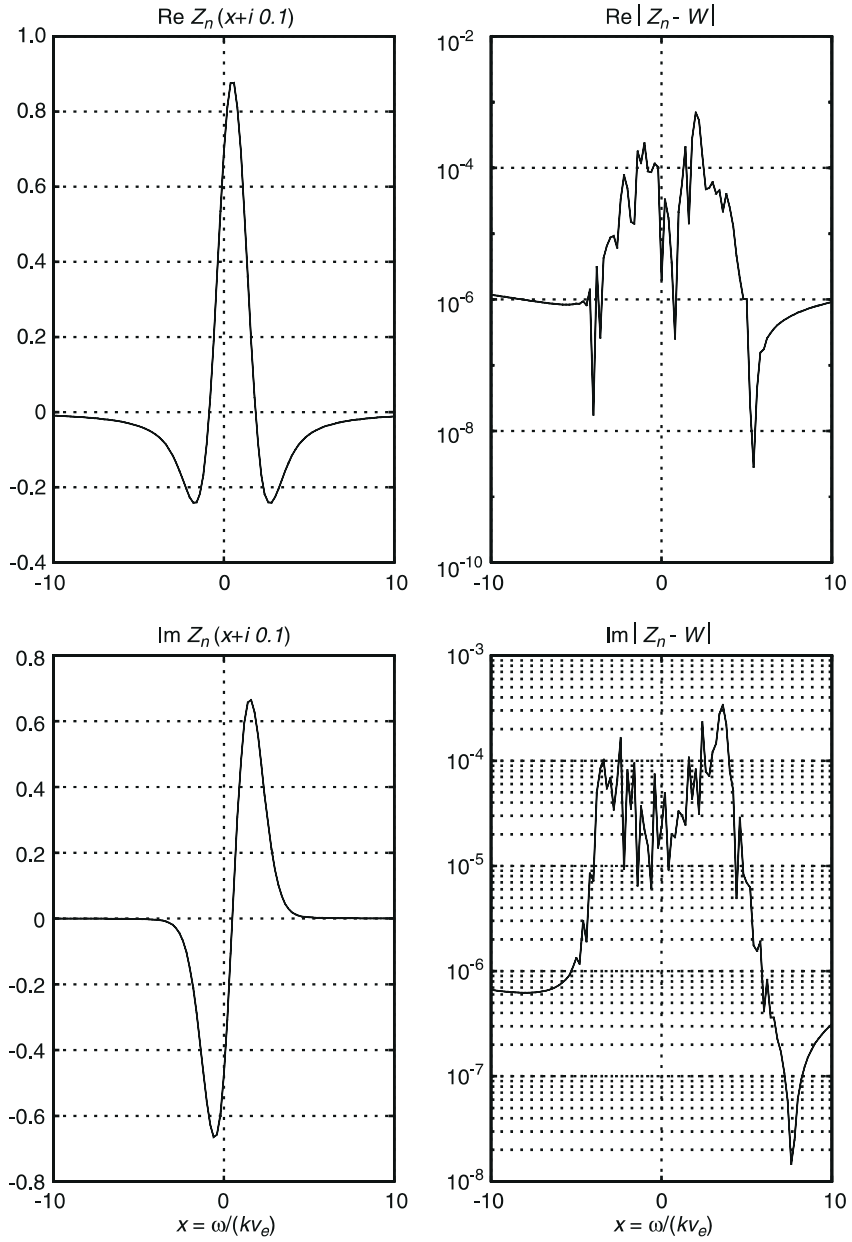


**Fig. 6.** On the left, the real and imaginary parts of the $Z_n$ function for same complex argument as in Fig. 5. On the right, their relative error with the real and imaginary parts of the $W$ function (Ichimaru, 1992). The normalized Doppler shift of the Maxwellian distribution is $x_d = 0.5$

$$+ i\pi \sum_{i=1}^{n/2} w_i \frac{|y|}{y} \frac{y^2}{\mu_i^3} v_e^3 \boldsymbol{n} \cdot \nabla_v f\left(\frac{y v_e}{\mu_i}, \mu_i\right)\Bigg], \quad (32)$$

where $\mathbf{n} = \boldsymbol{k}/k$ and

$$\boldsymbol{n} \cdot \nabla_v f(v, \mu) = \mu \frac{\partial f(v, \mu)}{\partial v} + \frac{1 - \mu^2}{v} \frac{\partial f(v, \mu)}{\partial \mu}. \quad (33)$$

When collisions are not negligible, the $P_n$ and $Z_n$ functions are modified to the following expressions

$$P_n(y + i\eta) = 2\pi \sum_{i=-n/2}^{n/2} w_i \times \int_{x_1}^{x_2} \frac{x^2}{\mu_i} v_e^3 \frac{f(x v_e, \mu_i)(x - y/\mu_i + i\eta)}{(x - y/\mu_i)^2 + \eta^2} dx, \quad (34)$$

and

$$Z_n(y + i\eta) = 2\pi \sum_{i=-n/2}^{n/2} w_i \times \int_{x_1}^{x_2} \frac{x^2}{\mu_i} v_e^3 \frac{\boldsymbol{n} \cdot \nabla_v f(x v_e, \mu_i)(x - y/\mu_i + i\eta)}{(x - y/\mu_i)^2 + \eta^2} dx, \quad (35)$$

The integral over the normalized velocity is either of Cauchy principal values type or integral of rational functions. Two different quadratures are used to calculate these integrals.

### *4.1 Test of $P_n$ and $Z_n$ on a Maxwellian*

We performed tests on the numerical evaluation of the $P_n$ and $Z_n$ functions for a Doppler-shifted two-dimensional Maxwellian distribution. The result for the $Z_n$

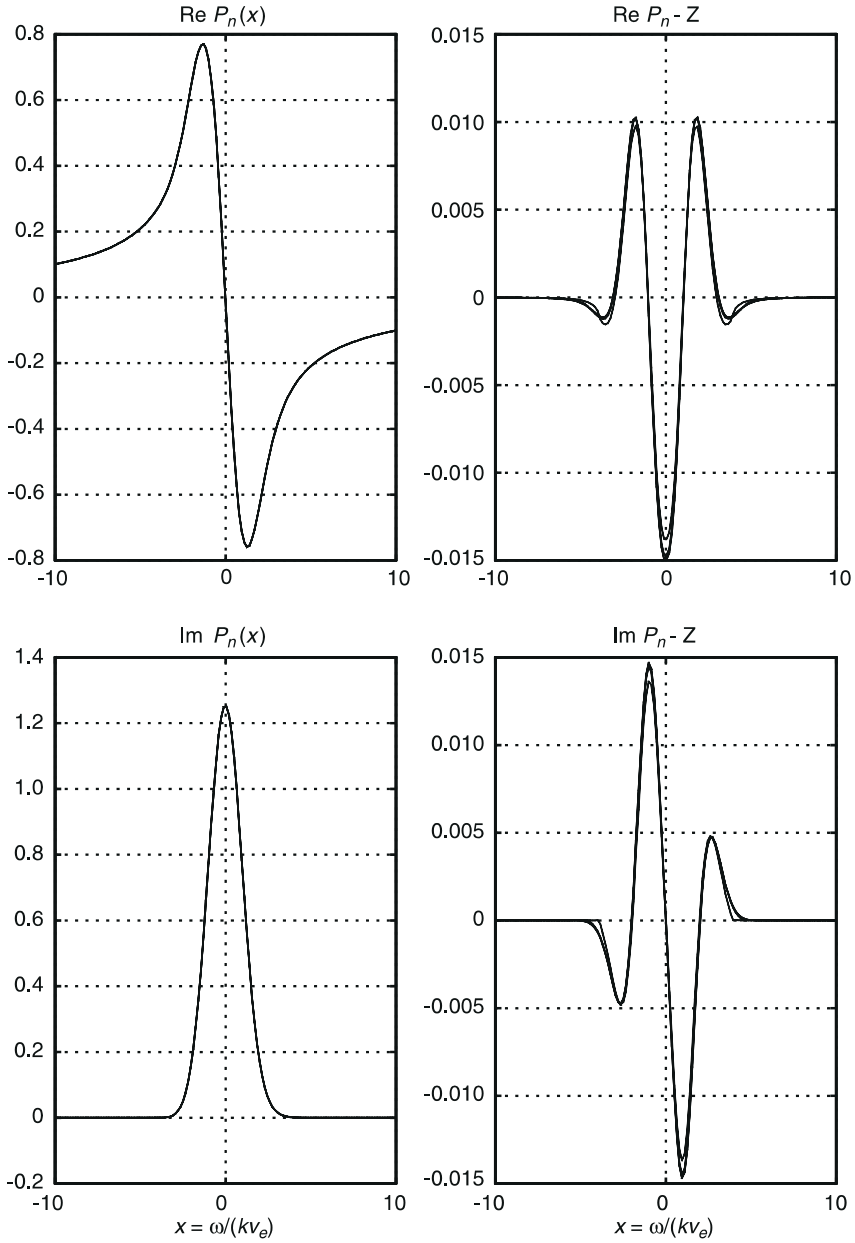


**Fig. 7.** On the left, the real and imaginary parts of $P_n$ for real argument ($\eta = 0$) and for Knudsen number $\epsilon_T = 5 \cdot 10^{-2}$ and $\epsilon_E = -3\epsilon_T\gamma_T/4\gamma_E$. On the right the difference between $P_n$ and $\mathbf{Z}(x/\sqrt{2})/\sqrt{2}$ for the four different values of $x_{\max}$ of Table 1

function is compared with the $W$ function of a reduced Doppler-shifted Maxwellian (Ichimaru, 1992). The result for the $P_n$ function is compared with $\mathbf{Z}(x/\sqrt{2})/\sqrt{2}$ where $\mathbf{Z}$ is the plasma dispersion function defined by Fried and Conte (1961).

The input for the code consists of a two-dimensional array filled with sampled data in both pitch angle and velocity. The velocity points are normalized to the mean drift velocity $v_e$. The parameters used for our test (Figs. 5 and 6) are, for the velocity space: 250 points ranging from 0 to $20v_e$. It is much more than required and it is seen that the accuracy is not improved by increasing the sampling rate, nor by taking more points in the tail of the distribution function. On the other hand, the test shows that the precision is highly dependent on the number of points in the pitch angle quadrature for the calculation in the near thermal region, i.e. for $|v| \leq 4ve$, but not too much for velocities $|v| > 4ve$.

In the thermal region, the accuracy is drastically improved by going from an eight-point double-Gauss quadrature (the relative error is about $10^{-1}$), to a 32-point quadrature where the relative error is better than $10^{-4}$. For larger velocities the accuracy is quite stable and is better than $10^{-7}$.

### *4.2 Test of $P_n$ and $Z_n$ on the Spitzer-Härm distribution*

We also performed tests on the Spitzer-Härm distribution function. We looked at the influence of the upper boundary of integration $x_{\max}$ of the $X_E$ and $X_T$ functions when evaluating $P_n$ and $Z_n$. The values of $x_{\max}$ we used are the ones listed in Table 1.

For our test we used $\epsilon_T = 5 \cdot 10^{-2}$, although the linear theory of heat conduction breaks down for such large values of $\epsilon_T$, that is these values give negative

values of the velocity distribution function (Forslund, 1970). We used the same velocity grid as for the Maxwellian distribution while we increased the number of points in the pitch angle grid to 256 points. The results are shown in Figs. 7 and 8. One can see in the real part of the difference between $Z_n$ and $W$ in Fig.8, the artifact of the discontinuity of the distribution function at $x_{\max}$. This effect is larger for the lowest value $x_{\max} = 2.8$ of the boundary i.e. $\omega/kv_e = \pm 2.8\sqrt{2}$. For larger values of $x_{\max}$ the discontinuity of the thermal distribution is pushed down at higher velocities and is attenuated due to the Maxwellian behaviour at large velocities.

### *4.3 Test of $P_n$ and $Z_n$ on the suprathermal distribution*

We used a 32-stream suprathermal calculation at an altitude of 202 km as input. The transport code calculation of the distribution function was then interpolated over a 1024 double-Gauss points. The $P_n$ and $Z_n$ functions were then computed using the distribution function evaluated on this denser $\mu$-grid. The suprathermal velocity distribution used are very much identical to the one presented in Fig. 3. When comparing with the $P_n$ and $Z_n$ functions of a Maxwellian or a Spitzer-Härm distribution, it is interesting to see how the characteristics of the distribution function are mapped on the $P_n$ and $Z_n$ shape. In order to integrate correctly the irregularities or 'spikes' corresponding to the discrete solar emission lines, we have to increase the order of the pitch angle quadrature up to 512 or even 1024 points. Increasing further the number of points in the $\mu$-grid space does not improve the results for large values of $\omega/kv_e$, i.e. above $|\omega/kv_e| > 5$. On the other hand, for $|\omega/kv_e| < 5$ the code is probably not so robust

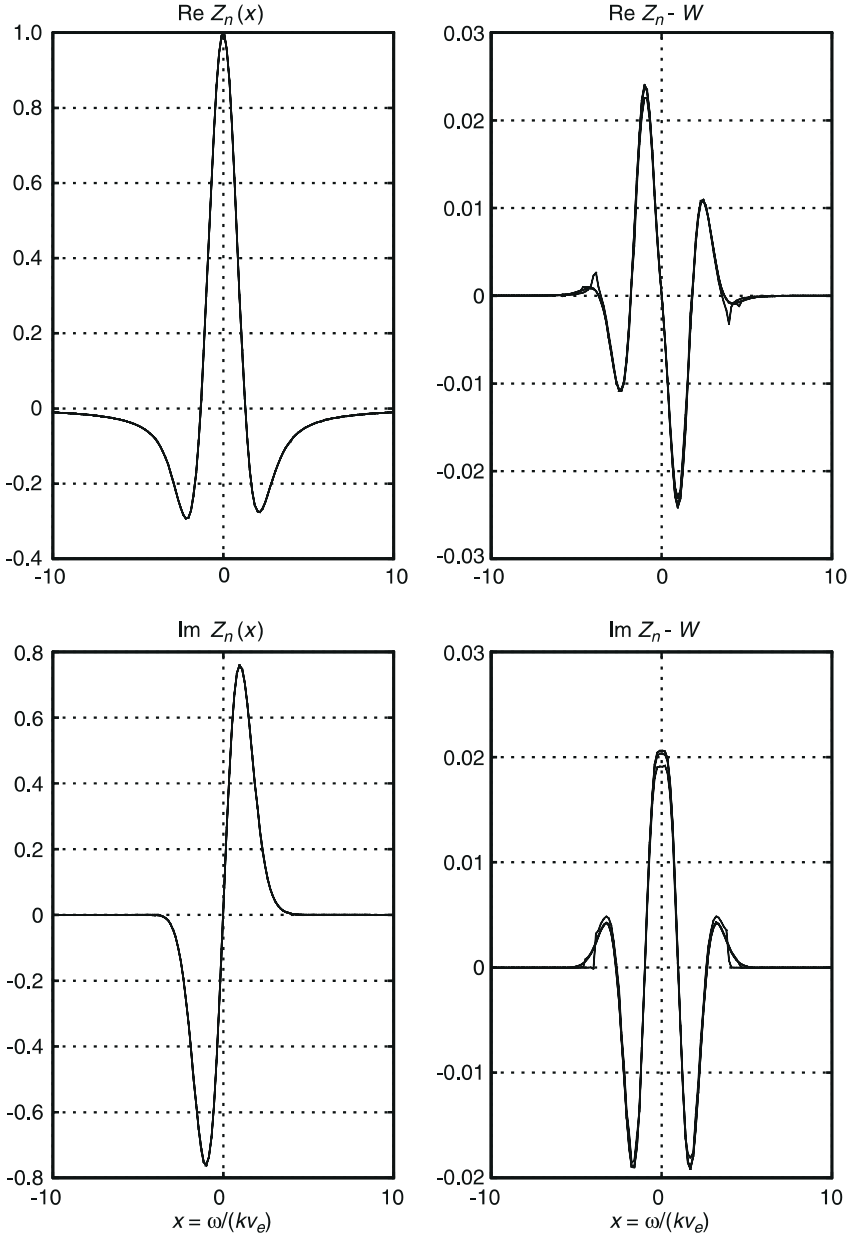


**Fig. 8.** On the left, the real and imaginary parts of $Z_n$ for real argument and for $\epsilon_T = 5 \cdot 10^{-2}$ and $\epsilon_E = -3\epsilon_T\gamma_T/4\gamma_E$. On the right the difference between $Z_n$ and $W$ for the four different values of $x_{\max}$ of Table 1

to the spikes, as can be seen in the upper left plate in Fig. 9, and further developments need to be made.

There are several remarks to be made about the $P_n$ and $Z_n$ functions. First about the imaginary part of the $P_n$ function (lower left plate in Fig. 9) which is proportional to the reduced distribution function as is seen in Eq. (28). If the distribution were isotropic the flat part around zero should be equal on both sides of zero up to the value corresponding to the minimum energy of the suprathermal distribution. The effect of the anisotropy on the reduced velocity distribution function is to create a discontinuity at zero velocity and thus introduce a zero-order skewness. Secondly, on both the real and imaginary parts of the $Z_n$ functions (right plates in Fig. 9.), one can observe the signature of the distribution function itself. In particular, the typical $N_2$ dip above 2 eV which corresponds to excitation of the vibrational levels in $N_2$ (see Fig. 2) can clearly be identified around $|\omega/kv_e| = 6.5$.

## 5 Results

We have used the two-dimensional code of the $P_n$ and $Z_n$ functions to calculate the frequency of the up- and downshifted Langmuir waves which are the high-frequency solutions of the plasma dispersion equation with the function $D(k, \omega)$ given in Eq. (18). We have performed these calculations for two different distributions, one that takes into account the deviation from the Maxwellian on the ambient part with the Spitzer-Harm distribution and the other one on the suprathermal part with the distribution calculated from the electron transport code.

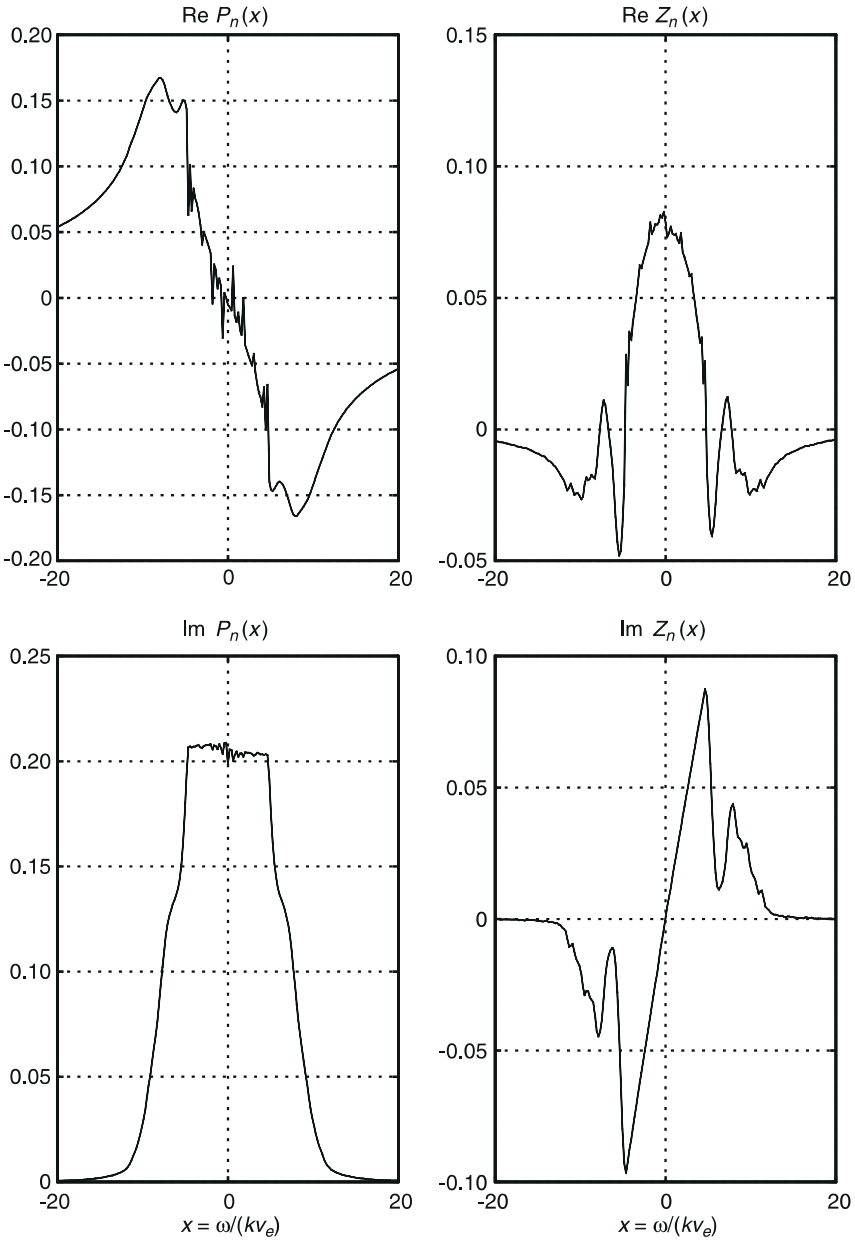


**Fig. 9.** On the left, the real and imaginary parts of $Z_n$ for real argument and on the right, the real and imaginary parts of $P_n$ for real argument of a suprathermal distribution at the altitude of 202 km. These calculations were performed using a 32-stream calculation of the transport code and the distribution function was then recalculated over 1024 double-Gauss points in order to perform the calculations of $P_n$ and $Z_n$ over this $\mu$-grid

We used the simulated data for 25 June 1994 at 14:00 UT over Tromsø assuming again an $A_p$ index of 3 and an F10.7 index of 75. The ionospheric parameters of the thermal part are shown in Fig. 10 and the velocity moments of the suprathermal distribution, as well as the moments of the Spitzer-Härm distribution, are shown in Fig. 11.

The lowest right plate in Fig. 10 shows the Knudsen number $\epsilon_T$ and $\epsilon_E$. The largest value is about $4.5\,10^{-3}$. Such values are reasonable and allow the use of the linear theory of Spitzer-Härm. The corresponding polarization electric field $E$ of $\epsilon_E$ is also of the order of the expected value i.e. under $10^{-2}\,\mu\mathrm{V\ m^{-1}}$ .

Figure 11 shows the calculated suprathermal centred velocity moments up to the third order, i.e the heat flow, for both the raw distribution as calculated by the transport code and the truncated distribution we use in our calculations and which have been processed according to the strategy described at the end of Sect. 3. The lower right plate in Fig. 11 also shows the heat flow $q_a$ of the ambient Spitzer-Härm distribution function calculated numerically and the heat flow used by Kofman *et al.* (1993) which was originally given by Banks (1966)

$$q_B = -7.710^5 T_e^{\frac{5}{2}} \nabla T_e \quad \mathrm{eV\ cm^{-2}\ s^{-1}}, \tag{36}$$

assuming a Coulomb logarithm $\log\Lambda = 15$ and $\delta_T$ calculated by Spitzer and Härm (see Table 1). We note that the heat flow given by Eq. (36) has larger values by a factor up to 1.5 than the heat flow $q_a$ we calculated. The reason for this is that the approximation given by Eq. (36) is valid for a fully ionized gas only. We have taken into account the electron-neutron collisions in the mean free

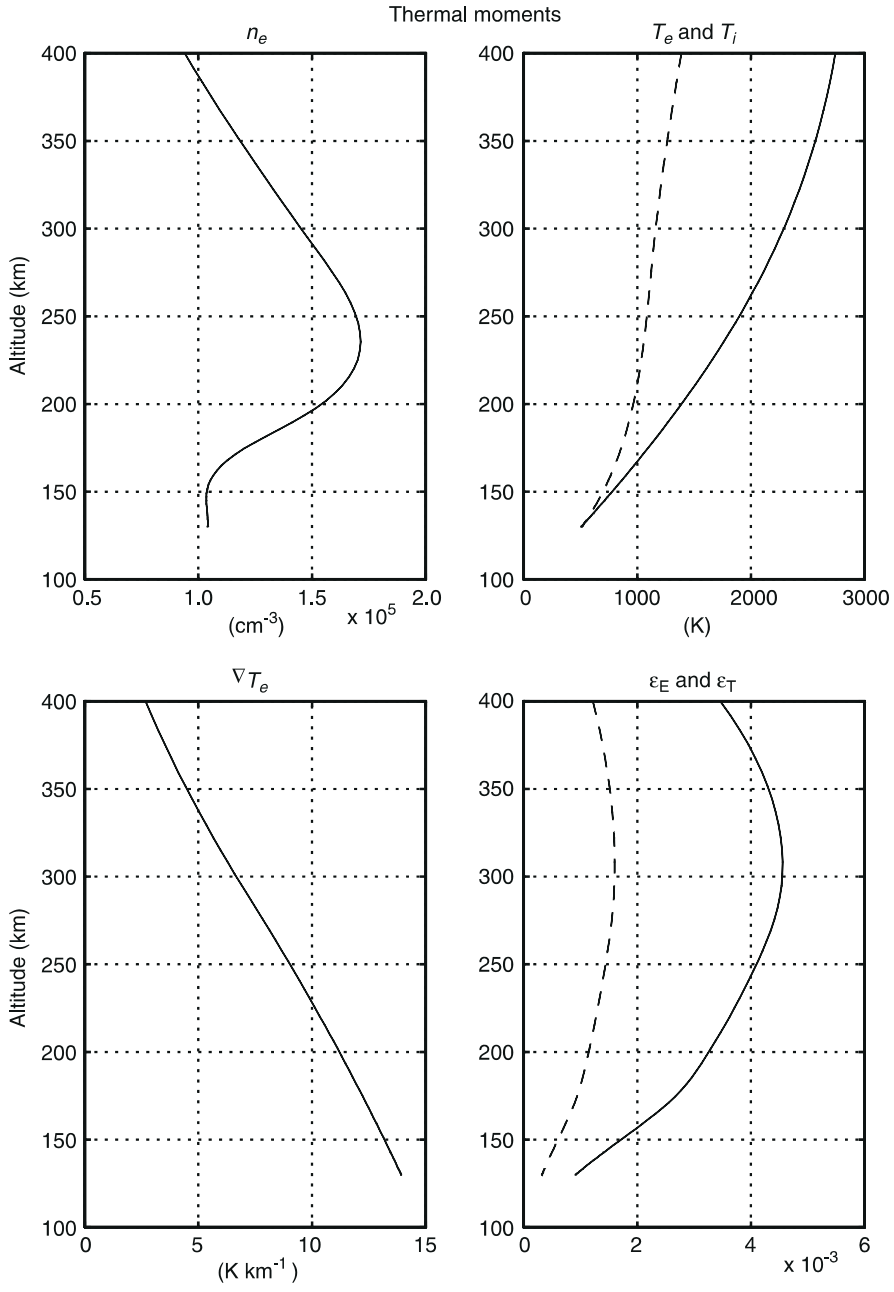


**Fig. 10.** The parameters for the ambient part of the distribution function, i.e. the electron density $n_e$, the electron and ion temperatures $T_e$ and $T_i$ (*solid line* and *dashed line*, respectively), the gradient of temperature $\nabla T_e$ and the two Knudsen numbers $\epsilon_T$ (*solid line*) and $\epsilon_E$ (*dashed line*)

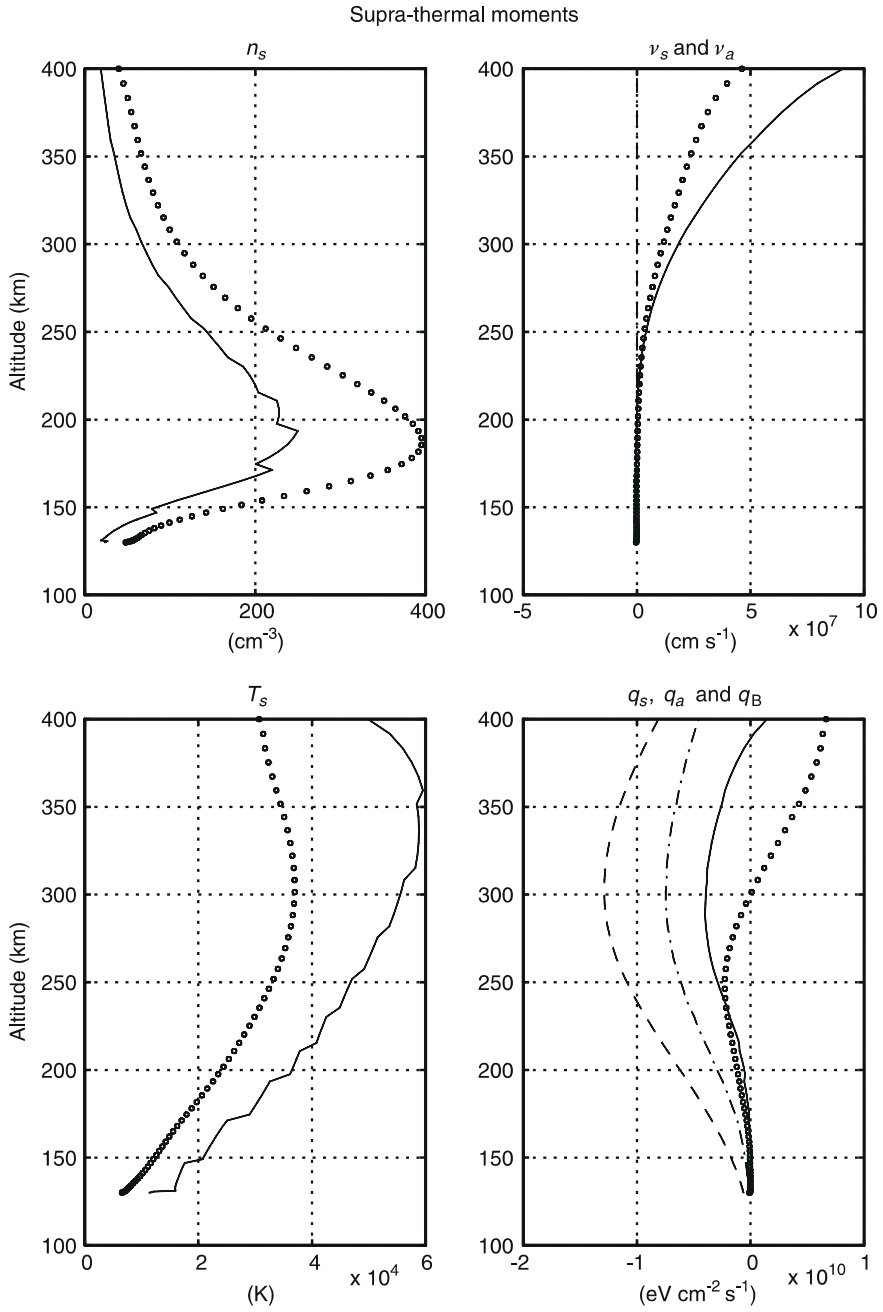


**Fig. 11.** The parameters of the suprathermal part of the distribution function and the two odd moments of the ambient (Spitzer-Härm) distribution. In all four plates, the moments of the raw suprathermal distribution function are represented by *circles* while the moments of the distribution we use for further calculations are represented by *solid lines*. In the upper right plate (mean drift velocity), the calculated mean Doppler velocity of the ambient distribution $v_a$ is represented by the *dash-dot line* and as expected is equal to zero (see Eqs. 11–13). On the lower right plate (heat flow), the calculated heat flow of the ambient distribution $q_a$ is represented by the *dash-dot line* and the *dashed line* corresponds to the heat flow $q_B$ given by Eq. (36)

path (Eq. 10) and the effect is to decrease the two Knudsen numbers and thus the net heat flow (Banks, 1966).

Figures 12 and 13 show the frequencies of the upshifted Langmuir waves of the plasma lines and the frequency difference for the three EISCAT radars: VHF (224 MHz), ESR (500 MHz) and UHF (931 MHz). Figure 12 shows the calculation for a deviation on the ambient part, i.e. the Spitzer-Härm distribution. The frequency asymmetry calculated is compared with the heat flow approximation of Eq. (9) of Kofman *et al.* (1993), Figure 13 shows the calculation in the presence of a suprathermal part and assuming that the ambient part is Maxwellian. The frequency asymmetry calculated is also compared with the results given by the heat flow approximation, assuming that the total distribution does not deviate dramatically from Maxwellian.

The best agreement between the full dispersion estimation and the heat flow approximation for the Spitzer-Härm distribution is for low-frequency radars like VHF radars. For these radars the phase velocity $v_\phi$ is between $12v_e$ and $25v_e$ as shown in Fig. 14. At such high velocities the moment approximation can be safely used, i.e. the classic expansion $(1-x)^{-1}=1+x+x^2+\cdots+x^n$ is to be valid at the third order. For the UHF radar the phase velocity $v_\phi$ is between $3v_e$ and $6v_e$ (see Fig. 14) and the approximation breaks and we note a large deviation between the two calculations. This deviation can be observed on the real part of the difference between $Z_n$ and $W$ (upper right plate in Fig. 8) and has to be compared with the asymptotic behaviour in $(\omega/kv_e)^{-5}$ that we would get by subtracting $W$ to the heat flow approximation of Eq. (9) in

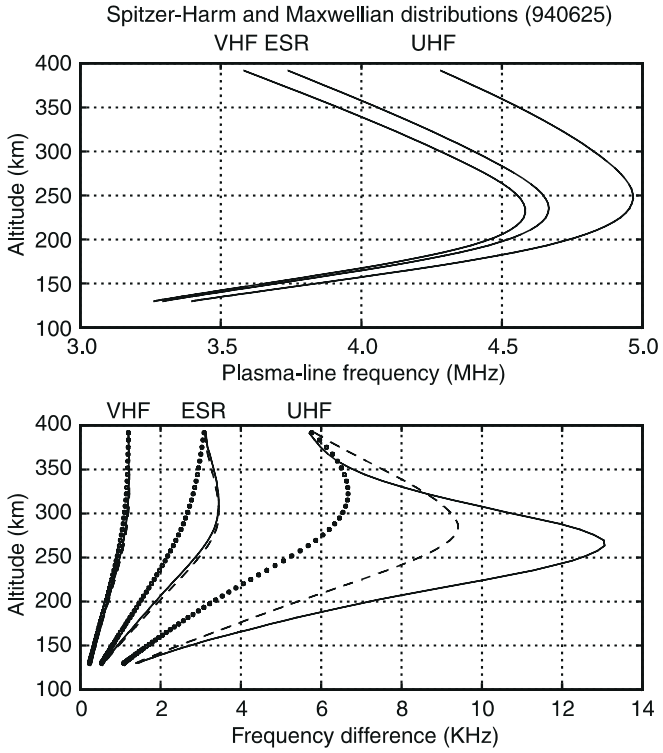


**Fig. 12.** The upper plate presents the calculated upshifted plasma frequency for the Spitzer-Härm distribution for the three different EISCAT radars. In the lower plate we present the frequency difference between up- and downshifted lines for the three radars. The Maxwellian approximation is shown with *circles*, the full two-dimensional dispersion estimation is the *solid line* and the heat flow approximation (Kofman *et al.*, 1993) is shown with the *dashed line*

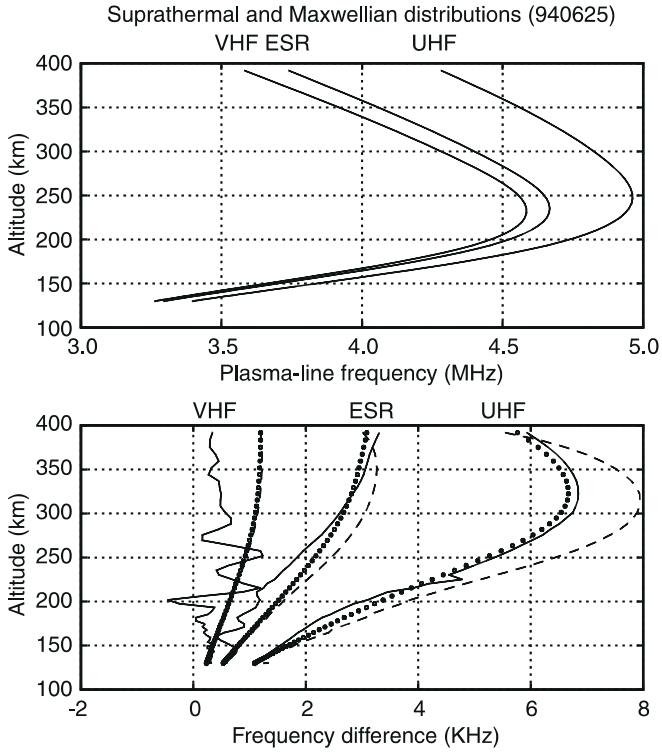


**Fig. 13.** Same plates as in Fig. 12. The compared distribution functions are a Maxwellian and a Maxwellian superposed with a suprathermal. The line codes are identical to the codes used in Fig. 12

Kofman *et al.* (1993), especially for values of $\omega/kv_e$ smaller than 5.

Another remark is about the very large asymmetry observed around 250 km, which is over 10 kHz for the full dispersion calculation. We can see that due to the behaviour of the dispersion function at $4 < \omega/kv_e < 5$, we do not need large heat flow values to observe large asymmetry between the up- and downshifted plasma line frequencies. This is very satisfying in that we do not need to invoke larger heat flow values through processes such as the electron thermal runaway (Mishin and Hagfors, 1994; Nilsson *et al.*, 1996) to explain the large deviation which were reported by Kofman *et al.* (1993), especially during 12 May 1992. On the contrary, our smaller heat flow values corrected for partially ionized plasma are in good agreement with the theory of Schunk and Walker (1970) and Banks (1966) and are able to create frequency asymmetry of the order of that observed by Kofman *et al.* (1993).

In the presence of a suprathermal distribution we can make the following remarks. For UHF radars, i.e. at phase velocity $v_\phi$ between $3v_e$ and $6v_e$, we note that the full dispersion calculation gives similar results as the Maxwellian approximation while the heat flow approximation gives larger deviation. In order to understand the small effect of the suprathermal distribution for high-frequency radars, we note that the real part of $Z_n$ of the thermal distribution (Fig. 6) has much larger amplitude than the one of the suprathermal distribution (Fig. 9) at the considered phase velocity. At large phase velocities $v_\phi$, i.e. for VHF radars, the thermal $Z_n$ is very small, whereas the one of the suprathermal is still not negligible. This is seen clearly when comparing the mean width of the real part of $Z_n$ in Fig. 6 and the real part of $Z_n$ in Fig. 9. Thus the effect of the suprathermal is important and should be taken into account. Another remark to be made is that if all the fine structures observed on the suprathermal $Z_n$ in Fig. 9 in the region $|\omega/k| < 6v_e$ are real and not artifacts of our calculations, they should map on the frequency asymmetry as it appears in Fig. 13.

## 6 Conclusion

We developed and tested a computer code to calculate the plasma dispersion function and the reduced distribution function for any arbitrary distribution function given in two dimensions: velocity and pitch angle. This code has been applied for two types of electron velocity distribution deviating from the Maxwellian distribution, one in the ambient part through a temperature gradient and the other one assuming the presence of a suprathermal electron population.

We used the code to estimate the frequency asymmetry between the up- and downshifted plasma lines which can be observed by incoherent-scatter radar technique. For high-frequency radars such as UHF radars we showed that the frequency asymmetry between the plasma lines is mostly due to a deviation from the Maxwellian in the ambient part of the electron

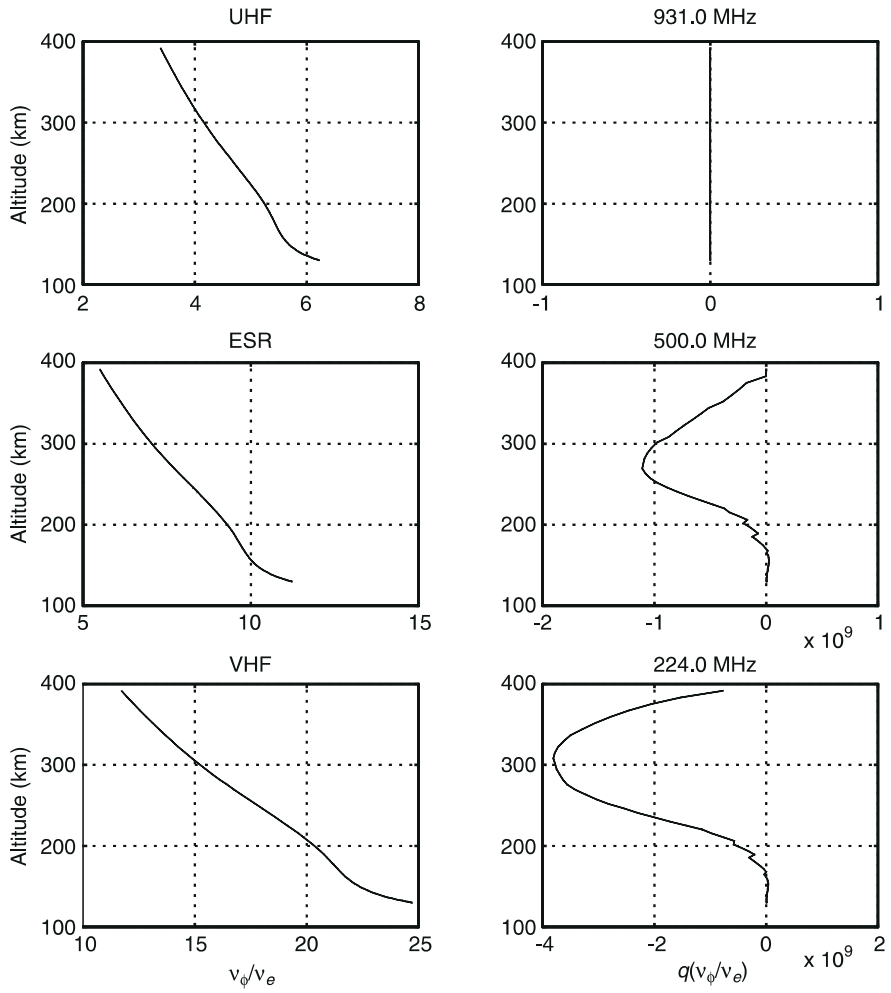


**Fig. 14.** In the left plates, the ratio $v_\phi/v_e$ where $v_\phi$ is the phase velocity of the Langmuir wave for the three different radars (from top to bottom UHF, ESR and VHF). In the right plates, the integrated heat flux up to the phase velocity $v_\phi$

distribution. On the other hand, for low-frequency radars such as VHF radars the Doppler frequency of the plasma lines is more influenced by the presence of a suprathermal electron population.

We also pointed out a discrepancy between the full estimation of the plasma dispersion function and the heat flow approximation for waves with phase velocity such that the moment expansion is not valid. The discrepancy is in the right direction and allows to explain large Doppler asymmetry of the plasma lines without need to increase the value of the heat flow. An analytic model of a distribution deviating from the Maxwellian distribution would be a very useful tool to study the difference between the exact calculation and the moment approximation of the plasma dispersion function.

*Acknowledgements.* The authors want to thank one of the referees for his very valuable remarks on the discussion of the results. This work was supported by the Norwegian Research Council (NFR). Topical Editor D. Alcaydé thanks J.-P. St.-Maurice and E.V. Mishin for their help in evaluating this paper.

## References

**Ashihara, O., and K. Takayanagi,** Velocity distribution of ionospheric low-energy electrons, *Planet. Space Sci.*, **22,** 1201–1217, 1974.

**Banks, P. M.,** Charged particle temperatures and electron thermal conductivity in the upper atmosphere, *Ann. Geophys.*, **22,** 577–587, 1966.

**Bauer, P., K. D. Cole, and G. Lejeune**, Field-aligned electric currents and their measurement by the incoherent backscatter technique, *Planet. Space Sci.*, **24,** 479–485, 1976.

**Bilitza D.**, *International reference ionosphere 1990*. National Space Science Data center/ World Data Center-A for Rockets and Satellites, 1990.

**Bjørnå, N., and J. Trulsen,** Effect of a power law particle flux on the ionospheric incoherent scattering cross section, *Phys. Scr.*, **33,** 284–288, 1986.

**Cohen, R. S., L. Spitzer Jr, and P. McRoutly,** The electrical conductivity of an ionized gas, *Phys. Rev.*, **80,** 230–238, 1950.

**Forslund, D. W.,** Instabilities associated with heat conduction in the solar wind and their consequences, *J. Geophys. Res.*, **75,** 17–28, 1970.

**Fried, B. D., and S. D. Conte,** *The plasma dispersion function: the Hilbert transform of the Gaussian*, Academic Press, New York, 1961.

**Gombosi, T. I., and C. E. Rasmussen,** Transport of gyration-dominated space plasmas of thermal origin. 1. Generalized transport equations, *J. Geophys. Res.*, **96,** 7759–7778, 1991.

**Gray, D. R., and J. D. Kilkenny,** The measurement of ion acoustic turbulence and reduced thermal conductivity caused by a large temperature gradient in a laser-heated plasma. *Plasma Phys.*, **22,** 81–111, 1980.

**Ichimaru, S.,** *Statistical plasma physics*, Vol. 1, Addison-Wesley, Redwood City, 1992.

**Jasperse, J. R.,** Boltzmann-Fokker-Planck model for the electron distribution function in the Earth's ionosphere, *Planet. Space Sci.*, **24**, 33–40, 1976.

**Kofman, W., J.-P. St-Maurice and A. P. van Eyken,** Heat flow effect on the plasma line frequency, *J. Geophys. Res.*, **98,** 6079–6085, 1993.

**Krinberg, I. A.,** Description of the photoelectron interaction with ambient electrons in the ionosphere, *Planet. Space Sci.*, **21,** 523–525, 1973.

**Krinberg, I. A., and L. A. Akatova,** Electron distribution function in the lower ionosphere and its relation with the rate of production and heating of electrons, *Geomagn. Aeron.*, **18,** 411–415, 1978.

**Lilensten, J., W. Kofman, J. Wisenberg, E. S. Oran and C. R. Devore,** Ionization efficiency due to primary and secondary photoelectrons: a numerical model, *Ann. Geophys.*, **7,** 83–90, 1989.

**Ljepojevic, N. N., and P. MacNeice,** Heat flux in a non-Maxwellian plasma, *Phys. Rev.*, **A 40,** 981–986, 1989.

**Lummerzheim, D., and J. Lilensten,** Electron transport and energy degradation in the ionosphere: evaluation of the numerical solution, comparison with laboratory experiments, auroral observations, *Ann. Geophysicae*, **12,** 1039–1051, 1994.

**Min, Q.-L., D. Lummerzheim, M. H. Rees, and K. Stamnes,** Effects of a parallel electric field and the geomagnetic field in the topside ionosphere on auroral and photoelectron energy distributions, *J. Geophys. Res.*, **98,** 19223–19234, 1993.

**Mishin, E. and T. Hagfors,** On heat flow contribution to plasma line frequency in the F-region, *J. Geophys. Res.*, **99,** 6537–6539, 1994.

**Nilsson, H., S. Kirkwood, and N. Bjørnå,** Bistatic measurements of incoherent-scatter plasma lines, *J. Atmos. Terr. Phys.*, **58,** 175–187, 1996.

**Schunk, R. W., and J. C. G. Walker,** Transport properties of the ionospheric electron gas, *Planet. Space Sci.*, **18,** 1535–1550, 1970.

**Sheffield, J.,** *Plasma scattering of electromagnetic radiation*. Academic Press, New York, 1975.

**Shkarofsky, I. P.,** Values of the transport coefficients in a plasma for any degree of, ionization based on a Maxwellian distribution, *Can. J. Phys.*, **39,** 1619–1668, 1961.

**Showen, R. L.,** The spectral measurement of plasma lines, *Radio Sci.*, **14,** 503–508, 1979.

**Spitzer, L. Jr and R. Härm,** Transport phenomena in a completely ionized gas, *Phys. Rev.*, **89,** 977–981, 1953.

**Stamnes, K., and M. H. Rees,** Inelastic scattering effects on photoelectron spectra and ionospheric electron temperature, *J. Geophys. Res.*, **88,** 6301–6309, 1983.

**Stamnes, K., S.-C. Tsay, W. Wiscombe, and K. Jayaweera,** Numerically stable algorithm for discrete-ordinate-method radiative transfer in multiple scattering and emitting layered media, *Appl Opt.*, **27,** 2502–2509, 1988.

**Vidal-Madjar, D., W. Kofman, and G. Lejeune,** Mesures de la raie de plasma par diffusion incohérente à Nançay, et premiers résultats morphologiques, *Ann. Geophys.*, **31,** 227–234, 1975.

**Woods L. C.**, *An introduction to the kinetic theory of gases and magnetoplasmas*. Oxford Science Publications, New York, 1993.

# ARTICLE III

**Ann. Geophysicae manuscript No.**
(will be inserted by the editor)

# A simple model for the velocity distribution of particles in a plasma with temperature gradient

**P. Guio**

The Auroral Observatory, Institute of Physics, University of Troms, N-9037 Troms, Norway, Fax: +47 77 64 62 80

21 September 1998

**Abstract.** In a plasma with a temperature gradient, the particle velocity distribution function deviates from the Maxwellian. A new simple analytic model for such a plasma, the two-temperature Maxwellian is introduced, hereafter referred to as the 2-$T$ Maxwellian, and not to be mistaken for the purely anisotropic bi-Maxwellian with parallel and perpendicular temperatures for a magnetised plasma. The velocity moments of the 2-$T$ Maxwellian are presented and compared with the moments from the classical transport theory of Spitzer. Furthermore a closed form of the dielectric response function for the 2-$T$ Maxwellian is derived. The dielectric response function is used to calculate the Doppler frequency of the plasma lines in an incoherent scatter experiment. The result is compared with the Doppler frequency given by the heat flow approximation of the dispersion relation. While a good qualitative agreement is seen between the heat flow approximation and the exact estimation of the dielectric response, it is shown that for accurate calculation of the Doppler frequency of the plasma lines an exact estimation of the dielectric response is important, especially for plasma lines observation corresponding to Langmuir waves with large wave vector and small resonance frequency.

**Key words.** Non-Maxwellian electron velocity distribution · Temperature gradient

## 1 Introduction

It is interesting in several contexts to take into account the local gradient of temperature in the velocity distribution function of particles in a plasma. Forslund (1970) and Singer (1977) used the theory developed by Spitzer and Härm (1953) while Lundin *et al.* (1996) used a linear combination of three Maxwellians to simulate a velocity distribution function that reproduces the downward flow of a thermal component in order to study instabilities due to heat conduction in a moderately inhomogeneous plasma. Kofman *et al.* (1993) and Guio *et al.* (1998) studied the dispersion relation for Langmuir waves in a plasma in the presence of a temperature gradient in the frame of plasma lines observation using the incoherent scatter technique. Implicitly associated with the heat conduction is a skewing of the particle velocity distribution function. This skewing has been directly observed by satellite measurements (Hundhausen, 1968) or inferred through heat flow estimation using incoherent scatter measurements (Blelly and Alcaydé, 1994). Theoretically Cohen *et al.* (1950) and Spitzer and Härm (1953) solved directly a kinetic equation. The solution of this kinetic equation, the Spitzer function, is restricted only to velocities not larger than a few times the thermal velocity of the electron population, introducing a discontinuity in the distribution function (Guio *et al.*, 1998). Moreover the kinetic equation presents the inconvenience to be numerically unstable.

In this paper, it is first described the two-dimensional inhomogeneous and anisotropic 2-$T$ Maxwellian. Expressions for the velocity moments of the 2-$T$ Maxwellian are given and compared with the moments given by the Spitzer theory. In the second part, a closed form for the dielectric response function associated to this distribution function is described. In the third part, the dielectric response function is used in the frame of incoherent scatter plasma line. The plasma lines are a pair of spectral lines produced by scattering of a radio wave by Langmuir waves of the ionospheric plasma. They are Doppler shifted up and down with respect to the transmitted frequency by an amount that corresponds to two waves travelling towards and away from the transmitter. By measuring the Doppler frequency of these spectral lines, one would be able to infer the mean Doppler velocity of the electrons by solving the dispersion relation with the dielectric response function associated to the electron velocity distribution (Bauer *et al.*, 1976; Showen, 1979) and in theory to estimate the ionospheric field-aligned current when combined with parameters obtained from the incoherent scatter ion line. A deviation of the velocity distribution function from the Maxwellian modifies the dispersion relation and thus the estimated mean Doppler velocity of the electron population. We apply the 2-$T$ Maxwellian to the estimation of the Doppler frequency of plasma lines in a plasma with temperature gradient and compare the result with the heat flow approximation of Kofman *et al.* (1993) which takes into account a temperature gradient through a corrective heat flow term. Finally, we discuss the results of our simulation.

*Correspondence to*: P. Guio
e-mail: patrick@phys.uit.no

## 2 The 2-$T$ Maxwellian

The 2-$T$ Maxwellian, denoted $f_{T_\pm}$, is defined as two half-Maxwellians with temperature $T_+$ and $T_-$ over the two half-spaces where, respectively $v_\parallel < 0$ and $v_\parallel \geq 0$ and a Maxwellian with temperature $T_\perp$ over the perpendicular velocity space $v_\perp$. The two half-Maxwellians along $v_\parallel$ are joined continuously at $v_\parallel = 0$ and are normalised such that the integral over the velocity space is equal to the particle density $n$. Thus the 2-$T$ Maxwellian can be seen as a modified bi-Maxwellian with a temperature inhomogeneity along the parallel velocity $v_\parallel$. The 2-$T$ Maxwellian is written

$$f_{T_\pm}(v_\parallel, v_\perp) = \begin{cases} \frac{n}{(2\pi)^{\frac{3}{2}}} \frac{1}{\theta_\parallel \theta_\perp^2} \exp - \left( \frac{v_\parallel^2}{2\theta_-^2} + \frac{v_\perp^2}{2\theta_\perp^2} \right), & v_\parallel \geq 0 \\ \frac{n}{(2\pi)^{\frac{3}{2}}} \frac{1}{\theta_\parallel \theta_\perp^2} \exp - \left( \frac{v_\parallel^2}{2\theta_+^2} + \frac{v_\perp^2}{2\theta_\perp^2} \right), & v_\parallel < 0 \end{cases} \quad (1)$$

where $\theta_\perp^2 = T_\perp/m$ is the square of the thermal velocity along the perpendicular direction, $\theta_\pm^2 = T_\pm/m$ are the square of the mean velocities in the parallel direction, $\theta_\parallel = (\theta_+ + \theta_-)/2$ is the normalisation constant such that the two half-Maxwellians are continuous at $v_\parallel = 0$ and $m$ represents the particle mass.

This velocity distribution function is both inhomogeneous and anisotropic and sketches the velocity distribution of particle at the particular point of space $r = 0$ between two regions of different temperature. Figure 1 shows the 2-$T$ Maxwellian between these two regions, and the two bi-Maxwellians with hot temperature $T_+$ (at $r > 0$) and cold temperature $T_-$ (at $r < 0$). This model mimics the situation where the hot plasma of temperature $T_+$ is diffusing toward the region of cold plasma of temperature $T_-$ and vice-versa.

The velocity moments of a species distribution function $f$ are expressed in the following way (Barakat and Schunk, 1982)

$$n\boldsymbol{u} = \langle \boldsymbol{v} \rangle, \quad (2)$$

$$\frac{3}{2} nT = \frac{1}{2} m \langle |\boldsymbol{v} - \boldsymbol{u}|^2 \rangle, \quad (3)$$

$$\frac{1}{2} nT_\parallel = \frac{1}{2} m \langle (v_\parallel - u_\parallel)^2 \rangle, \quad (4)$$

$$\frac{2}{2} nT_\perp = \frac{1}{2} m \langle (v_\perp - u_\perp)^2 \rangle, \quad (5)$$

$$\boldsymbol{q} = \frac{1}{2} m \langle |\boldsymbol{v} - \boldsymbol{u}|^2 (\boldsymbol{v} - \boldsymbol{u}) \rangle, \quad (6)$$

$$\boldsymbol{q}^\parallel = m \langle (v_\parallel - u_\parallel)^2 (\boldsymbol{v} - \boldsymbol{u}) \rangle, \quad (7)$$

$$\boldsymbol{q}^\perp = \frac{1}{2} m \langle (v_\perp - u_\perp)^2 (\boldsymbol{v} - \boldsymbol{u}) \rangle. \quad (8)$$

where the angle brackets denote the average

$$\langle \mathrm{A} \rangle = \int \mathrm{A} f(\boldsymbol{v}) d\boldsymbol{v} \quad (9)$$

Because of the symmetry around $v_\parallel$ of the 2-$T$ Maxwellian, the Doppler velocity $\boldsymbol{u}$, the heat flow $\boldsymbol{q}$, the heat flow for parallel energy $\boldsymbol{q}^\parallel$ and the heat flow for perpendicular energy $\boldsymbol{q}^\perp$ are parallel to the $v_\parallel$-axis and have components $u_\parallel$, $q_\parallel$, $q_\parallel^\parallel$ and $q_\parallel^\perp$ respectively and are given by

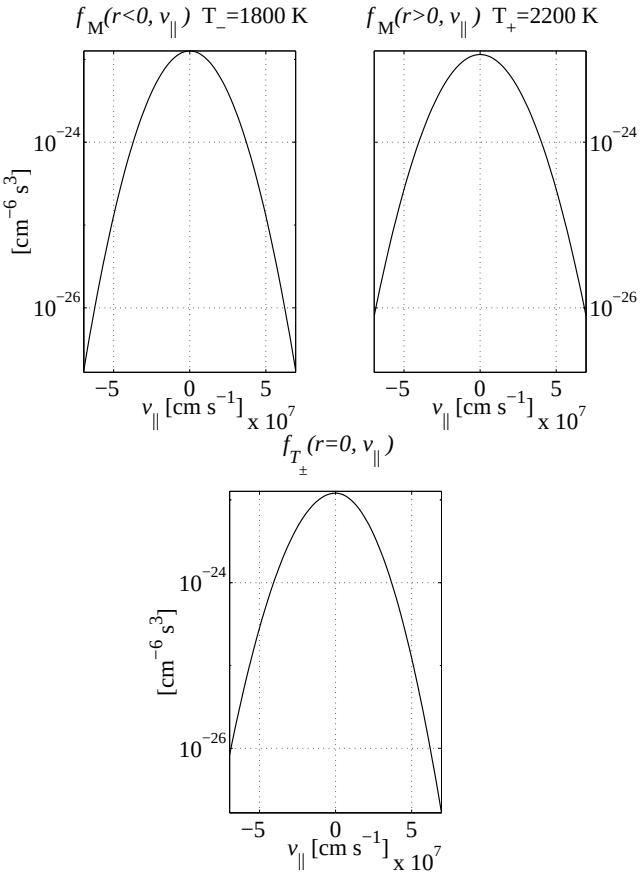


**Fig. 1.** The 2-$T$ Maxwellian with $T_- = 1800\,\mathrm{K}$ and $T_+ = 2200\,\mathrm{K}$ (*lower* plate) and the two bi-Maxwellians of the cold region (*upper left* plate) and the hot region (*upper right* plate) plotted as a function of $v_\parallel$ and for $v_\perp = 0$. The perpendicular temperature of the 2-$T$ Maxwellian and the two bi-Maxwellian was taken to be $T_\perp = 2000\,\mathrm{K}$

$$u_\parallel = -\frac{1}{\sqrt{2\pi}} \frac{\theta_+^2 - \theta_-^2}{\theta_\parallel} = -\frac{1}{\sqrt{2\pi}} \frac{1}{m\theta_\parallel} \delta T_\pm, \quad (10)$$

$$\frac{3T}{2} = \frac{1}{2} m \left( \frac{\theta_+^3 + \theta_-^3}{2\theta_\parallel} + 2\theta_\perp^2 \right) - \frac{1}{2} m u_\parallel^2 \quad (11)$$

$$T_\parallel = m \frac{\theta_+^3 + \theta_-^3}{2\theta_\parallel} - m u_\parallel^2, \quad (12)$$

$$T_\perp = m\theta_\perp^2, \quad (13)$$

$$q_\parallel = -\frac{n}{\sqrt{2\pi}} \frac{\theta_+^2 + \theta_-^2}{\theta_\parallel} \delta T_\pm - \frac{3}{2} n T_\parallel u_\parallel - \frac{1}{2} m n u_\parallel^3, \quad (14)$$

$$q_\parallel^\parallel = -\frac{2n}{\sqrt{2\pi}} \frac{\theta_+^2 + \theta_-^2}{\theta_\parallel} \delta T_\pm - 3 n T_\parallel u_\parallel - m n u_\parallel^3, \quad (15)$$

$$q_\parallel^\perp = 0, \quad (16)$$

where $\delta T_\pm$ represents the difference between the temperatures of the hot and the cold region $\delta T_\pm = T_+ - T_-$.

Assuming the plasma to be an electron gas, the velocity moments of the 2-$T$ Maxwellian can be compared with the velocity moments of the Spitzer distribution with elec-

tron temperature $T_e$, thermal velocity denoted $\theta_e$ and Knudsen number $\epsilon_T = 2\lambda_e \nabla T_e / T_e$ where $\lambda_e$ is the electron mean free path. The Knudsen number represents the ratio of the microscopic length scale $\lambda_e$ to the macroscopic length scale $T_e/\nabla T_e$ (Guio *et al.*, 1998). The velocity moments of the Spitzer distribution are written

$$u_\parallel = -\frac{6}{\sqrt{2\pi}}\theta_e \gamma_T \epsilon_T, \tag{17}$$

$$\frac{3T}{2} = \frac{1}{2}m_e(\theta_e^2 + 2\theta_e^2) - \frac{1}{2}m_e u_\parallel^2, \tag{18}$$

$$T_\parallel = m_e\theta_e^2 - m_e u_\parallel^2, \tag{19}$$

$$T_\perp = m_e\theta_e^2, \tag{20}$$

$$q_\parallel = -\frac{40n}{\sqrt{2\pi}}\theta_e^3 \delta_T \epsilon_T - \frac{5}{2}nTu_\parallel + \frac{1}{6}m_e n u_\parallel^3, \tag{21}$$

$$q_\parallel^\parallel = -\frac{48n}{\sqrt{2\pi}}\theta_e^3 \delta_T \epsilon_T - 3nTu_\parallel + m_e n u_\parallel^3, \tag{22}$$

$$q_\parallel^\perp = -\frac{16n}{\sqrt{2\pi}}\theta_e^3 \delta_T \epsilon_T - nTu_\parallel - \frac{1}{3}m_e n u_\parallel^3, \tag{23}$$

where $\gamma_T$ and $\delta_T$ are the normalised transport coefficients defined in Spitzer and Härm (1953).

There is a formal analogy between Eqs. (10)–(15) and Eqs. (17)–(22). It can be pointed out how the temperature difference $\delta T_\pm$ mimics $\nabla T_e$ which appears in the Knudsen number $\epsilon_T$. The temperature difference $\delta T_\pm$ can be thought as a temperature gradient between the two regions of different temperatures, and thus the Doppler velocity can be interpreted as a thermal diffusion process while the heat flow can be seen as a thermal conductivity process (Banks, 1966).

It is possible, for any value of the electron density $n_e$ and the electron temperature $T_e$, to determine values of $T_+$ and $T_-$ in order to get identical heat flow $q_\parallel$ for the 2-$T$ Maxwellian and the Spitzer distribution function and at the same time keeping the respective temperatures $T$ equal. The first term in the heat flow $q_\parallel$ of Eqs. (14) and (21) represents the thermal heat flow without Doppler velocity, we therefore require that these two terms should be equal. Moreover, if we take $\theta_\perp$ equal to $\theta_e$, we just have to require that the first term of the parallel temperature $T_\parallel$ of Eqs. (12) and (19) should be equal. The temperatures $T_-$ and $T_+$ are then uniquely determined by solving the following system of equations:

$$\begin{cases} (x-y)(x^2+y^2) & = 20\delta_T\epsilon_T \\ (x^3+y^3) & -(x+y) = 0 \end{cases} \tag{24}$$

where $T_+ = x^2 T_e$ and $T_- = y^2 T_e$. $(x, y)$ are the real solutions of Eqs. (24) such that $x > 1$ and $y < 1$. The first equation represents the condition on the first term of the heat flow and the second equation is the condition on the temperature. If we want the heat flows for parallel energy $q_\parallel^\parallel$ to be equal instead (as we will require in the last section) we simply replace the right hand side term of the first equation $20\delta_T\epsilon_T$ by $12\delta_T\epsilon_T$.

Figure 2 shows the parameters $u_\parallel$, $T$ and $q_\parallel$ for the 2-$T$ Maxwellian and the Spitzer distribution. The heat flow $q_\parallel$ of the two distribution functions will be equal by shifting the parallel velocity $v_\parallel$ of the distribution functions by a Doppler velocity of the same values as the one of the upper left plate of Figure 2 but of opposite sign. Note however that while

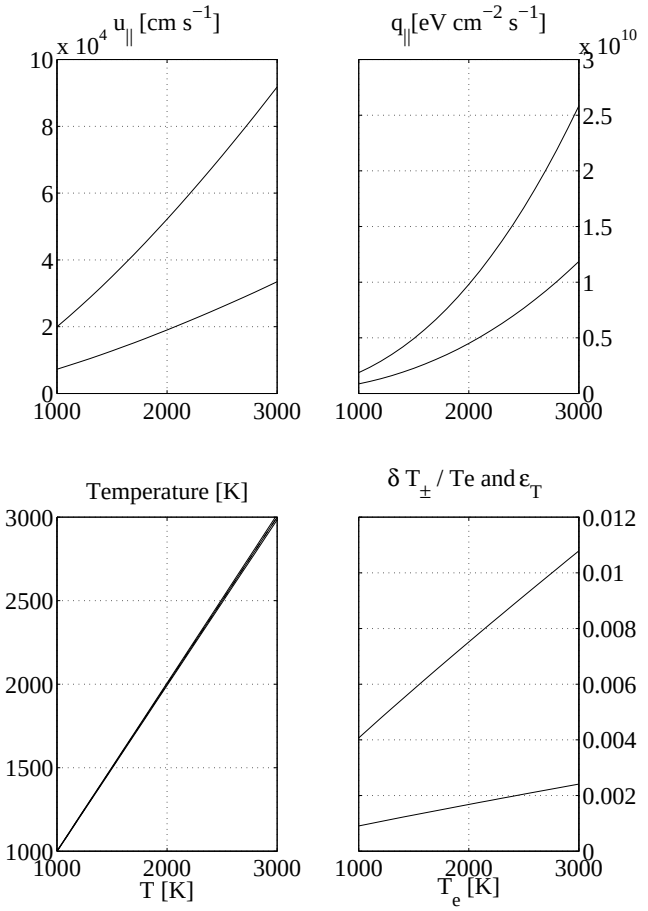


**Fig. 2.** The mean Doppler velocity $u_\parallel$ (upper left plate), temperatures $T$ (lower left plate) and heat flow $q_\parallel$ (upper right plate) of Eqs. (10)–(14) (*thick* line) and Eqs. (17)–(21) (*thin* line) as a function of the electron temperature $T_e$ and for an electron density $n_e = 10^6\ \mathrm{cm}^{-3}$ and an electron temperature gradient $\nabla T_e = 5\ \mathrm{K\,km}^{-1}$. The lower right plate shows the corresponding Knudsen number $\epsilon_T$ (*thin* line) and the ratio $\delta T_\pm / T$ (*thick* line)

the heat flows $q_\parallel$ will be equal, the heat flow of parallel energy $q_\parallel^\parallel$ will remain different since the anisotropy factor $\rho_e = q_\parallel^\parallel / q_\parallel^\perp$ for the 2-$T$ Maxwellian is different from the one of the Spitzer function. In the Spitzer theory, $\rho_e = 3$ while for the 2-$T$ Maxwellian $\rho_e = \infty$, which clearly means that for the 2-$T$ Maxwellian, the energy is only transported along the direction of the temperature gradient.

## 3 Dielectric response function

To calculate the dielectric response function of an unmagnetised and non-collisional plasma, the following integral of the normalised velocity probability distribution needs to be calculated

$$I_f(\boldsymbol{k}, \omega) = -\int \frac{\boldsymbol{k}\cdot\boldsymbol{\nabla}_{\boldsymbol{v}} f(\boldsymbol{v})}{\boldsymbol{k}\cdot\boldsymbol{v} - \omega} d^3\boldsymbol{v}. \tag{25}$$

In the geometry of a wave vector $\boldsymbol{k}$ parallel to the $v_\parallel$-axis oriented toward the cold region and in the convention that a

positive velocity $v_\parallel$ gives a positive Doppler frequency, the temperatures are swapped. Then the integration over $v_\perp$ is carried out independently and we define the one-dimensional reduced 2-$T$ Maxwellian $F_{T_\pm}$ by

$$F_{T_\pm}(v_\parallel) = \begin{cases} \frac{1}{\sqrt{2\pi}}\frac{1}{\theta_\parallel}\exp\left(-\frac{v_\parallel^2}{2\theta_+^2}\right), & v_\parallel \geq 0 \\ \frac{1}{\sqrt{2\pi}}\frac{1}{\theta_\parallel}\exp\left(-\frac{v_\parallel^2}{2\theta_-^2}\right), & v_\parallel < 0 \end{cases} \tag{26}$$

The integral $I_{f_{T_\pm}}(\boldsymbol{k},\omega)$ is then written as a one-dimensional integral function of the derivative of the reduced 2-$T$ Maxwellian $F_{T_\pm}^{'}$

$$I_{f_{T_\pm}}(k,\omega) = -\int_{-\infty}^{\infty}\frac{kF_{T_\pm}^{'}(v_\parallel)}{kv_\parallel-\omega}dv_\parallel \tag{27}$$

This integral has the following analytic form

$$I_{f_{T_\pm}}(k,\omega) = \begin{cases} \frac{1}{\theta_\parallel\theta_-}W_\pm\left(\frac{\omega}{k\theta_-}\right)+\frac{1}{\theta_\parallel\theta_+}W_\pm^c\left(\frac{\omega}{k\theta_+}\right), & \mathrm{Re}\,\omega>0 \\ \frac{1}{\theta_\parallel\theta_-}W_\pm^c\left(\frac{\omega}{k\theta_-}\right)+\frac{1}{\theta_\parallel\theta_+}W_\pm\left(\frac{\omega}{k\theta_+}\right), & \mathrm{Re}\,\omega<0 \end{cases} \tag{28}$$

$W_\pm$ and $W_\pm^c$ are defined for complex argument $\xi = x+iy$ such that $y \geq 0$ and are written

$$W_\pm(\xi) = \frac{1}{\sqrt{2\pi}}\int_0^\infty\frac{t\exp(-t^2/2)}{t+\xi^\dagger}dt, \tag{29}$$

$$W_\pm^c(\xi) = W(\xi) - W_\pm(\xi), \tag{30}$$

where

$$W(\xi) = \frac{1}{\sqrt{2\pi}}\int_{-\infty}^\infty\frac{t\exp(-t^2/2)}{t-\xi}dt \tag{31}$$

is the classical dispersion function for a Maxwellian that can be found for example in Ichimaru (1992) and $\xi^\dagger = |x| + iy\,\mathrm{sgn}\,x$. $W_\pm$ is related to the function

$$Z_\pm(\xi) = \frac{1}{\sqrt{2\pi}}\int_0^\infty\frac{\exp(-t^2/2)}{t+\xi}dt, \tag{32}$$

through the relation

$$W_\pm(\xi) = \frac{1}{2} - \xi^\dagger Z_\pm(\xi^\dagger). \tag{33}$$

Finally, $Z_\pm$ is written as a function of Dawson's integral $\mathrm{daw}$ and the exponential integral Ei; Dawson's integral can be expressed as a function of the modified complex error function $\mathrm{erfc}$ (Abramowitz and Stegun, 1972):

$$Z_\pm(\xi) = \frac{1}{\sqrt{2}}\,\mathrm{daw}\left(\frac{\xi}{\sqrt{2}}\right) - \frac{1}{2\sqrt{2\pi}}\exp\Big(-\frac{\xi^2}{2}\Big)\mathrm{Ei}\Big(\frac{\xi^2}{2}\Big) \tag{34}$$

$$\mathrm{daw}(\xi) = -i\frac{\sqrt{\pi}}{2}e^{-\xi^2}\big(\mathrm{erfc}(-i\xi)-1\big). \tag{35}$$

## 4 Plasma lines Doppler frequency

In an incoherent scatter plasma lines experiment, one measures two sharp and narrow spectral lines, the down- and upshifted plasma lines corresponding to two Langmuir waves $(\boldsymbol{k}_-,\omega_-)$ and $(\boldsymbol{k}_+,\omega_+)$ travelling away from and toward the radar. The frequency of the two plasma lines are solutions of the following dispersion relation

$$k_\pm^2 + \omega_e^2 I_f(\boldsymbol{k}_\pm,\omega_\pm) = 0, \tag{36}$$

where $\omega_e$ is the electron plasma frequency.

We investigate the two solutions $(\boldsymbol{k}_-,\omega_-)$ and $(\boldsymbol{k}_+,\omega_+)$ of Eq. (36) for the 2-$T$ Maxwellian and we define the Doppler frequency $\Delta F_\pm$ as

$$\Delta F_\pm = \frac{\omega_+ + \omega_-}{2\pi} \tag{37}$$

The Doppler frequency $\Delta F_\pm$ is then compared with the Doppler frequency given by solving the heat flow approximation of the dispersion relation of Kofman *et al.* (1993). To derive the heat flow approximation, the denominator of the integrand of Eq. (25) is expanded in power series of $\boldsymbol{k}\cdot\boldsymbol{v}/(\omega-\boldsymbol{k}\cdot\boldsymbol{u})$, then integrated by parts, each term containing an average – defined in Eq. (9) – of a power of the velocity of the probability distribution.

For $\boldsymbol{k}$ along the $v_\parallel$-axis, $I_f(\boldsymbol{k},\omega)$ takes the following form

$$I_f(k,\omega) = -\frac{k^2}{(\omega-ku_\parallel)^2}\Bigg(1+3\frac{k^2\langle(v_\parallel-u_\parallel)^2\rangle}{(\omega-ku_\parallel)^2} +4\frac{k^3\langle(v_\parallel-u_\parallel)^3\rangle}{(\omega-ku_\parallel)^3}+\cdots+(n+1)\frac{k^n\langle(v_\parallel-u_\parallel)^n\rangle}{(\omega-ku_\parallel)^n}\Bigg) \tag{38}$$

Assuming in addition that $|\omega-ku_\parallel| \gg kv_{T_\parallel}$ where $v_{T_\parallel}^2 = T_\parallel/m_e$ and that the distribution does not deviate dramatically from a Maxwellian, the even order moments are lumped into the $W$ function of Eq. (31) and the odd order moments are truncated at the third order, which gives the heat flow approximation

$$\tilde{I}_f(k,\omega) = \frac{1}{v_{T_\parallel}^2}W\left(\frac{\omega-ku_\parallel}{kv_{T_\parallel}}\right) - 4\frac{k^5 q_\parallel^\parallel/(m_e n)}{(\omega-ku_\parallel)^5}. \tag{39}$$

Results of the computation of $\Delta F_\pm$ using the analytic form of Eq. (28) and the heat flow approximation of Eq. (39) for the 2-$T$ Maxwellian as well as using a numerical code of the dielectric function with the Spitzer function (Guio *et al.* (1998)) are shown in Figure 3 for the EISCAT VHF radar (224 MHz) and in Figure 4 for the EISCAT UHF radar (931 MHz). The effect of the Doppler velocity $u_\parallel$ has been eliminated by subtracting from the parallel velocity $v_\parallel$ of the 2-$T$ Maxwellian and the Spitzer function the mean Doppler velocity $u_\parallel$ of Eqs (10) and (17) respectively. The difference from the Maxwellian when it comes to evaluate $\Delta F_\pm$ is therefore only the effect of the skewness of the velocity distribution function.

For the VHF radar, there is a good qualitative agreement of the Doppler frequency $\Delta F_\pm$ as a function of the electron density $n_e$ using: the exact expression of the dielectric response function for the 2-$T$ Maxwellian (Eq. 28), the heat

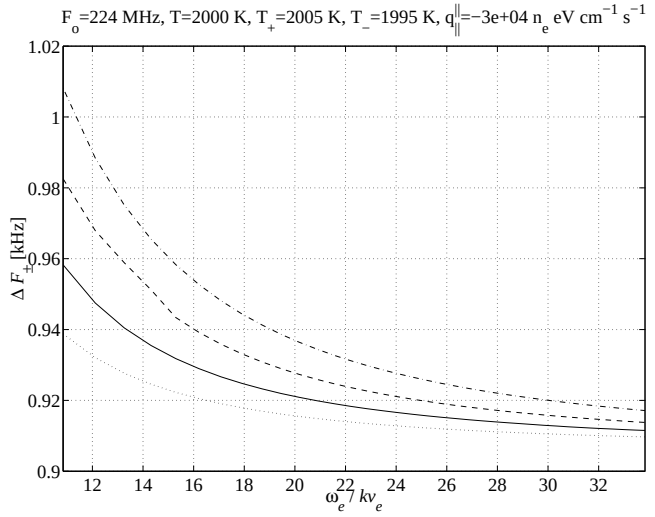


**Fig. 3.** EISCAT VHF radar. The calculated Doppler frequency $\Delta F_{\pm}$ using Eq. (28) (*solid* line) and Eq. (39) (*dashed dot* line), using a numerical code (Guio *et al.* (1998)) to calculate Eq. (25) for the Spitzer distribution (*dashed* line) and for a Maxwellian (*dotted* line). The Doppler frequency is plotted as a function of the ratio $\omega_e/kv_{T_\parallel}$, the electron temperature $T_e$ is $2000\,\mathrm{K}$ and the Knudsen number $\epsilon_T$ is $2 \cdot 10^{-3}$. The frequency $f_e$ that corresponds to $\omega_e/k\theta_\parallel$ varies from about $3\,\mathrm{MHz}$ to nearly $9\,\mathrm{MHz}$ and corresponds to an electron density $n_e$ varying from $10^5$ to $10^6\,\mathrm{cm}^{-3}$

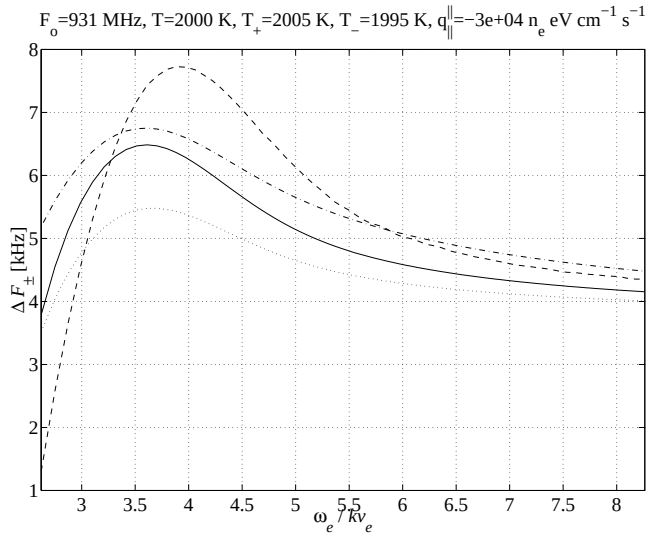


**Fig. 4.** EISCAT UHF radar. The calculated Doppler frequency $\Delta F_{\pm}$ using Eq. (28) (*solid* line) and Eq. (39) (*dashed dot* line), using the same numerical code to calculate Eq. (25) for the Spitzer distribution (*dashed* line) and for a Maxwellian (*dotted* line). The Doppler frequency is plotted as a function of the ratio $\omega_e/kv_{T_\parallel}$ for the same temperature $T_e$ and Knudsen number $\epsilon_T$ as in Figure 3. The corresponding frequency $f_e$ varies also from about $3\,\mathrm{MHz}$ to nearly $9\,\mathrm{MHz}$ which corresponds to an electron density $n_e$ varying from $10^5$ to $10^6\,\mathrm{cm}^{-3}$

flow approximation (Eq. 39) and the numerical calculation of the dielectric response function for the Spitzer distribution (Guio *et al.* (1998))). For such large values of the phase velocity $v_{\pm} = \omega_{\pm}/k_{\pm}$, i.e. when $|\omega_{\pm}| \gg k_{\pm} v_{T_\parallel}$, the three calculations predict a moderate increase of the observed Doppler frequency compared to the Maxwellian case (less than $100\,\mathrm{Hz}$) since the terms in the expansion of Eq. (38) are small. As a consequence, the effect of the skewness of the distribution function on the Doppler frequency is, as the heat flow approximation shows, to shift the Doppler frequency in the same direction as the heat flow and the heat flow behaves like a mean Doppler velocity.

For the UHF radar there is also a good qualitative agreement of the behaviour of the Doppler frequency $\Delta F_{\pm}$ as a function of the electron density at large plasma frequency $\omega_e$ between the three calculations. The three calculations of the dielectric response function predict an increase of the measured Doppler frequency compared to the Maxwellian which can be rather important. At low plasma frequency, the Doppler frequency calculated using the exact calculation of the dielectric response function differs from the one given by the heat flow approximation. While the heat flow approximation gives a relatively constant shift in the Doppler frequency compared to the Maxwellian, independent of the electron density, the exact calculations of the dielectric function for the 2-$T$ Maxwellian and the Spitzer function tend to give smaller Doppler frequency. The discrepancy is getting larger the smaller the plasma frequency is, i.e. when the condition $|\omega| \gg kv_{T_\parallel}$ is not well fulfilled.

This shows that the truncation done for the heat flow approximation has to be done very carefully and that the approximation breaks for ratio $|\omega|/kv_{T_\parallel}$ smaller than 5–6. Moreover it is seen that even though the two distribution functions considered have the same temperature and the same heat flow for parallel energy, the dielectric response behaves qualitatively in an identical way but quantitative differences are noteworthy. These differences have to be accounted to the differences in higher order moments of the distribution function.

## 5 Conclusion

We have presented a new tool, the 2-$T$ Maxwellian, to model the particle velocity distribution in a plasma with a temperature gradient and have compared the properties of the velocity moments to the results of the classical Spitzer distribution function. We have seen that it is possible to parametrise the 2-$T$ Maxwellian to get an equal heat flow to the Spitzer result. An analytic form of the dielectric response function has been presented for this new distribution, and has been used to calculate the Doppler frequency of plasma lines in an incoherent scatter experiment. The result has been compared to the Doppler frequency given by the heat flow approximation. It has been shown that good qualitative agreement is obtained between the heat flow approximation of the dielectric function and the exact calculation for low-frequency radars also for high-frequency radars if the plasma frequency is high. However for accurate calculations such as the calculation of the plasma line Doppler frequency, it is seen that the exact calculation of the dielectric function is important together with a good representation of the distribution function, especially for high-frequency radars and at low plasma frequency, i.e when the ratio $|\omega|/k\theta_e$ is smaller than 5–6.

The 2-$T$ Maxwellian is not expected to represent a true physical model of the distribution function in the presence of a gradient of temperature but nevertheless is a realistic tool for investigating this type of plasma. We expect that the 2-$T$

Maxwellian should be useful in the qualitative study of instabilities due to heat conduction in a plasma, especially in ionospheric studies where temperature gradients are present. The 2-$T$ Maxwellian could also be a good investigation tool to study the effect of an angle with the magnetic field on the Doppler frequency in incoherent scatter plasma lines observations.

*Acknowledgements.* The author would like to thank P. L. Blelly and F. Forme for their helpful discussions and comments.

## References

**Abramowitz, M. and I. A. Stegun**. *Handbook of mathematical functions with formulas, graphs and mathematical tables*. Dover Publications, New York, 1972. ISBN 0-48661-272-4.

**Banks, P. M.** Charged particle temperatures and electron thermal conductivity in the upper atmosphere. *Ann. Geophysicae*, **22**, 577–587, 1966.

**Barakat, A. R. and R. W. Schunk**. transport equations for multicomponent anisotropic space plasmas: a review. *Plasma phys.*, **24**, 389–418, 1982.

**Bauer, P., K. D. Cole, and G. Lejeune**. Field-aligned electric currents and their measurement by the incoherent backscatter technique. *Planet. Space Sci.*, **24**, 479–485, 1976.

**Blelly, P.-L. and D. Alcaydé**. Electron heat flow in the auroral ionosphere inferred from EISCAT-VHF observations. *J. Geophys. Res.*, **99**, 13181–13188, 1994.

**Cohen, R. S., L. Spitzer, and P. McRoutly**. The electrical conductivity of an ionized gas. *Phys. Rev.*, **80**, 230–238, 1950.

**Forslund, D. W.** Instabilities associated with heat conduction in the solar wind and their consequences. *J. Geophys. Res.*, **75**, 17–28, 1970.

**Guio, P., J. Lilensten, W. Kofman, and N. Bjørnå**. Electron velocity distribution function in a plasma with temperature gradient and in the presence of suprathermal electrons: application to incoherent-scatter plasma lines. *Ann. Geophysicae*, **16**, 1226–1240, 1998.

**Hundhausen, A. J.** Direct observations of solar-wind particles. *Space Sci. Rev.*, **8**, 690–749, 1968.

**Ichimaru, S.** *Statistical plasma physics: basic principles*. Addison-Wesley, Redwood City, Ca., 1992. ISBN 0-201-55490-9 (Vol. 1).

**Kofman, W., J.-P. St-Maurice, and A. P. van Eyken**. Heat flow effect on the plasma line frequency. *J. Geophys. Res.*, **98**, 6079–6085, 1993.

**Lundin, B., C. Krafft, G. Matthieussent, F. Jiricek, J. Shmilauer, and P. Triska**. Excitation of VLF quasi-electrostatic oscillations in the ionospheric plasma. *Ann. Geophysicae*, **14**, 27–32, 1996.

**Showen, R. L.** The spectral measurement of plasma lines. *Radio Sci.*, **14**, 503–508, 1979.

**Singer, C. E.** Microinstabilities in a moderately inhomogeneous plasma. *J. Geophys. Res.*, **82**, 2686–2692, 1977.

**Spitzer, L. and R. Härm**. Transport phenomena in a completely ionized gas. *Phys. Rev.*, **89**, 977–981, 1953.

# ARTICLE IV

Ann. Geophysicae 17, 903–912 (1999) © EGS – Springer-Verlag 1999

Annales Geophysicae

# Effect of suprathermal electrons on the intensity and Doppler frequency of electron plasma lines

**P. Guio**[1], **J. Lilensten**[2]

[1] The Auroral Observatory, Institute of Physics, University of Tromsø, Norway
[2] Laboratoire de planétologie de Grenoble, LIS-ENSIEG BP 46, F-38402 Saint-Martin-d'Hères, France

Received: 2 November 1998 / Revised: 10 February 1999 / Accepted: 11 February 1999

**Abstract.** In an incoherent scattering radar experiment, the spectral measurement of the so-called up- and downshifted electron plasma lines provides information about their intensity and their Doppler frequency. These two spectral lines correspond, in the backscatter geometry, to two Langmuir waves travelling towards and away from the radar. In the daytime ionosphere, the presence of a small percentage of photoelectrons produced by the solar EUV of the total electron population can excite or damp these Langmuir waves above the thermal equilibrium, resulting in an enhancement of the intensity of the lines above the thermal level. The presence of photo-electrons also modifies the dielectric response function of the plasma from the Maxwellian and thus influences the Doppler frequency of the plasma lines. In this paper, we present a high time-resolution plasma-line data set collected on the EISCAT VHF radar. The analysed data are compared with a model that includes the effect of a suprathermal electron population calculated by a transport code. By comparing the intensity of the analysed plasma lines data to our model, we show that two sharp peaks in the electron suprathermal distribution in the energy range 20–30 eV causes an increased Landau damping around 24.25 eV and 26.25 eV. We have identified these two sharp peaks as the effect of the photoionisation of $N_2$ and O by the intense flux of monochromatic HeII radiation of wavelength 30.378 nm (40.812 eV) created in the chromospheric network and coronal holes. Furthermore, we see that what would have been interpreted as a mean Doppler drift velocity for a Maxwellian plasma is actually a shift of the Doppler frequency of the plasma lines due to suprathermal electrons.

**Key words.** Ionosphere (electric fields and currents; solar radiation and cosmic ray effects).

*Correspondence to:* P. Guio
e-mail: patrick@phys.uit.no

## 1 Introduction

The enhancement process of the plasma line is well understood theoretically (Perkins and Salpeter, 1965; Yngvesson and Perkins, 1968; Bjørnå *et al.*, 1982; Bjørnå and Trulsen, 1986) and has been confirmed by measurements both during daytime (Perkins *et al.*, 1965; Yngvesson and Perkins, 1968; Lejeune and Kofman, 1977; Kofman and Lejeune, 1980) and in auroral conditions (Oran *et al.*, 1981; Kirkwood *et al.*, 1995). The problem of estimating the field-aligned electron net current from an incoherent scatter Doppler measurement of the electron plasma lines has also been studied for some time (Vidal-Madjar *et al.*, 1975; Bauer *et al.*, 1976; Showen, 1979), yet the work on the subject has progressed rather slowly, partly due to experimental problems (the spectra needs to be estimated) and partly due to the lack of theoretical understanding. It is expected that by simultaneous measurements of the frequency of the up- and downshifted plasma lines one could deduce the mean Doppler velocity $u_e$ of the electron velocity distribution function along the scattering direction.

At first, an additional asymmetry between the Doppler frequency of the plasma lines was identified for an isotropic Maxwellian plasma. This asymmetry is due to the difference in magnitude of the wave numbers of the up- and down-going Langmuir waves (Showen, 1979). This term is proportional to a temperature-dependent correction term (Debye correction) in the dispersion relation for Langmuir waves and was pointed out as a possible method for the independent determination of the electron temperature (Hagfors and Lehtinen, 1981). Later, Kofman *et al.* (1993) showed that by introducing in the dispersion relation a heat flow correction term that takes into account the effect of the temperature gradient of the electron temperature, that their data collected with the EISCAT UHF radar during daytime were in better agreement with the

prediction of no field-aligned. This heat flow correction term behaves as an additional mean Doppler velocity that artificially increases the difference of the Doppler shifts of the plasma lines. Guio *et al.* (1998) showed that the heat flow effect was underestimated for UHF radars by comparing the heat flow approximation of the dispersion relation with a full numerical estimation of the dielectric response function using the Spitzer velocity distribution for a plasma with a temperature gradient (Cohen *et al.*, 1950; Spitzer and Härm, 1953). It was also shown that for VHF radars, suprathermal electrons would contribute to modify the dielectric response function and thus the Doppler frequency of the plasma lines. It is noteworthy that while the suprathermal effect on the Doppler frequency has been investigated with a Maxwellian to represent the photoelectrons distribution (Bauer *et al.*, 1976), it has to our knowledge, never been observed in data.

In this paper we present a high temporal resolution data set collected on the EISCAT VHF radar. The plasma line analysis consists of two parts. First, the result of the analysis of the intensity of the plasma lines is compared with a model that calculates the theoretical enhancement caused by suprathermal electrons described by the angular velocity distribution derived form the electron angular intensity flux calculated by a transport code (Lummerzheim, 1987; Lummerzheim and Lilensten, 1994). Once we find an electron velocity distribution that gives correct intensity compared to the measured intensity, we use the full numerical calculation of the plasma dielectric response (Guio *et al.*, 1998) to estimate the mean Doppler velocity $u_e$ of the ambient electrons, and the plasma frequency $\omega_e$. The results are compared with the Maxwellian case.

## 2 The data

The plasma line data were collected with the EISCAT VHF radar (223.8 MHz) near Tromsø, Norway on 22 June 1994 from 15:00 UT to 16:00 UT. The antenna was pointed vertically which gives an angle of about 12° to the magnetic field line at 250 km. The ionospheric conditions were quiet, a F10.7 index of 75 and an $A_p$ index of 6 were measured.

The data were collected with the long pulse technique first described by Showen (1979) and the measurement of the plasma lines was done at the peak of the F-layer. A special tracking program that interacts with the radar, attempts to tune the radar receiver every dump so that the critical frequency of the peak of the F-layer is centred in the 100 kHz observation window filtered with a 80 kHz filter. Three receiving channels, one for the upshifted, one for the downshifted plasma line and one for the ion line, were used simultaneously, with the same spatial resolution. A single long pulse with length 450 μs was transmitted and signal was collected at a sampling rate of 10 μs. A 33-point autocorrelation function with correlation time between 0 and 320 μs by step of 10 μs was computed for five gates as a function of altitude, on each channel. The first gate was situated at 178 km, the gate separation was 37.5 km, thus the last gate is situated at 328 km, and the volume probed for one gate was about 45 km. In addition to the 450 μs long pulse, a very long pulse of 900 μs was transmitted to measure the ion line. Eleven gates were computed from 317 km up to 1217 km and the volume probed for one gate was about 100 km. The initial integration period was 2 s, and the up- and downshifted plasma lines autocorrelation functions were analysed at the same time resolution while the ion line data were post-integrated to a 30-s period before analysis.

Figure 1 presents the ionospheric parameters extracted from the ion line analysis as a function of altitude. Each panel presents the parameter obtained from both the 450 μs and 900 μs pulses. The two dashed lines on each panel represent the 1-$\sigma$ deviation of the parameter averaged over the 1-h period while the solid line is the averaged parameter. The fitting procedure did not converge for the 900 μs very long pulse above the altitude of 850 km due to low backscattered signal, as it is seen on the electron density $n_e$, the electron and ion temperature $T_e$ and $T_i$ and the ion mean velocity $u_i$. The ionospheric parameters remained very stable over the time period of the experience.

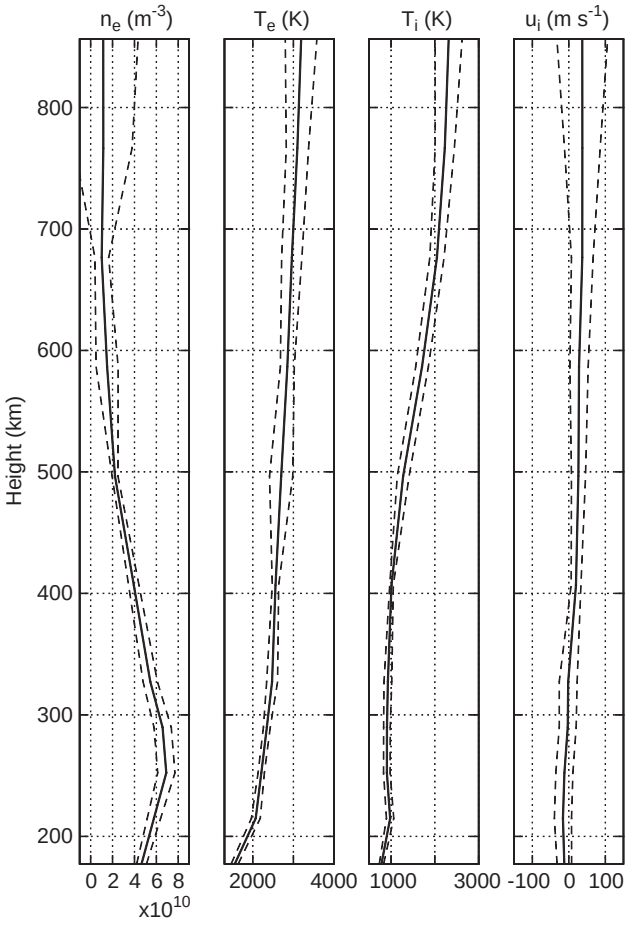


**Fig. 1.** The electron density $n_e$, the electron and ion line temperatures $T_e$ and $T_i$ and ion mean drift velocity $u_i$ as a function of altitude averaged over the 1-h period of the experiment run. The *dashed lines* represents the 1-$\sigma$ deviation from the averaged parameter (*solid line*)

The plasma line data were analysed using a least-square fit method that uses a model of the autocorrelation function adapted to the observation of plasma lines with the long pulse technique (Kofman *et al.*, 1981; Heinselman and Vickrey, 1992; Kofman *et al.*, 1993). The least-square fit method allows accurate extraction of the critical frequency at the electron density peak of the F-layer, the intensity and the frequency width of the plasma lines as well as the electron density scale height around the peak and the height of the F-region peak. Figure 2 shows an example of a fit of an autocorrelation function collected at a 2-s integration time. The intensity of the plasma line is fitted in terms of the antenna temperature and is then converted into electron plasma temperature (Yngvesson and Perkins, 1968) by taking into account the radar constant and the frequency-dependent effective antenna area (Guio *et al.*, 1996).

Figures 3 and 4 show the parameters extracted from the plasma line analysis, Fig. 3 is for the downshifted plasma line and Fig. 4 for the upshifted. The top panels present the critical frequencies $f_{r\pm}$ and the third panels the intensities of the lines $T_{p\pm}$. The second panels show the corresponding phase energies $E_{\phi\pm}$ of the Langmuir waves at the frequencies $f_{r\pm}$ defined by

$$E_{\phi\pm} = \frac{1}{2} m_e v_{\phi\pm}^2 \tag{1}$$

where $v_{\phi\pm} = 2\pi f_{r\pm}/k_\pm$ is the phase velocity of the wave, $k_\pm = 2\pi(f_0 + f_0 + f_{r\pm})/c$ is the scattered wave vector of the Langmuir wave in the backscatter geometry with a radar of frequency $f_0$, and $m_e$ is the electron mass. The lowest panel in each figure shows the bandwidth $\delta f_\pm$ of the plasma lines over the 1-h period of observation. Note that for low-frequency radars such as the EISCAT VHF radar, the difference $\Delta f_{r\pm} = f_{r+} + f_{r-}$ of Doppler frequency between up- and downshifted plasma lines is of the order of 1 kHz and it corresponds in term of

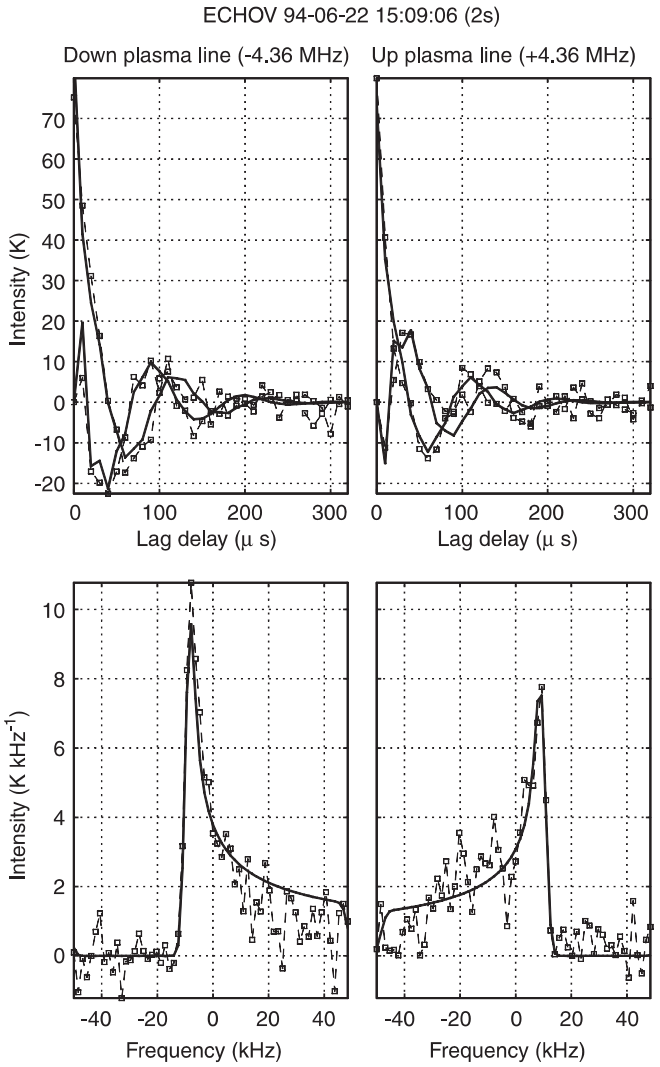


**Fig. 2.** Example of the result of a fit of the up- and downshifted plasma lines. The two *upper panels* show the measured complex autocorrelation functions expressed in units of antenna temperature (*dashed line*) and the theoretical model (*solid line*). The *curves* with the intensity equal to zero at the zero lag delay are the imaginary parts. The two *lower panels* present the corresponding power density spectrum where the critical frequency is more easily identified in the spectral shape

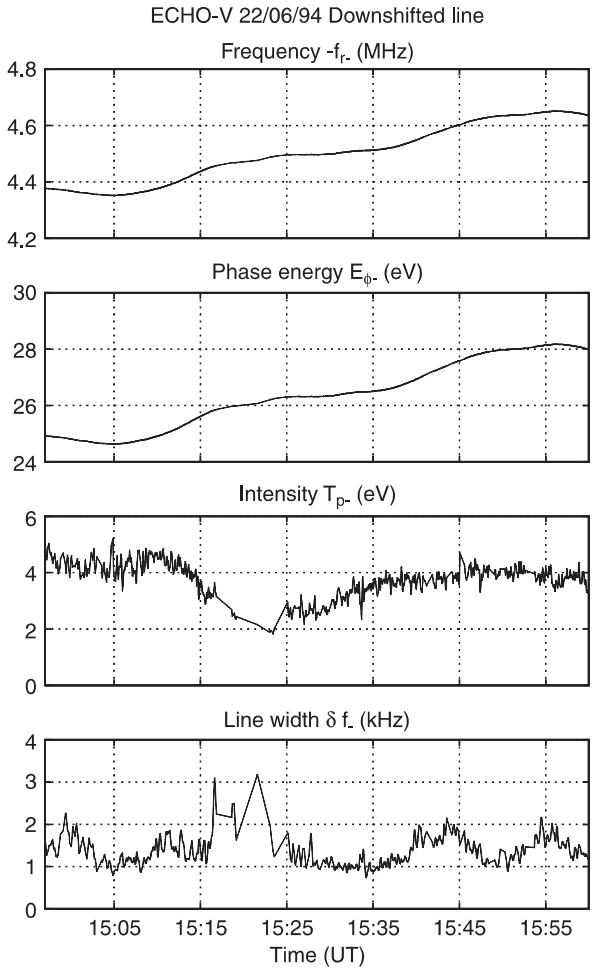


**Fig. 3.** The parameters extracted from the downshifted plasma line analysis for the 1-h period of observation. From *top to bottom*: the absolute value of the critical frequency $|f_{r-}|$, the corresponding phase energy $E_{\phi-}$, the intensity of the line (or plasma line temperature) $T_{p-}$ and the line width $\delta f_-$

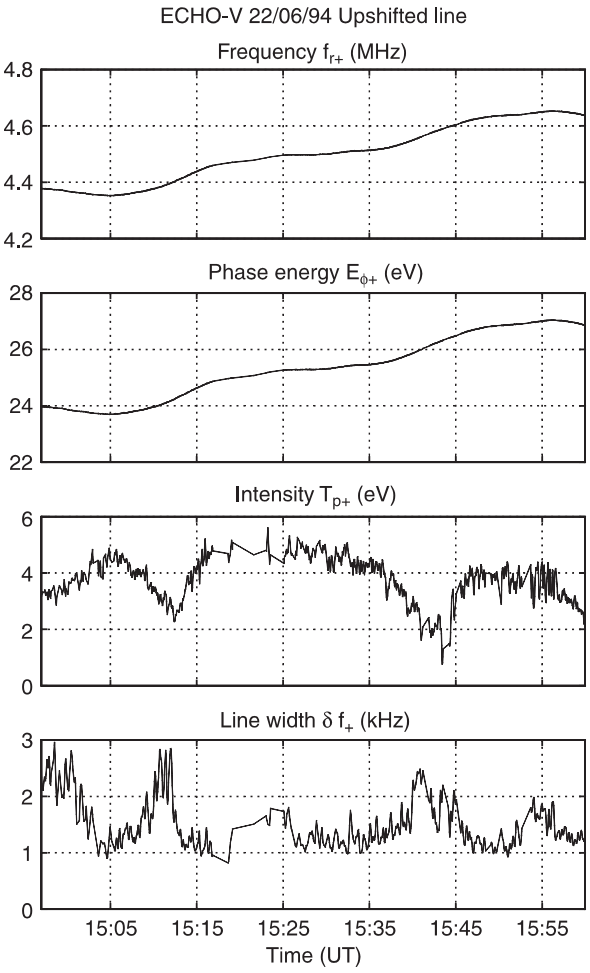


**Fig. 4.** The parameters extracted from the upshifted plasma line analysis for the 1-h period of observation. From *top to bottom*: the critical frequency $f_{r+}$, the corresponding phase energy $E_{\phi+}$, the intensity of the line (or plasma line temperature) $T_{p+}$ and the line width $\delta f_+$

phase energy into a difference $\Delta E_{\phi\pm} = E_{\phi+} - E_{\phi-}$ of the order of $-1$ eV.

The intensity of the plasma lines presents interesting variations in the 1–h observation period. At a first look, the intensity of the up- and downshifted line seems to have a very different behaviour as a function of time. In Fig. 4, the intensity of the upshifted plasma line around 15:12 UT, for phase energies $E_{\phi+}$ about 24.25 eV shows a significant drop. A similar drop can be observed around 15:43 UT, for phase energies around 26.25 eV. In Fig. 3 the intensity of the downshifted plasma line around 15:24 UT, for phase energies $E_{\phi-}$ around 26.25 eV exhibits also a similar drop. At the same time, the frequency width of the plasma lines is increasing (see the lowest panel of Figs. 3 and 4). For the VHF radar, the natural frequency width of the plasma lines is controlled by the collisional damping and the Landau damping of the suprathermal electrons. The collisional damping is a function of the electron-neutral and electron-ion collision frequencies (Newman and Oran, 1981) and of the phase velocity of the wave (Perkins and Salpeter, 1965). As seen in the third panel from the top in Fig. 6, the electron collision frequency derived from the ion line analysis, does not vary much over the observation period. The phase energy of the plasma lines, as seen in the second panel from top in Figs. 3 and 4, and thus the phase velocity is increasing smoothly. It is therefore very unlikely that the collisional damping could provoke such variations in the intensity, instead it is likely that the variations in the intensity of the plasma lines are caused by an increase in the Landau damping of the suprathermal electron population at these phase energies (Perkins and Salpeter, 1965). This explanation is reinforced by the fact that both the up- and downshifted plasma lines exhibit a drop in intensity for the same phase energy of 26.25 eV, i.e. for the same velocity in the electron velocity distribution. Note that the drop of intensity observed on the downshifted line at 15:24 UT is spread over a longer period because of the slow variation of the phase energy at this time. As seen in Fig. 5, the behaviour of the up- and downshifted plasma lines intensity *as a function of the phase energy* is very similar.

In order to analyse the intensity and Doppler frequency of the plasma lines, one needs an estimate of the parameters describing the ambient part of the electron distribution function (Guio *et al.*, 1998). These parameters are estimated directly from the ion line analysis or derived from the ion line analysis. Figure 6 presents the parameters of the ambient part of the electron distribution function interpolated at the altitude corresponding to the peak of the F-region where the plasma lines are measured. The electron density $n_e$ and electron temperature $T_e$ are directly estimated. The electron collision frequency $v_e$ includes the electron-neutral and electron-ion collision frequencies defined by (Newman and Oran, 1981)

$$v_{en} = 5.4 \times 10^{-10} n_n T_e^{1/2} \tag{2}$$

$$v_{ei} = \left(34.0 + 4.18\ \log\frac{T_e^3}{n_e}\right) n_e T_e^{-3/2} \tag{3}$$

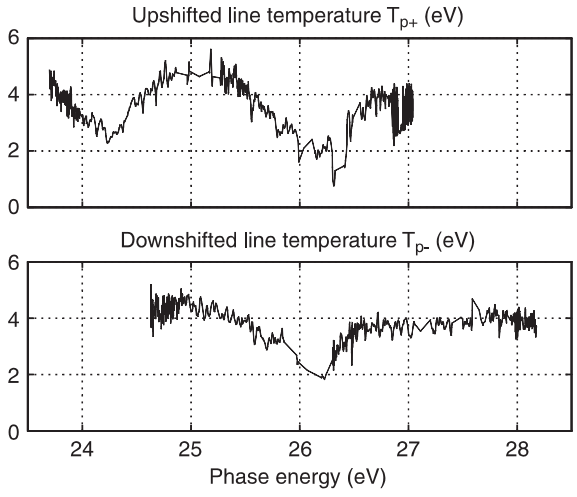


**Fig. 5.** The temperature $T_{p+}$ and $T_{p-}$ of the up- and downshifted plasma lines from the 1-h observation of Figs. 4 and 3 plotted as a function of their phase energy, respectively $E_{\phi+}$ and $E_{\phi-}$

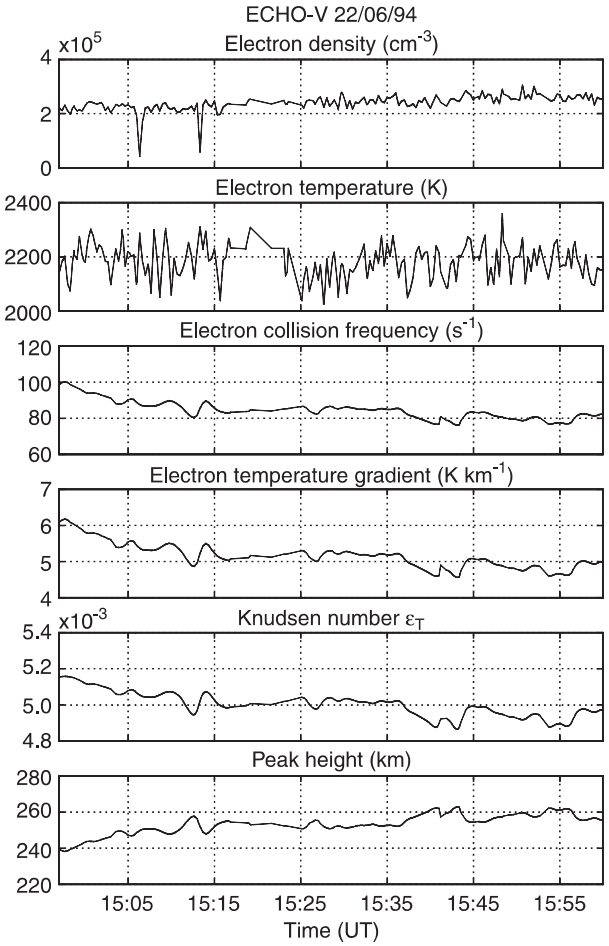


**Fig. 6.** The parameters for the ambient part of the electron distribution function interpolated at the altitude where the critical frequencies of the plasma lines are estimated (*bottom panel*)

where the density are in $\mathrm{cm}^{-3}$ and $n_n$ is the neutral density calculated by the MSIS-90 model (Hedin, 1991). The temperature gradient $\nabla T_e$ is estimated numerically from the ion line data. The Knudsen number $\epsilon_T = 2\lambda_e \nabla \log T_e$ (Guio *et al.*, 1998) where $\lambda_e$ is the electron mean free path, is a parameter used in the Spitzer function (Cohen *et al.*, 1950; Spitzer and Härm, 1953) to represent the electron ambient distribution function in presence of a temperature gradient.

## 3 Analysis

The analysis is split into two parts. First the electron suprathermal distribution function is adjusted so that the calculated intensity matches the measured intensity. When a satisfactory suprathermal distribution function is determined, it is then used to calculate the electron Doppler velocity $u_e$ as well as the plasma frequency $\omega_e$.

### *3.1 Intensity analysis*

In order to estimate the plasma line temperature theoretically, we need a model for the suprathermal electrons. We use the suprathermal velocity distribution $f_s$ which we derive from the angular energy flux $\phi$ calculated by the electron transport model code along the Earth magnetic field, described in Lilensten *et al.* (1989) and Lummerzheim and Lilensten (1994). The ionospheric parameters $n_e, T_e$ and $T_i$ we used as input to the transport code are the averaged parameters of Fig. 1. The code calculates the angular energy flux for 100 altitudes between 90 km and 400 km and we get seven angular fluxes in the altitude range 236–263 km.

Using a BGK model for the collisions, an expression for the intensity of the plasma line can be derived from the theoretical plasma line power spectrum for any arbitrary electron velocity distribution (Sheffield, 1975; Bjørnå and Trulsen, 1986) in the same way as done by Perkins and Salpeter (1965) for isotropic but not necessarily Maxwellian distribution. This new expression for the plasma line intensity expressed in terms of the two complex functions $P$ and $Z$ is valid for any arbitrary anisotropic velocity distribution that produces a stable plasma. The complex functions $P$ and $Z$ involved in the calculation can be replaced by their numerical approximations $P_n$ and $Z_n$ defined in Guio *et al.* (1998) and the intensity expressed as a temperature $T_{p\pm}$ of the plasma lines is written

$$k_b T_{p\pm} = k_b T_e \times \frac{v_{\phi\pm}\,\mathrm{Im}\,P_n\left(\frac{v_{\phi\pm}}{v_e}\right) - \frac{v_{\phi\pm}}{v_e}\frac{v_e}{k_\pm}\left|P_n\left(\frac{v_{\phi\pm}}{v_e}\right)\right|^2}{v_e\,\mathrm{Im}\,Z_n\left(\frac{v_{\phi\pm}}{v_e}\right) + \left(\frac{v_e}{v_{\phi\pm}}\right)^2 \frac{v_e}{k_\pm}\mathrm{Re}\,P_n\left(\frac{v_{\phi\pm}}{v_e}\right)} \tag{4}$$

where $v_e$ is the sum of the electron-neutral and electron-ion collision frequencies of Eqs. (2) and (3), $v_e = \sqrt{k_b T_e / m_e}$ is the electron thermal velocity and

$$P_n\left(\frac{v_\phi}{v_e}\right) = (1-\alpha) P^a_n\left(\frac{v_\phi}{v_e}\right) + \alpha P^s_n\left(\frac{v_\phi}{v_e}\right) \tag{5}$$

$$Z_n\left(\frac{v_\phi}{v_e}\right) = (1-\alpha) Z^a_n\left(\frac{v_\phi}{v_e}\right) + \alpha Z^s_n\left(\frac{v_\phi}{v_e}\right) \tag{6}$$

where $P^a_n$, $Z^a_n$ are the contributions from the ambient population while $P^s_n$, $Z^s_n$ are due to the suprathermal electrons. The dimensionless number $\alpha$ denotes the percentage of suprathermal electrons.

Our investigation to determine the ad hoc velocity distribution function for the suprathermal electrons shows that the detailed structure of the distribution in the concerned energy range (23–29 eV) is depending on the solar intensity flux responsible for the creation of photo-electrons. Figure 7 shows the model for the solar intensity flux spectrum (Torr and Torr, 1985) we basically used. The solar intensity for any F10.7 is deduced by interpolation between the two reference fluxes of Fig. 7. Since that time, a lot of work has been done in order to get a better estimate of this flux. Most recent results include Warren *et al.* (1998a, b); Tobiska and Eparvier (1998) and Woods *et al.* (1998). We tested several more recent models, but in the energy range relevant in this paper, we did not find significant

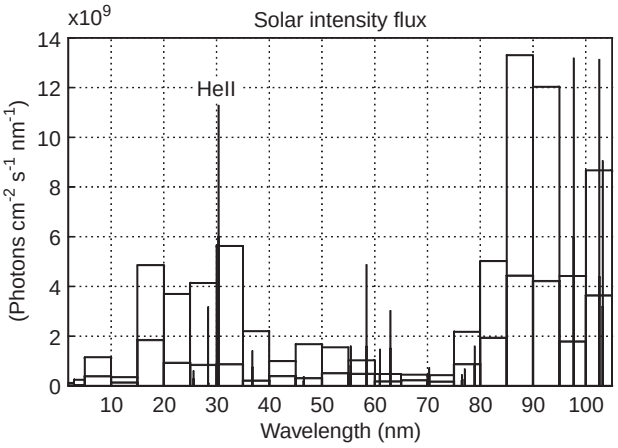


**Fig. 7.** The model for the solar intensity flux (Torr and Torr, 1985). The *thin line* is for solar maximum (F10.7 = 243) and the *thick line* for solar minimum (F10.7 = 68). The solar flux for any arbitrary F10.7 is deduced by interpolation between theses two references fluxes

differences. The cross section set is from Fennelly and Torr (1992). The two sharp peaks in the suprathermal angular velocity distribution function, seen in the top panel of Fig. 8, at energies 24.25 eV and 26.25 eV are the effect of the photoionisation of $N_2$ and O by the discrete line of photons of wavelength 30.378 nm (40.812 eV), corresponding to the solar emission of HeII in the chromospheric network and coronal holes. Indeed, ionisation thresholds are 15.58 eV for $N_2$ and 13.61 eV for O. During an ionisation, the electron leaves the ion with the energy of the input photon minus the threshold energy, which should give two peaks at energies 25.232 eV for $N_2$ photoionisation and 27.202 eV for O photoionisation. The discrepancy found can be interpreted as a mean energy left by the incident photon to the target atom or molecule during an ionization : in average, the nitrogen ion keeps about one electronvolt. This result was theoretically expected by chemists : the study of the dissociative ionisation of $N_2$ by photons between 23 and 30 eV has shown that the kinetic energy of the ion evolves with the initial energy of the photon (R. Thissen, personal communication). When the electron is left with no energy, the mean energy of the ion may be up to 1 eV, and even more (1.6 eV has been observed with initial photons of 30 eV). To our knowledge, if this interpretation and our comparison are correct it is the first time that it is conspicuous and that this energy can be numerically evaluated. It has a certain importance as far as electron density computations are concerned. Indeed, in the ionospheric models, the coefficients for the chemical recombinations involving $N_2^+$ are considered for a ground state ion. The coefficients involving excited ions can be multiplied by a factor of 10 (Chiu *et al.*, 1995). The effect of excited neutral nitrogen (and especially vibrational excitation) on calculation of electron densities has long been a subject of study [see for example Pavlov and Buonsanto (1996) and references herein], but the same effect for ions is still a new subject of investigation.

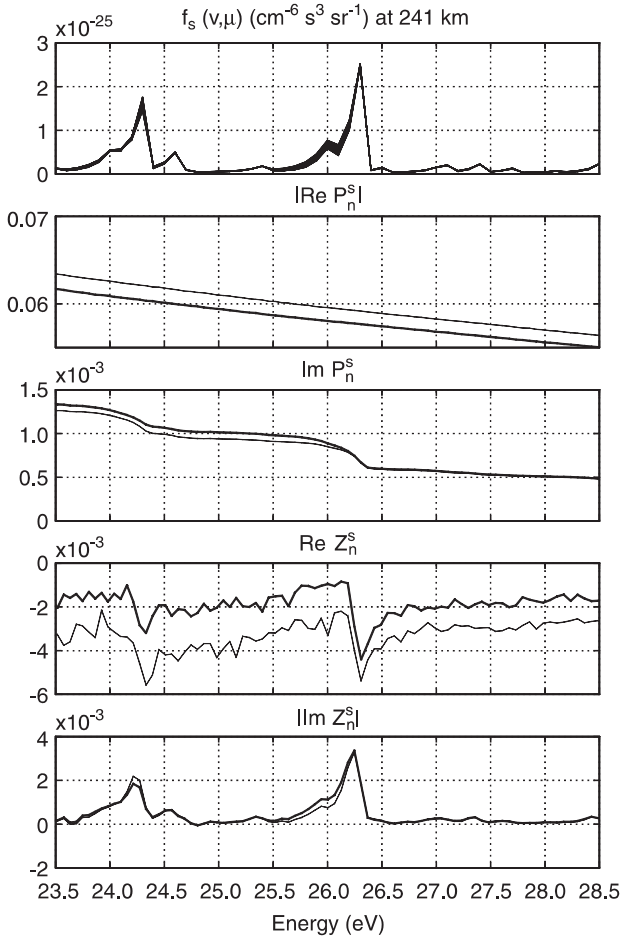


**Fig. 8.** The suprathermal electron angular velocity distribution function (*top panel*) at 241 km calculated by a 32-streams run of the transport code to gives the distribution at 32 angles and the complex functions $P_n^s$ and $Z_n^s$ calculated numerically with this distribution function, in the energy range 23.5–28.5 eV. The *thin line* is for downward phase energy and the *thick line* is for upward phase energy

Figure 8 shows the velocity angular distribution in the energy range 23.5–28.5 eV (top panel) calculated by the transport code at 241 km and the real and imaginary parts of both the $P_n^s$ and $Z_n^s$ functions estimated with this distribution. It is seen that the two sharp peaks at 24.25 eV and 26.25 eV in the angular distribution (top panel) transform into the imaginary part of $Z_n^s$ function (proportional to the Landau damping) as increases at the same energy and into the imaginary part of $P_n^s$ function (proportional to the one-dimensional reduced distribution along the scattering direction) as a sharp decrease in the suprathermal population.

The magnitude of the suprathermal distribution at the energies corresponding to the two sharp peaks at 24.25 eV and 26.25 eV is proportional to the flux of the solar discrete emission line of HeII and so is the imaginary part of $Z_n^s$. At the same time it does not influence significantly the magnitude of the distribution at other energies. So that, we had to actually reduce by five the intensity of the flux of the HeII discrete line (see Fig. 7) for the solar minimum i.e. F10.7 = 68, while keeping the same value for the continuum in order to get

a magnitude of the damping that reproduced correctly the temporal variations of the plasma line temperatures. Such variations of the intensity of the flux over time period of a few hour have been observed (J. Aboudarham, personal communication).

In addition to the adjustment of the intensity of the flux of the HeII discrete line and in order to resolve correctly the two peaks at these energies we modified the energy grid of the transport model in the range 20–32 eV to a higher resolution linear grid of energy step ·1 eV.

Figure 9 shows the results of the theoretical calculations of the intensities together with the data. After the adjustments of the parameters in the transport code, the calculated intensities are seen to be in good agreement with the measured ones. It is important to note that while these modifications in the parameter of the transport code influence substantially the distribution function at the energies corresponding to the two peaks, they do not change otherwise the global properties of the suprathermal electron distribution function.

### 3.2 Doppler frequency analysis

We now present a method to derive both the electron Doppler velocity $u_e$ of the ambient electron population and the electron plasma frequency $\omega_e$ from the measured up- and down shifted plasma line frequencies.

The down- and upshifted plasma lines correspond to two Langmuir waves $(k_-, \omega_-)$ and $(k_+, \omega_+)$ travelling away from and toward the radar, respectively, in the backscatter geometry. They are high-frequency solutions of the dispersion relation (Guio *et al.*, 1998)

$$1 + \left(\frac{\omega_e}{k_\pm v_e}\right)^2 \mathrm{Re}\ Z_n\left(\frac{2\pi f_{r\pm}}{k_\pm v_e}\right) = 0 \tag{7}$$

Eliminating $\omega_e$ and $v_e$ between these two equations and replacing $Z_n$ by its ambient and suprathermal components and replacing the frequencies $f_{r\pm}$ by the phase velocity $v_{\phi\pm}$, the electron Doppler velocity $u_e$ of the ambient electron population is the solution of the following equation

$$k_+^2\left((1-\alpha)\mathrm{Re}\ Z_n^a\left(\frac{v_{\phi-}-u_e}{v_e}\right) + \alpha\,\mathrm{Re}\ Z_n^s\left(\frac{v_{\phi-}}{v_e}\right)\right) = k_-^2\left((1-\alpha)\mathrm{Re}\ Z_n^a\left(\frac{v_{\phi+}-u_e}{v_e}\right) + \alpha\,\mathrm{Re}\ Z_n^s\left(\frac{v_{\phi+}}{v_e}\right)\right) \tag{8}$$

where the drift velocity $u_e$ appears only in the terms relative to the ambient component $Z_n^a$ and we will consider here two models of velocity distribution to describe the ambient population: a Maxwellian and a Spitzer function that takes into account the gradient of the electron temperature (Guio *et al.*, 1998).

Once the Doppler velocity $u_e$ is found, the plasma frequency $\omega_e$ is given by

$$\omega_e = (k_\pm v_e)\times \left|(1-\alpha)\mathrm{Re}\ Z_n^a\left(\frac{v_{\phi\pm}-u_e}{v_e}\right) + \alpha\,\mathrm{Re}\ Z_n^s\left(\frac{v_{\phi\pm}}{v_e}\right)\right|^{-\frac{1}{2}} \tag{9}$$

either evaluated for the down-going Langmuir wave with phase velocity $v_{\phi\pm}$ or the up-going one with phase velocity $v_{\phi-}$.

Figures 10–12 show the result of this analysis. Figure 10 presents the Maxwellian case whereas Fig. 11 is for the Maxwellian superimposed with the suprathermal distribution and Fig. 12 is for the Spitzer function superimposed with the suprathermal distribution.

The data set can be separated into three intervals where the Doppler velocity $u_e$ is constant: before the first

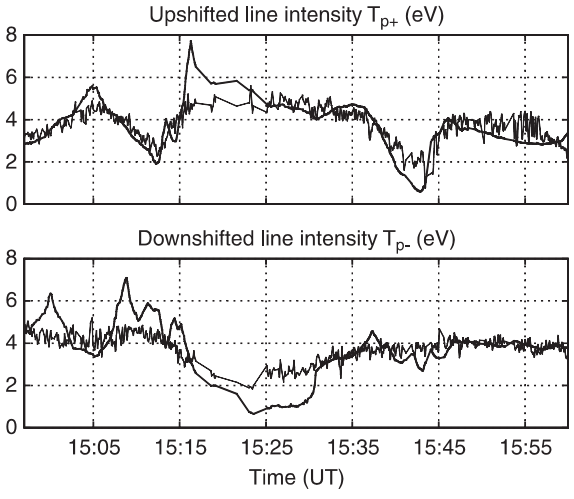


**Fig. 9.** Comparison between the measured plasma line intensities and the modelled intensities as a function of time. The modelled intensities are calculated using the $P_n^s$ and $Z_n^s$ functions of Fig. 8

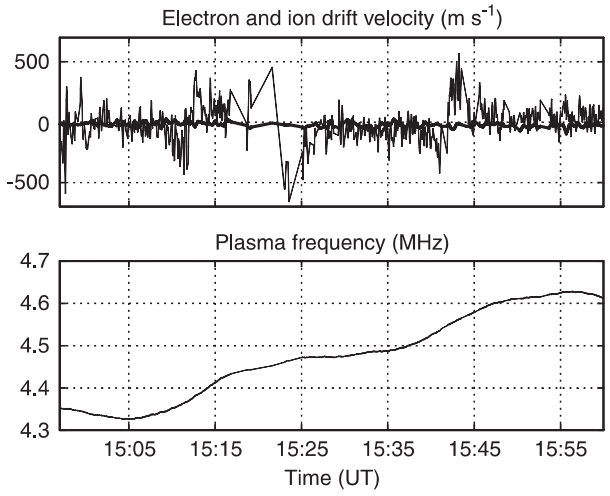


**Fig. 10.** The upper panel shows the estimated ion drift velocity $u_i$ (*thick line*) from the ion line analysis and the electron drift velocity $u_e$ (*thin line*) from the analysis method based on Eq. (8) without suprathermal population ($\alpha = 0$) and assuming a Maxwellian ambient population with the parameters of Fig. 6. The lower panel shows the estimated plasma frequency $\omega_e/2\pi$ given by Eq. (9)

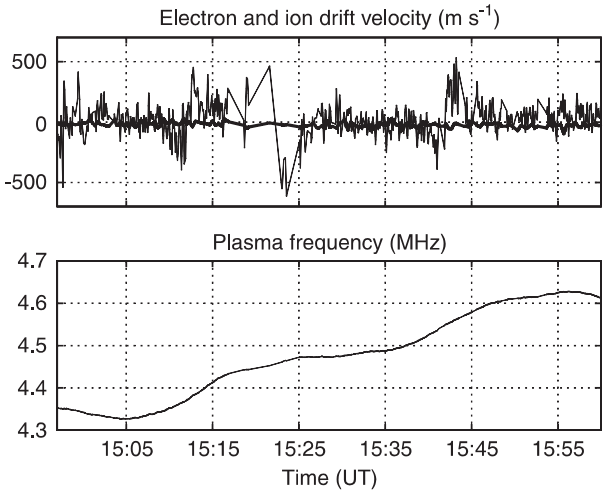


**Fig. 11.** The *upper panel* shows the estimated ion drift velocity $u_i$ (*thick line*) from the ion line analysis and the electron drift velocity $u_e$ (*thin line*) from the analysis method based on Eq. (8) with a suprathermal population described by the distribution function of Fig. 8 with a Maxwellian background of parameters of Fig. 6. The *lower panel* shows the estimated plasma frequency $\omega_e/2\pi$ given by Eq. (9)

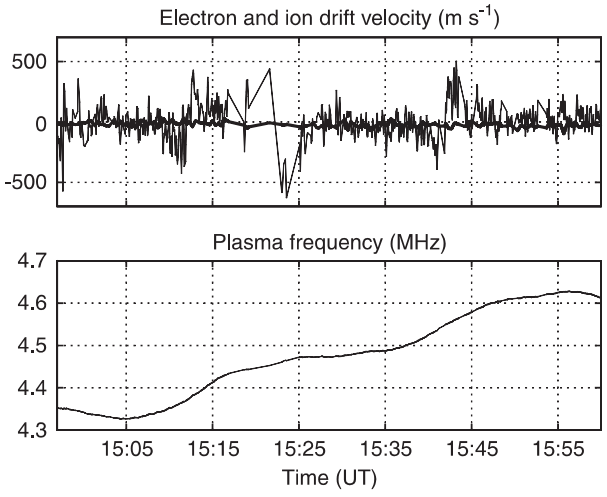


**Fig. 12.** The *upper panel* shows the estimated ion drift velocity $u_i$ (*thick line*) from the ion line analysis and the electron drift velocity $u_e$ (*thin line*) from the analysis method based on Eq. (8) with a suprathermal population described by the distribution function of Fig. 8 and a Spitzer function for the ambient electrons with parameters of Fig. 6. The *lower panel* shows the estimated plasma frequency $\omega_e/2\pi$ given by Eq. (9)

feature of change of sign at 15:12 UT, between the second feature at 15:23 UT and the third one at 15:43 UT and after this last one. Table 1 gives the mean value of the Doppler velocity $u_e$ for the different models considered as well as the mean value of the ion Doppler velocity $u_i$ for these three time intervals. The effect of the suprathermal electrons is clearly seen, our suprathermal velocity distribution reduces the relative differences of $u_e$ between the three intervals. The effect of the Spitzer function is thereafter to shift down the whole mean drift velocity, which we expected as the heat

**Table 1.** Mean value of the electron Doppler velocity $u_e$ for the four different models considered: a Maxwellian, a Spitzer function, a Maxwellian superimposed with a suprathermal distribution and a Spitzer superimposed with a suprathermal distribution as well as the ion Doppler velocity $u_i$ estimated from the ion line analysis. The suprathermal distribution is the one shown in Fig. 8 and the parameters of the Spitzer function are the one of Figure 6. The mean Doppler are calculated for the three time intervals considered. The first number in each column is the velocity in $ms^{-1}$ while the number in parenthesis is the equivalent frequency Doppler shift in Hz

| | 14:57–15:09 | 15:26–15:39 | 15:46–16:00 |
|---|---|---|---|
| Maxwellian | −25 (−74) | −72 (−214) | +37 (+112) |
| Spitzer | −57 (−169) | −95 (−282) | +17 (+50) |
| Maxwellian + Supra | +22 (+66) | −10 (−29) | +48 (+143) |
| Spitzer + Supra | −10 (−30) | −32 (−97) | +27 (+82) |
| Ion line Doppler $u_i$ | −15 (−45) | −27 (−81) | −29 (−86) |

flow effect behaves like a mean Doppler velocity. The superposition of the suprathermal distribution to the Spitzer function (with parameters of Fig. 6) gives estimates of $u_e$ in best agreement with $u_i$.

On the other hand, we were not able to reduce considerably the features at 15:12 UT, 15:24 UT and 15:43 UT even though they are probably the effect of the suprathermal electrons as it can be thought by examining carefully the real part of the $Z_n^s$ function of Fig. 8. Qualitatively, the real part of $Z_n^s$ around 24.25 eV and 26.25 eV has a correct shape to compensate these changes in the electron Doppler velocity $u_e$. These three events are characterised by an abrupt change of sign of the Doppler velocity. During the first feature at 15:12 UT the Doppler velocity first decreases, then increases. At this time, the phase energy of the upshifted plasma line moves across 24.25 eV where the real part of $Z_n^s$ first increases, then decreases while the phase energy of the downshifted plasma line is around 25.25 eV where the real part of $Z_n^s$ increases slowly (see Fig. 8). Thus the term $k_-^2 \mathrm{Re} Z_n^s(E_{\phi+})$ of Eq. (8) is varying qualitatively correctly so that Eq. (8) should be satisfied without such variations being reflected on the electron Doppler velocity $u_e$. During the two other features the same effect is observed. At 15:24 UT the phase energy of the downshifted plasma line moves across 26.25 eV which gives an opposite effect, it is now the term $k_+^2 \mathrm{Re} Z_n^s(E_{\phi-})$ of Eq. (8) that compensates. At 15:43 UT, the phase energy of the upshifted plasma line moves across 26.25 eV which gives an effect in the same direction as the first one. Moreover the first feature at 15:12 UT is not so emphasised as the two other ones. It corresponds to the $N_2$ photoionisation peak while the two other features correspond to the O photoionisation which effect on the real part of $Z_n^s$ is more emphasised than for the $N_2$ peak.

It can be pointed out that the frequency correction caused by our model of photoelectrons is of the same order as the one predicted with a Maxwellian photoelectron population (Bauer *et al.*, 1976). We note also that while the difference of the electron mean velocity $u_e$ is substantial, the difference in the estimated plasma frequency $\omega_e$ remains under 1 KHz.

## 4 Conclusion

We have discussed a high time resolution plasma line data set measured by the EISCAT VHF radar in the summer daytime ionosphere. We have presented a method to analyse both the intensity and the Doppler frequency shift of the plasma lines using a model taking into account the suprathermal electron population and the effect of the electron temperature gradient on the ambient population. The data set has been analysed with this method. Parameters of the electron transport code, such as the solar intensity flux and the ionisation threshold of $N_2$ and O had to be adjusted to take into account correctly the detailed structures of the suprathermal distribution in the energy range 23.5–28.5 eV. Our model reproduces well the temporal variations of the intensity of the plasma lines and we have identified the effect of $N_2$ and O photoionisation at 24.25 eV and 26.25 eV caused by the solar discrete emission line HeII. We then derived the electron mean Doppler velocity and the plasma frequency and identified also the effect of $N_2$ and O photoionisation. It is shown that our model for photoelectrons superimposed with a Spitzer function for the ambient electrons is able to reproduce the variations in the intensity of the plasma lines as well as explain substantially the variations of the Doppler frequency of the plasma lines for the data set measured with the EISCAT VHF radar.

*Acknowledgements.* The authors would like to thank Odile Dutuit de Lure and Roland Thissen for helpful discussions as well as the EISCAT personal for their efforts in making the radar available. EISCAT is funded by the CNRS of France, the SA of Finland, the MPG of Germany, the NFR of Norway, the NFR of Sweden, and the PPARC of United Kingdom.

Topical Editor D. Alcaydé thanks two referees for their help in evaluating this paper.

## References

**Bauer P., K. D. Cole, and G. Lejeune,** Field-aligned electric currents and their measurement by the incoherent backscatter technique, *Planet. Space Sci.*, **24,** 479–485, 1976.

**Bjørnå N., and J. Trulsen,** Effect of a power law particle flux on the ionospheric incoherent scattering cross section, *Phys. Scr.*, **33,** 284–288, 1986.

**Bjørnå, N., O. Havnes J. O. Jensen, and J. Trulsen,** Enhancement of the incoherent scattering plasma lines due to precipitating protons and secondary electrons, *Phys. Scr.*, **25,** 632–636, 1982.

**Chiu, Y.-H., H. Fu, J.-T. Huang, and S. L. Anderson,** Vibrational mode effects, scattering dynamics, and energy disposal in reaction of $C_2H_2^+$ with methane, *J. Chem. Phys.*, **102,** 1199–1216, 1995.

**Cohen R. S., L. Spitzer, and P. McR. Routly,** The electrical conductivity of an ionized gas, *Phys. Rev.*, **80,** 230–238, 1950.

**Fennelly J. A., and D. G. Torr,** Photoionization and photoabsorption cross sections of O, N2 and N for aeronomic calculations, *Atomic Data and Nuclear data tables*, **51,** 321–363, 1992.

**Guio P., N. Bjørnå, and W. Kofman,** Alternating-code experiment for plasma-line studies. *Ann. Geophys.*, **14,** 1473–1479, 1996.

**Guio P., J. Lilensten , W. Kofman, and N. Bjørnå,** Electron velocity distribution function in a plasma with temperature gradient and in the presence of suprathermal electrons: application to incoherent scatter plasma lines, *Ann. Geophys.*, **16,** 1226–1240, 1998.

**Hagfors T., and M. Lehtinen,** Electron temperature derived from incoherent scatter radar observations of the plasma line frequency, *J. Geophys. Res.*, **86,** 119–124, 1981.

**Hedin A. E.,** Extension of the MSIS Thermospheric Model into the Middle and Lower Atmosphere, *J. Geophys. Res.*, **96,** 1159–1172, 1991.

**Heinselman C. J., and J. F. Vickrey,** On the spectral analysis and interpretation of incoherent scatter plasma line echoes, *Radio Sci.*, **27,** 221–230, 1992.

**Kirkwood S., H. Nilsson, J. Lilensten, and M. Galand,** Strongly enhanced incoherent-scatter plasma lines in aurora, *J. Geophys. Res.*, **100,** 21343–21355, 1995.

**Kofman W., and G. Lejeune,** Determination of low energy photoelectron distribution from plasma line measurements at Saint Santin, *Planet. Space Sci.*, **28,** 661–673, 1980.

**Kofman W., G. Lejeune, T. Hagfors, and P. Bauer,** Electron temperature measurements by the plasma line technique at the french incoherent scatter radar facilities, *J. Geophys. Res.*, **86,** 6795–6801, 1981.

**Kofman W., J.-P. St-Maurice, and A. P. van Eyken,** Heat flow effect on the plasma line frequency, *J. Geophys. Res.*, **98,** 6079–6085, 1993.

**Lejeune G., and W. Kofman,** Photoelectron distribution determination from plasma line intensity measurements obtained at Nanay (france), *Planet. Space Sci.*, **25,** 123–133, 1977.

**Lilensten J., W. Kofman, J. Wisenberg, E. S. Oran, and C. R. Devore,** Ionization efficiency due to primary and secondary photoelectrons: a numerical model, *Ann. Geophys.*, **7,** 83–90, 1989.

**Lummerzheim D.,** Electron transport and optical emission in the aurora, PhD thesis, University of Alaska, Fairbanks, 1987.

**Lummerzheim D., and J. Lilensten,** Electron transport and energy degradation in the ionosphere: evaluation of the numerical solution, comparison with laboratory experiments, auroral observations, *Ann. Geophys.*, **12,** 1039–1051, 1994.

**Newman A. L., and E. S. Oran,** The effects of electron-neutral collisions on the intensity of plasma lines, *J. Geophys. Res.*, **86,** 4790–4794, 1981.

**Oran E. S., V. B. Wickwar, W. Kofman, and A. Newman,** Auroral plasma lines: a first comparison of theory and experiment, *J. Geophys. Res.*, **86,** 199–205, 1981.

**Pavlov A. V., and M. J. Buonsanto,** Using steady state vibrational temperature to model effects of $N_2^*$ on calculations of electron densities, *J. Geophys. Res.*, **101,** 26941–26945, 1996.

**Perkins F., and E. E. Salpeter,** Enhancement of plasma density fluctuations by nonthermal electrons, *Phys. Rev. A*, **128,** 55–62, 1965.

**Perkins F., E. E. Salpeter, and K. O. Yngvesson,** Incoherent scatter from plasma oscillations in the ionosphere, *Phys. Rev. Lett.*, **14,** 579–581, 1965.

**Sheffield J.,** *Plasma scattering of electromagnetic radiation*, Academic Press, New York, 1975.

**Showen R. L.,** The spectral measurement of plasma lines, *Radio Sci.*, **14,** 503–508, 1979.

**Spitzer L. Jr, and R. Härm,** Transport phenomena in a completely ionized gas, *Phys. Rev.*, **89,** 977–981, 1953.

**Tobiska W. K., and F. G. Eparvier,** EUV97: improvements to EUV irradiance modeling in the soft X-Rays and FUV, *Solar Phys.*, **177,** 147–159, 1998.

**Torr M. R., and D. G. Torr,** Ionization frequencies for solar cycle 21: Revised, *J. Geophys. Res.*, **90,** 6675–6678, 1985.

**Vidal-Madjar D., W. Kofman, and G. Lejeune,** Mesures de la raie de plasma par diffusion incohérente à Nançay, et premiers résultats morphologiques, *Ann. Geophys.*, **31,** 227–234, 1975.

**Warren H. P., J. T. Mariska, and J. Lean,** A new reference spectrum for the EUV irradiance of the quiet Sun 1. Emission measure formulation, *J. Geophys. Res.*, **103,** 12077–12089, 1998a.

**Warren H. P., J. T. Mariska, and J. Lean,** A new reference spectrum for the EUV irradiance of the quiet Sun 2. Comparison with observations and previous models, *J. Geophys. Res.*, **103,** 12091–12102, 1998b.

**Woods T. N., G. J. Rottman, S. M. Bailey, S. C. Solomon, and J. R. Worden,** Solar extreme ultraviolet irradiance measurements during solar cycle 22, *Solar Phys.*, **177,** 133–146, 1998.

**Yngvesson K. O., and F. W. Perkins,** Radar Thomson scatter studies of the photoelectrons in the ionosphere and Landau damping, *J. Geophys. Res.*, **73,** 97–100, 1968.

# References


**Ashihara, O. and K. Takayanagi**. Velocity distribution of ionospheric low-energy electrons. *Planet. Space Sci.*, **22**, 1201–1217, 1974.

**Balescu, R.** *Statistical mechanics of charged particles*. Interscience Publishers, London, 1963.

**Balescu, R.** *Transport processes in plasmas*. North-Holland, Amsterdam, 1988. ISBN 0-444-87093-8.

**Banks, P. M.** Charged particle temperatures and electron thermal conductivity in the upper atmosphere. *Ann. Geophysicæ*, **22**, 577–587, 1966.

**Banks, P. M., C. R. Chappell, and A. F. Nagy**. A new model for the interaction of auroral electrons with the atmosphere: spectral degradation, backscatter, optical emission, and ionization. *J. Geophys. Res.*, **79**, 1459–1470, 1974.

**Banks, P. M. and A. F. Nagy**. Concerning the influence of elastic scattering upon photoelectron transport and escape. *J. Geophys. Res.*, **75**, 1902–1910, 1970.

**Barakat, A. R. and R. W. Schunk**. transport equations for multicomponent anisotropic space plasmas: a review. *Plasma phys.*, **24**, 389–418, 1982.

**Bard, Y.** *Non linear parameter estimation*. Academic Press, New York, 1974. ISBN 0-12-078250-2.

**Bauer, P.** Theory of waves incoherently scattered. *Phil. Trans. Roy. Soc. London*, **280**, 167–191, 1975.

**Bauer, P., K. D. Cole, and G. Lejeune**. Field-aligned electric currents and their measurement by the incoherent backscatter technique. *Planet. Space Sci.*, **24**, 479–485, 1976.

**Berger, M. J., S. M. Seltzer, and K. Maeda**. Some new results on electron transport in the atmosphere. *J. Atmos. Terr. Phys.*, **36**, 591–617, 1974.

**Bhatnagar, P. L., E. P. Gross, and M. Krook**. A model for collision processes in gases. I. Small amplitude processes in charged and neutral one-component systems. *Phys. Rev.*, **94**, 511–525, 1954.

**Birkmayer, W. and T. Hagfors**. Observational technique and parameter estimation in plasma line spectrum observations of the ionosphere by chirped incoherent scatter radar. *J. Atmos. Terr. Phys.*, **48**, 1009–1019, 1986.

**Bjørnå, N. and J. Trulsen**. Effect of a power law particle flux on the ionospheric incoherent scattering cross section. *Physica Scripta*, **33**, 284–288, 1986.

**Bowles, K. L.** Observations of vertical incidence scatter from the ionosphere at 41 Mc/s. *Phys. Rev. Lett.*, **1**, 454–455, 1958.

**Brekke, A.**, editor. *Radar Probing of the Auroral Plasma*. Universitetsforlaget, Oslo, 1977. ISBN 82-00-02421-0.

**Chandrasekhar, S.** *Radiative transfer*. Dover, New York, 1960.

**Chapman, S. and T. G. Cowling**. *The mathematical theory of non-uniform gases - 3rd ed.* Cambridge University Press, New York, 1970. ISBN 0-521-40844-X (paperback).

**Cicerone, R. J.** Photoelectrons in the ionosphere: radar measurements and theoretical computations. *Rev. Geophys. Space Phys.*, **12**, 6709–6728, 1974.

**Cohen, R. S., L. Spitzer, and P. McRoutly**. The electrical conductivity of an ionized gas. *Phys. Rev.*, **80**, 230–238, 1950.

**Djuth, F. T., M. P. Sulzer, and J. H. Elder**. Application of the coded long-pulse technique to plasma line studies of the ionosphere. *Geophys. Res. Lett.*, **21**, 2725–2728, 1994.

**Djuth, F. T., M. P. Sulzer, J. H. Elder, and W. V. B.** High-resolution studies of atmosphere-ionosphere coupling at arecibo observatory, puerto rico. *Radio Sci.*, **32**, 2321–2344, 1997.

**Dougherty, J. P. and D. T. Farley**. A theory of incoherent scattering of radio waves by a plasma. *Proc. Roy. Soc. A.*, **259**, 79–99, 1960.

**Dougherty, J. P. and D. T. Farley**. A theory of incoherent scattering of radio waves by a plasma 3. scattering in a partly ionized gas. *J. Geophys. Res.*, **68**, 5473–5486, 1963.

**Farley, D. T.** A theory of incoherent scattering of radio waves by a plasma 4. the effect of unequal ion and electron temperatures. *J. Geophys. Res.*, **71**, 4091–4098, 1966.

**Farley, D. T.** Incoherent scatter correlation functions measurements. *Radio Sci.*, **4**, 935–953, 1969.

**Farley, D. T.** Multiple-pulse incoherent-scatter correlation function measurements. *Radio Sci.*, **7**, 661–666, 1972.

**Farley, D. T., J. P. Dougherty, and D. W. Barron**. A theory of incoherent scattering of radio waves by a plasma 2. scattering in a magnetic field. *Proc. R. Soc. Lond.*, **263**, 238–258, 1961.

**Folkestad, K., T. Hagfors, and S. Westerlund**. EISCAT: An updated description of technical characteristics and operational capabilities. *Radio Sci.*, **18**, 867–879, 1983.

**Fredriksen, Å., N. Bjørnaa, and T. L. Hansen**. First EISCAT two-radar plasma line experiment. *J. Geophys. Res.*, **94**, 2727–2731, 1989.

**Fredriksen, Å., N. Bjørnaa, and J. Lilensten**. Incoherent scatter plasma lines at angles with the magnetic field. *J. Geophys. Res.*, **97**, 16921–16933, 1992.

**Fried, B. D. and S. D. Conte**. *The plasma dispersion function: the Hilbert transform of the Gaussian*. Academic Press, New York, 1961.

**Galand, M.** *Transport des protons dans l'ionosphère aurorale*. PhD thesis, Université Joseph Fourier, Grenoble, 1996.

**Gombosi, T. I. and C. E. Rasmussen**. Transport of gyration-dominated space plasmas of thermal origin 1. generalized transport equations. *J. Geophys. Res.*, **96**, 7759–7778, 1991.

**Gordon, W. E.** Incoherent scattering of radio waves by free electrons with applications to space exploration by radar. *Proc. I.R.E*, **46**, 1824–1829, 1958.

**Gray, D. R. and J. D. Kilkenny**. The measurement of ion acoustic turbulence and reduced thermal conductivity caused by a large temperature gradient in a laser heated plasma. *J. Atmos. Terr. Phys.*, **22**, 81–111, 1980.

**Guio, P.** A simple model for the velocity distribution of particles in a plasma with temperature gradient. *Ann. Geophysicæ*, 1998. Submitted.

**Guio, P., N. Bjørnå, and W. Kofman**. Alternating-code experiment for plasma-line studies. *Ann. Geophysicæ*, **14**, 1473–1479, 1996.

**Guio, P. and J. Lilensten**. Effect of suprathermal electrons on the intensity and doppler frequency of electron plasma lines. *Ann. Geophysicæ*, 1998. Submitted.

**Guio, P., J. Lilensten, W. Kofman, and N. Bjørnå**. Electron velocity distribution function in a plasma with temperature gradient and in the presence of suprathermal electrons: application to incoherent-scatter plasma lines. *Ann. Geophysicæ*, **16**, 1226–1240, 1998.

**Gurevitch, A. V. and Y. N. Istomin**. Thermal runaway and convective heat transport by fast electrons in a plasma. *Sov. Phys. JETP*, **50**, 470–475, 1979.

**Hagfors, T.** Density fluctuations in a plasma in a magnetic field, with application to the ionosphere. *J. Geophys. Res.*, **66**, 1699–1712, 1961.

**Hagfors, T.** The scattering of E.M. waves from density fluctuations in a plasma. In Brekke (1977), pages 15–28. ISBN 82-00-02421-0.

**Hagfors, T.** Incoherent scatter radar observations of the plasma line with a chirped pulse system. *Radio Sci.*, **17**, 727–734, 1982.

**Heinselman, C. J. and J. F. Vickrey**. On the frequency of Langmuir waves in the ionosphere. *J. Geophys. Res.*, **97**, 14905–14910, 1992a.

**Heinselman, C. J. and J. F. Vickrey**. On the spectral analysis and interpretation of incoherent scatter plasma line echoes. *Radio Sci.*, **27**, 221–230, 1992b.

**Holt, J. M., D. A. Rhoda, D. Tetenbaum, and A. P. van Eyken**. Optimal analysis of incoherent scatter radar data. *Radio Sci.*, **27**, (3), 435–447, 1992.

**Ichimaru, S.** *Statistical plasma physics: basic principles*. Addison-Wesley, Redwood City, Ca., 1992. ISBN 0-201-55490-9 (Vol. 1).

**Iijima, T. and T. A. Potemra**. The amplitude distribution of field-aligned currents at northern high latitudes observed by TRIAD. *J. Geophys. Res.*, **81**, 2165–2174, 1976.

**Jasperse, J. R.** Boltzmann-Fokker-Planck model for the electron distribution functions in the Earth's ionosphere. *Planet. Space Sci.*, **24**, 33–40, 1976.

**Kirkwood, S., H. Nilsson, J. Lilensten, and M. Galand**. Strongly enhanced incoherent-scatter plasma lines in aurora. *J. Geophys. Res.*, **100**, 21343–21355, 1995.

**Kofman, W. and C. Lathuillere**. EISCAT multipulse technique and its contribution to auroral ionosphere and thermosphere description. *J. Geophys. Res.*, **90**, 3520–3524, 1985.

**Kofman, W., G. Lejeune, P. Bauer, K. Folkestad, and T. Hagfors**. Eiscat first plasma line experiment. *Ann. Géophys.*, **38**, 461–466, 1982.

**Kofman, W., G. Lejeune, T. Hagfors, and P. Bauer**. Electron temperature measurements by the plasma line technique at the french incoherent scatter radar facilities. *J. Geophys. Res.*, **86**, 6795–6801, 1981.

**Kofman, W., J.-P. St-Maurice, and A. P. van Eyken**. Heat flow effect on the plasma line frequency. *J. Geophys. Res.*, **98**, 6079–6085, 1993.

**Kofman, W. and V. Wickwar**. Plasma line measurement at chatanika with high-speed correlator and filter bank. *J. Geophys. Res.*, **85**, 2998–3012, 1980.

**Krinberg, I. A.** Description of the photoelectron interaction with ambient electrons in the ionosphere. *Planet. Space Sci.*, **21**, 523–525, 1973.

**Krinberg, I. A. and L. A. Akatova**. Electron distribution function in the lower ionosphere and its relation with the rate of production and heating of electrons. *Geomagn. Aeron*, **18**, 411–415, 1978.

**Ledley, B. G. and W. H. Farthing**. Field-aligned current observations in the polar cusp ionosphere. *J. Geophys. Res.*, **79**, 3124–3128, 1974.

**Lehtinen, M. S.** Statistical theory of incoherent scatter measurements. Technical Report 86/45, EISCAT Scientific Association, Kiruna, Sweden, 1986. Ph. D. Thesis, University of Helsinki, Helsinki, Finland.

**Lehtinen, M. S. and I. H. Häggström**. A new modulation principle for incoherent scatter measurements. *Radio Sci.*, **22**, 625–634, 1987.

**Lehtinen, M. S. and A. Huuskonen**. General incoherent scatter analysis and GUISDAP. *J. Atmos. Terr. Phys.*, **58**, (1-4), 435–452, 1996.

**Lejeune, G.** On the inversion problem of the plasma line intensity measurements in terms of photoelectron fluxes. *Planet. Space Sci.*, **27**, 557–560, 1979.

**Lejeune, G. and W. Kofman**. Photoelectron distribution determination from plasma line intensity measurements obtained at nançay (france). *Planet. Space Sci.*, **25**, 123–133, 1977.

**Ljepojevic, N. N.** Electron velocity distribution function in a fully ionized plasma slab with a large temperature gradient: solar flare transition region. *J. Quant. Spectrosc. Radiat. Transfer*, **44**, 203–208, 1990.

**Ljepojevic, N. N. and A. Burgess**. Calculation of the electron velocity distribution function in a plasma slab with large temperature and density gradients. *Proc. R. Soc. Lond.*, **A 428**, 71–111, 1990.

**Ljepojevic, N. N. and P. McNeice**. Heat flux in a non-Maxwellian plasma. *Phys. Rev. A*, **40**, 981–986, 1989.

**Luciani, J. F., P. Mora, and J. Virmont**. Nonlocal heat transport due to steep temperature gradients. *Phys. Rev. Lett.*, **51**, 1664–1667, 1983.

**Lummerzheim, D.** *Electron transport and optical emissions in the aurora*. PhD thesis, University of Alaska, Fairbanks, 1987.

**Lummerzheim, D. and J. Lilensten**. Electron transport and energy degradation in the ionosphere: evaluation of the numerical solution, comparison with laboratory experiments, auroral observations. *Ann. Geophysicæ*, **12**, 1039–1051, 1994.

**Min, Q.-L., D. Lummerzheim, M. H. Rees, and K. Stamnes**. Effects of a parallel electric field and the geomagnetic field in the topside ionosphere on auroral and photoelectron energy distributions. *J. Geophys. Res.*, **98**, 19223–19234, 1993.

**Mishin, E. V. and T. Hagfors**. On heat flow contribution to plasma line frequency in the F region. *J. Geophys. Res.*, **99**, 6537–6539, 1994.

**NAG**. *The NAG Fortran Library Manual Mark 16*. The Numerical Algorithms Group Limited, Oxford, 1993.

**Newman, A. L. and E. S. Oran**. The effects of electron-neutral collisions on the intensity of plasma lines. *J. Geophys. Res.*, **86**, 4790–4794, 1981.

**Nygren, T., A. Huuskonen, and P. Pollari**. Alternating-coded multipulse codes for incoherent scatter experiments. *J. Atmos. Terr. Phys.*, **58**, 465–477, 1996.

**Oran, E. S., V. B. Wickwar, W. Kofman, and A. Newman**. Auroral plasma lines: a first comparison of theory and experiment. *J. Geophys. Res.*, **86**, 199–205, 1981.

**Perkins, F. and E. E. Salpeter**. Enhancement of plasma density fluctuations by nonthermal electrons. *Phys. Rev. A*, **139**, 55–62, 1965.

**Perkins, F., E. E. Salpeter, and K. O. Yngvesson**. Incoherent scatter from plasma oscillations in the ionosphere. *Phys. Rev. Lett.*, **14**, 579–581, 1965.

**Press, W. H., S. A. Teukolsky, W. T. Vetterlin, and B. P. Flannery**. *Numerical recipes in C: the art of scientific computing*. Cambridge University Press, Cambridge, 1992. ISBN 0-521-43108-5.

**Rosenbluth, M. N. and N. Rostoker**. Scattering of electromagnetic waves by a nonequilibrium plasma. *Phys. Fluids*, **5**, 776–788, 1962.

**Rostoker, N.** Test particle method in kinetic theory of a plasma. *Phys. Fluids*, **7**, 491–498, 1964.

**Salpeter, E. E.** Electron density fluctuations in a plasma. *Phys. Rev.*, **120**, 1528–1535, 1960.

**Sheffield, J.** *Plasma scattering of electromagnetic radiation*. Academic Press, New York, 1975. ISBN 0-12-638750-8.

**Shkarofsky, I. P.** Values of the transport coefficients in a plasma for any degree of ionization based on a maxwellian distribution. *Can. J. Phys.*, **39**, 1619–1668, 1961.

**Showen, R. L.** The spectral measurement of plasma lines. *Radio Sci.*, **14**, 503–508, 1979.

**Showen, R. L.** Spectral plasma lines at Sondrestrom. *Radio Sci.*, **30**, 1841–1853, 1995.

**Spitzer, L.** *Physics of fully ionized gases*. Interscience Publishers, New York, 1962.

**Spitzer, L. and R. Härm**. Transport phenomena in a completely ionized gas. *Phys. Rev.*, **89**, 977–981, 1953.

**Stamnes, K.** Analytic approach to auroral electron transport: extensions of Stolarski's (1972) work. *J. Geophys. Res.*, **82**, 2391–2395, 1977.

**Stamnes, K.** Analytic approach to auroral electron transport and energy degradation. *Planet. Space Sci.*, **28**, 427–441, 1980.

**Stamnes, K.** A unified theory of interhemispheric electron transport and energy degradation. *Geophysica Norvegica*, **33**, 41–51, 1985.

**Stamnes, K. and M. H. Rees**. Inelastic scattering effects on photoelectron spectra and ionospheric electron temperature. *J. Geophys. Res.*, **88**, 6301–6309, 1983.

**Stamnes, K., S.-C. Tsay, W. Wiscombe, and K. Jayaweera**. Numerically stable algorithm for discrete-ordinate-method radiative transfer in multiple scattering and emitting layered media. *Applied Optics*, **27**, 2502–2509, 1988.

**Strickland, D. J., D. L. Book, T. P. Coffey, and J. A. Fedder**. Transport equation techniques for the deposition of auroral electrons. *J. Geophys. Res.*, **81**, 2755–2764, 1976.

**Sulzer, M. P.** A radar technique for high range resolution incoherent scatter autocorrelation function measurements utilizing the full average power of klystron radars. *Radio Sci.*, **21**, 1033–1040, 1986.

**Sulzer, M. P.** Recent incoherent scatter techniques. *Adv. Space Res.*, **9**, 153–162, 1989.

**Sulzer, M. P.** A new type of alternating code for incoherent scatter measurements. *Radio Sci.*, **28**, 995–1001, 1993.

**Takayanagi, K. and Y. Itikawa**. Elementary processes involving electrons in the ionosphere. *Space Sci. Rev.*, **11**, 380–450, 1970.

**Trulsen, J. and N. Bjørnå**. The origin and properties of thermal fluctuations in a plasma. In Brekke (1977), pages 29–54. ISBN 82-00-02421-0.

**Tsytovich, V. N.** *Lectures on non-linear plasma kinetics*. Springer-Verlag, Berlin, 1995. ISBN 3-540-57844-7.

**Turunen, T.** The Universal Correlator Program - a versatile tool for calculating the target autocorrelation function in incoherent scatter radar measurements. Technical Report 83/8, EISCAT Scientific Association, Kiruna, Sweden, 1983.

**Turunen, T.** The GEN-System for the EISCAT incoherent scatter radars. Technical Report 85/44, EISCAT Scientific Association, Kiruna, Sweden, 1985.

**Turunen, T.** GEN-SYSTEM - a new experimental philosophy for EISCAT radars. *J. Atmos. Terr. Phys.*, **48**, 777–785, 1986.

**Turunen, T. and J. Silen**. Modulation pattern for the EISCAT incoherent scatter radars. *J. Atmos. Terr. Phys.*, **46**, 593–599, 1984.

**Vallinkoski, M.** Error analysis of incoherent scatter measurements. Technical Report 89/49, EISCAT Scientific Association, Kiruna, Sweden, 1989.

**Wannberg, G.** The G2-system and general purpose alternating code experiments for EISCAT. *J. Atmos. Terr. Phys.*, **55**, 543–557, 1993.

**Wannberg, G., I. Wolf, L.-G. Vanhainen, K. Koskenniemi, J. Röttger, M. Postila, J. Markkanen, R. Jacobsen, A. Stenberg, R. Larsen, S. Eliassen, S. Heck, and A. Huuskonen**. The EISCAT Svalbard radar: a case study in modern incoherent scatter radar design. *Radio Sci.*, **32**, (6), 2283–2307, 1997.

**Weinstock, J.** New approach to the theory of fluctuations in a plasma. *Phys. Rev. A*, **139**, 388–393, 1965.

**Weinstock, J.** Correlation functions and scattering of electromagnetic waves by inhomogeneous and nonstationary plasmas. *Phys. Fluids*, **10**, 2065–2072, 1967.

**Woods, L. C.** *An introduction to the kinetic theory of gases and magnetoplasmas*. Oxford University Press, Oxford, 1993. ISBN 0-19-856393-0.

**Yngvesson, K. O. and F. W. Perkins**. Radar Thomson scatter studies of the photoelectrons in the ionosphere and Landau damping. *J. Geophys. Res.*, **73**, 97–100, 1968.

**Zmuda, A. J. and J. C. Armstrong**. The diurnal flow pattern of field-aligned currents. *J. Geophys. Res.*, **79**, 4611–4619, 1974.